Deploying nature-based solutions in urban areas : thermal performance and urban feasibility across scales

Leydy Castellanos Diaz

École des Ponts ParisTech

THÈSE DE DOCTORAT
de l'École des Ponts ParisTech

Deploying Nature-Based Solutions in urban areas: Thermal performance and urban feasibility across scales.

Déploiement des Solutions fondées sur la nature en milieu urbain : Performance thermique et faisabilité urbaine à toutes les échelles.

École doctorale N° 531, Sciences, Ingénierie et Environnement (SIE)
Spécialité : Sciences et Techniques de l'Environnement
Thèse préparée au sein des laboratoires HM&Co et LVMT

Thèse soutenue le 21 avril 2022, par

Leydy Alejandra CASTELLANOS DIAZ

Composition du jury :

Georges, NAJJAR Université de Strasbourg	*Rapporteur*
Čedo, MAKSIMOVIĆ Imperial College London	*Rapporteur*
Claudia Hedwig, YAMU Oslo Metropolitan University	*Examinatrice*
David, RAMIER CEREMA	*Examinateur*
Rosa, VICARI Vinci	*Examinatrice*
Ioulia, TCHIGUIRINSKAIA École des Ponts ParisTech	*Directrice de thèse*
Oliver, BONIN Université Gustave Eiffel	*Co-Directeur de thèse*
Pierre-Antoine, VERSINI École des Ponts ParisTech	*Co-Directeur de thèse*

HM&Co HYDROLOGY METEOROLOGY and COMPLEXITY

LVMT Laboratoire Ville Mobilité Transport

Acknowledgements

I would like to convey my special gratitude to Ioulia, Olivier and Pierre-Antoine for your scientific guidance during these years. I really appreciated our discussions, your insightful advice, and comments, that helped me to improve my research. My sincere gratitude to the thesis committee: Professor George Najjar, Professor Čedo Maksimovic, Professor Claudia Yamu, Dr. David Ramier, Dr. Rosa Vicari. Thank you for your time and dedication to review this dissertation and providing me with contributions.

A special thanks to David Ramier (Cerema) for his valuable technical and scientific advice, and to lend me the evapotranspiration chamber to carry out this research. To Frederique Bourdignon and the ISC-PIF team for their introduction to text-mining approaches. To Daniel Schertzer and August Gires to carry out multifractal coffees and webinars, that helped me with the understanding of multifractal framework.

Particular thanks must go to HM&Co team that help me with the campaign of measure in the BGW every summer: August, Filip, Julian, Jerry, Mario and Pierre-Antoine. Thanks to Yangzi and Xin to be the best office friends always with snacks and teas. I'm a tea and hot water lover now. Many thanks to all the rest of HM&Co colleagues for their support during this time: Guillaume, Rosa, Ilecktra, Jisun, Angel, Hai, Arun, Adashm. Thanks to Catherine and Albertine, who always assisted me with administrative matters.

Undoubtedly, this thesis would not have been reached without the unconditional support, the patience and comprehension of Camilo. Your encouragement words during the most difficult times of this journey were my biggest calm. Thanks for the energy to read this document, and the good and practical advice.

A special gratitude to my family and friends. Despite the distance, I always feel you by my side, with your support and motivation. ¡Infinitas gracias abuelita!

Abstract

The urbanisation process and the reduction of the natural land cover, have altered energy balance and climate within cities, enhancing the Urban Heat Island (UHI) effect. This effect occurs when elevated temperatures are experienced in high dense areas, mainly at night. Climate change could increase extreme events (as heatwaves) in terms of intensity and frequency, and exacerbate the UHI phenomena. Therefore, Nature-Based Solution (NBS), such as green roofs, emerged as a relevant high elevated temperatures mitigation strategy, due to the shading effect and evapotranspiration (ET) from vegetation. Nevertheless, the performance of NBS to cool the air and its variability across different temporal and spatial scales are still unclear. As well, the conditions that can influence their implementation in complex urban environments are little studied.

In this context, throughout this thesis, the elements likely to influence the installation of NBS across scales have been evaluated. For this purpose, first some measurement campaigns of the ET process were carried out in the Blue Green Wave (BGW), a green roof located in Bienvenüe building in front of the Ecole des Ponts ParisTech (eastern of Paris). The thermal performance of the BGW was characterised through three different methods: the surface energy balance (SEB), an evapotranspiration chamber and the water balance during dry conditions. Differences in the three measurement methods were observed and the errors causing these were discussed. A sensitivity analysis served to determine principal variables affecting SEB estimations and formulate recommendations for further measurement campaigns.

Second, the fractal geometry was used to analyse the complexity and heterogeneity of the spatial distribution of urban elements in the case study of Est-Ensemble (eastern of Paris), and to develop some multiscale scenarios of NBS deployment. More specifically, fractal dimension helped to analyse the hierarchical organisation of the built-up structure and NBS across different scales. These scaling properties (fractal

organisations of both NBS and built-up structure spatial fields) were used to produce multiscale scenarios making possible the insertion of NBS of different sizes within the urban environment not occupied by buildings (lacunas).

Finally, in order to improve the understanding of thermal flux variability measured in the BGW and to make the link with the previous spatial analysis, statistical multiscale data analysis was carried out. The spectral analysis exhibited the scale invariance behaviour of air temperature and structure parameter of refractive index of air ($C_n{}^2$), both fluxes impacting ET. Moreover, the structure function highlighted the intermittence and multifractality of $C_n{}^2$ and temperature fluctuations. The scale invariant properties of fluctuations were characterised through the Universal Multifractal (UM) framework. The results demonstrated the multifractality of $C_n{}^2$ was stronger than the temperature, indicating the influence of additional turbulent processes than heat convection on $C_n{}^2$ fluctuations. This suggested the need to investigate the additional meteorological parameters affecting turbulent activity in the BGW, such as wind speed. In this way, the scaling behaviour of ET could be fully characterised and spatial scales of NBS installation could be determined based on their cooling effect.

Key words: Nature-Based Solutions; evapotranspiration; spatial organisation; multiscales; fractal and multifractal, lacunas.

Résumé

L'urbanisation et l'imperméabilisation des sols naturels qu'elle a provoquée ont engendré une modification du bilan énergétique et du micro-climat dans les villes, favorisant l'effet d'Ilot de Chaleur Urbain (ICU). Cet effet se produit lorsque des températures plus élevées sont enregistrées dans des zones à forte densité, notamment pendant la nuit. Dans un contexte du changement climatique, l'intensité et occurrence des événements extrêmes (comme les vagues de chaleur) pourraient être plus élevées, ce qui exacerberait ce phénomène. Les Solutions fondées sur la Nature (SFN), telles que les toitures végétalisées, apparaissent aujourd'hui comme une stratégie pertinente d'atténuation des températures élevées, en raison de l'effet d'ombrage et de l'évapotranspiration (ET) produits par la végétation. Néanmoins, la performance réelle des SFN pour rafraichir l'air, ainsi que sa variabilité à différentes échelles temporelles et spatiales, sont encore mal connues. De plus, les conditions qui peuvent influencer leur mise en œuvre dans des environnements urbains complexes ont été très peu étudiées.

Dans ce contexte, cette thèse s'intéresse à l'évaluation d'éléments susceptibles d'influencer la mise en place de SFN à travers les échelles. Dans un premier temps, des campagnes de mesure de l'ET ont été réalisées dans la Blue Green Wave (BGW), une toiture végétalisée située sur le bâtiment Bienvenüe, placé en face de l'Ecole des Ponts ParisTech. Les performances thermiques de la BGW ont été caractérisées par trois méthodes différentes d'estimation de l'ET, utilisant respectivement : le bilan énergétique de surface (SEB), une chambre d'évapotranspiration et le bilan hydrique par temps sec. Des différences dans les trois méthodes de mesure ont été observées et les erreurs à l'origine de celles-ci ont été discutées. Une analyse de sensibilité a permis de déterminer les principales variables affectant les estimations et de formuler des recommandations pour de futures campagnes de mesure.

Dans un second temps, la géométrie fractale a été utilisée pour analyser la complexité et l'hétérogénéité de la distribution spatiale des formes urbaines au sein du cas d'étude

d'Est-Ensemble (est de Paris), et pour développer des scénarios multiéchelles de déploiement de SFN. Plus précisément, la dimension fractale a permis d'analyser l'organisation hiérarchique de la structure bâtie et des SFN à différentes échelles. Ces propriétés d'échelle ont ensuite été utilisées dans la réalisation de scénarios multiéchelles à concilier structure bâtie existante et futures SFN. Cette approche à base fractale a permis de proposer des installations de SFN de différentes tailles dans les espaces non occupés par les bâtiments (lacunes), mais également sur les bâtiments existants (végétalisation des toitures par exemple).

Enfin, afin d'améliorer la compréhension de la variabilité temporelle des flux thermiques mesurés sur la BGW et de faire le lien avec l'analyse spatiale précédente, une analyse statistique multi-échelle des données a été réalisée. L'analyse spectrale a démontré le comportement scalant de la température de l'air et le paramètre de structure de l'indice de réfraction de l'air ($C_n{}^2$), impactant tous deux le flux d'ET. De plus, la fonction de structure a mis en évidence l'intermittence et multifractalité des fluctuations de $C_n{}^2$ et température. Ainsi, les propriétés d'invariance d'échelle des fluctuations ont été caractérisées dans le cadre des multifractals universels. Les résultats ont démontré la multifractalité de $C_n{}^2$ était plus forte que celle de la température, indiquant l'influence des processus turbulents supplémentaires à la convection thermique sur les fluctuations de $C_n{}^2$. Cela suggère la nécessité d'étudier paramètres météorologiques supplémentaires affectant l'activité turbulente, telle que la vitesse du vent. De cette manière, l'invariance d'échelle du flux d'ET pourrait être entièrement caractérisé et les échelles spatiales pour l'installation des SFN seraient déterminées en fonction de leur effet de refroidissement.

Mots clés : Solutions fondées sur la nature ; évapotranspiration ; organisation spatiale ; multiéchelles ; fractale et multifractale ; lacunes.

Table of Content

List of Tables

List of Figures

Abbreviations

ABL	Atmospheric Boundary Layer
BGS	Blue Green Solutions
BGW	Blue Green Wave
BO	Bolgiano Oubkhov
Cerema	Centre D'études Et D'expertise Sur Les Risques, L'environnement, La Mobilité Et L'aménagement
CICES	Common International Classification of Ecosystem Services
DFT	Discrete Fourier Transform
DoE	Design of Experiments
DTM	Double Trace Moments
EbA	Ecosystem-Based Adaptation
EC	European Commission
ECO	Eddy Covariance method
EEA	European Environment Agency
EM	Electromagnetic pulse-beam
ET	Evapotranspiration
ESS	Ecosystem services
EU	European Union
FFT	Fast Fourier Transform
IFS	Iterative Function System
ISC-PIF	CNRS Complex Systems Institute of Paris Île-de-France

K41	Kolmogorov Self-Similarity Hypothesis
LAS	Large Aperture Scintillometer
LHS	Latin Hypercube Sampling
METEO FRANCE	National meteorological service of France
MOST	Monin-Obukhov Similarity Theory
MAES	Mapping Assessment of Ecosystem and their Services
MGP	Metropolis of Greater Paris
NBS	Nature-Based Solutions
NATURVATION	NATure-based URban innovation
N4C	Nature 4 Cities
MEA	Millennium Ecosystem Assessment
PBL	Planetary Boundary Layer
Pdf	probability density function
RSH	Refined Similarity Hypothesis
SEB	Surface Energy Balance
SuDS	Sustainable Urban Drainage Systems
TDR	Time Domain Reflectometry technique
TM	Trace Moments
UGI	Urban Green Infrastructure
UHI	Urban heat island
UM	Universal Multifractal
WHO	World Health Organization

List of symbols

α	Multifractal index (-)
A_{ch}	Area of the evapotranspiration chamber (m^2)
$B_{uu\ldots u}$	Statistical moment
β	Spectral exponent (-)
β_r	Bowen ratio (-)
${C_n}^2$	Structure parameter of refractive index of air ($m^{-2/3}$)
C_p	Specific heat capacity of air at constant pressure (J/K kg)
C_1	Mean singularity (-)
$c(\gamma)$	Codimension function (-)
D	Aperture diameter of LAS (m)
D_f, $f(\alpha)$	Fractal dimension (-)
$Demod$ or I	Signal strength or demodulated signal (mV)
d	Zero-displacement height (m)
ET	Evapotranspiration flux (mm/d)
ϵ	Turbulent kinetic energy dissipation rate
ε	Size of boxes side (-)
f_T	Universal stability function (-)
g	Gravity force (m/s^2)
γ, a_D	Singularity (-)
H	Hurst exponent (-)
H_2O	Water vapour (absolute humidity) (g/m^3)
h	Height of obstacles, crop height(m)
I	Irrigation (mm/d)
$K(q)$	Moment scaling function (-)
k	Soil thermal conductivity (W/m K)
k_a	Dielectric permittivity of the soil (-)
k_v	Von Karman constant (-)

L	Outer scale
l_o	Observation scale
l_k, L_k	Inner and outer scale energy cascade (m)
L_v	Latent heat flux of vaporization of water (J/kg)
Lw_{in}	Incoming long-wave radiation (W/m²)
Lw_{out}	Reflected long-wave radiation (W/m²)
λ	Scale ratio or resolution (-)
λ_s	Wavelength of electromagnetic wave signal (nm)
n	Refractive index of air (-)
P	Air pressure (Pa)
Pr	Precipitation (mm/d)
$PUCn_2$	Scaled value of Cn_2 ($m^{-2/3}$)
ρ_a	Air density (kg/m³)
ρ_w	Water density (kg/m³)
Q	Humidity (kg/m³)
dQ/dt	Absolute humidity variation (g/m³s)
Qe	Latent heat flux (W/m²)
Qg	Conduction heat flux (W/m²)
Qh	Sensible heat flux (W/m²)
Qr	Surface runoff (mm/d)
q	Statistical moments order (-)
R	Horizontal path length between transmitter and receiver (m)
RH	Relative humidity (%)
Rn	Net radiative flux of energy in a green roof (W/m²)
R_v	Specific gas constant for water vapour (J/K kg)
r	Position (space or time)
S_q	Structure function of any moment q (-)
S_{uu}	Second order structure function
Sw_{in}	Incoming short-wave (solar) radiation (W/m²)

Sw_{out}	Reflected short-wave (solar) radiation (W/m²)
ΔS	Soil water content variation (mm/d)
ψ_m	Stability function for momentum (-)
σ_I	Standard variation of intensity fluctuations (mV)
σ_{UCn_2}	Standard variation of log of ${C_n}^2$ (V)
$\sigma_{ln\,I}^2$	Variance of the intensity fluctuations natural logarithm (-)
T	Absolute air temperature (K)
T_*	Temperature scale (K)
T_{ext}	Air temperature outside the chamber (C)
T_{int}	Air temperature inside the chamber (C)
T_{soil}	Soil temperature (°C)
$T_{z1\ldots4}$	Soil temperature at different depths $z_{1\ldots4}$ (m)
dT/dz	Soil temperature gradient (K/m)
τ	Time increments
U	Wind speed (m/s)
UCn_2	Log of ${C_n}^2$ (V)
u_*	Friction velocity (m/s)
u	Atmospheric variable
V_{ch}	Volume of the evapotranspiration chamber (m³)
VWC	Volumetric water content (m³/m³)
ν	Kinematic viscosity (m²/s)
WD	Wind direction (°)
z_0	Aerodynamic roughness length (m)
z_{LAS}	Effective height of the scintillometer beam above the surface (m)
z_s	Soil layer thickness (m)
z_R	Height of receiver (m)
z_T	Height of transmitter (m)
z_u	Height wind speed measurements (m)
$\zeta(q)$	Structure function scaling exponent (-)

Introduction

The world's population has increased very rapidly since 1950 and nowadays most of this is living in urban areas. According to the last revision of the UN (United Nations, Department of Economic and Social Affairs, Population Division, 2019) in 2018, 55% of total world's population (i.e., 4.2 billion of people) resided in cities, and is expected to reach 68% by 2050. Therefore, this urban growth has led to the replacement of natural surfaces within cities by impermeable materials, such as cement or asphalt, for construction of buildings and roads. These changes of surface properties impact mass and energy balances of the space (Oke, 1987). Thus, processes involved in water cycle, such as infiltration or evapotranspiration (ET), may be reduced, and the airflow dynamics may be modified.

Consequently, some phenomena have appeared in urban environments. Such is the case of the Urban Heat Island (UHI), characterised by higher air temperatures within the cities that in the nearest rural spaces. In the most recent report of the IPCC, AR6 Climate Change 2021 (IPCC, 2021), the effects of the climate change due to anthropogenic emission of greenhouse gases is warned. Specially, the intensity of global surface temperature rise, as well as greatest frequency of extreme events, particularly heatwaves. In this context, the UHI effect may be exacerbated, and generating environmental and health risks for the population in the cities.

Within the framework of the Sustainable Development Goal 11 of the United Nations (UN), "Sustainable cities and communities", the adaptation of cities is imperative as well as the improvement of urban resilience strategies, to facing the challenges created jointly by rapid urbanization and climate change. In consequence, the modification of urban microclimate and the accessibility to natural green spaces have become central concerns of the research community and local authorities. To mitigate such challenges and enhance urban resilience, the Nature-Based Solutions (NBS) have emerged as they can restore natural processes, while providing a variety of valuable environmental,

economic and social advantages (European Commission & Directorate-General for Research and Innovation, 2015).

One benefit of NBS widely claimed is the temperature reduction or urban cooling (Norton et al., 2015; Qiu et al., 2013), thanks to the action of shading and evapotranspiration (ET) provided by vegetation. Hence, their installation seems suitable with regards to the mitigation of the UHI intensity. Nevertheless, in practice the deployment of NBS to cool the air is complex as no consensus has been reached on the real value of this benefit. Additionally, the cost of installation and maintenance of NBS requires their location ensures their cooling performance is efficient across scales of urban space.

Therefore, the NBS deployment to regulate urban microclimate implies understanding their physical and thermal behaviour, investigating the most appropriated approach for their installation, and evaluating the variability of NBS performance across scales. In this way, the effective NBS performance could be integrated in the method of NBS deployment in a territory at different scales.

Various methodologies have been applied to quantify and characterise the processes involved in the temperature reduction, more specifically the ET process. However, measurements are not homogeneous (DiGiovanni et al., 2013; Meili et al., 2021), and further research is necessary to fully understand the physical and thermal behaviour of the NBS.

One of difficulties understanding the ET process is related to the gap between scales of measure of NBS. On one side, numerous studies have performed measurements at the local or site scale of the NBS, such as the green roofs (Coutts et al., 2013; Heusinger & Weber, 2017; Marasco et al., 2015; Thorp, 2014; Wadzuk et al., 2013). Conversely, some investigations have used other methods to measure the reduction of temperature at larger scales, such as urban parks (Fung & Jim, 2017; Shashua-Bar et al., 2009) or cities (Masoudi & Tan, 2019; Zhang et al., 2017). In consequence, the characterisation of the spatial and temporal behaviour of thermal processes from NBS across scales is

necessary, as this would allow determining reliable conditions of NBS' deployment that effectively mitigate the temperatures.

The complexity of urban space is another barrier to overcome for the successful NBS' installation (Cohen-Shacham et al., 2019). The hierarchies and the organisation of urban settlements at different scales, as well as spatial interactions and greening policies, would influence the conditions of NBS integration within the urban space (Versini, Gires, et al., 2020). Thus, it results convenient the analyse of the most efficient way to marry built-up areas and NBS, to provide benefits across different scales of the urban space.

Hence, the integration of NBS to effectively reduce the temperature of air is conditioned by the variability of the ET flux, as well as the social dynamics within the cities, at different spatial and temporal scales. In this context, the main objective of this PhD is the evaluation of the thermal performance of NBS and their deployment across different urban scales. For achieve that goal, this research shall have the following specific objectives:

- Evaluation and quantification of the thermal performance of NBS at the local scale. More precisely, the characterisation of the ET process on a green roof and related thermal conditions.
- Assessment of the most efficient strategies of NBS implementation across different urban scales, without disrupting spatial organisation of an urban space.
- Analysis of spatial and temporal variability of thermal fluxes of NBS, that determine their performance across different scales, through scaling approaches.

The thesis is developed in two parts. First, the services provided by NBS are investigated and then a more extensive investigation is conducted about the ET process in a green roof. Then, the scale invariance properties of the spatial organisation of an urban environment are analysed, to develop spatial scenarios of NBS

deployment. Moreover, the scale invariance properties of the thermal fluxes measured in the green roof are examined and characterised.

In the first part, the benefits from the implementation of the NBS are explored. In the Chapter 1, the main ecosystem services provided by NBS in urban environment, as well as some approaches for their implementation in Europe, are investigated through a text-mining analysis coupled with data visualization. This analysis defines the scientific framework in which this PhD was conducted. More specifically, it underlines the necessity to assess properly the urban cooling benefit through relevant indicators across different scales. This leads to quantify and characterise the thermal fluxes of such infrastructures. Thus, the Chapter 2 aims to describe the ET process on a green roof through the utilisation of three different methods of measurement: the surface energy balance, the evapotranspiration chamber, and the water balance during dry periods.

In the second part, the scaling properties of the urban space as well as the geophysical fluxes measured on the green roof have been investigated. Therefore, the fractal geometry that serves to describe complex forms, such as the urban patterns, is introduced in the Chapter 3. The fractal properties of such patterns in an existing territory, near the green roof where the ET monitoring campaign was carried out, are analysed, and used for the development of multiscale scenarios of NBS deployment.

To determinate the scaling behaviour of the thermal fluxes at different scales, statistics-based methods as the spectra and the structure function, have been analysed in the Chapter 4. Then, from geometrical fractals, the multifractals and the Universal Multifractal framework are be introduced, to characterise the spatial and temporal scaling properties of the thermal fluxes on the green roof.

Chapter 1 Integration of Nature-Based Solutions in urban areas

In this chapter, NBS are introduced like a strategy responding to several urban challenges. For this purpose, the text-mining technique coupled with a data visual representation was applied to analyse literature review reports regarding benefits offered by NBS. Therefore, the text-mining software Gargantex (https://gargantext.org/) was employed to explore the key-terms of each report based on its co-occurrence. Later, the software Gephi (https://gephi.org/) was used to create a visual representation of these key-terms, designing networks of terms for each report. This allowed to convert text of reports (corpus) into a meaningful structure analysis.

The results indicated despite different methodologies used in every literature review, this methodology allowed to objectively compare findings, just as recognize patterns of most important attributes of NBS implementation in urban spaces. Some common trends exhibit the NBS installation as a strategy of urban resilience, the recognition of ecosystem services (ESS) delivered by nature and the use of indicators to quantify their performance at different spatial scales. By contrast, some specific attributes were noted in each report, such as, the economic valuation and monetisation of NBS and their services, or the participatory planning approach to NBS implementation and maintenance.

1.1 Introduction

The challenges induced by urbanization and climate change encourage the integration of green and blue infrastructures in the functioning of our cities. This aims to mitigate the intensity of extreme events, such as floods and heat waves, to moderate the hot spots of dense urban areas (e.g., Urban Heat Island, UHI), and overall to improve

urban resilience capacity to negative impacts of climate change. Several concepts have emerged to refer to these infrastructures promoting nature reintegration into build environment (Kabisch et al., 2017); such as Ecosystem-Based Adaptation (EbA), Sustainable Urban Drainage Systems (SuDS), Urban Green Infrastructure (UGI) or Nature-Based Solutions (NBS).

Aiming to build urban resilience, the European Commission (EC) introduced the NBS concept in its Horizon 2020 Program as "living solutions inspired and continuously supported by nature, which are designed to address various societal challenges in a resource-efficient and adaptable manner and to provide simultaneously economic, social, and environmental benefits" (European Commission Directorate General, Research and Innovation, 2015). Moreover, the EbA concept has a climate change adaptation focus and aims towards the management and use of biodiversity and ecosystem services (ESS) as part of an overall adaptation strategy, reducing vulnerability and building resilience (Secretariat of the Convention on Biological Diversity, 2009). Besides, SuDs were conceived to reduce the impact on surface water drainage systems of urban flooding and pollution of surface water, such as rainwater runoff or sewer overflows. Meanwhile, the UGI concept is defined as a hybrid infrastructure of green spaces and built systems (Demuzere et al., 2014), which can contribute to ecosystem resilience and human benefits through ESS. The EIT Climate-KIC Blue Green Dream project (https://hmco.enpc.fr/portfolio-archive/blue-green-dream/) appears as a pioneering European project devoted to this topic (Rozos et al., 2013). It first valued the role of NBS in the holistic management of urban green asset and water resources. Afterwards, this approach has been expanded to exploit the full range of ESS that NBS provide to society, yielding the Blue Green Solutions (BGS, Bozovic et al., 2017).

During the last decade, the research community has studied NBS worldwide to provide the impacts and co-benefits of these structures within cities, generating a huge amount of literature regarding this topic. This is the case of regulating services like storm-water management or temperature reduction. For instance, it was demonstrated

an important reduction of the peak flow in the Avola (southern Italy) stormwater sewer because the implementation of green roofs and permeable pavements (Pappalardo et al., 2017). Further, the implementation of different NBS facilities—such as green roofs, rain gardens, green spaces, green swales, permeable pavements and retention basins—proved the minimization of both peak discharge and runoff volumes by up to 90% on the full range of rainfall event return periods at the urban project scale (Versini et al., 2018).

Regarding UHI mitigation, a literature review indicated that thanks to evapotranspiration (ET) and shading of urban vegetation, there was a reduction of urban temperatures ranging from 0.5 to 4.0 °C, depending mainly on the green area and wind dynamics (Qiu et al., 2013). Similarly, a reduction of 1°C in land surface temperature during a heatwave event was performed by a 10% increase in vegetation cover in Melbourne (Australia) (Coutts et al., 2013). Meanwhile, further studies have targeted the analysis of "park cool island" to prove the cooling effect of urban park vegetation (Fung & Jim, 2017; Shashua-Bar et al., 2009). Other services provided by NBS, like noise reduction (Kabisch et al., 2017; Lopez et al., 2018), biodiversity restoration (Ives et al., 2016; Threlfall et al., 2017) and well-being (Faivre et al., 2017), have been analysed and quantified less.

Since these solutions are of interest to tackle the urban sustainability challenges of European cities, the EC has funded several projects to develop frameworks or guidelines for NBS implementation. To improve the base knowledge of physical, social, and economic impact, extensive literature reviews have been carried out. However, it is quite difficult to compare the results of these literature reviews in order to consolidate the analysis and to find a consensus about the actual outcomes and benefits of all the proposed NBS. In this context, the next sections of the chapter aim to objectively compare the NBS literature review of three Horizon 2020 (H2020) NBS projects: EKLIPSE, MAES-Urban Ecosystems and NATURVATION, by exploring their latest deliverables through a text-mining technique. These three projects were chosen since they were pioneers in mapping NBS at the European scale and understanding

their efficiency in tackling urban challenges. Consequently, these compose a reference widely cited by the scientific community and used by local governments as urban adaptation guides.

The purpose of text-mining is to extract meaningful structured information from text data. Thus, text-mining enables us to identify the key concepts and the main stakeholders described in the corpus, as well as their relationships. Text-mining goes beyond lexical analysis by identifying patterns and attributes. Recently, text-mining tools were used to investigate and characterise how climate risk management issues are represented in 12 online strategic documents released by public authorities in Paris (Vicari et al., 2019). The applied method allowed to expose results not revealed through a qualitative analysis of the document (classic literature review), such as the integrated approach of public authorities to manage urban risk and the advocacy of NBS. Similarly, this approach was applied to understand the conceptual difference between urban resilience and urban sustainability, as well as the multi-level perspective for urban resilience and regional residence on peer-review literature of the Scopus database (Rogov & Rozenblat, 2018).

The next section is structured as follows. Firstly, the text data of the H2020 NBS projects are presented, and their approaches and methodologies are identified (Section 1.2.1). Then, for each document, a mapping of the text data allows to extract the list of key terms used to create a graph. This graph exposes the main statistical properties of each text (Sections 1.2.2 and 1.2.3). Finally, the results of each document are analysed individually (Section 1.3), and then compared to each other and to the scientific literature (Section 1.4), enabling to identify common and different approaches.

1.2 Methodology

1.2.1 Corpus

In a general way, to proceed with text-mining, the first step is the collection of texts to be analysed, known in linguistics as “text corpus”. The corpus used in this study

corresponds to three full-text reports. These reports are the final deliverables of the EC projects published between 2016 and 2017 about NBS impacts in urban areas at the European scale (Table 1.1): EKLIPSE, MAES-Urban Ecosystems and NATURVATION. These projects are presented bellow with some details summarized in Table A.1.

The EKLIPSE Project was launched under the Horizon 2020 framework and aimed to build a sustainable and innovative EC support mechanism for evidence-based policy on biodiversity and ESS (https://www.eklipse-mechanism.eu/). The EKLIPSE Project was selected by the EC to establish a sustainable framework of design, development, implementation, and assessment of NBS demonstration projects in the urban context using a holistic approach. The methodology was based on the study of scientific literature conducted either in research publications (320 peer-review articles or books) or in unpublished "grey" literature provided by organizational websites and web search engines (1223 units). Finally, additional references were added by the EKLIPSE Working Group (EWG) members and coordinators of NBS European Union (EU) projects (247 articles, books, and reports). The resulting framework suggests 10 challenges that would support climate resilience at different spatial and temporal scales. These challenges were selected from the expert report on NBS supported by DG Research and Innovation-EC (European Commission, 2016) and a recent review of the NBS frameworks (Kabisch et al., 2016). Each challenge and the potential actions to mitigate, manage or promote it by means of UGI are included in the final report entitled "An impact evaluation framework to support planning and evaluation of nature-based solutions projects." The expected impacts and the effectiveness indicators based on the results of the literature review are included in this report; for this reason, this document constitutes the first text corpus for this study.

The Mapping Assessment of Ecosystem and their Services (MAES) initiative was launched by the EC in response to Action 5 of the EU Biodiversity Strategy to 2020 (https://biodiversity.europa.eu/maes). It aimed to define actions and plans to mitigate and stop biodiversity loss in the EU. To achieve this goal, the ecosystem's condition and their services were assessed and mapped. The 4th report of MAES initiative

published in 2016 was exclusively dedicated to urban ecosystems and, for this reason, it constitutes the second corpus for analysis in this study. In this report, a survey and review of 54 scientific articles was used as a source of information to map urban green spaces, assess their condition, and measure the ESS they provide. Additionally, ten case studies in Europe provided the base for real applications of NBS, allowing for a wide variety of ecosystem conditions to set the service assessment indicators. The results of the MAES initiative were used in the ESMERALDA project (Enhancing ecoSysteM sERvices mApping for poLicy and Decision mAking) to develop a 'flexible methodology' for pan-European, national, and regional ESS mapping and assessment (http://www.esmeralda-project.eu/).

The technical feasibility of NBS implementation, as well as the assessment of their benefits to tackle urban challenges, have been widely analysed by the academic community. However, despite the fact that NBS provide benefits and values for different stakeholders (Toxopeus & Polzin, 2017), there are very few studies on their economic valorisation, like cost-benefits analysis (Faivre et al., 2017). Hence, the NATure-based URban innoVATION (NATURVATION) project was launched to develop a comprehensive NBS assessment tool for urban areas with their economic implications (https://naturvation.eu/about). For this purpose, a literature review of 105 studies from the academic fields related to the financial and economic values of NBS was carried out, linking a monetary value to ESS (ecological and societal effect) and urban challenges. Because of the economic character of this report, it was considered as third corpus for the text-mining.

All the reports have commonly aimed to perform a literature review focused on current scientific knowledge of impacts, benefits and trade-offs provided by the implementation of NBS. However, each one adopted a specific methodology depending on its main objective and the stakeholders' involvement in the project. The complementarity of these three reports (urban challenges and NBS assessment through indicators (EKLIPSE); mapping of key urban ESS through successful experiences supported by public authorities (MAES) and the economic and financial

review of NBS (NATURVATION)) suggests to study the ensemble of approaches and stakeholders that could influence the impacts and benefits of NBS deployment. Such ensemble has not been yet identified in a classic qualitative literature review.

Table 1.1. The three corpuses of text-mining analysis: NBS oriented projects.

Report	Literature	Source
EKLIPSE- An impact evaluation framework to support planning and evaluation of nature-based solutions projects. Publication: 2017.	320 peer-review scientific articles or books. 1223 pieces of grey literature. 247 articles, books, and reports.	Data-bases searches. Organizational website and web search engines. EKLIPSE Working Group.
Mapping and Assessment of Ecosystems and their Services (MAES) Urban ecosystems 4th Report. Publication: May 2016.	54 scientific articles. 10 case studies.	Science Direct Data-base research. Proposed by the research community.
NATURVATION- Review of Economic Valuation of Nature Based Solutions in Urban Areas. Publication: May 2017.	105 studies from the academic work.	Data-bases searches (meta-analysis).

Given that every report is the result of a literature review of numerous articles, each report constitutes a text corpus that could first be explored individually.

1.2.2 Text-Mining analysis

Usually, literature review documentation has an extent which easily allows its reading and synthesis. However, while doing so, each reader would be biased by their own field of expertise. It is for this reason that even though the H2020 NBS reports are easily readable, this research proceeded to analyse and compare them independently from the author's scientific domain of research through a text-mining analysis.

To evaluate the content of each document, the text-mining analysis was carried out through Gargantex Blue Jasmine Version (Chavalarias & Delanoe, 2017), an open source software developed by the CNRS Complex Systems Institute of Paris Île-de-France (ISC-PIF) and its partners. The main purpose of Gargantex is to analyse the publication information of a large set of scientific literature articles (up to 1000). In this research, the publication information of articles (i.e., keywords, abstract, title, date of publication and author) is replaced by smaller units from the corpus texts, generally from the length of a paragraph (500 words approximately).

The Gargantex algorithm automatically extracts a list of words (or terms) from each corpus, based on their co-occurrence taking into consideration the integrality of the text. Each term is characterised by a status, according to three possibilities: map, stop and not flagged. The "map-list" contains the key or meaningful terms with the highest occurrences, which are used in the data visualization (Figure 1.1). The "stop-list" regroups the terms with few occurrences or without a meaningful conceptual contribution in the text (e.g., lists, tables, or figures). Finally, the "not flagged" words are not classified in any of the previous lists (e.g., concentration, percentage, or projects).

To refine the term-list, a terms-status modification and a lexicographic analysis is done by the user. This means keeping relevant terms with high occurrence that refer to NBS, environmental impacts, NBS governance and/or stakeholders (e.g., "blue spaces", "air pollutants", "local communities"). Likewise, the user can remove the meaningless words marked as "map", such as the author's name (e.g., "Baro", "Cohen", "Kabish",

etc.) or nouns themselves (e.g., "tables", "units", etc.) Furthermore, synonyms and acronyms can be aggregated (e.g., "assessment", "valuation" or "report", "document"), as well as singular and plural forms (e.g., urban green infrastructure, green infrastructure or ugi), creating groups of terms and increasing their occurrences and co-occurrences.

Statistical properties of the corpus texts, such as their length, will impact the output statistical text-mining analysis. Length can be expressed in term of pages or paragraphs. Table 1.2 displays the statistical characteristics of the three corpus texts.

Table 1.2. Statistical features of corpus text.

Length	EKLIPSE	MAES	NATURVATION
Pages	82	94	34
Paragraphs	143	254	58

1.2.3 Data Visual Representation and Quantitative Analysis

To facilitate the understanding of the text-mining results, the map-list terms are used to elaborate a visual representation in a graph or network form. A graph is a mathematical representation of interconnections between different elements and is composed of nodes (map-list terms) connected by edges (connections between terms). The networks are built with respect to the conditional proximity, an absolute measure that reflects the highest co-occurrences between two key terms in the same textual context (Rogov & Rozenblat, 2018). Gargantex uses the Louvain Modularity Cluster Algorithm to create communities of nodes in the network (known as clusters), regrouping the nodes strongly related with the same colour on the map. Each cluster is supposed to represent one approach, concept or idea conveyed by the text. According to the node topics, a name is allocated to each cluster by the user.

In order to characterise the properties of the network and the related clusters, a Gargantex GEXF file is extracted to be used as input data in the open-access interactive software of graph visualization and network analysis Gephi (URL: https://gephi.org/).

By means of Gephi, all the statistic properties (attributes) of the network can be viewed and analysed by the user. The attributes analysed in this study are the node degree and the edge weight. They correspond respectively to the number of edges connected to a node and the strength of link between nodes (probability of co-occurrence between a pair of nodes). The node degree is a measure of centrality, which determines the influence or importance of a node in the network. Therefore, the centrality concept depends on the studied context. In the case of NBS, it might refer to the most significant NBS benefit or the most valuable solution in a complex urban context.

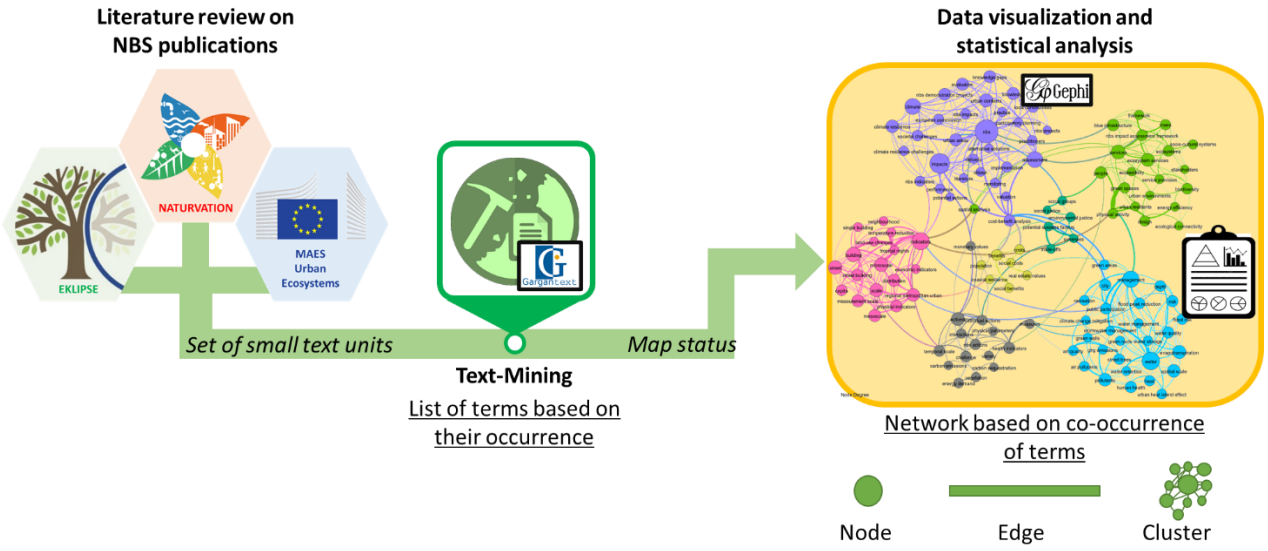

Figure 1.1. Text-mining and data visualization process.

The size node and the edge thickness in the networks indicate the node degree and the edge weight, respectively. Note that only nodes characterised by a degree higher than 3 are conserved in the analysis. Finally, the Gephi topological tools are used to improve the readability of the network by saving its original attributes (node degree and edge weight).

1.3 Results

In this section, the network representations of each corpus text are analysed individually. The clusters composing the network are discretized and analysed relying on the number of nodes integrating each cluster and their accumulated degree (sum

of nodes degree). Furthermore, the resulting network attributes (node degree and edge weight) are examined deeply. This allows to draw conclusions or statements, which were supported by the scientific publication review.

1.3.1 EKLIPSE

The most important nodes in the EKLIPSE network were identified visually (Figure 1.2) and according to their degree (Table A.2). They include "nbs" with the highest degree (36), followed by "impacts" (29) and "indicators" (22). This node degree classification suggests how NBS appears in the urban context, as a strategy to face environmental impacts and urban challenges. Then, "water" (22) appears as the environmental resource most impacted by "climate change" (19), compared with "air" (10) and "soil" (not even mentioned). "Management" and "assessment" are both positioned as keywords (with a node degree of 19), highlighting the possibility to gain services for the population. With a lower but nonnegligible degree (16 to 14) appear the terms related to scales like "building", "street" or "microscale", illustrating the importance of knowing well the NBS' scale of implementation to assess their performance in the urban planning process.

The NBS implementation evaluation framework in the EKLIPSE project is structured through seven clusters (Figure 1.2 and Table 1.3). Due to the quantity of nodes and their degrees, two clusters are particularly significant. We have named them "*NBS planning, governance and stakeholders" and "NBS to tackle urban challenges*".

The first of these clusters includes nodes like "nbs", "impacts", "climate", "assessment" and "urban context" characterised by the highest degrees (Table A.3). Following the connections in this cluster, it is possible to identify: "nbs"-"urban areas", "nbs"-"societal challenges", "nbs"-"climate", "nbs"-"impacts", "nbs"-"participatory planning", "climate"-"societal challenges", etc. The nodes and connections show how the promotion of the NBS in urban areas through urban planning tools becomes a climate resilience strategy to create urban sustainability, as argued in recent literature

(Bush & Doyon, 2019; Faivre et al., 2017; Rogov & Rozenblat, 2018). This cluster also stresses the strong support of EC to deploy NBS in cities and its ambition to position Europe as a world leader in responsible innovation related to NBS (Zwierzchowska et al., 2019). Moreover, the inclusive approach and the involvement of local communities in the urban planning process known as collaborative planning (Bush & Doyon, 2019) are represented by the nodes called "participatory planning", "local communities" or "citizen". Indeed, it has been noticed that NBS recognition by means of public participation ensures NBS viability and maintenance (Kabisch et al., 2016).

Table 1.3. Clusters of EKLIPSE project, number of nodes and accumulated degrees.

Cluster	Colour	Number of Nodes	Accumulated Degree
NBS planning, governance, and stakeholders	Purple	34	311
NBS to tackle urban challenges	Pink	30	207
NBS indicators and scale	Blue	18	175
Ecosystem services provided by the NBS	Green	30	171
Action, temporal scale, and health benefits	Grey	15	88
Social and economic benefit of NBS	Yellow	11	42
Social opportunities	Dark green	7	26

The "*NBS to tackle urban challenges*" cluster is the second most relevant cluster. It stands out in water management terms (e.g., "flood peak reduction", "flood risk", "water quality", etc.), emphasizing this regulation service provided by NBS. Furthermore, different types of UGI (e.g., "green roofs", "green walls", "street trees") are part of this cluster, stressing their capacity to attenuate the impacts produced by the urbanization process and climate change, improving the resilience capacity of urban spaces (Millennium Ecosystem Assessment, 2003). Last but not least, several additional

environmental urban challenges are noted in the cluster, such as "ghg emissions", "air pollutants" and "UHI effect".

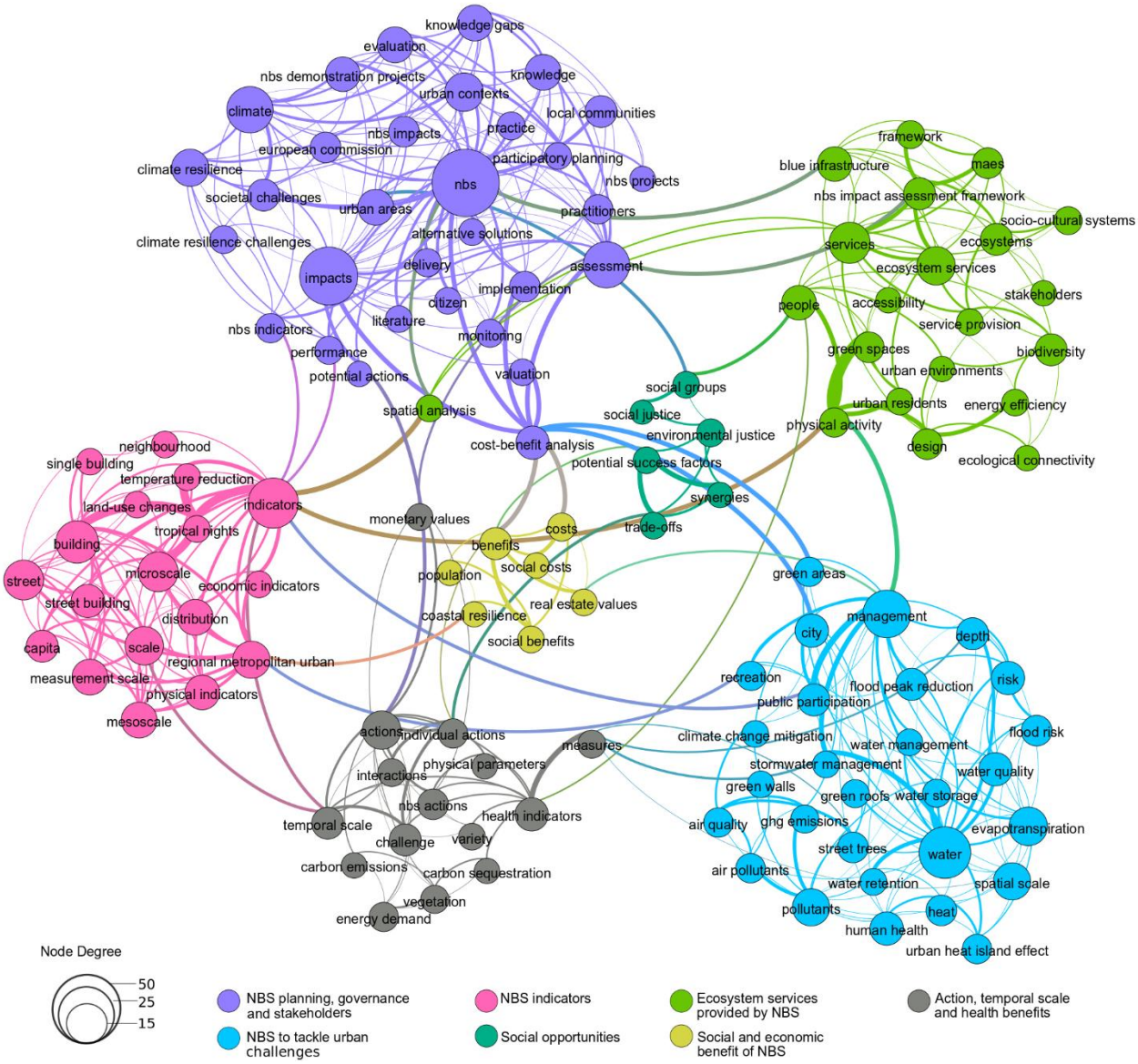

Figure 1.2. EKLIPSE Network, co-occurrence of terms by conditional distance.

The need to quantify the NBS' impacts and their efficiency has led to proposing some indicators. Hence, the "*NBS indicators*" cluster highlights this feature, taking into consideration the spatial scale where the solution is implemented, the impact to mitigate and the ESS delivered. The EKLIPSE network particularly emphasizes some "physical indicators" related to the assessment of urban temperatures reduction, underlying the thermal regulation service of vegetated spaces. This is supported by the thickness of the edges connecting "indicators" to the "temperature reduction" and

"tropical nights" nodes (Table A.2). The multi-scale framework in which these indicators are computed also must be underlined. Various scales are mentioned ("building", "street", "neighbourhood", "mesoscale", "regional metropolitan", and so on) illustrating that NBS can act at different levels while they are implemented at the local scale. Thus, thermal comfort, energy use reduction and CO_2 sequestration/storage become significant in large areas (mesoscale) despite acting at the site/block scale (building) (Demuzere et al., 2014).

The next cluster, characterised by fewer nodes and accumulated degrees, corresponds to the "*Ecosystem services provided by NBS*", where nodes refer to ESS and additional intangible benefits like "accessibility", "recreation", "green spaces" and "blue infrastructure". Contrary to the quantitative evaluation of the physical impacts by means of indicators in the previous cluster, the qualitative feature of these cultural services is dominant in this case. This cluster also contains the strongest connection of the whole network, between "physical health" and "green spaces" (Table A.2). In this sense, Faivre et al., 2017 pointed out that access to recreational green spaces may help to prevent socioeconomic inequality by promoting physical activity and public health. Likewise, it has been stressed that low quality of green spaces and public services in poor socio-economic neighbourhoods make the population more vulnerable to the negative health impacts of extreme heat (Norton et al., 2015).

The remaining clusters are less remarkable due to a reduced number of nodes and lower node degrees. This is caused by a lower term occurrence along the text, leading to nodes with fewer connections in the network. However, we have attributed a name to each cluster; they correspond to "*Actions, temporal scale and health benefits*", "*Social benefit and economic opportunities of NBS*" and finally, "*Social opportunities*" for deprived groups and environmental justice addressed by urban green spaces. This implies that these topics have been studied less, or their impact is less known by the scientific community.

1.3.2 MAES-Urban Ecosystems

In MAES-Urban ecosystems, five nodes have degrees higher than 25 (Table A.4). In order to assess the ESS in urban areas (the aim of MAES), "urban" and "ecosystems" stand out as the most important nodes of the network (Figure 1.3) with 35 and 34 degrees, respectively. Then, the distribution of "green landscape" (33) appears with the third highest degree of centrality, followed by "services" (30) and "urban ecosystems" (28).

Six clusters summarized the MAES-Urban Ecosystem report content (Table 1.4). The most important cluster is called "*Urban policies and NBS*", with 47 nodes and 420 accumulated node degrees. This cluster highlights the link between NBS and the way to integrate them in a sustainable urban planning policy. The highest computed node degrees ("urban ecosystems", "ecosystems", "nature-based solutions", "city council", "policy" or "local policymaking") strengthen this statement. In this context, the city council appears not only as a legitimated stakeholder that conciliates urbanization and urban ecosystems by means of policy at the city scale. It also has a protection and management role for the environment and the biodiversity, as demonstrated by the two strongest edges in the whole network (Table A.4). According to Zwierzchowska et al., 2019, urban policy documents are particularly relevant for the practical implementation of NBS. These define and organize the development of a city through the identification of key urban challenges and required actions to implement, in order to improve both environment and life quality. Furthermore, the European scope of MAES and its impact on local urban policies is well-stressed by nodes like "European commission", "European environment agency" or "member states".

The "*Ecosystem services provided by NBS*" cluster appears to be the second most important by its accumulated degree (266) in the MAES report. Many nodes refer to different ESS: provisioning (e.g., "food", "crop fields", "community gardening", "urban allotments"), regulatory (e.g., "climate and temperature regulation", "water flow regulation", "flood protection", "noise", "pollination") and cultural services.

Table 1.4. Clusters of MAES-Urban ecosystems, number of nodes and accumulated degrees.

Cluster	Colour	Number of Nodes	Accumulated Degree
Urban policies and NBS	Blue	47	420
Ecosystem services provided by NBS	Brown	36	266
Urban land use	Pastel Blue	34	260
Urban planning	Green	28	117
Ecosystem services assessment	Pink	19	97
Tools to assess ES	Yellow	18	92

The cluster "*Urban land use*" only presents the typology terms, such as "green", "land", "agriculture land", "land use" or "green spaces" without a distinction of NBS type, except for "green roofs" and "riverbanks". ESS and NBS benefits are integrated in the territory management at different administrative spatial scales in the "*Urban planning*" cluster, where terms like "urban", "land use plans", "management", "policy context", "implementation" or "plans" have a relevant node degree (Table A.5). These nodes reveal some official planning instruments ("land use plans" or "spatial planning"), as a way to make operational the NBS policy and contribute to urban resilience (Bush & Doyon, 2019).

In MAES, the need to assess the state of the urban ecosystems and their services via indicators is exposed through the "*Ecosystem services assessment*" cluster. Consequently, this cluster includes nodes like "ecosystem services" and "indicators" with a high centrality (high number of connections). In fact, this report developed two indicator frameworks based on the evidence of study cases to map urban green infrastructure, to assess their condition and to measure the urban ecosystem services delivered. Nodes such as "quality", "ecosystem condition" or "water framework directive" highlight the ecosystem assessment approach, while "air quality" or "noise reduction" nodes point to urban ecosystem services delivered. Finally, the tools to

estimate these ESS at different spatial scales, such as "data", "maps" or "information", concern the cluster "*Tools to assess ESS*."

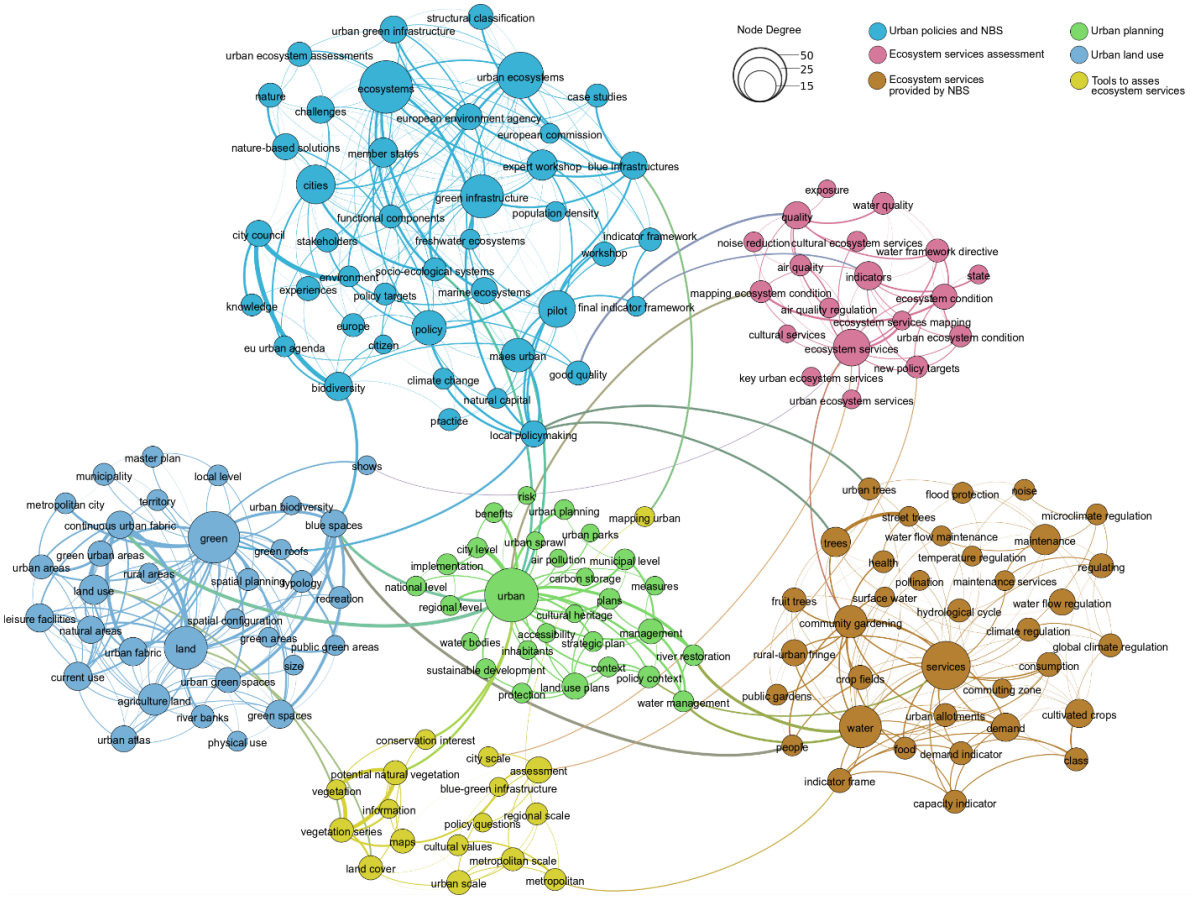

Figure 1.3. MAES-Urban Ecosystem Network, co-occurrence of terms by conditional distance.

1.3.3 NATURVATION

A noticeable characteristic of the NATURVATION network is its small size, with a reduced number of nodes (Figure 1.4). This is due to a shorter document length. Hence, there are fewer connections between terms than the other networks, as well as lower weight values (Table A.6). Furthermore, the most relevant nodes were extracted, finding 22 and 20 as the highest degrees of the network for "nbs" and "services" nodes, respectively.

In the NATure-based URban innoVATION report analysis, five clusters are identified (Table 1.5). "*Economic valuation*" represents the main cluster with 21 nodes and 137

accumulated degrees. The nodes with the highest degrees within this cluster correspond to "nature" (18), "valuation" (18) and "monetization" (12) (Table A.7); revealing the economic approach chosen to assess the nature.

NBS and their impacts can be reflected as monetary benefits to be used as a support tool in public decision-making process. In case of area changes in open spaces, Brander & Koetse (2011) pointed out that the estimated value per hectare of urban open space can be multiplied by the proposed changing hectares under an urban scenario policy, to provide the total annual value associated with the change. Such information can be used to decide whether to increase open space areas or to keep the existing ones.

Table 1.5. Clusters of NATURVATION, number of nodes and accumulated degrees.

Cluster	Colour	Number of Nodes	Accumulated Degree
Economic valuation	Pink	21	137
Types of NBS	Blue	19	110
Ecosystem Services provided by NBS	Green	21	109
NBS terms	Orange	12	91
Economic values of nature	Dark green	11	54

In parallel, the financial benefits and monetization of green buildings can also support private investments (Kabisch et al., 2017). Indeed, the monetary impact of NBS recreational, aesthetic or social benefits on the housing prices has also been demonstrated (Czembrowski & Kronenberg, 2016; Francis & Jensen, 2017; Luttik, 2000; O'Malley et al., 2015). In fact, in the "*Economic valuation*" cluster appears the "housing prices" node close to "hedonic pricing". The former refers to an economic valuation method widely used to analyse the impact of UGI proximity (and their related amenities) on property values. The application of this method has displayed a different kind of recognition to NBS, in functions of their type. For example, there is a significant positive effect on housing prices for those facing water structures (Luttik, 2000) or

those close to forests and large parks. However, there is a negative impact on apartment prices surrounding cemeteries (Czembrowski & Kronenberg, 2016).The second most important cluster with 19 nodes emphasizes the variety of "*Types of NBS*" and refers to urban "spaces", including "green spaces" and "blue areas" nodes. Additionally, the "services" node is highlighted by the highest degree within the cluster, illustrating the importance of recognizing ESS. In this sense, the significant thickness of edges linking UHI effect with "services", "mitigation" and "recreation" (Table A.6) reveals the need to promote NBS to improve thermal comfort perception and reduce UHI effects, but also to preserve the physical well-being of inhabitants, as indicated by O'Malley et al., 2015.

The third cluster, "*Ecosystem Services provided by NBS*", extends in detail a set of ESS. It contains nodes like "local climate regulation", "air quality" or "carbon storage". All of them are recognized in the literature as regulating services, widely claimed, accepted and scientifically quantifiable (Francis & Jensen, 2017). Surprisingly, regulatory services related to water (stormwater management and flooding reduction) were not revealed by the network, meaning the node degrees were not high enough to be conserved.

Provisioning and cultural services are also present in this cluster; however, they are not widely detailed like the regulating services. Moreover, the "habitat" node appears close to "nbs", with a higher degree than "provisioning services". Indeed, NATURVATION methodology used the ESS classification from the Millennium Ecosystem Assessment (MEA) (Millennium Ecosystem Assessment, 2003) , which includes habitat as a "supporting" service in the urban ecosystem.

NATURVATION follows the environmental economic valuation framework proposed by Hein et al. (2006). Then, four kinds of values are attributed to nature depending on their ESS usability principle: direct use value, indirect use value, option value and non-use value. These categories stand out in the "*Economic Values of Nature*" cluster, which guides the economic assessment. This cluster does not have a direct connection with

"*ESS provided by NBS*" cluster. Instead, these are linked through the "*Economic valuation*" cluster. This means that the monetary value of an ESS delivered by NBS can be assessed by an economic valuation approach as the "preference method", depending on the value that people can gain from ESS usability.

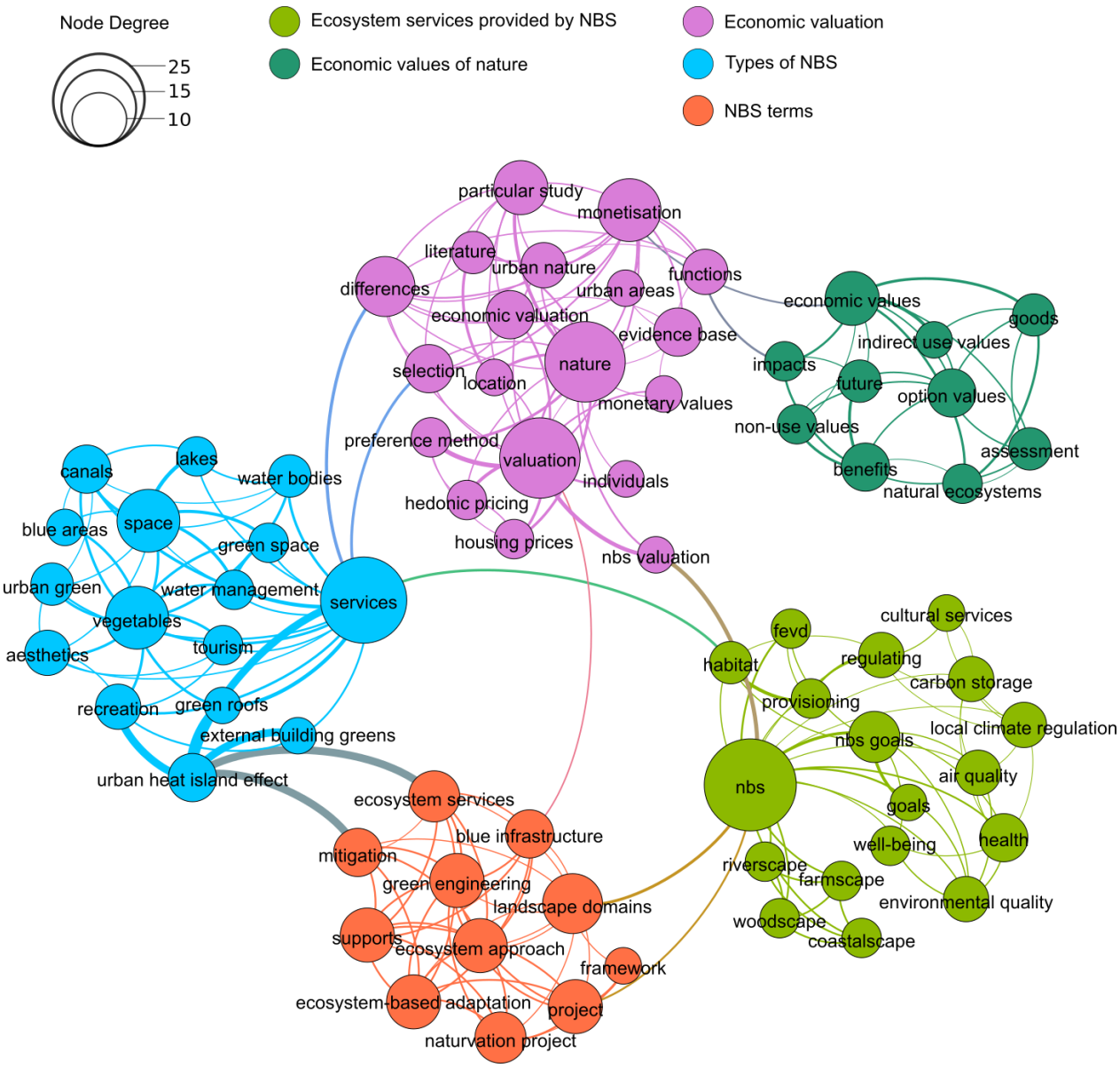

Figure 1.4. NATURVATION Network, co-occurrence of terms by conditional distance.

The "*NBS terms*" cluster presents nodes supporting the NBS concept, such as "green engineering", "blue infrastructure", "ecosystem approach", etc. This cluster is characterised by the highest homogeneity, with nodes degrees ranging from 7 ("blue infrastructure") up to 11 ("landscape domains"), as seen in Table A.7.

1.4 Discussion

From the individual analysis of the networks, it was possible to identify the main approaches and synergies of each document. Thank to this, a comparison of the H2020 NBS reports was developed. Just like in previous section, this comparison is supported by the literature review.

Before making a cross comparison of these results, it must be recalled that the statistical properties of the corpora (paragraphs ang pages length, Table 1.2) determine the quality of the text-mining analysis (number of terms co-occurrence and clustering). The larger the corpus is, the more statistically relevant are the extracted outcomes. Consequently, the MAES—Urban Ecosystems and EKLIPSE networks propose consistent approaches with well-defined clusters since they have a higher modularity. They have dense connections between nodes within clusters, but sparse connections between nodes belonging to different clusters. Concerning the NATURVATION network, the modularity decreases even if there are sparse connections between clusters. The connections within clusters are fewer and the nodes' degrees are more uniform.

It is important to note that some network connections may be missed or be false. In this study, the missing connections were easily detectable because of the length of the documents, which were analysed in detail by the authors before exploiting them with text-mining software.

Nevertheless, this slight heterogeneity in the corpora does not seems to affect the results of this analysis, as they revealed some common advantages of NBS, as well as some differences (Table 1.6). Both are discussed below.

1.4.1 Ecosystem Services (ESS)

Firstly, the three reports highlight different types of ESS delivered by NBS, and do not use the same framework to analyse them. EKLIPSE and NATURVATION both have a

common ESS classification based on MEA (Millennium Ecosystem Assessment, 2003), differentiating provisioning, regulating, supporting and cultural services. In the case of MAES—Urban ecosystem, the Common International Classification of Ecosystem Services (CICES) framework from the European Environment Agency (EEA) is used, which does not cover the supporting services defined in MEA.

In details, the regulating services provided by green spaces (e.g., climate regulation, water management, air quality regulation, etc.) appear at a higher rate of occurrence in the EKLIPSE and NATURVATION networks. These services are accented as a strategy of urban resilience, to mitigate environmental impacts resulting from urban sprawl and climate change effects. Usually, regulating services concerning climate mitigation and stormwater management are put forward by the scientific literature as the services predominantly appreciated in urban areas (Francis & Jensen, 2017; Kabisch et al., 2016) In consequence, the lack of reference to stormwater and flood management services is particularly surprising in the NATURVATION network, even if this was declared in the original corpus text.

Regarding the MAES—Urban ecosystems report, the full range of ESS is highlighted to tackle urban challenges. For example, the cultural services are well-identified, showing the benefits that the urban population gains from access to green and blue spaces: recreation, physical health promotion and socioeconomic inequality prevention.

1.4.2 NBS assessment

The assessment of NBS efficiency to face urban challenges through indicators is well-exposed in two of the corpora but with different approaches. While EKLIPSE stresses the assessment of the delivered services (e.g., temperature reduction) and the multi-scale characteristic of their spatial impacts (e.g., building, neighbourhood, microscale, regional), in MAES, two indicators' frameworks are proposed: first to assess the urban ecosystem (e.g., state and condition) and then to measure the ESS delivered.

Additionally, in MAES, the spatial scale is rather focused on the largest ones (e.g., regional, metropolitan, and urban scale) to assess the impacts of a wide implementation of NBS (and their associated ESS). It is also important to highlight the preference for quantitative or physical indicators in EKLIPSE and MAES reports, to assess regulatory services. They are widely used and studied on a small scale (e.g., street, building), whereas qualitative assessment is usually chosen for cultural services.

Conversely, in the NATURVATION network, the term "indicators" is not put forward since its occurrence in the corpus was too low to be considered by the statistical analysis. Nonetheless, the notion of assessment is present in the *Economic Values of Nature* cluster, pointing out a monetary value of the ESS delivered by NBS based on its usability.

Thus, the three corpora highlight NBS assessment as a useful mean to trace NBS effectiveness regarding a targeted urban challenge. As stressed by (Kabisch et al., 2016), this assessment becomes an useful support tool, which facilitates public and private decision-making processes on NBS investment and maintenance of sustainable urbanization.

Table 1.6. Main NBS characteristics, revealed by text-mining and data visualization.

Topic	**EKLIPSE**	**MAES**	**NATURVATION**
ESS classification	MEA, 2003	CICES	MEA, 2003
ESS highlighted	Regulation services Cultural services	Regulating services Provisioning services Cultural services	Regulating services Provisioning services Cultural services Habitat and supporting services

Topic	EKLIPSE	MAES	NATURVATION
Assessment approach of NBS benefits	Indicators and multi-scale	Quality and condition of urban ecosystem	Assessment of nature value
Spatial scale approach and stakeholders of NBS deployment	Europe: EC Mesoscale: Local communities, citizen	Europe: EC, EEA, European states. Mesoscale: City council	Local: landscape domains.

1.4.3 Multi-scale framework

As stated above, in the EKLIPSE project, the indicators proposed to assess NBS, and their associated spatial scopes are studied in a multi-scale framework. However, a similar multi-scale approach is also observed in the networks concerning the stakeholders responsible for NBS deployment. EKLIPSE and MAES—Urban ecosystems emphasize a macroscale with a key role of the EU in NBS promotion. Indeed, different scientific studies argue that EC aims to position Europe as a world leader in global sustainability development by means of NBS and innovative sustainable solutions (Faivre et al., 2017; Zwierzchowska et al., 2019). Text-mining analysis allowed to recognize the stakeholder role at the mesoscale (metropolitan or city level). At this scale, NBS implementation is performed by the local authorities through urban planning policies. In fact, MAES emphases the legitimated role of city councils to promote the goals and actions plans of NBS implementation, while EKLIPSE insists on the role of citizens in the decision-making process by the development of participatory initiatives. Various studies focusing on NBS governance highlight that NBS creation, design and implementation are successfully achieved when they involve multiple actors, mainly the citizens ensuring NBS recognition, acceptance and appreciation in the long term (Frantzeskaki, 2019; Kabisch et al., 2016). Regarding NATURVATION, no stakeholder is particularly associated with a spatial

scale. However, it mentions different landscape domains where all kinds of UGIs are framed.

1.5 Conclusions and Perspectives

In this chapter, the main issues covered by three literature review EC projects reports of NBS impacts, benefits and trade-offs were explored and compared. Text-mining and visual data representation techniques were implemented to create networks based on the occurrence and co-occurrence of terms in the documents (copora). Then, through the analysis of networks and their clusters, several hypotheses were made and supported by a conventional review of scientific literature.

The results of this methodology are very valuable taking into consideration the variety of approaches and opinions of stakeholders involved in NBS deployment: EC, local communities and authorities, organizations, studies, etc. Particularly, the data visual representation of each corpus becomes a means or tool which facilitates communication between stakeholders.

The results are limited mainly on the length of the documents and the authors' approach. To get more accurate results in the future and a variety of opinions, this methodology could be applied to more documents, as well as to a set of documents in such a way as to create a large corpus. This will improve the statistical properties of the networks and the hypotheses supported.

Among the main NBS topics identified through this methodology, we found the large set of benefits offered by NBS in urban areas and their recognition as ESS. The regulatory services, such as temperature mitigation or local climate regulation by shading and ET of NBS, are one of the most standing ESS. Besides, the results enabled us to discover the relevance of defining assessment tools of the benefits, such as performance, quality, or value indicators, while considering the spatial scale where the ESS is delivered. In the case of urban microclimate regulation, an evaluation of NBS's

performance requires the quantification of the service provided, and more specifically the study of the linked processes.

In parallel, the NBS issues addressed in these reports demonstrated the understudied NBS horizons, which opens new perspectives concerning NBS impacts and benefits assessment. Regarding the convergence and the complementarity of the studied corpora, it appears relevant to define some new tools to assess NBS performances, not at a specific scale, but through scales. Moreover, such required tools should perform in an integrated way to consider every service provided by NBS (provisioning, regulating, supporting and cultural). It should be helpful for stakeholders to produce optimized NBS deployment scenarios depending on the targeted benefit(s) by estimating their potential impacts. Some initial works were carried out in this direction by conducting a fractal analysis on green roof implementation, to evaluate the relevance of the promoting policies (Versini, Gires, et al., 2020).

The revealed challenges of the NBS implementation regarding climate regulation motivated the questions that are addressed through the next chapters. In the Chapter 2, the thermal performance of NBS is characterised. Specifically, the ET process over a single extensive green roof is quantified through different methods of measure. This would allow to better understand the physical and thermal properties that would influence the cooling benefit of NBS.

Then, to deal with the scaling issue, more specifically the implementation of the NBS at different scales, scale invariance approaches are used. In the Chapter 3, fractal geometry is used for the analysis and deployment of the NBS that fit the urban organisation. Meantime, in Chapter 4 the thermal performance properties of NBS across scales are studied through multifractals. The concepts and the state of art necessaries to understand every of these issues are introduced in the corresponding chapter.

Chapter 2 Evapotranspiration measurements over a wavy extensive green roof

As the literature review of the Chapter 1 demonstrated, NBS provide shade and evapotranspiration (ET), both of which help to reduce air temperature and Urban Heat Island (UHI) strength. Elevated temperatures and their effects on public health represent a major concern for urban decision makers, which is why the urban cooling has become one of the most widely demanded benefits of NBS.

This Chapter 2 is devoted to the experimental investigation and characterisation of the thermal performance of NBS. More specifically, it aims to analyse the ET process during summer on a specific green roof through three different measurement techniques. Indeed, several sensors assessing the Surface Energy Balance (SEB), an enclosed evapotranspiration chamber and a network of soil water content sensors were used to monitor and analyse ET on an extensive green roof during dry periods.

In this section, the statistical bases of turbulent atmosphere that served for the development of some techniques for measuring atmospheric fluxes are first introduced. From there, the physical principle of each ET method of measuring is included, as well as the details of the experimental campaign carry out on the green roof located at the Ecole des Ponts (the Blue Green Wave). Finally, the data and the trends of the ET flux obtained by every method were analysed individually and then they were compared between them.

According to the method used, the results indicated that several factors influenced the rates and trends of ET. These include the spatial and temporal scale of measure, the accuracy of measure of each device and estimation of additional parameters, as well as the thermal and hydric conditions that favour the process of ET, such as the net radiative flux or the soil moisture.

2.1 Green roofs to mitigate UHI

Among NBS, green roofs are often proposed for sustainable urban adaptation. They have been widely recognized to reduce urban stormwater runoff (Ayata et al., 2011; Stovin et al., 2012; Versini, Stanic, et al., 2020) and Urban Heat Island (UHI) phenomenon (Cascone, Coma, et al., 2018; Coutts et al., 2013; Sharma et al., 2016; Wadzuk et al., 2013).

The UHI phenomenon is characterised by a difference of air temperature between urban and rural areas (Figure 2.1), mainly at night (Oke, 1982). According to Sharma et al. (2016) several factors contribute to the UHI, among them, the conversion of vegetation by water-proof surfaces, which reduces cooling rates from vegetation evapotranspiration (ET) process. Several studies have found that buildings' roofs represent around 25% of land surface in urban areas (Cascone, Coma, et al., 2018; Yang et al., 2018). Therefore, the implementation of vegetated structures like green roofs into new constructions or retrofitted ones is highly promoted as a solution of UHI mitigation.

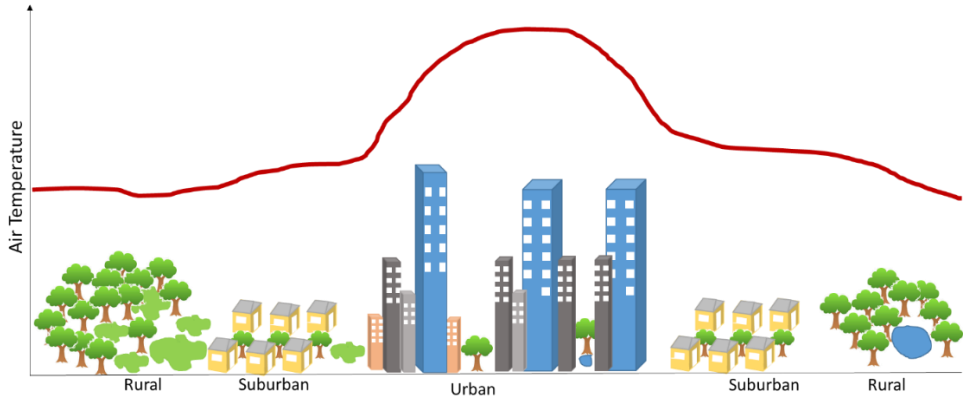

Figure 2.1. Urban Heat Island profile. Adapted from Oke (1982).

In consequence, understanding the ET process is key to identifying the conditions in which green roofs provide the highest cooling benefit. For this purpose, we proceeded to characterise the ET on a specific green roof. However, first some statistical bases of the turbulence in the atmosphere are introduced, to understand the dynamics of turbulent exchanges and their measurement. Furthermore, they serve as a theoretical

basis for the development of techniques measuring surface heat fluxes: the scintillometry more specifically, used in this investigation for the analysis of the energy balance in the green roof (Section 2.4.2).

2.2 Challenges of turbulent fluxes measurements in the atmosphere

The lowest layer of the atmosphere, where humans live and anthropogenic activity takes place, it is known as the Planetary Boundary Layer (PBL). The energy and mass transfers of the city - atmosphere system and UHI phenomenon occur there.

The depth of this layer is not constant, and it ranges from hundreds to thousands of meters. The PBL is in direct contact with the Earth's surface, which influences its mechanical and thermal response in temporal scales of minutes or hours (Stull, 1988). The thermal response of the PBL can be perceptible with the diurnal variation of temperature near the ground, having too a diurnal cycle.

The Earth's surface is warm because of the solar radiation during the day, which generates an upward transfer of warm air from the ground into the cooler atmosphere by convection. In consequence, the depth of the PBL grows during the day about 1 and 2 km. On the contrary, at night without solar radiation, the Earth's surface loss the energy absorbed during the day, decreasing its temperature. This produces cooler air near to the surface than the upper atmosphere, generating a downward transfer heat. This effect reduces the PBL depth to less than 100 m.

The layer above the PBL is called the free atmosphere. In this layer, the flux of the air is almost in equilibrium since it is free of the Earth's surface influence. Hence, micrometeorological measurements as surface heat fluxes are usually conducted in the PBL. The understanding of PBL dynamics of heat and moisture transfer is relevant to characterise the surface fluxes near the Earth's surface.

One of the main processes controlling matter and energy transfer in the PBL is the turbulence, characterised by boundary layer dynamics, velocity distribution, as well as unsteady and chaotic swirling motion in all directions, named vortices (eddies). The

turbulence is created by wind shear with obstacles near to the surface (i.e., mechanical turbulence) and buoyancy of warm and humid air caused by temperature and humidity (i.e., convective turbulence). Most of the transfer of heat and water in the PBL comes from the process of turbulence (Oke, 1987).

The vertical motion of eddies is affected by the atmosphere instability. Depending on the character of the atmospheric resistance to discourage vertical motion, the stability of the atmosphere is classified as follows:

- The *unstable atmosphere* is produced by buoyancy effects and negative vertical gradient of temperature. The parcels of warmer air from the ground buoyant and rising, enhancing free convention. These conditions typically occur during daytime because solar heating, generating strong turbulence and a homogeneous vertical motion of eddies.
- The *stable atmosphere* inhibits the vertical motion, as cold and dry air at the ground level is negatively buoyant. In these cases, atmospheric fluxes are only driven by wind shear. Therefore, the vertical motion of eddies is not so strong. These conditions usually occur during the night-time.
- The *neutral atmosphere* does not have a vertical gradient as the temperature of the parcel is the same as its surroundings. However, during fair weather (i.e., calm weather without precipitation, or extremes of temperature or wind) conditions over land, the PBL touching the ground is rarely neutral (Stull, 1988).

2.2.1 Statistics of turbulence

Based on space and time changes of convective and mechanical turbulence, the eddies observed in a variety of turbulent atmospheric fluxes have different sizes and lifetime. This leads to atmospheric fluxes appear stochastic with structure at all scales, and its behaviour difficult to predict. In fact, the chaotic nature of atmospheric turbulence is governed by the non-linearity of Navier-Stokes's equations.

The scientific community has been interested by this issue for years and has proposed statistical methods as an appropriate approach to describe turbulence. In this way, statistical properties such as the Reynolds decomposition, the statistical moments, the structure function, and the Fourier series are used to characterise turbulent fluxes. These statistical properties are quite useful for the analysis of spatial and temporal variability of an atmospheric variable observed at some fixed point over long periods, as well as the underlying physical processes. The spatial approach of the structure function will serve in this section to derive the structure function parameter of a scalar, which is the basis for scintillometry technique; while the temporal approach of the structure function is used in the Chapter 4 to analyse the statistical properties and the scaling behaviour of thermal fluxes measured at a fixed point.

2.2.1.1 Reynolds' decomposition

A random atmospheric variable u can be generally described into two parts: the mean $\langle u \rangle$ and the fluctuating about the mean u', as follows:

$$u = \langle u \rangle + u' \tag{2.1}$$

The mean of turbulent fluctuations is zero ($\langle u' \rangle = 0$). This decomposition is applied for every turbulent flux in the atmosphere, for example, air temperature T, $T = \langle T \rangle + T'$, or air pressure P, $P = \langle P \rangle + P'$.

2.2.1.2 Statistical moments

The random variable u at any position (r) of a four-dimensional space (time or space), can be described with the statistical additive moments $B_{uu\ldots u}$ (Moene et al., 2004). The m-th order moments were defined by Monin & Yaglom (1971), as the mean values of products of m values of the field:

$$B_{uu\ldots u}(r_1, r_2, \ldots, r_m) = \langle u'(r_1)u'(r_2) \ldots u'(r_m) \rangle \tag{2.2}$$

where $uu \ldots u$ are integers of which the sum gives the order of the moment. Following the Reynolds' decomposition of the variable u:

$$B_{uu\ldots u}(r_1, r_2, \ldots, r_m) = \langle (u(r_1) - \langle u(r_1) \rangle)(u(r_2) - \langle u(r_2) \rangle) \ldots (u(r_m) - \langle u(r_m) \rangle) \rangle \quad (2.3)$$

The first central moment is zero when defined the probability distribution with reference to the mean, and the second central moment is the variance. The general second order moment corresponds to the covariance (B_{uu}) and it is generally used to define three cases of a field (Kesteren, 2012): stationary, homogeneous and isotropic turbulence (Monin & Yaglom, 1971):

- For a *stationary turbulent field*, the mean value $\langle u(t) \rangle$ is constant and invariant under a translation in time $\tau = t_1 - t_2$. Thus, the covariance B_{uu} does not depend on t_1 and t_2:

$$B_{uu}(t_1, t_2) = B_{uu}(t_1 - t_2) \quad (2.4)$$

- For a *homogeneous turbulent field*, the mean value $\langle u(r_m) \rangle$ is constant and invariant under a spatial translation. B_{uu} only depends on $r_1 - r_2$:

$$B_{uu}(r_1, r_2) = B_u(r_1 - r_2) \quad (2.5)$$

- For the *isotropic turbulent field*, the mean value $\langle u(r_m) \rangle$ is constant in all directions and B_{uu} only depends on the distance between two points $r = |r_1 - r_2|$ and not on its direction or position:

$$B_{uu}(r_1, r_2) = B_{uu}(|r_1 - r_2|) = B_{uu}(r) \quad (2.6)$$

2.2.1.3 Structure function

Since atmospheric fields are hardly stationary when the time interval between two measurements is too large (the mean value $\langle u(t) \rangle$ is not constant), Kolmogorov introduced in 1941 the principle of stationary increments. He argued the use of the difference $\Delta u(\tau) = u(t + \tau) - u(t)$, which is constant, is more practical than $\langle u(t) \rangle$ (Kesteren, 2012). Then, the second order moment of $\Delta u(\tau)$ (Eq. (2.4)) becomes:

$$B_{uu}(t_1, t_2) = \langle \Delta u(t_1) \Delta u(t_2) \rangle \quad (2.7)$$

$$B_{uu}(\tau) = \langle \big(u(t_1 + \tau) - u(t_1)\big)\big(u(t_2 + \tau) - u(t_2)\big) \rangle \quad (2.8)$$

Thus, statistical moments applied to increments of a stochastic process are called structure function. Then, as $B_{uu}(t_1, t_2)$ only depends on the time interval τ, the structure function, between t_1 and t_2, can be introduced as the mean of the difference of the variations of the flux between t_1 and t_2 (Tatarski et al., 1961), as follows:

$$S_{uu}(\tau) = \langle (u(t + \tau) - u(t))^2 \rangle \quad (2.9)$$

In conditions of stationary increments, the second order moment or covariance B_{uu} is related to the second order structure function S_{uu} by:

$$S_{uu}(\tau) = 2(B_{uu}(0) - B_{uu}(\tau)) \quad (2.10)$$

where, $B_{uu}(0)$ and $B_{uu}(\tau)$ correspond to the statistical moments at any time and at the time interval τ, respectively.

Apart from stationary increments, the principles of locally homogeneous and isotropic fields, for analysing the spatial evolution of the flux between two points of the space can be assumed too. Then, the structure function can be expressed as:

$$S_{uu}(r) = \langle (u(r_1 + r) - u(r_1))^2 \rangle \quad (2.11)$$

In this way, the structure function is a statistical property than only depends on the distance r.

2.2.1.4 Fourier Analysis

The Fourier analysis is a widely known method used to decompose the time-domain series of turbulence, into trigonometric functions such as sines and cosines. Hence, the Fourier series of a periodic function $S(t)$ can be expressed as:

$$S(t) = a_0 + \sum_{n=1}^{\infty} a_n \cos(2\pi n f_0 t) + \sum_{n=1}^{\infty} b_n \sin(2\pi n f_0 t) \quad (2.12)$$

where, f_0 is the fundamental frequency ($1/T$), and a_0, a_n and b_n, the corresponding Fourier coefficients.

Because of the periodicity of events in nature, the Fourier analysis is used with the object to study these amplitudes, frequencies and cycles present on the signal of the turbulent field, as well as its noise. For this purpose, the Fourier transform is used to express a non-periodic function in time $y(t)$ as a continuous series of harmonics, as follows:

$$y(t) = \int_{-\infty}^{+\infty} Y(f)\, e^{2\pi j f t} df \tag{2.13}$$

where, j is the imaginary unit, f is the frequency, and $Y(f)$ corresponds to the Fourier transform of $y(t)$. Hence, $Y(f)$ converts the signal $y(t)$ to its transform:

$$Y(f) = \int_{-\infty}^{+\infty} y(t)\, e^{-2\pi j f t} dt \tag{2.14}$$

Let's now consider a discrete version of the Fourier transform known as Discrete Fourier Transform (DTF), where the time series $y(t)$ is measured at just a finite number of times B. So, the DTF results from evaluating the integral from 0 to time T over which the signal is measured:

$$Y(f_b) = \sum_{b=0}^{B-1} y_k\, e^{-2\pi j k_b / B} \tag{2.15}$$

where, b is the index of the data array of length B, and k_b the harmonic number. The inverse transform is given by:

$$y(t) = \frac{1}{B} \sum_{b=0}^{B-1} Y(f_b)\, e^{2\pi j k_b / B} \tag{2.16}$$

The applicability of DFT was globally extended because of its usability and the development of the Fast Fourier Transform (FFT) algorithm, for which the DFT has been factored and restructured to take advantage of the binary computation processes of the digital computer (Stull, 1988).

Based on the Fourier transform, the power spectral density (or energy spectrum) enables to examine the energy distribution of a turbulent time series data over the frequencies. Therefore, characteristic time scales of processes can be analysed or noise in measurements signals can be identified (Stull, 1988):

$$E(f) = |Y(f)|^2 \quad (2.17)$$

The FFT algorithm is usually used to compute $Y(f)$. It is important to note that the FFT is restricted to data sizes 2^b, where $b \leq log_2 S$ and S is the sample size.

The spectral analysis is an approach used to verify the scale invariant properties of a field. In the case of a scaling field, the power spectral density $E(f)$ has a power law relationship with a range of frequency f (temporal analysis) or wavenumber k (spatial analysis) as follows:

$$E(f) \sim f^{-\beta} \quad (2.18)$$

When this relationship is represented in a log-log scale, the spectral exponent β is deduced from the (absolute) spectral slope.

2.2.2 Energy cascade and statistical laws

Apart from statistical properties that decompose the turbulent field, since the XIX century, theories and statistical laws have been proposed to describe the turbulence of the atmosphere. In 1922, Lewis Richardson stated large eddies sizes (i.e., produced by wind shear and buoyancy of daytime) are unstable, and they break down into identically smaller eddies (Richardson, 1965). In this model, energy of large eddies is transferred by non-linear interactions to the small ones. Then, the energy of small eddies is dissipated into heat, by molecular viscosity.

This process is known as the energy cascade, and Richardson described it in a poem:

"Big whirls have little whirls,

Which feed on their velocity,

And little whirls have lesser whirls,

And so on to viscosity,

-in the molecular sense."

This postulate has been essential for the development of theories of fully developed turbulence (Schertzer & Lovejoy, 1991). In fact, this postulate was formalised in 1941 by Andrei Kolmogorov in a statistical theory, known as Kolmogorov Self-Similarity Hypothesis (K41). It describes the transfer of turbulent kinetic energy from large to small eddies, as well as the characteristic length scales of eddies. This theory became one of the most quoted and fundamental theories of turbulence.

Three lengths ranges characterise the energy cascade of a turbulent flux:

- The injection or production range of no isotropic eddies as large as the PBL (Kesteren, 2012).
- The dissipation range of small eddies, where their energy is dissipated into heat due to viscosity.
- The intermediate range or universally known as inertial range, where eddies get energy from large unstable eddies and transfer it successively to the smaller eddies.

The inertial range without eddies production or viscosity influence, is delimited by two length scales:

- The inner scale l_k, which corresponds to the boundary between the inertial and dissipation range.
- The outer scale L_k, which represents the boundary between the production and inertial range.

For Kolmogorov, in the inertial range ($l_k \ll r \ll L_k$) the anisotropy of large eddies is removed, so the turbulent flux could be considered locally isotropic and homogeneous. Two hypotheses were considered by Kolmogorov for an isotropic turbulent flux:

Hypothesis 1: At high Reynolds number (Re), all the small-scale statistical properties of velocity increments would be determined uniquely by the length scale r, the average turbulent kinetic energy dissipation rate ϵ (or just dissipation rate) and the viscosity ν.

Hypothesis 2: In the inertial range of very high Re, all small-scale statistical properties of velocity increments would only depend on the average dissipation rate ϵ, because the cascade is independent of the viscosity ν.

Among the main results of Kolmogorov's hypotheses highlights the 2/3 law. This indicates for a turbulent flux in the inertial range, the mean square of velocity fluctuations $\langle \Delta u(r)^2 \rangle$ between two points separated by a distance r, behaves approximately as the two-thirds power of the distance.

Since the statistics of $\langle \Delta u(r)^2 \rangle$ were previously defined, the second-order structure function of the ensemble average is defined by:

$$S_{uu}(r) = \langle \Delta u(r)^2 \rangle = \langle (u(r_1 + r) - u(r_1))^2 \rangle \quad (2.19)$$

From Kolmogorov's second universality hypothesis, S_{uu} of velocity increments only depends on the dissipation rate ϵ and the distance r. From the dimensional analysis of S_{uu} and ϵ, it results:

$$S_{uu}(r) = C\epsilon^{2/3} r^{2/3} \quad (2.20)$$

where, C is a universal constant.

In 1941, Alexandre Obukhov got a similar law in Fourier space (using the Eq. (2.17) and Eq. (2.18)) for homogeneous and isotropic turbulence, from Kolmogorov's 2/3 law in physical space. He demonstrated in the inertial range, the power spectral density $E(k)$ follows a power-law (Obukhov, 1941):

$$E(k) = \epsilon^{2/3} k^{-\beta} \quad (2.21)$$

where, k is the wavenumber (as this is a spatial analysis) and $\beta = 5/3$. The three ranges of turbulent energy distribution of velocity from eddies are represented in the Figure

2.2, as well as the 5/3 power-law follows in the inertial range. Due to intermittency of turbulent fluxes some discrepancy in the exponent 5/3 could take place.

This law will be widely verified and used to describe fully developed turbulence for the inertial range. Sometimes this law is referred to as the "Kolmogorov-Obukhov law".

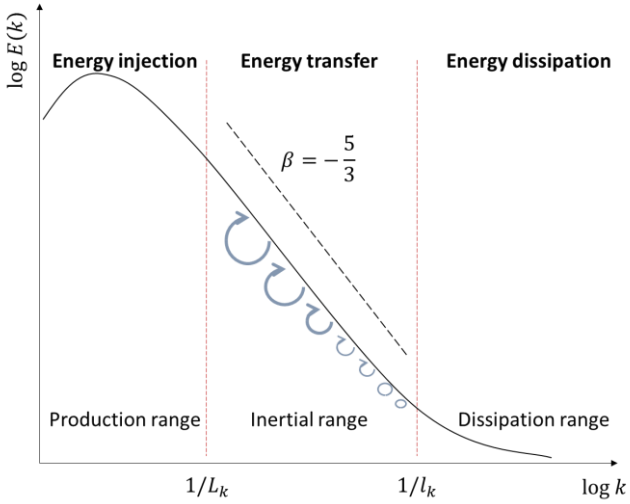

Figure 2.2. Energy cascade of turbulence and characteristic scales in the Fourier space Adapted from Kesteren (2012).

Inspired by Kolmogorovs' hypothesis of local isotropic and homogeneous velocity field, represented by the Eq. (2.20), Corrsin (1951) and Obukhov (1949) derived a universal form of the second order structure function for any scalar quantity θ (i.e. a physical quantity which not depend on direction, such as temperature, humidity or the refraction index):

$$S_{uu}(r) = {C_\theta}^2 r^{2/3} \tag{2.22}$$

Thus, for any r between L_k and l_k, the structure function can be related to the structure parameter of the scalar C_θ. This statistical property will serve as basis for the analysis of the electromagnetic wave propagation in the turbulent atmosphere, and the development of scientific devices to measure atmospheric fluxes, such as the scintillometer, see more in Section 2.4.2.1.

2.3 Evapotranspiration in green roofs

The ET is a combined process by which water is transferred to the atmosphere by evaporation from surfaces and by transpiration from the plants. The evaporation is the physical process of change from liquid water to vapour, while the transpiration is the transfer of liquid water from the plant root system to the leaves, where water is evaporated. The transformation of liquid water to vapour requires sufficient energy to overcome liquid-phase intermolecular forces. In consequence, the heat (i.e., as a form of energy) is removed from the atmosphere because of ET.

In green roofs, mass and heat transfer of water vapour involved in the ET process makes air becoming moist, and reduces surface temperature of the roofs and the nearest environment (Ayata et al., 2011; Cascone, Catania, et al., 2018; Cascone, Coma, et al., 2018; Coutts et al., 2013).

Different conditions can affect the ET efficiency of green roofs. These can include external conditions (e.g., local climate, surface albedo, soil moisture, etc.) or internal factors (e.g., substrate and vegetation properties). External conditions as local climate determines the amount of energy available for ET (Brown, 2014; Cascone, Coma, et al., 2018), whereas internal factors govern the water retention and water loss rate (Coutts et al., 2013).

Since a large number of physical, meteorological and vegetation parameters are involved in the ET process of green roofs, several methods for ET measurement have been developed at different scales.

One of the most widely applied methods to measure ET over green roofs is the weighing lysimeter, which is considered as the only direct quantitative technique of ET estimation (Rana & Katerji, 2000). This method monitors weight changes in containers of soil and vegetation, due to ET water losses. Measurements carried out

with this equipment over extensive green roofs[1] with *Sedum* plants in Amsterdam (built plot of 18 m² with 25 mm thick drainage mat and 4 cm substrate layer), New York (extension of 500 m², green roof built with 10 cm thick media layer) and Philadelphia (retrofit roof of 53.4 m²) over periods longer than one year showed ET rates around 3 mm/d (up to 4 mm/d) in summer (Cirkel et al., 2018; DiGiovanni et al., 2013; Wadzuk et al., 2013). Likewise, laboratory set-up experimentations carried out by Ayata et al. (2011) with weighing lysimeters and water balance methods reported ET flux varying around 150 W/m² (5 mm/d). The main advantage of lab experiments is the full control of environmental conditions (e.g., temperature, humidity, solar radiation).

Some cheaper devices than lysimeters to monitor green roofs' weight change have been used. For example, in New Zealand, mass changes due to water loss by ET of eight green roof trays were monitored with a weight sensor (single beam load cells). Measurements were completed with a water balance method and ET values of 2.2 and 2.1 mm/d were observed from *Sedum mexicanum* and *Dysphyma austral* plants respectively, in well-watered conditions (Voyde et al., 2010). Besides, experimentations of mass balance and soil moisture variations in green roof plots (laboratory scale) inside a climate chamber were implemented in some studies (Poë et al., 2015; Tabares & Srebric, 2012). Results demonstrated maximum ET rates ranging from 2.5 up to 4.5 mm/d in plots with abundant soil moisture during summer.

Plant physiology approaches, such as chamber systems have been used on green roofs too. In New York, an experimentation used a portable dynamic closed chamber to survey the water vapor concentration on extensive green roofs. The absolute humidity variations over *Sedum* plants noted an average daily ET flux of 1.5 and 1.9 mm/d in a vegetated mat and a built-in place system green roof (Marasco et al., 2015). Likewise, measurements from a chamber during warm and sunny days in Melbourne (Coutts et

[1] Extensive green roofs are characterised by having a thin layer of substrate and minimal maintenance requirements.

al., 2013) demonstrated the link between the soil moisture and ET. Rates of ET ranged from 3.5 mm/d on a roof without irrigation, and 9 mm/d the day after irrigation were observed during summer.

Moreover, micrometeorological approaches of ET used at large scales in agricultural experimentation, such as the Eddy Covariance (ECO) have been deployed in urban environments too. The ECO technique derives convective fluxes from the covariance of fluctuations in the vertical wind velocity and the atmospheric scalars by turbulent eddies. In consequence, its utilisation has been recognized as a useful method to investigate green roofs and surrounded atmosphere energy exchanges. Experiments conducted with ECO during a year on a green roof located in the California Academy of Sciences, to characterise annual variability of the Surface energy Balance (SEB) parameters (Thorp, 2014), showed the sensible heat flux was the SEB's dominant component during the daytime, meanwhile the latent heat was only higher in the first daytime hours. The ET rates were around 1.8 mm/d, and the soil heat storage was the lowest term of the SEB. The ECO application by Heusinger & Weber (2017) over an unirrigated extensive green roof of 8600 m² in Berlin, confirmed the dominant fraction of sensible heat in the warmer periods. As well, he noticed the high variability of ET in the summer, with mean daily rates of 0.8, 1.77 and 0.76 mm/d in June, July and August, respectively.

Apart from ECO, additional micrometeorological approaches frequently used in agriculture to deduce latent heat flux by means of the SEB imply the estimation of the sensible heat by scintillometry. This technique is deployed to measure the fluctuations of the air reflective index, induced by temperature changes over a horizontal path (more details in Section 2.4.2.1). However, because of its implementation limitation over small horizontal distances, this method has not yet been used in green roofs.

Due to the wide variability of methodologies and conditions of measuring the ET, the misunderstanding about the ET and the thermo-physical performance of green roofs persists. In this context, the aim of this chapter is the characterisation of three methods of ET measure, taking into consideration their spatial and temporal variability. For this

purpose, several experimental campaigns were conducted on an extensive wavy-shape green roof, called Blue Green Wave (BGW). The experiments involve three ET methods of measurement: i) a surface energy balance (SEB) to deduce latent heat fluxes (Section 2.4.2) from measurements of sensible heat flux by the scintillometry technique; ii) the variation of absolute humidity within an evapotranspiration chamber (Section 2.4.3); and iii) an analysis of water balance during dry periods, to deduce ET by means of water content loss in the ground (Section 2.4.4). Then, the results were analysed and compared to investigate the measurement accuracy and the source of differences or similarities between them (Section 2.5).

2.4 Evapotranspiration Experimentation

2.4.1 The experimental site: The Blue Green Wave

The experimental campaigns were carried out on the Blue Green Wave (BGW), a non-irrigated extensive-wavy green roof of 1 ha (see Figure 2.3) located in front of the Ecole des Ponts Paristech at Cité Descartes, the greatest research and education core at the east of Paris.

Since 2013, the BGW has been part of the EIT Climate-KIC Blue Green Dream Project, becoming one experimental site to study and understand the hydrological and thermal behaviour of extensive green roofs. A permanent monitoring of water balance components (e.g., rainfall, soil water content and temperature, and run-off) has started in 2018, while energy balance and evapotranspiration campaigns were conducted punctually during summer months from 2018 to 2020.

The vegetation of the BGW includes mainly green grass and a mix of perennial planting, grasses and bulbous. The depth of the substrate layer varies from 21 cm and 28 cm, depending on vegetation type. The substrate is a composition of volcanic soil completed by organic matter (around 13%).

Figure 2.3. The Blue Green Wave (BGW) in the Cité Descartes (France).

The methods used to monitor and investigate the process of ET in the BGW are explained in the next sections.

2.4.2 Surface Energy Balance (SEB)

On green roof surfaces, most radiative energy comes from solar short-wave radiation and, to a lesser degree, from long-wave radiation issue of the ground, the leaves, and the sky. This radiative energy received in the green roof can be partially absorbed or reflected by the vegetation and the ground of the roof. Thus, the net radiative flux (Rn) is the difference between the incident and reflected radiative fluxes. Therefore, the energy can be exchanged with the green roof, the surrounding atmosphere, and the building structure, resulting in an energy balance, see Figure 2.4.

The net radiative flux of energy in a green roof (Rn) is the main input of the surface energy balance (SEB), which is accounted by three heat fluxes: the sensible heat flux (Qh) produced by convection, the latent heat flux (Qe) due to evapotranspiration from vegetation and soil, and the heat conduction into the soil substrate (Qg) (De Munck et al., 2013; Marasco et al., 2015). In this way, the energy balance on a green roof can be defined as follows:

$$Rn = Qh + Qe + Qg \quad (2.23)$$

All terms of the energy balance are expressed in terms of energy transfer per unit area (W/m²). The terms of right-hand side of Eq. (2.23) can be either positive or negative, when they represent losses or gains of heat for the surface, respectively. By opposite, the sign of Rn is positive when there is a gain and negative when a loss of heat (Oke, 1987). Additional heat fluxes transferred by advection, anthropogenic sources, photosynthesis process and heat stored in the substrate matrix are neglected.

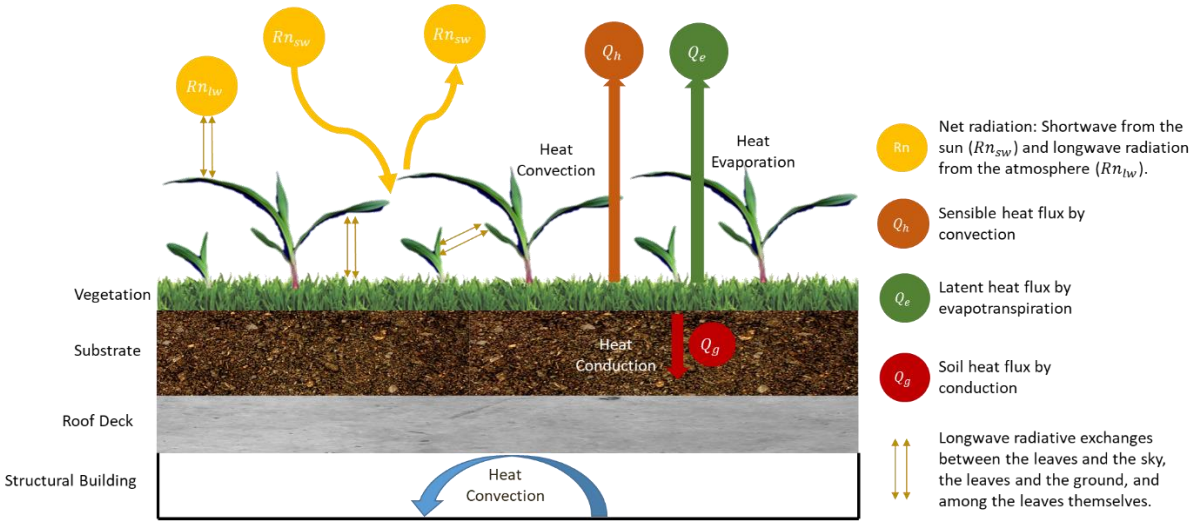

Figure 2.4. Energy balance in a green roof.

Qe can be expressed in mass flux too, that corresponds to the height of water lost from a surface during a period, and it is named ET (mm/d). The relationship between Qe and ET is given by:

$$Qe = ETL_v\rho_w \quad (2.24)$$

where, L_v (2.45×10⁶ J/kg at 20°C) is the latent heat of vaporisation of water and ρ_w (1000 kg/m³ at 20°C) is the water density.

In case that Rn, Qh and Qg are measured, Qe can be deduced like the residual component of SEB, Eq. (2.23) becomes:

$$Qe = Rn - Qh - Qg \quad (2.25)$$

Below, the methods used to measure Rn, Qh and Qg on the BGW are introduced and its setup to estimate Qe on the BGW.

2.4.2.1 Scintillometer

The dynamic foundations of turbulence in the PBL and the related theories for the description of thermodynamic fluxes introduced in the Section 2.2, served for the study of optical turbulence in the PBL. As a result, devices such as the scintillometers were developed to measure the heat transport, by analysing the travel of an electromagnetic beam (EM) through the atmosphere.

A scintillometer is an instrument that consists of a transmitter that emits an electromagnetic wave signal (with a specific wavelength λ_s) to a receiver, which records the intensity variations of this signal (Yee et al., 2015). The variations in signal intensity are caused by the fluctuations of the refractive index of air (n) along a propagation path (see Figure 2.5). The fluctuations of n are due to eddies created by variations of temperature, humidity, or pressure in the PBL.

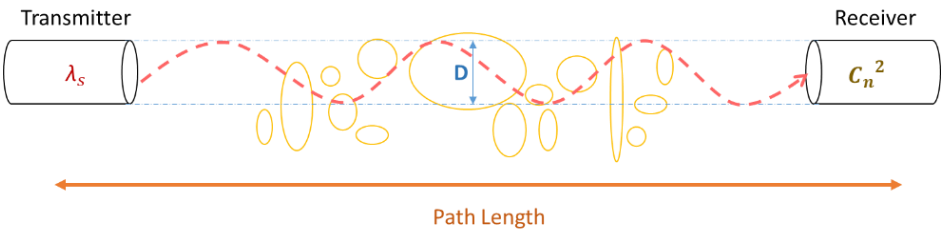

Figure 2.5. Operational principle of a scintillometer.

Various types of scintillometers can be found depending on the aperture diameter (D) and the wavelength (λ_s): Large Aperture Scintillometer (LAS, see more details in Section 2.4.2.2), Microwave Scintillometer (MWS), Boundary Layer Scintillometer (BLS) and Surface Layer Scintillometer (SLS). The LAS, SLS, and BLS are optical scintillometers with a λ_s of 850 nm, 670 nm and 880 nm respectively. The path length between the transmitter and the receiver is 250 m to 4.5 km for the LAS (diameter of 15 cm), 50 m to 250 m for the SLS (diameter of 2.5 mm) and 100 m to 6 km for the BLS (diameter of 14.5 cm). Regarding the MWS, it uses microwaves beams of 160.8 GHz

over a path length of 500 m to 10 km (with a diameter of 30 cm). Depending on the type of scintillometer, the combination of scintillometers and additional meteorological measurements, heat fluxes such as of Qh and Qe can be calculated.

The magnitude of variations of a scalar, the refraction index of air (n), can be described by the structure function parameter of the scalar ${C_n}^2$, which quantify the strength of atmospheric optical turbulence, as indicated in the Eq. (2.22), then:

$$S_{uu}(r) = {C_n}^2 \, r^{2/3} \tag{2.26}$$

$${C_n}^2 = \langle [n(x) - n(x+r)]^2 \rangle r^{-2/3} \tag{2.27}$$

where, x and $x + r$ are two points in space with displacement r at time t in the inertial range of the energy cascade.

Optical scintillometry methods have been recognized by various authors as an accurate and suitable tool to estimate turbulent fluxes, such as the Qh, over homogeneous and heterogeneous surfaces (Guyot et al., 2009; Meijninger et al., 2002; Moene, 2003; Moorhead et al., 2017; Valayamkunnath et al., 2018; Yee et al., 2015).

The spatial fluctuations of n along the path-length are associated with fluctuations of temperature (T), humidity (Q) and to a lesser extent, air pressure (P). Hence, the structure parameter ${C_n}^2$ can be related to the thermodynamic structure parameters of air temperature ${C_T}^2$, humidity ${C_Q}^2$ and the covariant term C_{TQ} (and ignoring pressure fluctuations) (Hill et al., 1992):

$${C_n}^2 = \frac{{A_T}^2}{\bar{T}^2} {C_T}^2 + \frac{2 A_T A_Q}{\bar{T}\bar{Q}} C_{TQ} + \frac{{A_Q}^2}{\bar{Q}^2} {C_Q}^2 \tag{2.28}$$

where, A_T and A_Q are constants, functions of the beam wavelength and $\bar{T}$ is the mean value of air temperature, and $\bar{Q}$ is the mean humidity. According to Andreas, (1988) A_T and A_Q are given in the visible and near-infrared wavelength region of scalar spectra, as follows:

$$A_T = -0.78 \times 10^{-6} \left(\frac{P}{T}\right) + 0.126 \times 10^{-6} R_v Q \tag{2.29}$$

$$A_Q = -0.126 \times 10^{-6} R_v Q \quad (2.30)$$

where, R_v is the specific gas constant for water vapour (461.5 J/K·kg). The Eq. (2.29) and Eq.(2.30) has been solved for normal atmospheric conditions[2], and finding $A_T = -0.27 \times 10^{-3}$ and $A_Q = -0.70 \times 10^{-6}$. However, ${C_n}^2$ is more influenced by the temperature than the humidity, thus, this can be expressed by a direct function of ${C_T}^2$ (Guyot et al., 2009; Moene, 2003), as follows:

$${C_n}^2 \approx \frac{{A_T}^2}{T^2} {C_T}^2 \left(1 + \frac{0.03}{\beta_r}\right)^2 \quad (2.31)$$

where, the β_r term corresponds to the ratio between the turbulent heat fluxes ($\beta_r = Qh/Qe$) and known as the Bowen ratio. The term of β_r is a correction for humidity fluctuations. Nevertheless, as demonstrate by Moene (2003) this correction is not necessary in most situations, because this is insignificant for large β_r values, whereas for small β_r, (i.e., for weak sensible heat fluxes), the absolute correction on Qh remains small with respect to the other energy fluxes. Hence, the form with β_r can be neglected and then ${C_T}^2$ is directly proportional to ${C_n}^2$:

$${C_n}^2 \approx \frac{{A_T}^2}{T^2} {C_T}^2 \quad (2.32)$$

2.4.2.2 Surface sensible flux from structure parameters

From ${C_T}^2$, it is possible to estimate Qh applying the Monin-Obukhov Similarity Theory (MOST), jointly with additional meteorological data: air temperature, relative humidity, wind speed and air pressure.

MOST derived the universal dimensionless relationship for ${C_T}^2$:

$$\frac{{C_T}^2 (z_{LAS} - d)^{\frac{2}{3}}}{{T_*}^2} = f_T\left(\frac{z_{LAS} - d}{L_{MO}}\right) \qquad (L_{MO} < 0) \quad (2.33)$$

and

[2] Normal atmospheric conditions: T = 228 Kelvin, P = 1×10^5 Pa and Q = 0.012 kg/m^3

$$T_*^{\,2} = \frac{C_T^{\,2}(z_{LAS} - d)^{2/3}}{f_T\left(\frac{z_{LAS} - d}{L_{MO}}\right)} \tag{2.34}$$

where, d is the zero-displacement height (the height at which the mean velocity is zero due to large obstacles such as buildings/canopy), z_{LAS} is the effective height of the scintillometer beam above the surface, L_{MO} is the Monin-Obukhov length, T_* is the temperature scaling variable and f_T corresponds to the universal stability function. According to several authors, the latter varies depending on atmospheric stability conditions. In this work, the expression used for f_T is that proposed by Andreas (1988):

- For unstable conditions (daytime, $L_{MO} < 0$):

$$f_T\left(\frac{z_{LAS} - d}{L_{MO}}\right) = c_{T1}\left(1 - c_{T2}\frac{z_{LAS} - d}{L_{MO}}\right)^{-2/3} \tag{2.35}$$

- And for stable conditions (night-time, $L_{MO} > 0$):

$$f_T\left(\frac{z_{LAS} - d}{L_{MO}}\right) = c_{T1}\left(1 + c_{T3}\left(\frac{z_{LAS} - d}{L_{MO}}\right)^{2/3}\right) \tag{2.36}$$

where, $c_{T1} = 4.9$, $c_{T2} = 6.1$ and $c_{T3} = 2.2$.

The universal stability function f_T and the temperature scaling are defined by the Obukhov length L_{MO}, a parameter that describes the effects of buoyancy on turbulent flows in function of the air temperature T, the gravity force g, the von Karman constant ($k_v = 0.4$), and the friction velocity u_*:

$$L_{MO} = \frac{{u_*}^2 T}{g k_v T_*} \tag{2.37}$$

Furthermore, u_* is estimated iteratively using the Eqs. (2.34) – (2.37)[3] and the integrated stability function for momentum (ψ_m) in the following manner:

$$u_* = \frac{k_v U}{\ln\left(\frac{z_u - d}{z_0}\right) - \psi_m\left(\frac{z_u - d}{L_{MO}}\right) + \psi_m\left(\frac{z_0 - d}{L_{MO}}\right)} \tag{2.38}$$

[3] The iterative calculation of u_* and additional parameters T_* and L_{MO}, starts with the initial guess of neutral atmospheric conditions $L_{MO} = 1000$ m.

where, z_0 is the roughness length and U the wind speed at the height z_u. Just like for f_T, Panofsky & Dutton, 1984 introduced ψ_m following the atmospheric stability, so:

- For unstable conditions (daytime, $L_{MO} < 0$):

$$\psi_m\left(\frac{z_u - d}{L_{MO}}\right) = 2\,ln\left[\frac{1+x}{2}\right] + ln\left[\frac{1+x^2}{2}\right] - 2\,arctan(x) + \frac{\pi}{2} \quad (2.39)$$

$$\text{With } x = \left(1 - 16\,\frac{z_u - d}{L_{MO}}\right)^{1/4} \quad (2.40)$$

- And for stable conditions (night-time, $L_{MO} > 0$):

$$\psi_m\left(\frac{z_u - d}{L_{MO}}\right) = -5\left(\frac{z_u - d}{L_{MO}}\right) \quad (2.41)$$

From the Eq. (2.34) to the Eq. (2.37), additional aerodynamic parameters of the surface are necessary. These includes roughness length or surface roughness (z_0) and zero-displacement height (d). Both terms related to the crop height (h), as follows (Kipp & Zonen B.V, 2003):

$$z_0 = 0.1h \quad (2.42)$$

$$d = 0.7h \quad (2.43)$$

In this way, from ${C_n}^2$ measurements, meteorological and terrain parameters, and the application of MOST relationships, T_*, L_{MO} and u_* are iteratively estimated. Then, Qh can be computed as follows (a diagram for Qh estimation procedure is presented in the Figure 2.6):

$$Qh = -\rho_a C_p u_* T_* \quad (2.44)$$

where, ρ_a is air density (~1.12 kg/m^3 at sea level) and C_p is the specific heat capacity of air at constant pressure (~1005 J/K kg).

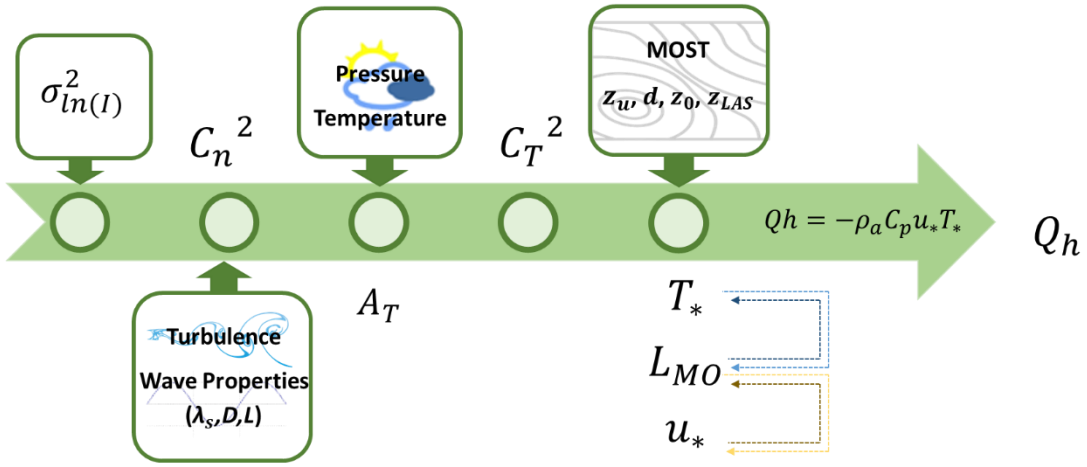

Figure 2.6. Procedure to estimate the sensible flux by the scintillometer.

The Large Aperture Scintillometer (LAS)

In our experiment, a Large Aperture Scintillometer (LAS) MKI produced by Kipp&Zonen® was installed at the highest levels of the BGW. The path length range of a LAS is 250 up to 4.5 km for a diameter (D) of 15 cm. However, shorter distances between 100 m to 1 km could be measured if the aperture diameter is reduced to 10 cm by a diaphragm. Another specification of the LAS is the infrared beam λ_s, which corresponds to 850 nm.

The LAS MKI was implemented on the BGW during punctual days (sunny or not) during the 2018-2020 summers over some average periods of 7 hours. Each scintillometer unit (transmitter and receiver) was situated on the highest points of the roof separated about approximately 100 m. Diaphragms for short range applications were placed in front of the units, reducing the aperture diameter D from 15 to 10 cm.

LAS MKI provides spatially average measurements of $C_n{}^2$. Indeed, LAS MKI measures the variance of the intensity fluctuations natural logarithm ($\sigma^2_{ln\,I}$), which is related to the path-average refractive index structure parameter $C_n{}^2$, as follows:

$$C_n{}^2 = 1.12\sigma^2_{ln\,I} D^{7/3} R^{-3} \qquad (2.45)$$

where, D is the aperture diameter of both transmitter and receiver, and R is the path-length between both LAS units.

When the intensity of ${C_n}^2$ is too elevated, the signal becomes saturated and the intensity fluctuations of the scintillometer $\sigma_{ln(I)}^2$ are no longer proportional to ${C_n}^2$. This phenomenon is known as the saturation effect. To avoid this, the pathlength, the aperture diameter and the wavelength are used to evaluate the criterion of ${C_n}^2$ for saturation-free conditions, with the formula ${C_n}^2 < 0.18 D^{5/3} R^{-8/3} {\lambda_s}^{2/6}$.

Since the path length and the height of the LAS units are the only variables than can be modified to maintain ${C_n}^2$ below the saturation criterion, the transmitter and receiver heigh (z_T and z_R) were adjusted to respect ${C_n}^2 < 1.7x10^{-10}\ m^{-2/3}$ in the BGW.

The LAS MKI manufacturer provides a software to users, which performs estimations of Qh by applying the iterative procedure presented previously. This software called EVATION (Kipp & Zonen B.V, 2015) includes a calculator of effective beam height (z_{LAS}). Then, z_{LAS} was calculated from a detailed topographic characterisation of the BGW transect profile in EVATION (see in Figure 2.7).

Table 2.1. LAS MKI Setting Experiment.

Feature	Value
D (cm)	10
R (m)	100
z_{LAS} (m)	1.56
z_u (m)	10
z_0 (m)	0.25
d (m)	0
z_T (m)	1.4
z_R [m]	1.6
Duration	≈7h (11:00 – 18:00)

Additional parameters related to the terrain, such as z_0 and d, were adopted following the LAS MKI manual. For z_0, the BGW was considered as a rough terrain with open landscape and obstacles separated by $\sim 15h$, while d was considered negligible since

the roughness elements of the BGW are not closely packed. The setting of the LAS MKI over the BGW is presented in Table 2.1.

As the measurement campaigns were carried out during summer daytime and usually sunny conditions, MOST functions for unstable atmospheric conditions were used, assuming effects of convection ($Qh > 0$). The footprint analysis or the source area[4] of measurements with the scintillometer was not conducted because in-situ wind speed and direction data were missing.

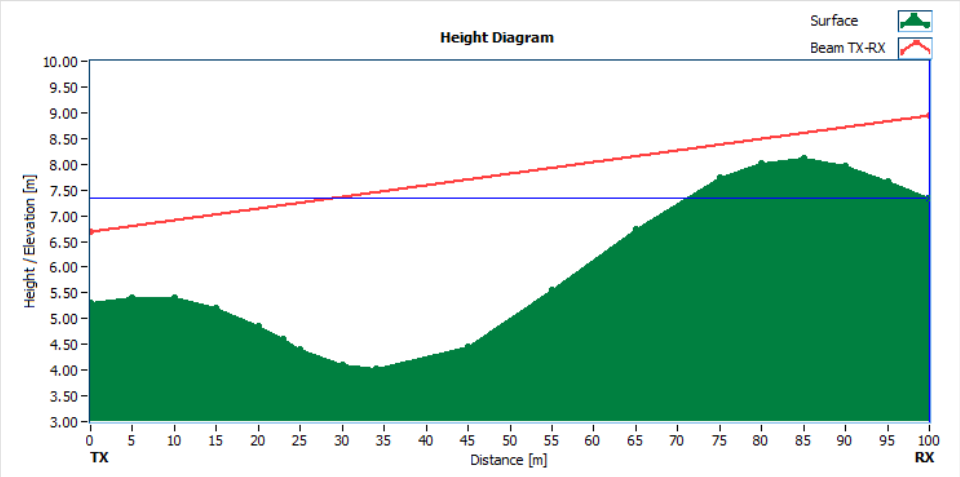

Figure 2.7. Horizontal path length and effective height of LAS beam (red).

2.4.2.3 *Net radiation*

To analyse the main components that supply energy to the BGW, a CNR4 radiometer from Kipp&Zonen® was installed close to the LAS receiver unit and 1.5 m over the ground. The objective was the measurement of Rn, the ratio between the incoming and outgoing short and long-wave radiation.

CNR4 radiometer includes two pyranometers to measure incident Sw_{in} and reflected Sw_{out} solar or short-wave radiation, and two pyrgeometers to estimate long-wave radiation from the sky Lw_{in} and the ground Lw_{out}. Because of the gain of energy for

[4] Footprint or source area represents the area that directly influences the measurements of the scintillometer. This area depends on the installation height of the scintillometer, the wind speed and wind direction.

the surface from the incident radiation, Sw_{in} and Lw_{in} are positive, while the energy reflected, Sw_{out} and Lw_{out} is negative. All radiation components are used to calculate the net total radiation on the BGW like this:

$$Rn = (Sw_{in} - Sw_{out}) + (Lw_{in} - Lw_{out}) \quad (2.46)$$

As two temperature sensors are incorporated in the CNR4, a Pt-100 and thermistor, air temperature records were also stored for Qh computation.

Additional necessary meteorological data, such as, wind speed and direction, relative humidity, and air pressure were not available in-situ. In consequence, they were gathered from the Orly Airport weather station, from the national meteorological service of France (METEO FRANCE), located 50 km from the BGW. The timestep of the dataset was 3 hours.

2.4.2.4 Soil Heat Conduction

According to the first law of heat conduction (Fourier's law), the conduction of heat flux into the soil is linearly proportional to the soil temperature gradient dT/dz of the soil layer (expressed in °K/m units), and the capacity of the soil to transfer heat, property known as soil thermal conductivity k (W/m°K):

$$Qg(z,t) = -k\frac{dT}{dz} \quad (2.47)$$

During the energy balance measurement campaigns, four thermocouples were placed in the BGW substrate, between the LAS receiver and the CNR4. They were vertically separated from 1 to 2 cm, aiming to estimate the soil thermal gradient as a direct application of the one-dimensional form of Fourier's Law, and quantify the heat flux transfer (Qg) by means of the Eq. (2.47).

The experimental data of temperature gathered by the thermocouples placed in the deepest and superficial location of the soil ($z_1 = 2$ and $z_4 = 6$ cm, respectively) as shown in Figure 2.8, was used to calculate the temperature gradient.

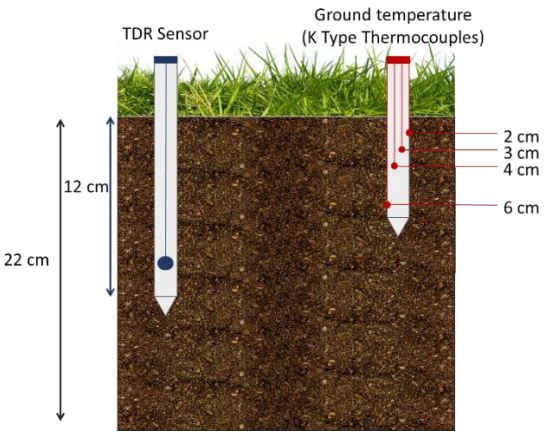

Figure 2.8. TDR sensor and K type thermocouple set-up on the BGW.

Since soil thermal conductivity k is a function of several factors, such as soil density, porosity, water content or thermal conductivity of individual particles (Vera et al., 2018), there is a great difficulty in obtaining accurate k measurements under field conditions.

In our experiment, a value of k was set according to a literature review of Vera et al. (2017), which is based on soil moisture conditions of the green roofs. Measurements of water content in the BGW's substrate were carried out with wireless Time Domain Reflectometry (TDR) sensors (see Section 3 for details). They served to get soil moisture information and determine the value of k: 0.15 and 0.85 (W/mK) were used for dry and wet soil, respectively.

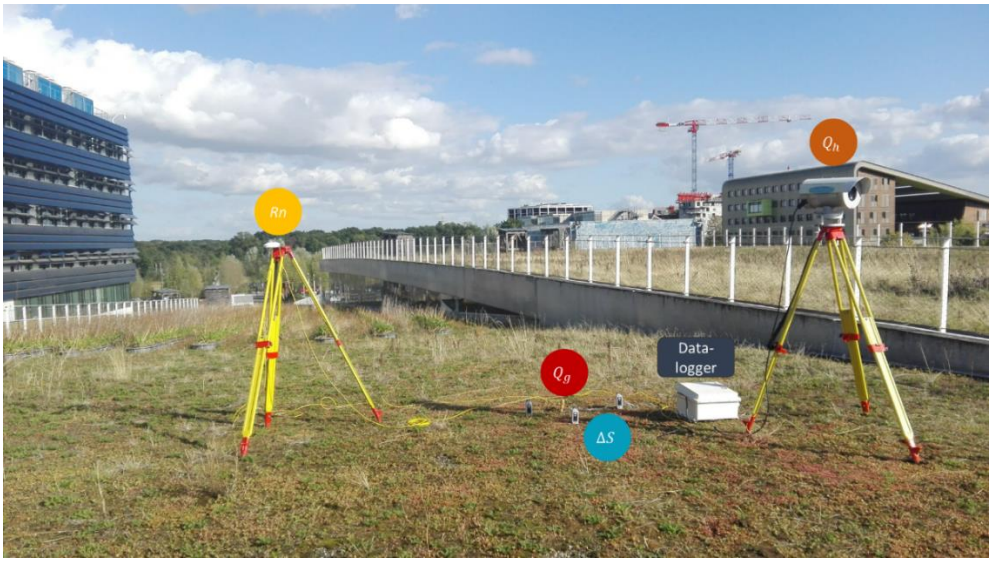

Figure 2.9. Implementation of CNR4 (yellow), LAS MKI-receiver (orange), Type K Thermocouples (red) and TDR sensors (cyan) on the BGW.

2.4.2.5 SEB data collection and processing

BGW measurements from the LAS MKI, CNR4 and thermocouples were collected with a CR3000 Datalogger (from Campbell Scientific®). A program was created through the software LoggerNet (i.e., from the same Datalogger manufacturer) to communicate with the sensors, and to collect and store the data.

The sampling frequency of the data-logger was 1 Hz, but different intervals were used to store data. An average interval of 10 min was used for LAS MKI measurements, while CNR4 and soil temperature measurements were averaged each 5 min. After each campaign, the raw data were validated using a quality control (QC) parameter, and the minimum analogue voltage outputs were checked.

LAS MKI provides two main signals outputs $Demod$ and UCn_2. The first signal corresponds to the intensity fluctuations or signal strength recorded at the receiver. This is also called "demodulated signal" ($Demod = I$) and is used as a QC parameter: if $Demod$ signal is between 0 and -50 [mV], the data is not reliable and not used.

The average of $Demod$ or intensity (I) and the standard deviation (σ_I) for 10 minutes interval, were used to transform normal distributed variance to log-normal distributed variance ($\sigma^2_{ln(I)}$). The latter is used to deduce ${C_n}^2$ with the Eq. (2.45), as was described by Van Kesteren & Hartogensis, (2011):

$$\sigma^2_{ln(I)} = ln\left(1 + \frac{\sigma_I^2}{\bar{I}^2}\right) \tag{2.48}$$

The second signal recorded in the data-logger is UCn_2, the log of ${C_n}^2$ signal. The value of ${C_n}^2$ was calculated directly from the EM intensity fluctuations and the Eq. (2.45) at the LAS receiver unit (jointly with D and R values). In addition, the standard deviation of the interval averaged UCn_2 $\left(\sigma_{UCn_2}\right)$ was computed by the data-logger. Then, UCn_2 and σ_{UCn_2} were linked to estimate ${C_n}^2$ by:

$$C_n{}^2 = 10^{(UCn_2 - 12 + 1.15\sigma^2_{UCn_2})} \quad (2.49)$$

Apart of $Demod$ and UCn_2, there is another way to calculate $C_n{}^2$ from LAS signal outputs. After each measurement cycle (1 Hz), the data-logger calculates $PUCn_2$ from the output signal UCn_2 ($PUCn_2 = 10^3 \cdot 10^{UCn_2}$). Because of the restricted capacity of data acquisition systems to store small values of $C_n{}^2$, which ranges between 10^{-11} and 10^{-17} $m^{-2/3}$, the $PUCn_2$ signal is a scaled value of $C_n{}^2$. Then, $C_n{}^2$ can be re-computed as follows:

$$C_n{}^2 = PUCn_2 \cdot 10^{-15} \quad (2.50)$$

The results findings of Dooley & Creech-Eakman (2018) were taken into consideration to establish the most relevant equation to estimate $C_n{}^2$. His study analysed the accuracy of $C_n{}^2$ estimation from Eq. (2.45), Eq. (2.49) and Eq. (2.50). He concluded the Eq. (2.49) should be privileged, since Eq. (2.45) needs highly accurate path length measurements, meanwhile the non-linearity of $C_n{}^2$ is not considered in the Eq. (2.50).

From raw data and in order to deduce Qe, each component of SEB was calculated with a time step of 10 minutes, as described below and represented in Figure 2.10:

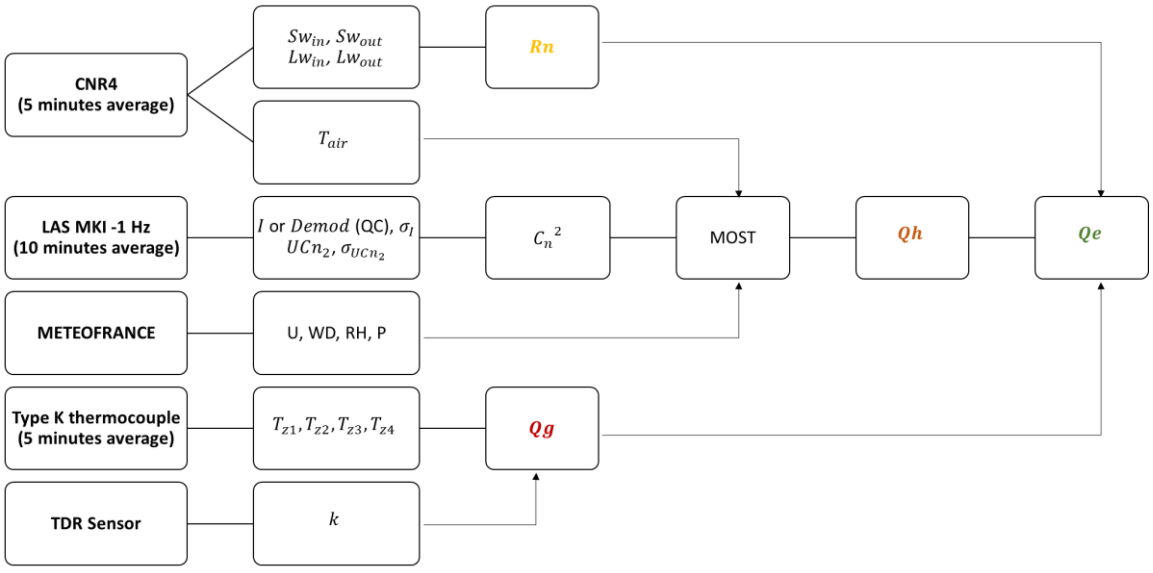

Figure 2.10. Data processing of SEB components.

- The value of Rn was estimated through Eq. (2.46).

- Moisture conditions and k were determined from the TDR sensor water content lectures.
- The temperature gradient was calculated from thermocouples, and then Qg was computed by means of Eq. (2.47).
- The value of ${C_n}^2$ was evaluated through the Eq. (2.45), Eq. (2.49) and Eq. (2.50); but results from Eq. (2.49) were privileged for estimation of Qh.
- Meteorological data gathered from METEO FRANCE and T_{air} from the CNR4 were utilised jointly with ${C_n}^2$ to process Qh.

Since several meteorological variables (U, P, etc.,) and some BGW field parameters (k, h) are used to calculate Qh and Qg, their impact on the final estimation of the energy balance components was analysed through a sensitivity analysis (Section 2.5.1.1). Thus, to explore the variation of SEB components through different input parameter combinations, a Design of Experiments (DoE) was applied.

2.4.2.6 Design of Experiments

The DoE method used to evaluate the variation of SEB components was a Latin Hypercube Sampling (LHS), a statistical approximation that estimates the iteration output model, from the probability density function (pdf) of input parameters N. Each pdf is divided into M intervals of equal probability, for which a value is randomly selected. The number of intervals M should be at least N+1 (or larger).

The purpose of this method is to explore the entire range of each parameter, and recreate the input distribution through less samples (for details of LHS, see Marino, Hogue, Ray, & Kirschner, 2008). Then, LHS matrix is composed by the number of parameters (N) in columns and number of simulations (N+1) in rows.

The probability distribution of meteorological data (wind speed and direction, relative humidity, and air pressure) was simulated as a uniform distribution based on 2018 and 2019 minimum and maximum records. In parallel, the uncertainty of soil thermal conductivity k value over Qg was analysed, considering a uniform distribution with a

minimum and maximum of 0.15 and 0.85 W/mK, which corresponds to the dry and wet soil, respectively.

Table 2.2. Parameters of sensitivity analysis.

Input		Range of Values	
Parameter	**Units**	**Minimum**	**Maximum**
z_u	m	1.5	10
h	m	0	0.5
k	W/m°K	0.15	0.85
P	Pa	1000	1015
U	m/s	2	5
WD	°	20	80
RH	%	20	50

The impact of field parameters, such as z_0 and d, which are a direct function of h (Eq. (2.42) and Eq. (2.43)), was analysed through h which is the only parameter known. During the measurement campaigns, two types of vegetation characterised the BGW: green grass and a mix of perennial planting and bulbous (which achieves a maximum height of 50 cm). In consequence, h was simulated as a uniform distribution with a minimum and a maximum of 0 and 50 cm, respectively.

Since the height of the wind speed anemometer (z_u) is used to derive Qh by MOST iteration, but no measurements of wind speed were taken, this parameter was included in the sensitivity analysis with a minimum of 1.5 m (equal to the height of the LAS receiver) and a maximum of 10 m (theoretical height of anemometer). All the details of every parameter and its range of values is presented in Table 2.2.

From the output LHS matrix (Table 2.3), all the input value combinations (model simulations) were applied in EVATION software and then a correlation analysis between the input parameters and EVATION model output were evaluated, through the Pearson correlation coefficient. The results are analysed later in Section 2.5.1.1.

Table 2.3. LHS matrix presenting the selected values for each parameter.

Test	z_u	h	k	P	U	WD	RH
1	9.53	0.16	0.40	1001	3.03	41.76	39.68
2	3.27	0.02	0.39	1009	4.60	47.46	39.98
3	5.09	0.42	0.23	1012	3.81	44.48	43.68
4	8.24	0.42	0.75	1004	3.47	62.70	34.95
5	4.33	0.21	0.71	1003	4.71	40.94	40.73
6	4.37	0.16	0.33	1004	2.66	68.83	23.18
7	9.78	0.24	0.58	1010	3.99	54.73	22.13
8	6.13	0.17	0.73	1004	2.88	45.05	27.51

2.4.3 Latent heat flux by Evapotranspiration chamber (Ch)

In addition to measuring SEB's components to deduce Qe, a portable evapotranspiration chamber built by the Cerema (*Centre D'études Et D'expertise Sur Les Risques, L'environnement, La Mobilité Et L'aménagement*) was punctually installed over the BGW vegetation to measure Qe. This device consists of a one square-meter enclosed chamber of Plexiglas of 0.3 m^3 (1 m^2 x 0.3 m) total volume. Gas exchanges specifically water vapour (absolute humidity) H_2O and carbon dioxide CO_2 were monitored inside the chamber through a LI-COR 850 gas analyser.

In addition, the chamber was equipped with two small rotating fans (making the air sample representative of outside-real conditions), two T107 temperature sensors and a NR-Lite radiometer (Figure 2.11), in order to control microclimate variation parameters inside the ventilated chamber.

Figure 2.11. Evapotranspiration chamber and TDR sensors installed in the BGW on 20th of June 2018.

The latent heat flux rate of the volume enclosed by the chamber is deduced from the rise of the absolute humidity concentration (Coutts et al., 2013), specifically from the slope of the absolute humidity linear regression (Ramier et al., 2015) during the first minute of measurement (see Figure 2.12), as follow:

$$Qe = 10^{-3} L_v \frac{V_{ch}}{A_{ch}} \frac{dQ}{dt} \quad (2.51)$$

where, Qe is the latent heat flux (W/m^2), L_v is the latent heat of vaporisation of water, V_{ch} and A_{ch} correspond to the volume and area of the chamber (0.3 m^3 and 1 m^2, respectively), dQ/dt represents the absolute humidity variation during the first minute of measurement (g/m^{3}s), and 10^{-3} is a conversion factor.

In summer days of 2018 and 2019, the evapotranspiration chamber was placed over the ground of the BGW for two minutes every ten minutes to monitor the variation of absolute humidity, carbon dioxide, net radiation, and temperature. The chamber was connected to a CR800 Datalogger (from Campbell Scientific®) to collect measurements every second.

The duration of the measurement (2 minutes) is assumed to be short enough to not generate microclimate changes inside the chamber and attain the saturation vapour pressure.

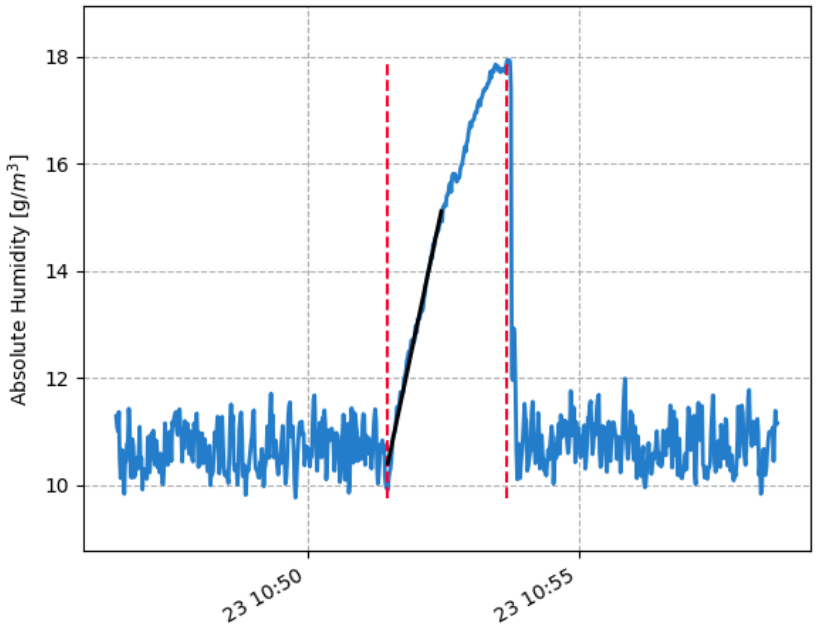

Figure 2.12. Time series of absolute humidity variation (blue) for two minutes (star and end time in red dotted lines) and linear regression (black) on 23rd of August 2019.

2.4.4 *Evapotranspiration by Water balance (WB)*

In a green roof, water input fluxes as precipitation (or irrigation) can be released to the discharge/sewage network by runoff or to the atmosphere by ET (see Figure 2.13). The water balance in a green roof over a given time can be expressed as follows:

$$Pr + I = Qr + ET + \Delta S \tag{2.52}$$

where, Pr represents the precipitation, I the infiltration, Qr is the runoff and ΔS corresponds to the variation of the stored water in the soil. All the terms of the Eq. (2.52) are expressed in terms of mass flux (mm/d).

In extensive green roofs, where no irrigation system is usually comprised (i.e., as BGW case), and during long dry periods without precipitation, there is no water infiltration in the substrate nor runoff. Therefore, for these periods, the ET flux (mm/h) can be estimated from the water balance equation as the soil water content variations:

$$ET = -\Delta S \tag{2.53}$$

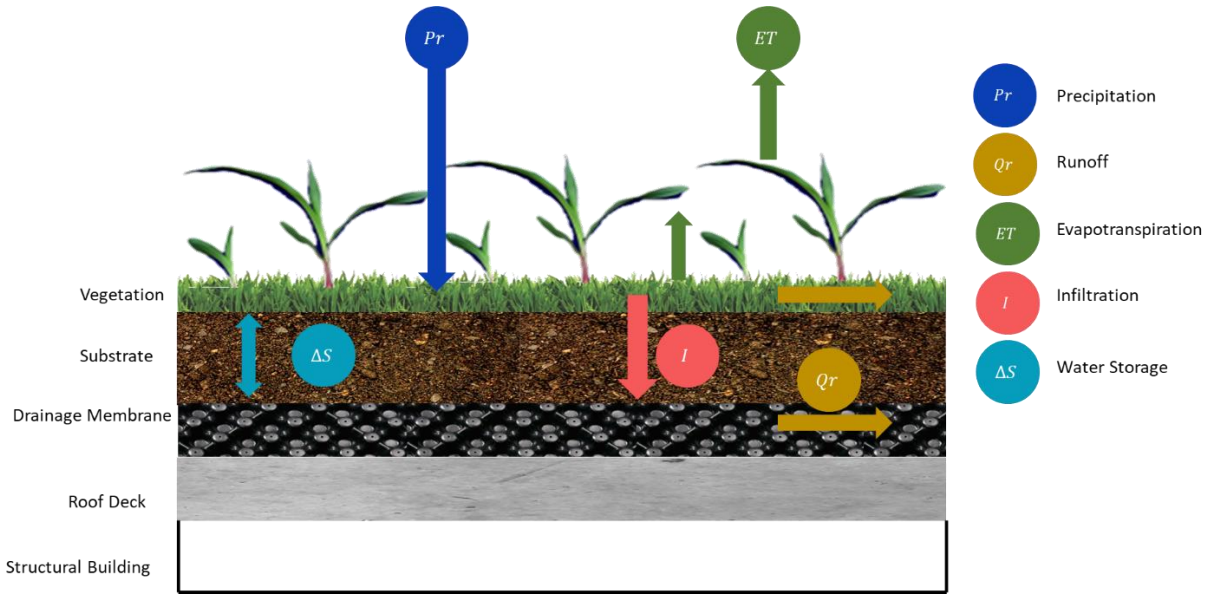

Figure 2.13. Water Balance in a green roof without irrigation.

The space-time variability of local water content and soil temperature (T_{soil}) was monitored on the BGW by means of a wireless network of 16 CWS665 sensors (produced by Campbell Scientific®) placed in different locations of the roof (Figure 2.14.d). The sensors use Time Domain Reflectometry (TDR) technique to measure the propagation time of an electromagnetic (EM) pulse. This pulse is applied to a pair of 12-cm metallic rods inserted into the soil. The time necessary of the incident EM to reach the end of the rods and its reflection will depend on the dielectric permittivity (k_a) of the soil.

An empirical universal relationship between the dielectric permittivity (k_a) and the volumetric water content (VWC) for a homogeneous mineral soil was established by Topp et al. (1980). This relationship is widely known as Topp's Equation (1980):

$$VWC = -5.3 \times 10^{-2} + 2.92 \times 10^{-2} k_a - 5.5 \times 10^{-4} k_a^2 + 4.3 \times 10^{-6} k_a^3 \qquad (2.54)$$

From VWC (m^3/m^3) measurements, the variations of soil water content were determined as follows:

$$\Delta S = \frac{\Delta VWC}{\Delta t} z_s \qquad (2.55)$$

where, z_s the substrate layer thickness (assuming uniform distribution) and Δt is the time step of soil water storage variation. Then, ET in the BGW was deduced from the

Eq. (2.53) and Eq. (2.55). It represents the height of water loss by soil evaporation and plant transpiration over a dry period.

$$ET = -\Delta S = -\frac{\Delta VWC}{\Delta t} z_s \tag{2.56}$$

The time step to measure k_a and T_{soil} with the CWS665 sensors was 1.5 min. The measurements were transmitted to a CWB100 wireless base, which stores the measurements of multiple sensors, and later transfers them to a CR6 Datalogger (from Campbell Scientific®).

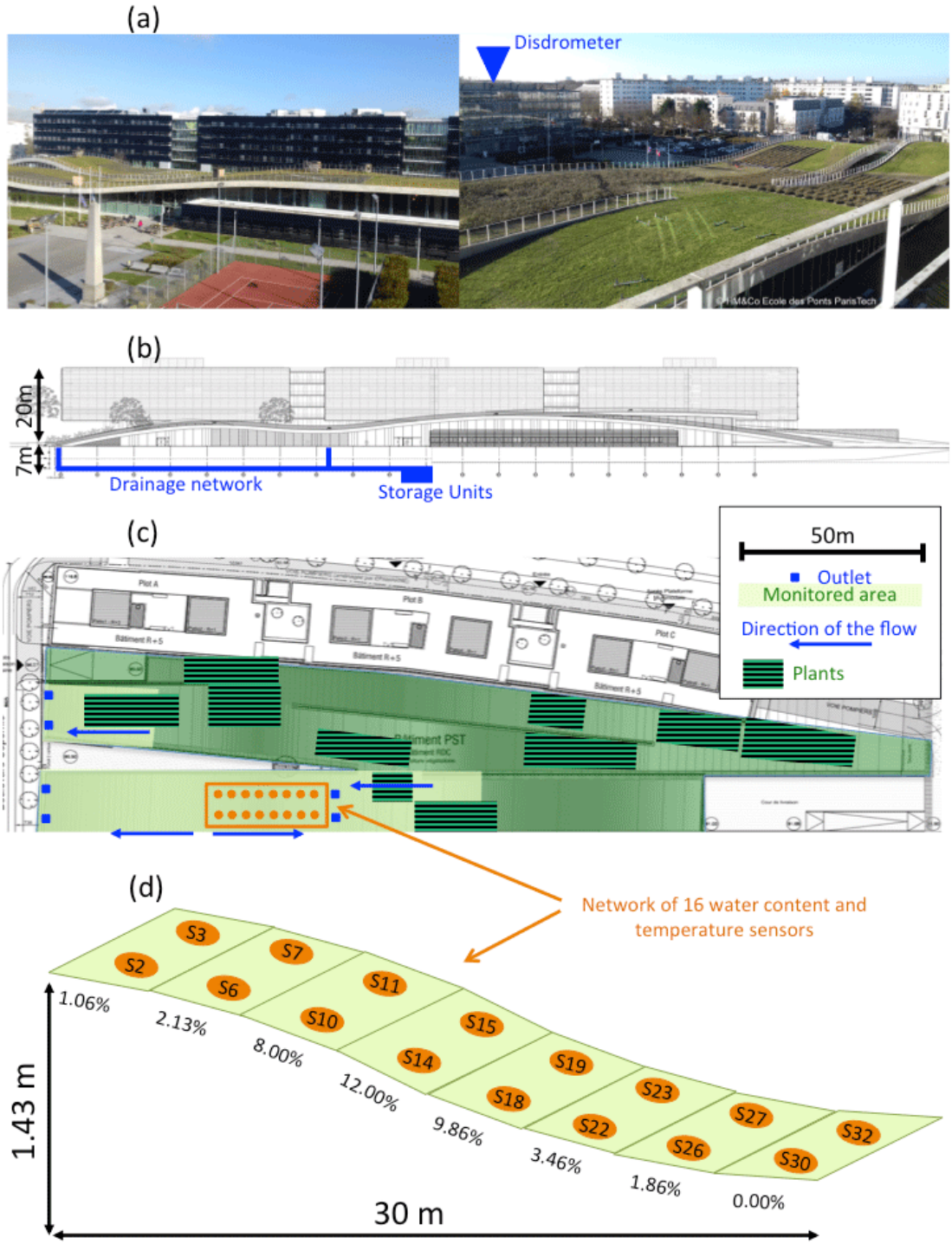

Figure 2.14. Water balance monitoring components on the BGW, (a) pictures, (b) vertical representation and flow path lengths, (c) aerial representation showing the monitored area, and (d) profile of the section where the water content sensors were implemented indicating the slopes. Source: Versini, Stanic, et al. (2020).

2.5 Study of the ET campaign

The measuring equipment was not permanently installed on the BGW. Due to technical and safety conditions, most measurements were carried out during one day and not all measuring equipment was used at the same time. Table 2.4 summarises all the dates of measurement, and the data that were collected are marked with a 'X'. The three measurement methods were used simultaneously on the following dates: 2018/09/26, 2018/09/27, 2019/07/10, 2019/08/08, 2019/08/23 and 2019/08/29.

Table 2.4. Dates and methods of ET measurement on the BGW.

<table>
<tr><th rowspan="2">Date</th><th colspan="4">SEB</th><th colspan="5">Ch</th><th colspan="2">WB</th></tr>
<tr><td>Rn</td><td>C_n^2</td><td>T_{z1},T_{z2},T_{z3},T_{z4}</td><td>T_{air}</td><td>H_2O</td><td>CO_2</td><td>T_{int}</td><td>T_{ext}</td><td>Rn</td><td>k_a</td><td>T_{soil}</td></tr>
<tr><td>2018/06/20</td><td colspan="4" rowspan="2">–</td><td colspan="5" rowspan="4">X</td><td colspan="2">X</td></tr>
<tr><td>2018/08/21</td><td colspan="2">–</td></tr>
<tr><td>2018/09/26</td><td colspan="4" rowspan="11">X</td><td colspan="2" rowspan="2">X</td></tr>
<tr><td>2018/09/27</td></tr>
<tr><td>2019/06/20</td><td colspan="5" rowspan="2">–</td><td colspan="2">–</td></tr>
<tr><td>2019/07/04</td><td colspan="2" rowspan="2">X</td></tr>
<tr><td>2019/07/10</td><td colspan="5" rowspan="3">X</td></tr>
<tr><td>2019/08/08</td><td colspan="2">–</td></tr>
<tr><td>2019/08/23</td><td colspan="2" rowspan="2">X</td></tr>
<tr><td>2019/08/29</td></tr>
<tr><td>2019/09/30</td><td colspan="5" rowspan="4">–</td><td colspan="2" rowspan="3">–</td></tr>
<tr><td>2019/10/02</td></tr>
<tr><td>2019/10/03</td></tr>
<tr><td>2020/06/30</td><td colspan="2" rowspan="8">X</td></tr>
<tr><td>2020/07/01</td><td colspan="5" rowspan="7">–</td></tr>
<tr><td>2020/07/08</td></tr>
<tr><td>2020/07/09</td></tr>
<tr><td>2020/07/16</td></tr>
<tr><td>2020/07/17</td></tr>
<tr><td>2020/07/22</td></tr>
<tr><td>2020/07/23</td></tr>
</table>

2.5.1 SEB

Before exploiting the gathered data from the LAS MKI, dates with $Demod$ signal exceeding the QC parameter and the positive values of UCn_2 were discarded. This led to removal of some campaigns of measurement: September 26th and 27th of 2018, June 20th of 2019 and data collected after 15:30 on September 30th of 2019. The errors in data collection were attributed to electrical overload at the transmitter, scintillometer calibration and battery troubles. Once reliable ${C_n}^2$ data was selected, the estimation of Qh was carried out with the similarity theory, meanwhile Qe was deduced from the energy balance.

This analysis uses data collected under unstable daytime, after 11:00 h (to avoid the fluctuations during the first hour of optical alignment and mounting) with the same signal strength conditions. The Figure 2.15 shows surface energy balance components and ${C_n}^2$ along a 100 m long transect over the BGW. The atmospheric conditions range from almost completely full sunny and cloudless sky (2019/07/04, 2019/07/10, 2019/08/23 and 2020/07/22) to partially cloudy.

During the sunny, clear sky days of observation, such as 2019/07/10 or 2020/07/22, the maximum incoming energy fluxes of Rn occurred at noon, as expected. Regarding the air temperature measured with the CNR4, this was above 20 °C at the start of most measurement campaigns (Figure 2.16), except for the dates of the beginning of autumn 2019: 2019/09/30, 2019/10/02 and 2019/10/03. Meanwhile, during all campaigns of measurement the wind speed (measured every 3 hours which explain the sudden spikes and drops) was light and moderate, and it never exceeded 8 m/s.

Figure 2.15. Surface Energy Balance (SEB) and $C_n{}^2$ from LAS.

Regarding the fluctuations of Qe in the Figure 2.15, they seem to be phased with Rn despite different atmospheric conditions. With regards to the intensity of Qh and the strength of ${C_n}^2$, they are not so elevated. However, it was expected high values of Qh as measurements were done during warm and unirrigated periods, which generally leads to measure high values of ${C_n}^2$. Indeed, the magnitude of ${C_n}^2$ in the BGW was around 10^{-13} $m^{-2/3}$. Higher values of ${C_n}^2$ (around 10^{-12} $m^{-2/3}$) were documented by Savage (2009) with a Small Layer Scintillometer (SLS) under similar conditions of measure in a flat terrain with grass vegetation and a horizontal path length of 100 m in South Africa. Thereby, the sensible heat fluxes Qh derived from ${C_n}^2$ were, in all dates, lower than Qe, except for 2019/07/04 where Qh is higher after midday. In this case, high temperatures and the heatwave episode that occurred at the end of June could have depleted the water storage in the soil matrix and suppress the Qe. This was confirmed later by the low levels of soil water content (see more in Figure B.7).

The maximum Qe rate was attained the 2020/07/17 (677 W/m²) at the mid-afternoon (around 15:00), when Rn reach the maximum value around 800 W/m². The temperature followed a similar pattern and it increased too, while the rates of convective heat decreased. During this campaign, the value of U was less than 2.5 m/s from 15:00 (see Figure 2.16), the lowest record of U, which would confirm the cause of low fluxes of Qh. This low rate impacts the closure of the energy balance by transferring the available energy from Rn to the deduced Qe. A quite similar behaviour was observed during the last two campaigns of 2020. By contrast, on 2020/07/01 the low rates of Qh were mainly affected by low ${C_n}^2$ and not U (around 5 m/s), since this day was very cloudy and the BGW had a low contribution of Rn, which inhibited convection fluxes.

The energy from thermal conduction in the ground is in general very low, and this can be confirmed with

Figure 2.17, which shows the average of the surface energy balance components on the BGW. Qg only represents on average 6% of the net energy to the roof (Rn). This may be explained in part by the maintenance characteristics of this extensive green roof,

which does not include watering practices and only depends on rainfall events. Hence, the low occurrence of rainfall during the summer would lead

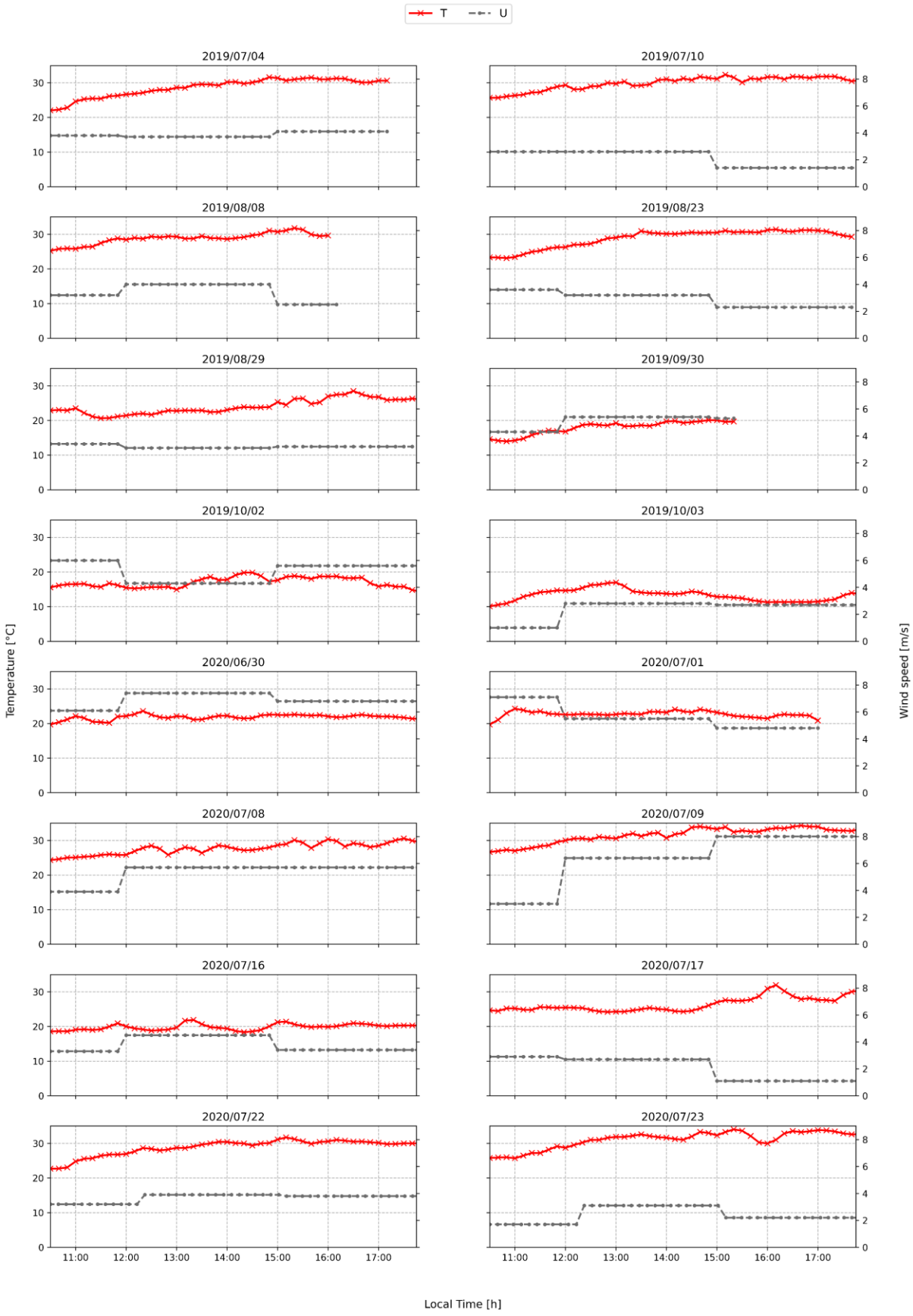

Figure 2.16. Air temperature (cross red line) and wind speed (dotted grey line).

to impact water content and reduce the thermal conductivity of the substrate. Likewise, a negative value of Qg is observed on 2020/07/16. This is explained as an energy gain (or storage) in the soil matrix, since on this day the soil temperature gradient increased with depth.

Contrary to Qg, the total average of Qe accounts for 55% of Rn in the BGW, and thus the main component of the energy balance for all dates, followed by Qh. A similar percentage of net energy dissipated by latent heat was found in an experiment with *Sedum* plants on an extensive green roof. According to the energy balance model and experimental field of Feng et al. (2010), Qe represented 58% of the total energy gained by a green roof (15.87 MJ/m²) during 24 h in a typical summer day in Guangzhou, China.

Nevertheless, in larger urban scales with less vegetation, the distribution of SEB fluxes is generally different. For example, a campaign of measurements carried out over the old downtown area of Toulouse, France, found that 78% of the total energy is dissipated by Qh and only 22% accounts for Qe (Masson et al., 2008).

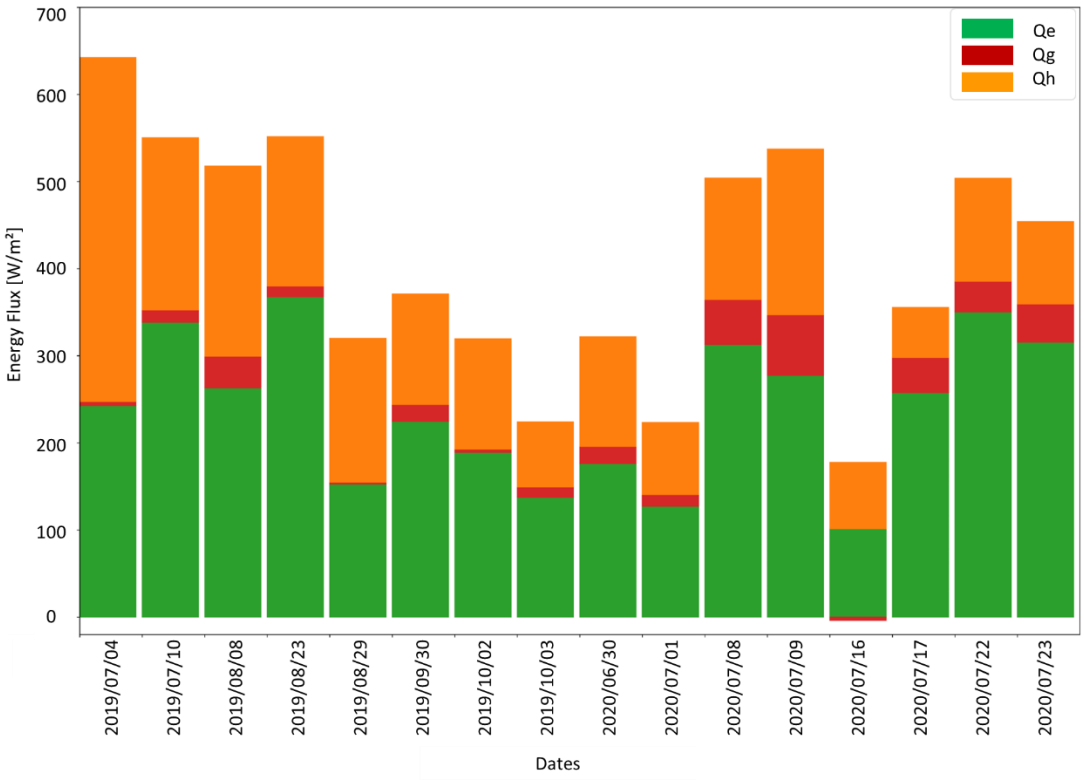

Figure 2.17. Average energy balance components on the BGW.

2.5.1.1 Sensitivity analysis of input variables

Aiming to understand the variables that most impact the iterative process of Qh calculation, as well as Qg estimation, a sensitivity analysis was performed through a Latin Hypercube Sampling (LHS). This analysis was conducted with the data collected on 4th of July/2019, a representative day of summer with unstable atmospheric conditions.

The results of the Pearson's Correlation coefficient, used as a sensitivity index in this analysis, are presented in Figure 2.18. They initially showed that Qh has a moderate positive relationship with air temperature (0.67), as well as a fairly strong positive correlation with ${C_n}^2$ (0.90). Therefore, it is important to ensure that the in-situ air temperature measurements are carried out close to the LAS unit to increase final accuracy of the Qh estimate, just like BGW setting was done.

Regarding Qe, there is a significant linear relationship with Rn (0.76), since Rn determines the energy available to close the energy balance. Meanwhile, Qe has negative correlation with the air temperature (-0.41), as well as a weak relationship with wind speed U (-0.26). Similar outcomes with regard to air temperature were found by Cascone, Coma, et al. (2018), from the literature analysis of factors influencing the ET in green roofs.

The Pearson's Correlation coefficient showed that soil thermal conductivity k only has a moderate negative linear relationship with Qg (-0.69), this is due to the sign of the Eq. (2.47). However, as explained in Section 2.4.2.4, k is assumed constant according to the literature values, so this relationship is altered by the uncertainty of k value on the BGW substrate, which later impacts SEB Eq. (2.25).

Regarding the terrain parameter h, the value of Pearson's coefficient close to zero (0.08) demonstrates a neutral correlation with Qh. However, it should be noted that h determines z_0 and d, which affect z_{LAS} and which, in turn, has been shown to have a low impact on Qh up to ±6%, according to Crawford et al. (2017). In the BGW study, z_0

and d were established following manual recommendations. In consequence, the final estimation of Qh might be weakly influenced by these field parameters.

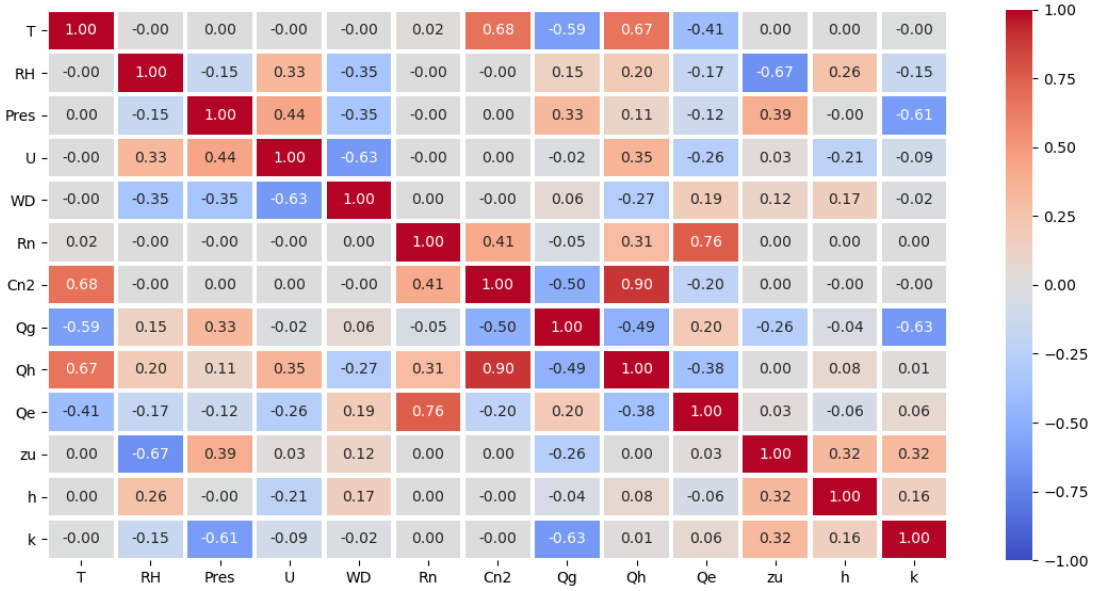

Figure 2.18. Heatmap of Pearson Correlation Coefficient.

Finally, among the meteorological parameters simulated from the minimum and maximum records of METEO FRANCE, the wind speed U is the most correlated to Qh, because having a moderate positive coefficient (0.35). As U is not in-situ measured, it could be not representative of the BGW conditions, and affect the final value of Qh. By contrast, the rest of meteorological parameters, WD, RH and P have positive correlations with Qh, but these are weak and negligible.

2.5.2 *Evapotranspiration chamber (Ch)*

The 2018 chamber measurements were carried out at the lowest point of the BGW, where the slope of the roof is very slight, and which are expected to have higher water content in dry periods than the top of the BGW, according to Versini et al. (2020). In 2019 the chamber was placed at the most elevated point of the green roof and near to the LAS receiver. Finally, because of technical issues in 2020, the chamber was not used.

Raw data collected from the Ch during a typical day is presented in Figure 2.19. The spikes of absolute humidity and temperature (mainly the internal one) correspond to their increment, during the two minutes the Ch is placed over the vegetation. Every start time was used to fit the linear regression of dq/dt and to deduce instantaneous Qe rates.

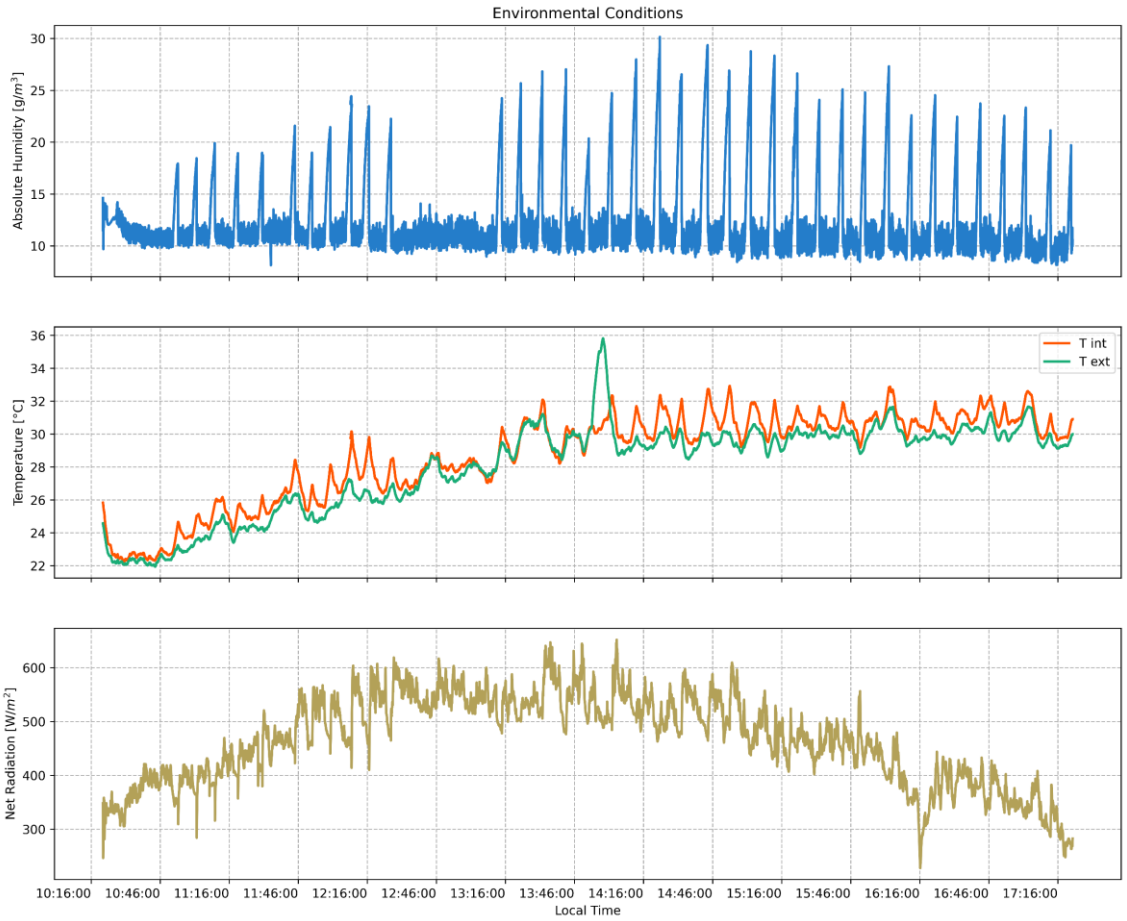

Figure 2.19. Absolute humidity, temperature, and net radiation measurements during 23rd of August 2019.

As mentioned earlier, the solar radiation and air temperature are among the parameters that the most impact Qe. The variation of these parameters within the Ch is one of the most important considerations when using this method, because of the greenhouse effect that changes its microclimate. Indeed, in Figure 2.19 one can notice that the air temperature inside the chamber is slightly higher than the temperature outside, and this difference is around 0.4 °C. This small difference confirms the short measurement period of two minutes with the Ch is not enough to create significant

changes of microclimate parameters inside the chamber. The period when outside air temperature is higher coincides with sensor drops over the plant canopy.

Regarding net radiation, it is possible to follow a diurnal cloudless solar cycle despite net radiation fluctuations in Figure 2.19. These can be due to the shadow effect of chamber installation and removal over the ground, as well as the influence of human activity around the chamber.

Figure 2.20. Evapotranspiration chamber measurements.

Results of Qe estimation from every campaign of measure with the Ch are presented in Figure 2.20, as well as the microclimate conditions of the measurement. The maximum fluxes of Qe were 142 W/m² (4.99 mm/d) and 140 W/m² (4.92 mm/d), measured on 2019/08/08 and 2018/06/20, respectively. Likewise, the highest records of

Rn (measured with the NR-Lite radiometer) and temperatures were reached during these days. Conversely, on 2019/07/10 the Qe rate barely reached 13 W/m² at 11:40, while the internal and external temperatures are above 25 °C and the Rn around 400 W/m². In fact, Qe measurements on 2019/07/10 were the lowest rates registered on the BWG and daily average was 8.6 W/m² (0.3 mm/d).

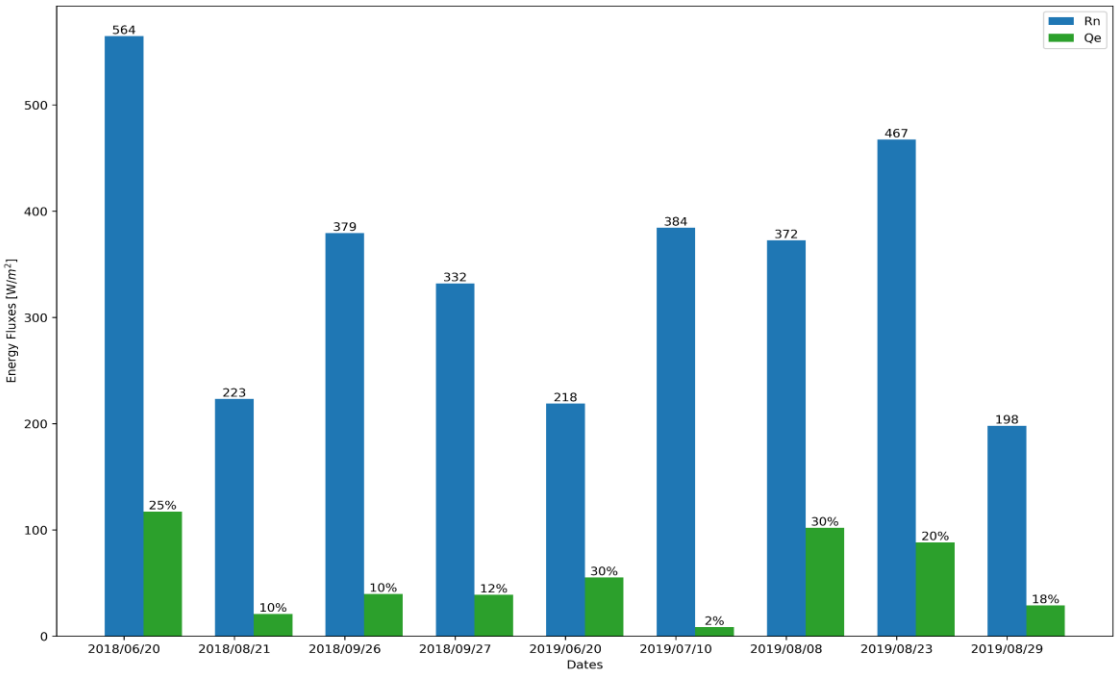

Figure 2.21. Average of net radiation and latent heat flux from Ch.

To grasp the partitioning of thermal fluxes of the SEB on the BGW, the average of Rn and Qe, as well as the percentage of Rn dissipated by Qe, were plotted in the Figure 2.21. The results obtained for 2019/06/20, 2019/08/08 and 2018/06/20, showed the highest average values of Qe represent 30% and 25% of Rn. Similar values of Qe were found by Bevilacqua et al. (2016), from the measurement of the difference between minimum and maximum value of soil water content. The rates of Qe reached maximums of 100 W/m², which represented about 26% to 35% of the incident solar radiation on a well-watered extensive green roof in Italy. By contrast, in 2019/07/10 the BWG average rates of Qe barely reach the 2% of the total radiation. The main cause of this low rate would be associated with low moisture in the green roof substrate, since a heat wave event occurred at the end of June, depleting water in the BGW for ET. The

drought conditions were confirmed by the records of water content, which varies between 0.02 and 0.04 m^3/m^3 (see more in Figure B.7).

2.5.3 WB in dry periods

During some days of 2018 and 2019, CWS665 sensors of soil volumetric water content (VWC) were installed in the surface covered by the evapotranspiration chamber (Figure 2.11), a few minutes before Ch or SEB campaigns started. Then, sensors were removed from the ground once the campaign ended. For these campaigns, the recorded signals of k_a and T_{soil} exhibited not negligible fluctuations.

By contrast, during the summer of 2020, the sensors were permanently installed in a larger surface of the BGW, ensuring data stability and signal transfer, which makes this data series the object of study in this section. With the support of the Tanaris Observatory from HM&Co Laboratory (Ecole des Ponts ParisTech campus) and the rainfall data collected with a Band X Radar tower located in the building roof next to the BGW, the days without rainfall were identified to respect the simplified water balance during dry periods (Eq. (2.53)). At least 4 consecutive days without rainfall were chosen to deduce ET, to ensure stabilisation of measurements, after rainfall events. Three dry periods were selected: 5th to 14th of July, 16th to 24th of July and September 15th to 18th.

Disruptions in the signal transmission and data collection from sensors are easily detected in all periods (see appendix Figure B.1, Figure B.2 and Figure B.3). There are signal discontinuity and drops of dielectric permittivity k_a absolute value. Such signal interruption is then reproduced in the values of the VWC, when using Topp's Equation (Eq. (2.54)). In July, eight sensors worked properly and only 0.5% of time steps have missing data on the entire duration of the ET campaign. Meantime, only six sensors worked partially and 12% of time steps were missing in the September period. Given noticeable breaks and noise of VWC signal, a moving window was implemented to average and smooth VWC data, and consequently to reduce signal peaks and drops

impacting ΔVWC and ET estimates. The window includes 40 samples (number of samples collected hourly) and VWC values below 0 were discarded from the ET analysis, since the minimum value of VWC should be zero.

In all locations, VWC slightly decreases during the period of analysis (Figure B.1, Figure B.2 and Figure B.3), despite water input due to the condensation effect in the early morning hours. Maximum VWC values range from 0.016 up to 0.07 m^3/m^3. Sensors located at the bottom (S30, S32) as well as those at the top (S3, S7) of the BGW, registered the highest ranges of soil moisture for all periods, but they reported minimum VWC values too (S2 in July and S32 in September). It seems that the spatial configuration of TDR sensors (and the local slope) does not influence or determine the maximum VWC and T_{soil}. So, the analysis of ET has been conducted with the average values provided by all sensors.

The Figure 2.22 shows the average values of VWC, T_{soil} and ET during each dry period computed with the moving window. The daily pattern of VWC and T_{soil} is easily observed and the simultaneity of maximum and minimum values of both series too. The daily maximum and minimum of VWC difference is higher when the daily amplitude of the T_{soil} is wider. Besides, the VWC reduces throughout each period and its lowest rates are registered in the second period of July, while maximum T_{soil} remains above 40 °C after the second day. By contrast the highest values of VWC were noticed in September, when T_{soil} decreases along the three days of measurements.

Loss of water by ET during dry periods usually starts around 9 a.m. and the daily average of ET rates were 0.55, 0.34 and 0.78 mm/d for each period, respectively. This means higher soil moisture levels led to find the highest average of ET rates (Jul/05-Jul/14 and Sep/15-Sept/18), while low soil moisture and elevated T_{soil} reported lowest daily average ET (Jul/16-Jul/24).

The highest ET values are reached in the afternoon, according to the variation of VWC (but easier appreciable with the T_{soil} trend). Multiple spikes of ET are reached during the day, specifically in the two periods of July. In fact, these ET trends pursue the VWC

pattern, influenced by T_{soil}, which in most days of July periods increase during the morning until reaching a given temperature and then starts to fluctuate until reaching its maximum value.

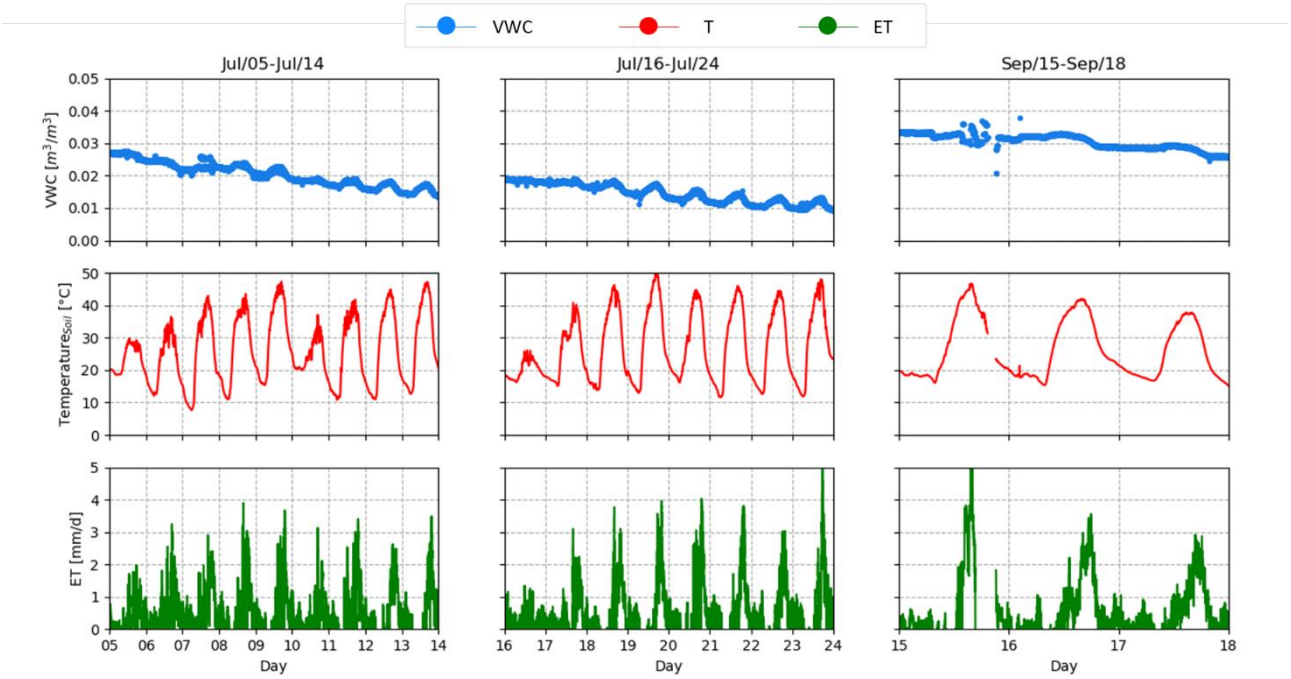

Figure 2.22. VWC (blue), Soil temperature (red) and Evapotranspiration (green) by water balance during three dry periods in 2020, after removing spikes.

The maximum rates of ET are 3.90, 5.08 and 5.92 mm/d for each period, respectively. In the first and third period, the ET decreases slightly over time, as well as the water content in the soil is reduced. For the second period, the maximum value is reached on the last day of measurement, while from the 17 to the 23 of July, the maximum ET is higher than 3 mm/d. It can be noticed the maximum rates of ET are derived during the second period, which corresponds to the driest one and with soil temperature above 40 °C. These conditions generate a reduction of reliability of the sensor measurement, as this would represent the k_a variations of air (instead of water) in the substrate pores around the sensor because of dry soil.

2.5.4 Comparison of ET measurement methods

Since data from each ET method were collected independently, the trend and magnitude of Qe fluxes were compared in terms of ET units. Because latent heat flux from the evapotranspiration chamber (ET_{Ch}) is a direct measure, this was considered as the measure of reference. The comparison procedure includes statistical indicators as the coefficient of correlation (r^2) and the root-mean-square- error (RMSE).

- ET_{SEB} *vs.* ET_{Ch}

First, the latent heat values measured with the SEB (ET_{SEB}) and the evapotranspiration chamber (ET_{Ch}) in 2019 are compared. The most highlighted feature of the linear regressions in Figure 2.23 is the weak positive correlation between ET_{Ch} and ET_{SEB}, with scattered points that do not fit the regression lines and that led to compute r^2 values lower than 0.5. Besides, the values of RMSE indicated a difference of at least 5.13 mm/d, confirming ET_{SEB} was largely higher than ET_{Ch}. In fact, ET_{Ch} reach maximum values of 5 mm/d, while only few values of ET_{SEB} are lower than 3 mm/d.

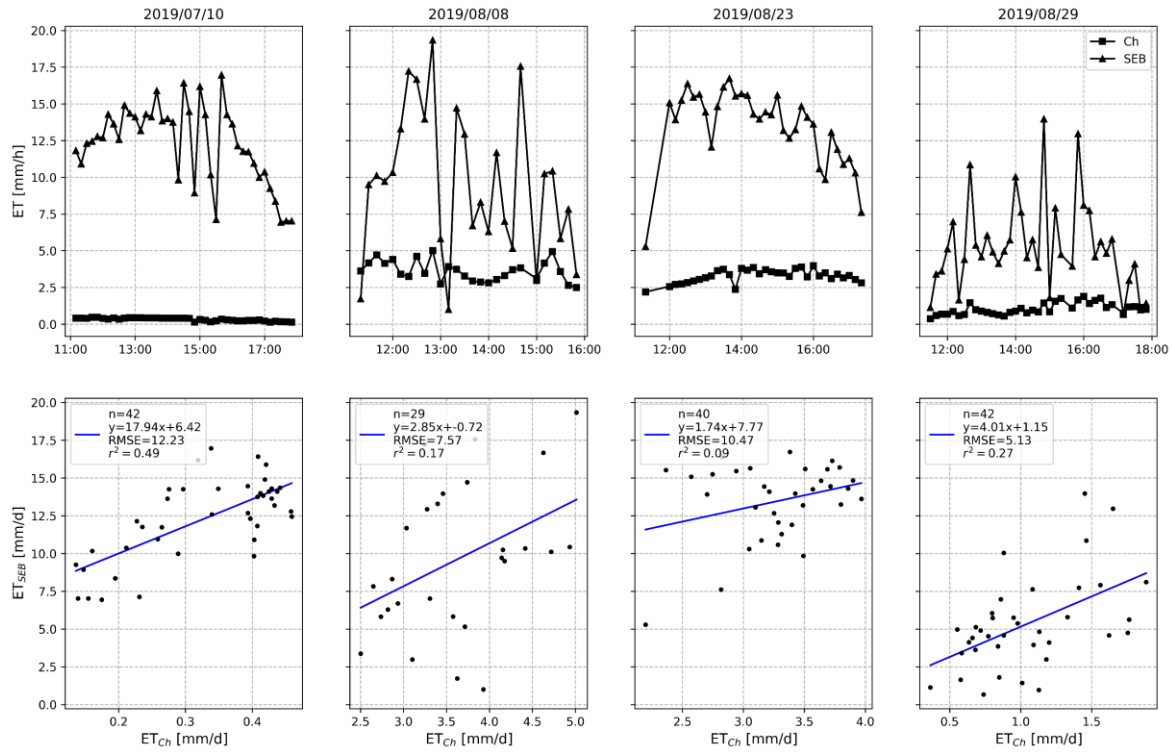

Figure 2.23. ET deduced from SEB and ET measured with the Ch (top). Comparison of ET_{SEB} and ET_{Ch} (bottom). Solid blue line: fitted line from linear regression.

This difference may be attributed to two factors: i) the spatial scale of measurements, while ET_{Ch} is a local and instantaneous measure over 1 m², ET_{SEB} is deduced from measurements of Qh that are based on the average of the turbulent parameter ${C_n}^2$ over 100 m of heterogeneous and inclined terrain in the BGW ; and ii) the individual measurement errors of energy balance components (Rn, Qg and Qh), likewise parameters and variables used to estimate them, studied in the sensitivity analysis section.

Since ET_{SEB} is mainly driven by net radiation fluxes (Rn_{SEB}), which was measured with the CNR4 radiometer, it would be interesting to compare with the Rn measurements from the NR-Lite Net radiometer (Rn_{Ch}), used to characterise the net radiation within the chamber.

As can be seen in Figure 2.24, the values of Rn are not as different as those of ET, except for 2019/08/08 when there were intermittent cloud passages. For cloudless days the slopes of the linear regressions are higher than 0.94 and the values of r² greater than 0.7. In fact, on sunny days as 2019/08/23 the agreement between both radiometers is the best (Table 2.5). Thus, the measurements with the NR-Lite Net radiometer Rn_{Ch} are lower than Rn_{SEB} measured with the CNR4 radiometer.

Table 2.5. Correlation coefficient and RMSE of ET from Ch and SEB; and Rn from NR-Lite and CNR4.

	ET_{Ch} and ET_{SEB}		Rn_{Ch} and Rn_{SEB}	
Date	**r²**	**RMSE**	**r²**	**RMSE**
2019/07/10	0.49	12.23	0.73	173.24
2019/08/08	0.17	7.57	0.27	178.84
2019/08/23	0.09	10.47	0.94	90.27
2019/08/29	0.27	5.13	0.75	112.51

According to the RMSE this divergence of Rn is greater than 115 W/m² in cloudless and sunny days. This discrepancy may be due to the height of both devices, which were installed at 1.5 m (CNR4 radiometer) and 0.30 cm (NR-Lite Net radiometer) from

the ground. Because of the proximity of the NR-Lite Net radiometer to the ground, the shading effects of sensors surrounding the radiometer would affect the measurement. It is confirmed that the availability of net energy at the LAS receiver position Rn_{SEB} is greater than with Rn_{Ch}.

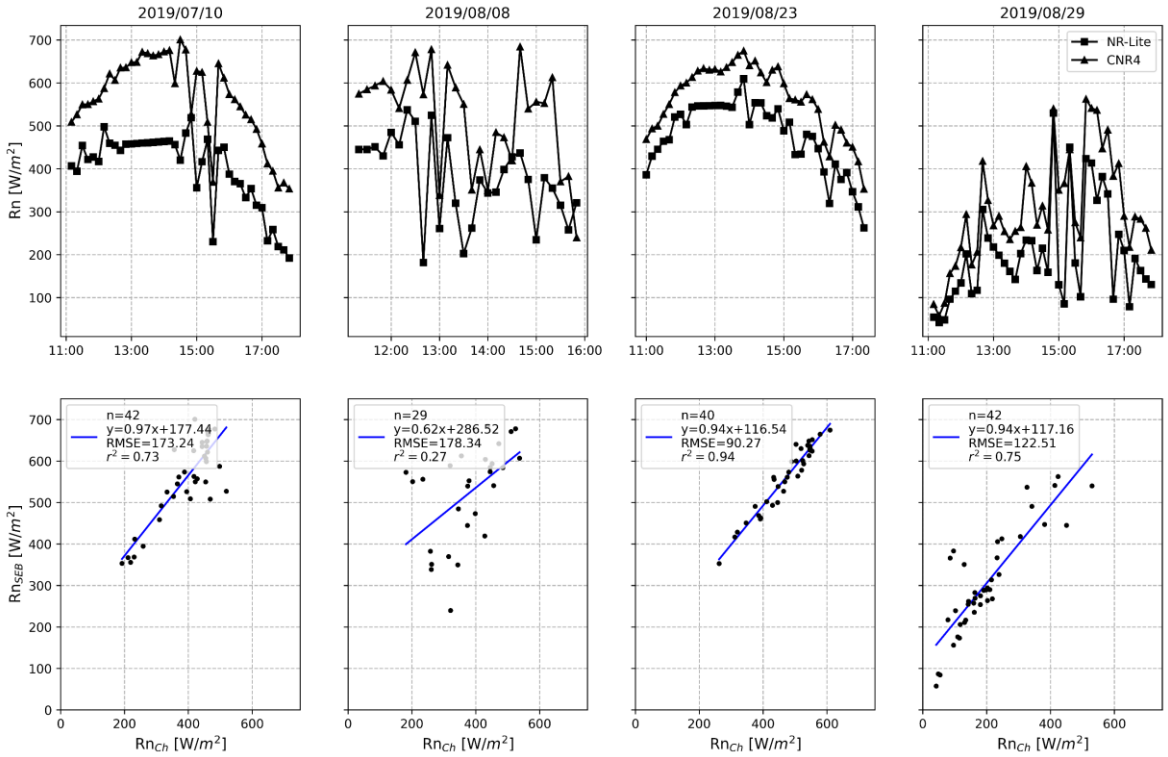

Figure 2.24. Comparison of Rn values measured with the CNR4 and the NR-Lite. Solid blue line: fitted line from linear regression.

- ET_{Ch} *vs.* ET_{WB}

To compare the measurements of the evapotranspiration chamber (ET_{Ch}) with the water balance method (ET_{WB}), the data collected in 2018 and 2019 were used. As shown in Figure B.4 and Figure B.5, on 2018/06/20, the VWC values from the 16 CWS665 sensors vary between 0.10 and 0.2 m³/m³, while on 2018/09/26 and 2018/09/27, the values range between 0.05 and 0.075 m³/m³. Regarding the water content measurements carried out in 2019 (see Figure B.6 to Figure B.9), some severe drought conditions of the BGW can be observed, with VWC values from a few sensors that rarely overpassing 0.05 m³/m³.

The large variability of VWC data series from CWS665 sensor exhibits some significant drops and rises of VWC during the period of measurement. This behaviour is observed at any moment of the measurement, and it may be attributed to signal interference. To correct this, the moving window was used, as explained in Section 2.5.3.

Results of the filter application over VWC data and the deduction of ET_{WB} are presented in Figure 2.25. Even with the filter use, some of these sudden variations remain. In the case of 2018/06/20 and 2018/09/27, these behaviours appear at the beginning and the end of the campaigns, respectively. Meantime, in 2019 (2019/08/23 and 2019/08/29) it can be observed some sudden reductions during the measurement campaign. However, it can be noted a very slight gradual reduction of VWC occurs despite fluctuations, mainly when level of soil moisture is greater (e.g., on 2018/06/20).

Concerning the comparison between both methods, the linear agreement between ET_{Ch} and ET_{WB} is not satisfying for almost all campaigns. Nevertheless, the data collected on 2018/06/20 are well phased, compared to the other campaigns. According to the RMSE, the values of ET_{Ch} were 2.85 mm/d higher than those computed from the water balance (see Table 2.6). This be associated with a greater soil moisture content (0.12 m^3/m^3) compared to the other dates (lower than 0.06 m^3/m^3).

The remaining days with low VWC showed different correlation coefficient values. On 2018/09/26, the divergence between both methods was 0.68 mm/d. A similar pattern was noticed on 2019/06/20. However, the number of observations was very low on both dates. On the contrary, a longer number of observations on 2018/09/27, 2019/07/10 and 2019/08/29 led to find the linear regression between ET_{Ch} and ET_{WB} does not fit well, with r^2 values close to 0.

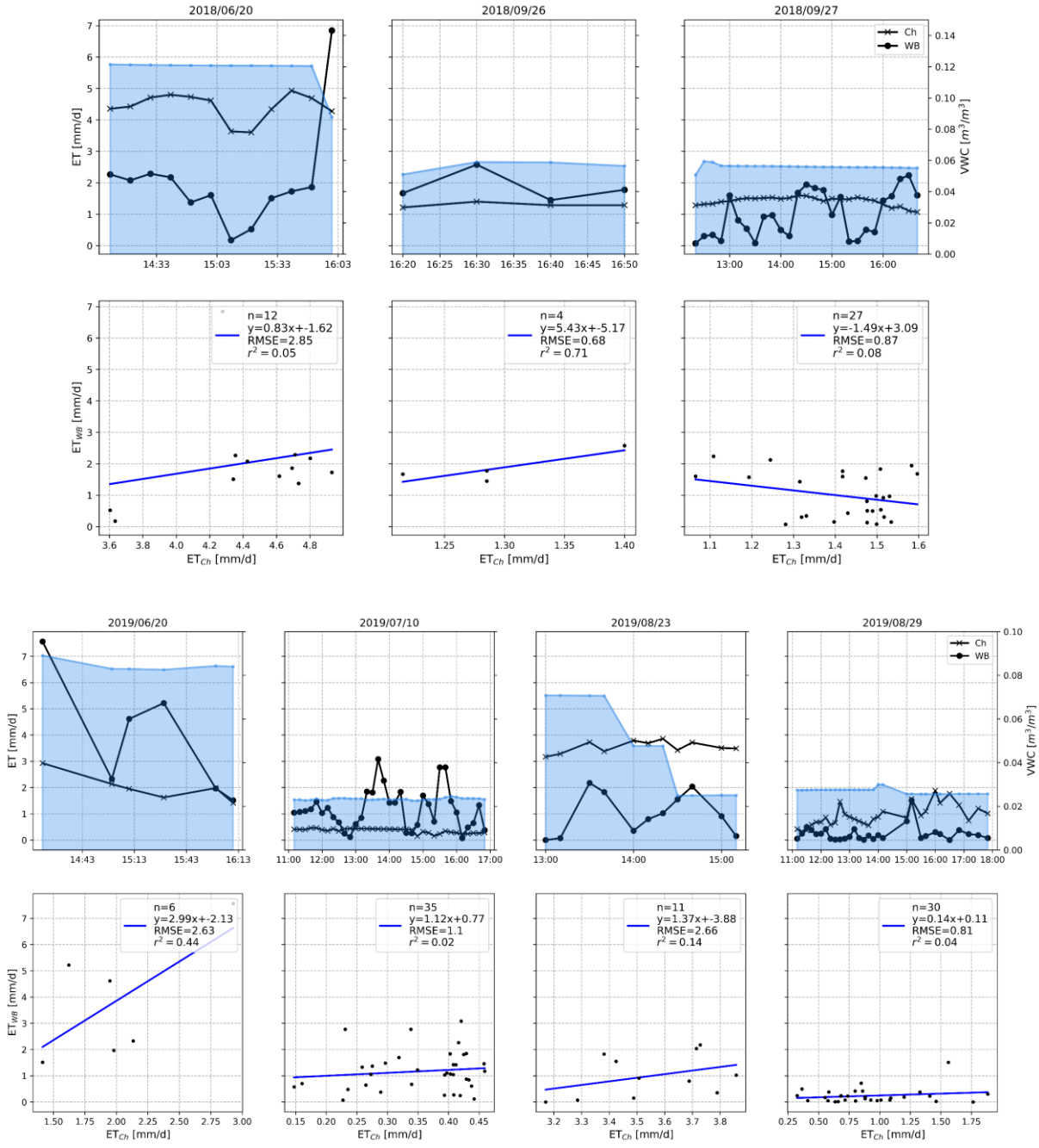

Figure 2.25. ET deduced from the WB and ET measured with the Ch (top). Blue area represents the VWC level measured with the CWS665 sensors. Comparison of ET_{WB} and ET_{Ch} (bottom). Solid blue line: fitted line from linear regression.

These results illustrated that when the soil matrix has higher moisture that support ET, higher flux of ET_{Ch} was detected compared to the days with low VWC. As well, for these days the difference between ET_{Ch} and ET_{WB} is smaller.

Table 2.6. Correlation coefficient and RMSE of ET from Ch and SEB.

Date	r^2	RMSE
2018/06/20	0.04	2.85
2018/09/26	0.71	0.68
2018/09/27	0.08	0.87
2019/06/20	0.44	2.63
2019/07/10	0.02	1.1
2019/08/23	0.14	2.66
2019/08/29	0.04	0.81

- ET_{SEB} *vs.* ET_{WB}

As explained earlier, the Ch could not be used during the campaigns of 2020, but on the contrary the CWS665 sensors were permanently placed on the BGW. Thus, only ET from SEB (ET_{SEB}) and WB (ET_{WB}) can be compared in 2020. Just like for the 2019 campaigns, drought conditions were observed during the summer and water content in the substrate barely reached 0.025 m^3/m^3 at the beginning of July. In the Figure 2.26 the two series of ET_{SEB} and ET_{WB} are compared and the linear agreement between both is represented.

The first remark about this comparison is the stability of VWC compared to 2018 and 2019 data. Besides, there is a general progressive reduction of soil moisture during the measurements, starting from 0.025 m^3/m^3 and finishing around 0.01 m^3/m^3. However, during the last day of measurement (2020/07/23), it seems VWC increased even though there were no water inputs. As assumed previously, this behaviour might be attributed to dry soil conditions and high soil temperatures, which generates a k_a value closer than that of air from soil pores.

The days when ET_{SEB} reduce during the afternoon (2020/07/09, 2020/07/22 and 2020/07/23) exhibit an increase of ET_{WB}, which led to obtain a negative linear correlation between ET_{WB} and ET_{SEB}. Nevertheless, the values of ET_{SEB} were

significantly higher than ET_{WB}, and the RMSE was above 9 mm/d for all days of measure, except for 2020/07/16. Moreover, no linear correlation was found between both series, as it was confirmed by correlation coefficients close to 0, see Table 2.7.

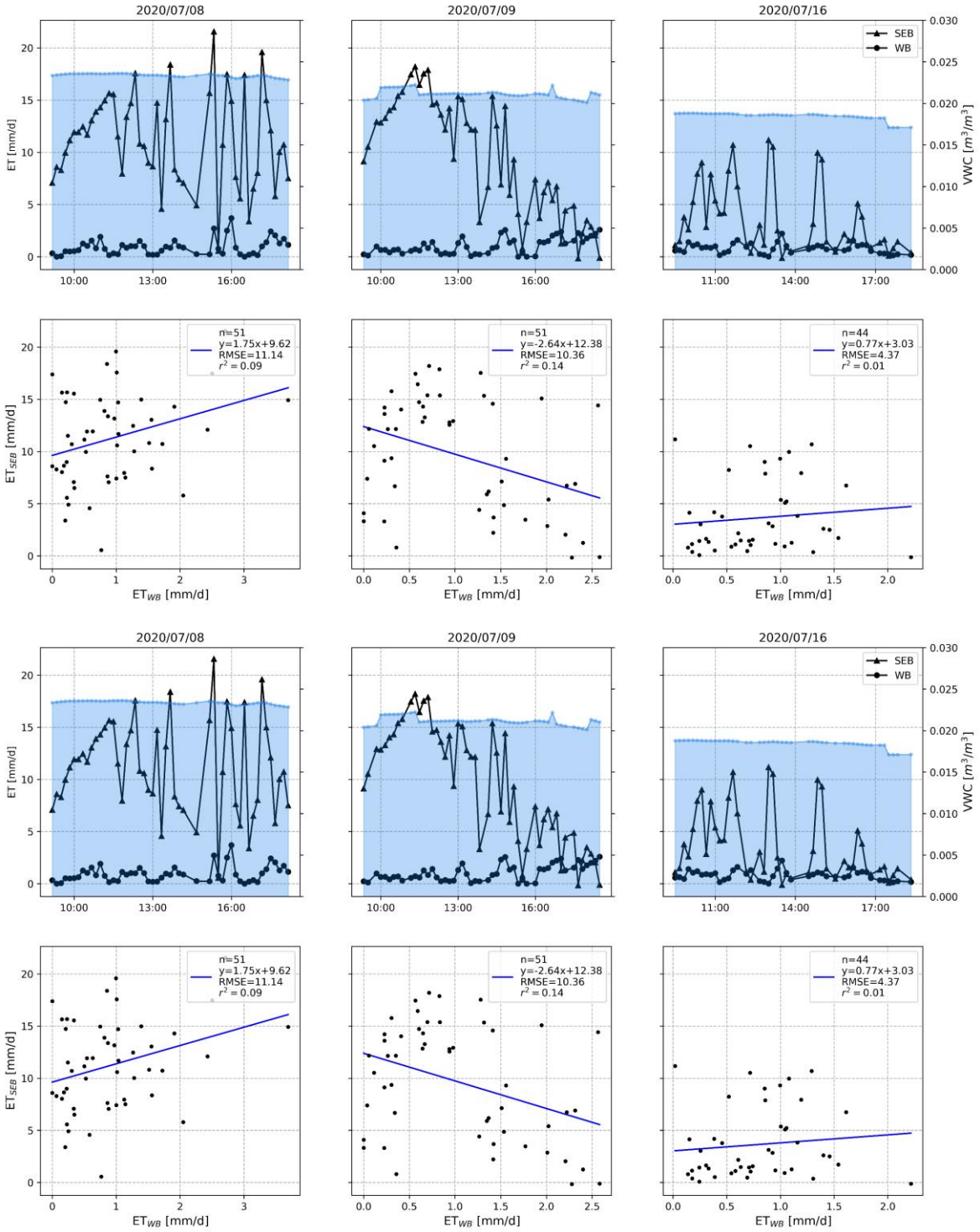

Figure 2.26. ET deduced from the WB and ET derived from the SEB in 2020 (top). Blue area represents the VWC level measured with the CWS665 sensors. Comparison ET_{WB} and ET_{SEB} (bottom). Solid blue line: fitted line from linear regression.

Table 2.7. Correlation coefficient and RMSE of ET from WB and SEB.

Date	r^2	RMSE
2020/07/08	0.09	11.14
2020/07/09	0.14	10.36
2020/07/16	0.01	4.37
2020/07/17	0.13	9.09
2020/07/22	0.24	11.84
2020/07/23	0.14	10.67

- ET_{WB} *vs.* ET_{SEB} *vs.* ET_{Ch}

The three ET measurement methods could be analysed simultaneously on 2019/07/10, 2019/08/23 and 2019/08/29 campaigns. Hence, a comparison of values between these was undertaken. As already mentioned for ET_{WB} and ET_{SEB} series in 2020, an overestimation of ET_{SEB} with respect to ET_{WB} and ET_{Ch} can be observed (Figure 2.27).

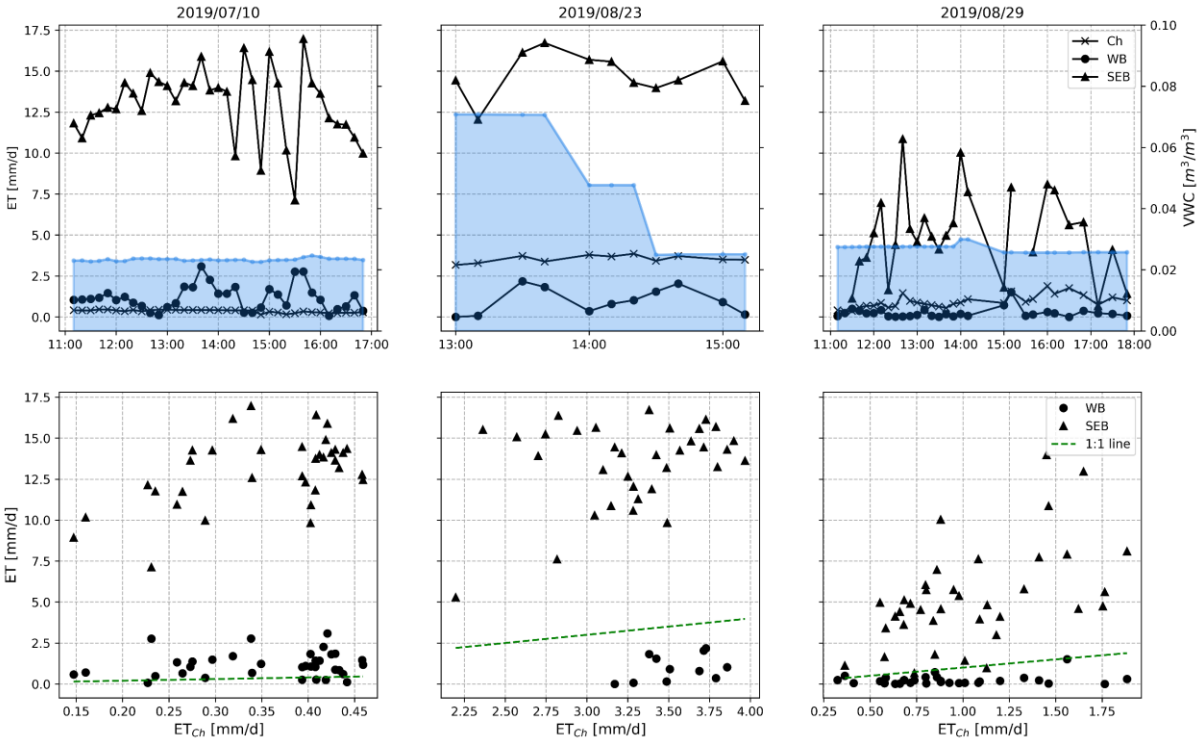

Figure 2.27. ET deduced from the WB, ET derived from the SEB, and ET measured with the Ch (top), in three dates of 2019. Blue area represents the VWC level measured with the CWS665 sensors. Comparison of ET_{Ch}, ET_{SEB} *and* ET_{WB} *(bottom).*

For clear sky conditions on 2019/07/10 and 2019/08/23, the RMSE indicated the difference between ET_{Ch} and ET_{SEB} reach up to 12.8 mm/d and 10.47 mm/d (Table 2.8). In the case of ET_{Ch} and ET_{WB}, the difference between values is greater for these dates too, with RMSE equal to 1.10 and 2.66 mm/d. By contrast, on the cloudy day of 2019/08/29 the values ET_{Ch} were 0.81 and 5.13 mm/d different, respecting to ET_{WB} and ET_{SEB} respectively. When exploring the linear agreement between the methods, the coefficients of correlation demonstrate there is no relationship between them, which would be associated to the overestimation of ET_{SEB} (more details in Section 2.6).

Table 2.8. Correlation coefficient and RMSE of ET from Ch, WB and SEB.

Date	ET_{Ch} and ET_{WB}		ET_{Ch} and ET_{SEB}	
	r^2	**RMSE**	**r^2**	**RMSE**
2019/07/10	0.02	1.10	0.25	12.81
2019/08/23	0.14	2.66	0.09	10.47
2019/08/29	0.04	0.81	0.27	5.13

Finally, the method of ET measurement using the WB in dry conditions did not provide reliable measurements of ET_{WB}, because of the high variability of CWS665 sensor signals. This variability might be associated with several causes: i) interferences between CWS665 sensors and the CWB100 wireless base (where the data is stored, before transferring it to the data-logger); ii) the adaptation period of the CWS665 sensors to the substrate few minutes before starting of measurement campaign (such as 2018 and 2019 case), may not have been sufficient to ensure the effective data transfer; and iii) the reliability of the sensor reading when the substrate is extremely dry, since this could represent the conditions of dry air within the pores. In consequence, the VWC data of 2018 and 2019 were kept as an indicator of soil moisture, but not as a method of ET measurement.

2.6 Discussion

The ET process on green roofs is highly variable, and complex to measure, because several atmospheric, ground and vegetation interactions limit the transfer of water vapour to the surrounding urban environment. The application of three methods of ET measurement at different scales on the BGW showed different rates of ET depending on the method of measurement used as well as the conditions of measurement.

As the results demonstrated, the SEB method using the LAS MKI scintillometer over a horizontal path of 100 m, reported higher values of Qe compared with those computed by the Ch and WB methods. Based on the experimental configuration, this overestimation of Qe may be attributed to i) the individual errors of measurement impacting closure of the energy balance, and ii) the spatial scale of the LAS MKI measurement.

Since Qe is derived from SEB, inaccuracy of Rn, Qh and Qg measurements may be transferred into Qe. This could include errors and uncertainty of individual parameters and variables, such as k, z_o and d, adapted from the literature and LAS MKI manual. However, as it was demonstrated by Crawford et al. (2017), these latter parameters could impact the z_{LAS} estimation, and hence Qh computation up to ±6%. In addition, it is important to take into consideration uncertainty of meteorological variables from the station further 50 km from the BGW. In accordance with the sensitivity analysis, U is the parameter with the highest linear correlation to Qh (Pearson's Correlation Coefficient=0.35). This parameter was highlighted by Ward et al. (2015), as a key factor for the well-development of turbulence over the path length.

Linked to U and WD, the question of the source area of turbulent measurements or footprint could be underlined. This determines the influence of the heterogeneity of the BGW's surface on the fluxes measured by the LAS. However, this was not assessed because of missing meteorological in-situ measurements. Some prior studies (Crawford et al., 2017; Irvine et al., 2011) have demonstrated the complexity of using

LAS scintillometer in urban areas. A campaign of measurements, conducted in the city of Nantes (France) with a LAS over a path length of 3 km, indicated "rather large variability" of the turbulent flux of $C_n{}^2$ because footprint of LAS measurements (Irvine et al., 2011). Indeed, it noted the footprint of urban areas is affected by building and vegetation distribution, which impact wind direction and flux variability. This remark was shared by (Crawford et al., 2017), from LAS measurements over a path length larger than 1 km. The distribution of scintillometer measurements is influenced by the irregularity of the footprint, which is variable in urban environments because landcover diversity and heat sources.

Besides topographic and meteorological uncertainties, it is the first time that a LAS' set-up with a horizontal path length distance as short as 100 m is explored in urban areas. The shorter distance reported in the literature is 400 m, used for the calibration of two LAS (from Kipp&Zonen) generations (Dooley & Creech-Eakman, 2018). Therefore, the saturation criterion of $C_n{}^2$ calculated in Section 2.4.2.2 from the path length distance, was used to validate LAS measurements. Thus, the values of $C_n{}^2$ in the BGW (around 10^{-13}) indicated reliability, as they obey $C_n{}^2 < 1.7 \times 10^{-10}$ $m^{-2/3}$.

Most studies that performed Qe measurements from scintillometer and SEB, compare the fluxes with the micrometeorological method of Eddy Covariance (ECO). Comparisons between local measurements of ECO and two-wavelength scintillometer (over a path length of 5.5 km), from a suburban environment of UK, demonstrated Qe from scintillometers tend to be larger than from ECO while Qh is similar during the day (Ward et al., 2015). This outcome was shared by Cohard et al. (2018), who compared Qe from a Surface Layer Scintillometer (SLS) of small aperture (path length of 70 m) and ECO in an experiment site close to Nantes (France), on an asphalt concrete pavement under rain events. Another comparison showed Qh values measured a LAS were higher than those computed from ECO in the urban centre of London, with path lengths greater to 1 km (Crawford et al., 2017). Finally, measurements with a SLS in South Africa over 100 m of grass, demonstrated a good agreement between Qe deduced from both methods (Savage, 2009). Measurement differences in most cases

are mainly attributed to the heterogeneity of the surface and footprint, as could be assumed in the BGW case because of relief and the nearest urban environment.

From authors knowledge, it is the first time that the Qe_{SEB} are compared to measurements from a plant physiology method as the evapotranspiration chamber Qe_{Ch}. Since the uncertainties of individual measurements of SEB, footprint of LAS measurements, scale difference (in space and time) between LAS measure and local Qe_{Ch} measurements, the overestimation of Qe_{SEB} could be explained.

Concerning the ET measurements with the Ch, few applications on green roofs have been reported in the scientific literature. One of them was conducted in Melbourne (Coutts et al., 2013), and the measurements were compared to those obtained on a cool roof. Results reported low values of Qe from the green roof under warm and sunny conditions and limited soil moisture. The strong influence of soil moisture on Qe was corroborated in the BGW, as lowest values of Qe were detected by the Ch when levels of VWC in the substrate were lower. Application of ET chamber in agricultural experiences showed similar results even if the type of vegetation was different (Garcia et al., 2003; McLeod et al., 2004).

Earlier researches with the Ch found the air mixing conditions has an impact on Qe values. Marasco et al. (2015) demonstrated systematic errors of Qe from *Sedum* vegetation, on two different green roofs in New York, because of changes in air turbulence, water vapour saturation in the air, and the adhering effect of water vapour molecules to the surfaces between the system's chamber and humidity sensor. In the case of McLeod et al. (2004), the measurements from a portable chamber were compared with the BR method. It proved that the agreement between both methods varied depending on the fan speed. At greater fan speed, the humid air near the chamber's soil surface can be introduced into the atmosphere of the Ch, which produces overestimations of Qe. However, the analysis of this effect in BGW measurements is beyond the scope of this research because fans speed cannot be modified under field conditions.

Regarding the method based on the WB in dry periods, its application was conditioned to the stability and transfer of CWS665 sensor signals. Only prolonged periods of measurement allowed to analyse the real daily pattern of VWC during dry periods. The short frequency of measure led to find a large variability of VWC, which is phased with T_{soil}. This would explain the trend followed by ET.

The low values of VWC in most of the campaigns are a consequence of extremely dry conditions of the BGW substrate during summer. Hence, low values of k_a from CWS665 sensors corresponds to that of the air ($k_a = 1.0006$ at 25 °C). In consequence, in days with records of k_a close to 1 the application of water balance from CWS665 sensors is not recommended.

The differences of the VWC values were quite significant between locations of the sensors in 2020. Those located at the bottom of the BGW were expected to report higher VWC, as was stated by Versini et al. (2020). This assumption was partially respected since the higher content of water appeared not only at the slope's bottom, but at the highest BGW's elevation too. Both locations are characterised by the lowest inclinations in the roof. According to the study carried out by Domínguez-Niño et al. (2020), the large variability of soil moisture measurements from capacitance and Frequency Domain Reflectometry sensors, is explained by the heterogeneity and porosity of the soil around the sensor, which can change from a sensor location to another.

During BGW drought conditions in 2020, the daily average of ET rates computed by means of the WB were 0.5-0.7 mm/d, and maximum values were higher than 3 mm/d. These results contrast with the ET estimations of (Voyde et al., 2010), by means of water balance in green roof plots under drought-stressed conditions. The maximum average rates of ET from *Disphyma austra* and *Sedum mexicanum*, reached values of 1.2 and 0.48 mm/d, respectively. In contrast, according to Cirkel et al. (2018), the mean value of ET reached 3 mm/d on a well-irrigated green roof with *Sedum* vegetation. This demonstrates the reduction in ET rates under limiting conditions of soil moisture

during the summer, which is contrary to the BGW results from VWC changes measured with CWS665 sensors.

2.7 Conclusions and Perspectives

Understanding the exchanges of thermal fluxes, such as the evapotranspiration (ET), between the green roofs and the nearest atmosphere, is crucial to promote the installation of those structures as a cooling solution and UHI mitigation. As shown in the state of the art of ET in green roofs, several methods of quantification of the ET at different temporal and spatial scales have been used, under different climatic and plant-based conditions. Nevertheless, the complexity of the process has led to finding different values of ET, depending on the scale of measure, the external conditions (such as local climate) and internal factors (such as soil moisture). As a consequence, this Chapter aimed to characterise the process of ET in the experimental green roof site, the Blue Green Wave (BGW). Hence, three different methods of measurement of the ET were used: a Surface Energy Balance (SEB), an Evapotranspiration Chamber and a Water balance (WB) in dry conditions.

By examining the results of each method of measure, it can be concluded that they are highly dependent on the accuracy of measurement of parameters involved in their estimation and their spatial and temporal scale of measurement. In the case of SEB, through the sensitivity analysis, it was demonstrated both the underestimation and the overestimation of the SEB components will impact the value of Qe because of balance closure. As well, the uncertainties of variables and parameters impact the estimation of SEB components, like k and Qg, or U and Qh. Regarding the WB, the variability of ET is strictly relying to VWC fluctuations. Then, accuracy of the signal is critical to ensure ET daily pattern in sunny conditions. Conversely, Qe from the Ch deduced from the humidity variation were impacted by the soil moisture, as during dates with similar net radiation but lower soil moisture levels, the values of Qe were lower.

Concerning the spatial and temporal scale, they differ between the three methods, which might explain some divergences of ET measurements. For SEB, the estimation of Qh is representative of the ${C_n}^2$ path-average over 100 metres on the BGW, every 10 minutes. Meantime, the chamber of evapotranspiration characterises a local variation of absolute humidity in an area of 1 m² for 30 seconds. Finally, the WB variation represents a point variation of water content in the green roof every 1.5 minutes, which is influenced by the spatial heterogeneity of the soil (i.e., porosity, grain size, hydric and thermal properties, etc).

In response to these difficulties, it is recommended to perform experiments on the BGW with a scintillometer for short distances, such as the Surface Layer Scintillometer (SLS), jointly with meteorological measurements, such as temperature, wind speed and direction. In this way, the source area or footprint of turbulent fluxes detected in the scintillometer and the influence of the wavy shape of the BGW might therefore be evaluated.

Although Qe values from SEB are overestimated, the saturation limit proved LAS MKI measurements of ${C_n}^2$ are valid and they may be an indicator of the turbulence due to convective activity on the BGW. Therefore, the use of statistical-based approaches, such as the Universal Multifractal framework, seems convenient for the analysis of spatial and temporal variability of fluxes measured in the BGW at different scales.

Chapter 3 Multiscale spatial scenario of deployment of NBS

A special interest in the implementation of NBS may be foreseen to mitigate the UHI's intensity and more generally to improve urban system's resilience. Nevertheless, the complexity of social and economic dynamics occurring at different urban scales makes it difficult to find a spatial organisation that harmonises the urbanisation and installation of NBS. The competition of NBS with other usages of urban space, as well as the question of implementing new NBS or densifying the existing ones on a territory requires to conciliate different constraints. For example, the densification of NBS can be either small, disconnected patches, such as individual gardens or green roofs, or green strips, or large parks; a multitude of scales should be considered.

Through this chapter, the development of a spatial modelling that optimise the location of NBS across several urban scales is investigated. For this purpose, multiscale approaches are introduced, more specifically the fractal geometry and its properties for the analysis of complex forms observed at different scales. Then, the utility of those concepts in the analysis of urban morphologies and the development of spatial modelling is explored by means of a case study. Hence, the fractal geometry is used operationally as a multiscale logic of generation of urban structures, in the spatial software Fractalopolis.

3.1 Spatial optimisation principle to install NBS

Several approaches have explored the most appropriate way to deploy NBS, and specifically several kinds of NBS on an existing territory. Some of them, based on urban planning, use quantitative indicators of population distribution and its proximity to NBS, such as "public green area per capita" or "distance/time to green areas" (Neuvonen et al., 2007; World Health Organization, 2016). Other approaches

tend to maximise a particular ESS from the NBS. For the reduction of temperature, the study results of Bao et al. (2016) and Zhang et al. (2017) demonstrated the installation of a single NBS on a large scale, such as the urban parks, offers a lower land surface temperature mitigation, compared to a disperse location of smaller NBS. By contrast, Masoudi & Tan (2019) stressed land surface temperature is lower with less fragmented and more aggregated large patches of NBS, because the proximity of NBS creates ventilator corridors of cool air. In this context, both approaches are not necessarily different, but can be envisioned as complementary rather than in competition.

The spatial organisation of urban structures, as well as the social and environmental contexts of the NBS's installation can vary from one site to another, which might affect the performance of NBS to tackle urban challenges. According to Cohen-Shacham et al. (2019), such context should be integrated in the analysis to determining the deployment of NBS. But this also includes the different spatial scales of analysis, from metropolis up to individual buildings. Nevertheless, the latest represents a major challenge for urban planners since most scientific evidence is framed at local scales where the NBS benefit is perceived. Correspondingly, scientific community and urban planners have been interested in investigating how NBS can be integrated into the built-up space to maximise their benefits at different urban scales, without disrupting the existing spatial organisation, the social and economic dynamics of the cities. This question may look like an optimisation problem that could be addressed through a scale invariance indicator.

The fractal geometry has demonstrated to be a helpful tool to characterise and simulate the complexity and hierarchy of cities. According to Tannier & Pumain (2005), fractal geometry is useful for describing non regular spatial patterns, characterised by alternate patterns of continuity and fragmentation, or some degrees of concentration, and include similar structures at different scales of analysis. Hence, resorting to fractal geometry appear as a convenient approach to develop multiscale urban planning scenarios of NBS deployment. Let's introduce just below the fractal geometry and its properties to better understand their use in analysis and modelling of urban patterns.

3.1.1 The fractal geometry

In 1982, the American-French-Polish mathematician Benoit Mandelbrot introduced the notion of Fractal, inspired by the Latin word "fractus" and the irregular and fragmented objects that do not fit with the classical Euclidean geometry. Formally Mandelbrot defined a fractal as "a set for which the Hausdorff-Besicovitch dimension is greater than its topological dimension" B. Mandelbrot (1982).

The fractal object is characterised by an invariance of scale when zoom-in and zoom-out, which makes this looks similar at different scales of observation. This property is known as self-similarity and it was pointed out as the core feature of fractals in the paper "How long is the coast of Britain?" of B. Mandelbrot (1967). Indeed, in this paper Mandelbrot examined through lines of different sizes the length of the coastline of Great Britain, arguing geographical curves can be considered as superpositions of features of widely scattered characteristic size. In this way, it was demonstrated that depending on the scale of the line used, the total length of the coast will vary. Because, as finer features are taken into account, the measure total length increases.

Despite the notion of fractal being introduced during the second half of the 20th century, numerous objects with self-similarity properties were early invented, such as the Cantor set which appeared in 1883, the Koch curve in 1904 or the Sierpinski carpet in 1916 (see Figure 3.1).

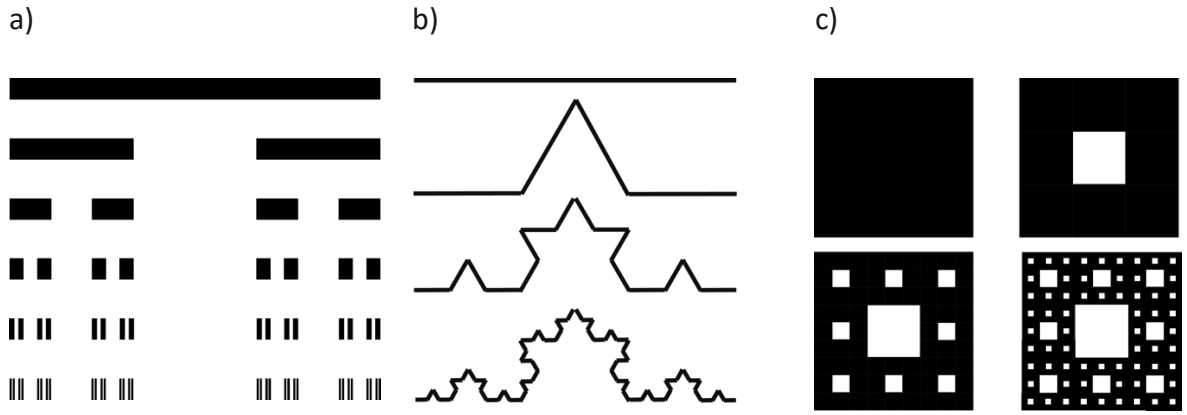

Figure 3.1. Fractal objects a) the Cantor set, b) the Koch curve and c) the Sierpinski carpet.

These geometrical objects are built iteratively. In the Cantor set case, at each iteration the open middle third of a set of line segments is deleted, leaving two segments. Then, the length of the Cantor set decreases, as the length of the segment is reduced with the number of iterations. The Koch curve is created from a straight line divided into three equal segments. At each iteration the middle third of each interval is replaced by the two sides of an equilateral triangle of the same length as the segment being removed. The shape of the figure is very irregular, and its length increases with the number of iterations, since four copies of the line segment reduced to 1/3 of the original length are created at each iteration. Regarding the Sierpinski carpet, initially a square is necessary, which is divided into nine equal squares (based on a 3x3 grid) and the central square is removed. For the remaining eight subsquares, the process division is repeated iteratively. As a part of the square is removed at each iteration, its area tends to zero as the number of iterations tends to infinity.

3.1.2 The fractal dimension

The topological dimension in the fractal framework refers to the classical geometry used to describe regular spaces. This geometry recognizes major categories of integer dimensions: 0D is a point, 1D is a straight line or curve, 2D is a planar figure and 3D is a volume.

If we have an object embedded in a Euclidean dimension, N smaller models (copies of itself) will be necessary to constitute the whole object, with a scale factor λ used to create the model. In this way the dimension of an object (D), can be defined as follows:

$$N = \lambda^D \tag{3.1}$$

The scale ratio (λ) is defined as the relationship between the outer scale (L) and the observation scale (l_o):

$$\lambda = \frac{L}{l_o} \tag{3.2}$$

For classical geometry objects (see Figure 3.2):

- A straight line (1D) needs N lines of l_o length, to describe the initial line.
- A planar figure (2D) like as a square, requires N copies of l_o length size to reproduce the original object.
- A solid (3D) demands N copies of l_o length size to cover the original volume.

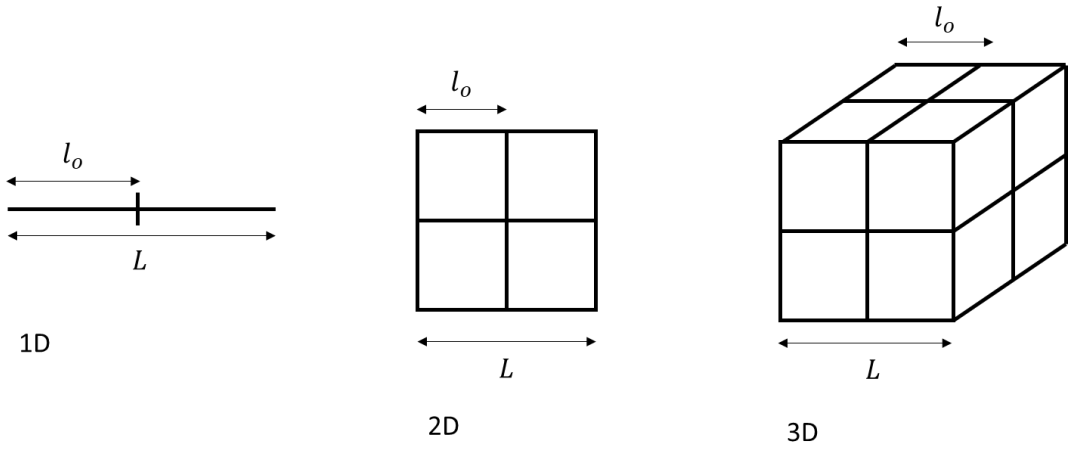

Figure 3.2. Fractal dimension of classical Euclidean objects.

Since the irregularity of fractal objects makes not possible to describe them with the topological dimension, the concept of fractal dimension (D_f) emerged. Then, D_f characterises the surface roughness of an object, which could be not-integer.

Let us consider an exactly self-similar fractal object as the Sierpinski triangle, which is based on an equilateral triangle of size $L = 1$ (see Figure 3.3). The mid points of each side of the triangle are used as vertices of an equilateral smaller triangle ($l_o = 1/2$), which is removed from the original and resulting three exact smaller copies of the original ($N = 3$). This iterative process yields to find $D = \frac{log(3)}{log(2)} \approx 1.58$ at all the scales of analysis. Then, D_f characterises the scaling property of the object over different scales.

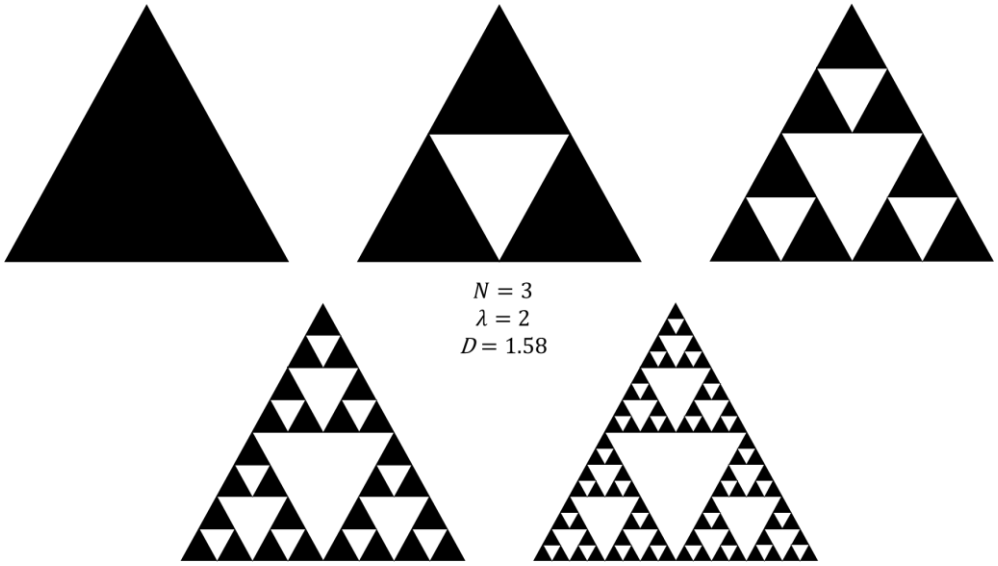

Figure 3.3. Sierpinski triangle at different iterations with a scale ratio $\lambda = 2$.

The D_f of not exact or statistically self-similar structures, such as a natural coastline, is rather complex to handle analytically as it was demonstrated by Mandelbrot. The Minkowski-Bouligand dimension or box-counting dimension was developed as a practical estimation of Hausdorff dimension (Mandelbrot, 1982; Schertzer & Lovejoy, 1991), see more details in the Appendix C. The principle of this technique is to completely cover a fractal set with boxes (instead of balls) of a fixed size ε, creating a regular grid and counting the number of elements necessary to cover the set $N(\varepsilon)$. The size of the boxes is changed, and the fractal dimension (D_f) is given by the relationship:

$$D_f = \lim_{\varepsilon \to 0} \frac{\log N(\varepsilon)}{\log\left(\frac{1}{\varepsilon}\right)} \tag{3.3}$$

Through the linear regression between ε and $N(\varepsilon)$ at the logarithmic scale, the parameter D_f can be estimated. If D_f is close or equal to 2, the set is homogeneously distributed over the plan. In the case where the set is better represented by a line (or curve), the values of D_f will be close to 1. Finally, D_f will be close to 0 if the fractal set is punctually located or isolated.

In practice, there are different approaches to implement the box counting method. One of them is based on the grid-counting method, which is implemented in Fractalyse version 3 (http://www.fractalyse.org/), an open-source software, developed in the

Franche-Comté University (Théma research laboratory), which analyses the fractal dimension of 2D images. Fractalyse follows a simple iteration principle that modifies artificially the level of the image analysis.

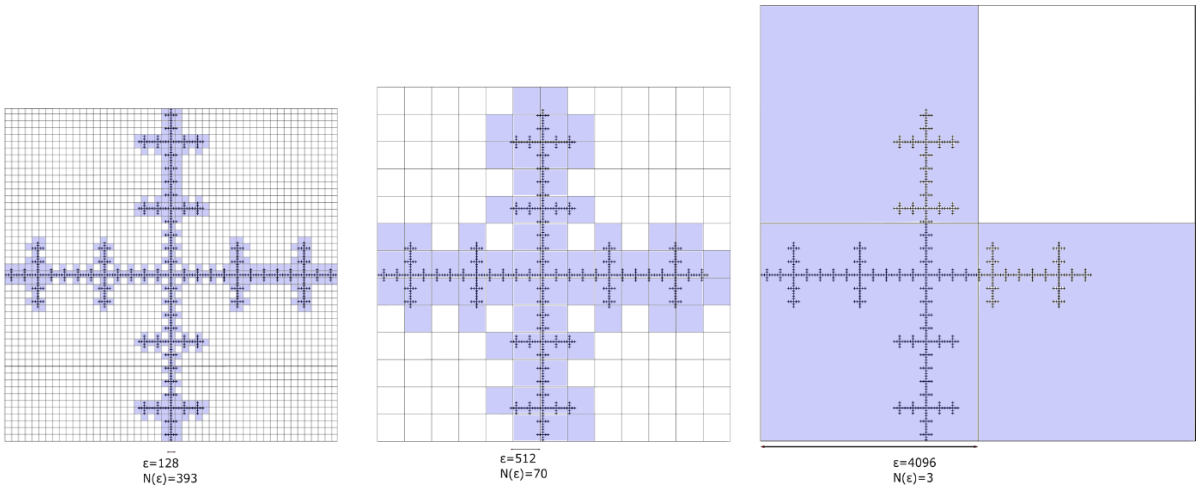

Figure 3.4. Box-counting technique by the grid approach.

At each iteration, a quadratic grid with boxes of size ε covers the image and the number of boxes that include part of the image is counted $N(\varepsilon)$, as shown in Figure 3.4. The process is repeated by increasing the size of the boxes, by an increment or coefficient (i) until a maximum size (power of i) set by the user. Usually, the minimum or the smallest grid size is 1, having:

$$\varepsilon = min \times i^p \rightarrow \varepsilon = 1 \times i^p \tag{3.4}$$

where, p corresponds to the iteration step.

The empirical series of points ε and $N(\varepsilon)$, are used to fit a theoretical curve that corresponds to the fractal law, and that defines the dimension as:

$$N(\varepsilon) = \varepsilon^{-D_f} \tag{3.5}$$

By means of a logarithmic approximation of this relationship, the D_f can be deduced as the slope value of the regression line. One issue of this approach is the way the grid is set over the object and the size of the box (Bouda et al., 2016; Frankhauser, 1997), which could lead to "ambiguities" or errors in the counting of boxes, affecting the real

value of D_f. To deal with this issue, in Fractalyse the coefficient (i) can be tuned, adjusting the grid to cover the whole image with the lowest number of $N(\varepsilon)$.

A complement of the D_f is the lacunarity. In fact, the gaps or boxes not counted through the iteration process, also reveals information about the fractal set. The notion of lacunarity was introduced by Mandelbrot, from the Latin word Lacuna, which means lack or hole. Mandelbrot stated "Lacunarity concerns the tendency to have holes". In that sense, the lacunarity of a fractal set characterises the distribution of its gaps. Thus, two fractal sets with the same D_f could fill the space in different ways and look different.

3.1.3 Fractality of urban structures

The fractal geometry has been accepted as a suitable approach for describing complex forms, such as the urban spatial patterns (Jevric & Romanovich, 2016; Tannier & Pumain, 2005); as fractal objects and urban systems have similar properties, such as irregularities and fragmentation (Tannier & Pumain, 2005). Several works have recognised a hierarchical distribution of urban objects, such as the built-up structure, that fits the self-similarity feature of fractals, which generates regular spatial hierarchies at different scales (Frankhauser, 1998; Li et al., 2015; Tannier, 2009; Tannier & Pumain, 2005).

Indeed, some territorial economic approaches have found hierarchical spatial and self-similar distributions. This is the case of the centrality principle proposed by Christaller in 1933 (Chen, 2011), for which there is a nested organisation of centres of different size (Figure 3.5) uniformly distributed in space (Euclidean dimension of 2). Christaller's model is based on the use of certain types of services and commercial offers, according to the order of the central place (Tannier, 2009). Hence, big cities with a large catchment area offer a wide range of services, and the village hosts the few services that only ensure supply in daily needs (Frankhauser, 2012).

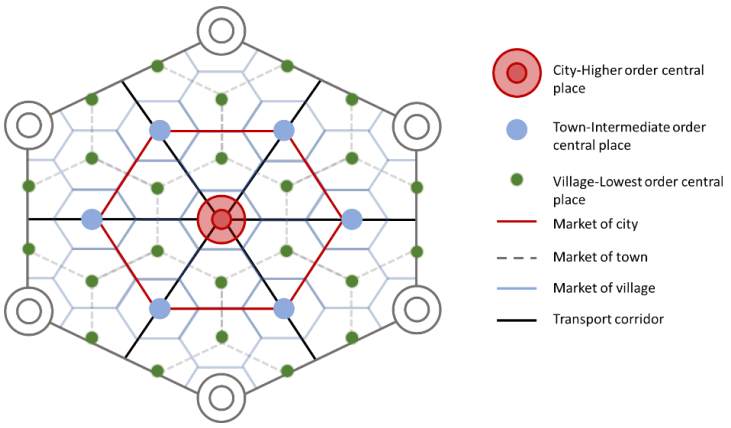

Figure 3.5. Central place model of Christaller.

Another spatial approach with hierarchical distribution is Zipf's law, which determines that the distribution of a system of cities follows a power law. This means, the hierarchical organisation of the cities is given by the rank-size distribution of the population, as a Pareto function. Thus, Zipf's law is an analogy with the fractal distribution.

Therefore, the fractal properties can be used to characterise the scale invariance of the urban organisation. Frankhauser (1997) highlighted the "fractal parameters characterise the degree of concentration and of non-homogeneity" of urban elements across scales. The most frequent use of fractal properties in urban geography has involved the measure of the D_f of some urban patterns, such as the built-up areas (Chen, 2011; Frankhauser, 1997, 1998; Li et al., 2015), the urban sewer networks (Gires et al., 2017), the green roofs (Versini, Gires, et al., 2020), or the green spaces distribution (Juidías, 2017; Liang et al., 2013). Thus, the D_f provides information about the urban morphology and mass distribution over the plane (Tannier & Pumain, 2005).

Apart the characterisation of the scaling laws of the urban organisation, the fractal geometry, and specifically the properties of the fractal primitives make them interesting for the spatial modelling:

- The scale-invariance, which allows creating a multiscale planning scheme where the same distribution principle is repeated, for instance the diversity of densities or the proximity of built areas to green areas.

- The lengthening of the boundary of fractal primitives with scale. This means that as spatial resolution increases, the scenario increases the interface between different kinds of urban objects, such as the built-up areas and the NBS.

Then, there are always two ways of looking at a fractal 2D object: either focus on the object itself, or on the empty space that is left, this means the lacunas of the fractal. In an urban setting, we can consider that the main urban form is composed of the buildings, and that other urban objects, such as roads as well as green and blue areas are located inside the lacunas of the fractal built form.

A practical example in spatial modelling of fractal primitives is the Fournier's dust as presented by Frankhauser in Borsdorf & Zembri (2021). As shown in Figure 3.6.a, this fractal recreates a hierarchical organisation where the elements (i.e., buildings) are not connected and form aggregates (i.e., urban blocks). The way the elements are placed resembles a large empty space at the core of the set of blocks (i.e., neighbourhood or districts), which would be representative of a large public urban park.

Another particular case of a constructed fractal that can be useful to represent a spatial pattern organisation with highly irregular shape, is the teragon (i.e., created from a self-similar curve). Over iterations, teragon surface remains constant and homogeneous, while the boundary becomes more complex and fractal, as represented in Figure 3.6.b. The representation of NBS with a teragon would match the irregularity of the built-up structure and create connectivity between NBS.

Apart from the construction of spatial models that resemble the spatial organisation and urban patterns, the fractal geometry and specifically the fractal dimension, provide a measure of the heterogeneity of the way urban structures fill space across scales. This measure is convenient when modelling spatial organisation, to define the characteristics of a fractal primitive representing an actual urban settlement within one territory across a range of scales.

a)

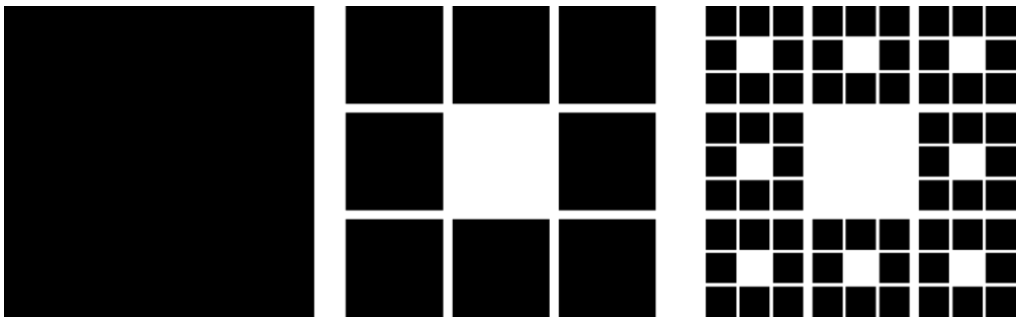

b)

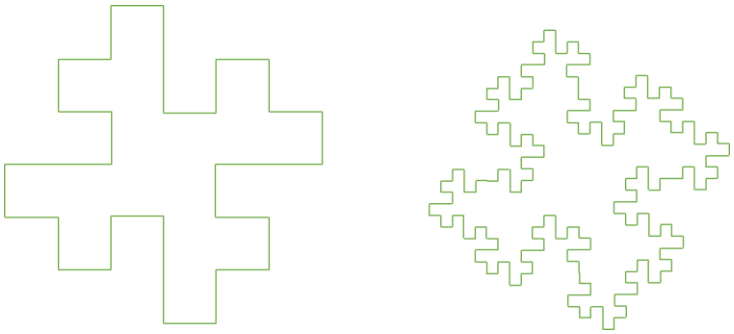

Figure 3.6. Fractal primitives after two iterations: a) Fournier's Dust, and b) Teragon.

In this context, we will explore a spatial multiscale simulation of NBS's location across different scales, while preserving current scaling properties of urban buildings and green spaces in the territory of Est-Ensemble. The spatial simulation software Fractalopolis, based on the scaling properties of fractal geometry, that develops self-similar scenarios of urban planning is used for these purposes.

3.1.4 Fractalopolis: the urban fractal planning modelling

Inspired by the usefulness of fractal geometry for analysing urban morphology, the GIS-based open-source software Fractalopolis was created (https://sourcesup.renater.fr/www/fractalopolis/) as a land planning simulation model, that aims at reinforcing a hierarchy of urban centres, with a mixture of densities at all scales, good accessibility to amenities and the preservation of green and blue infrastructures.

An iterative downscaling logic, specifically an Iterative Function System (IFS)[5] is used in Fractalopolis to create geometric fractal urban forms (e.g., urban centres) across several scales. This implies the creation of a hierarchical urban system, linked, and articulated to subsystems with social and economic interactions. One of the main advantages of this spatial modelling is the conservation principle of the urban structure that currently exists, without disrupting urban morphology and lifestyle of the inhabitants.

In Fractalopolis, the fractal form defines the "development areas" that acts as centres for urban development. The "lacunas", which is the complementarity of the urban fractal forms, are areas where nominal urban development will continue and where other kinds of urban objects, such as NBS, can take place. Hence, two zones are created in the model: urban fractal centres for potential future development and lacunas for limited or no development. In real case studies, these "lacunas" may contain several urban structures, such as green spaces, railway networks or transport axes.

In this way, properties of self-similarity and lacunarity are used as main planning principles in Fractalopolis (see the Figure 3.7). Generally, the transit-oriented logic that promotes the construction of an urban settlement system linked to the transportation network is used as a principle of development too. Therefore, urban centres are preferably located near access points of the transport network, promoting the use of the public transport system, the reduction of traffic flows, and the pollution. The main objective of these principles is the creation of a resilient urban development that limits urban sprawl, conserves natural green corridors, and incorporates green facilities in built-up areas.

The iterative downscaling logic is framed in two main spatial scales in Fractalopolis: one from regional up to city scale and other from the city up to the neighbourhood scale. In given way, these scales resemble the multi-scale framework of MAES report

[5] The IFS is a common method to creating self-similar forms as fractals, through the iteration of one or more affine transformations.

(in Section 1.4.3), which defines the spatial scale where the impact of implementation of NBS is assessed (i.e., regional, metropolitan, and urban). Thus, Fractalopolis's scales will be summarised as regional and urban scales.

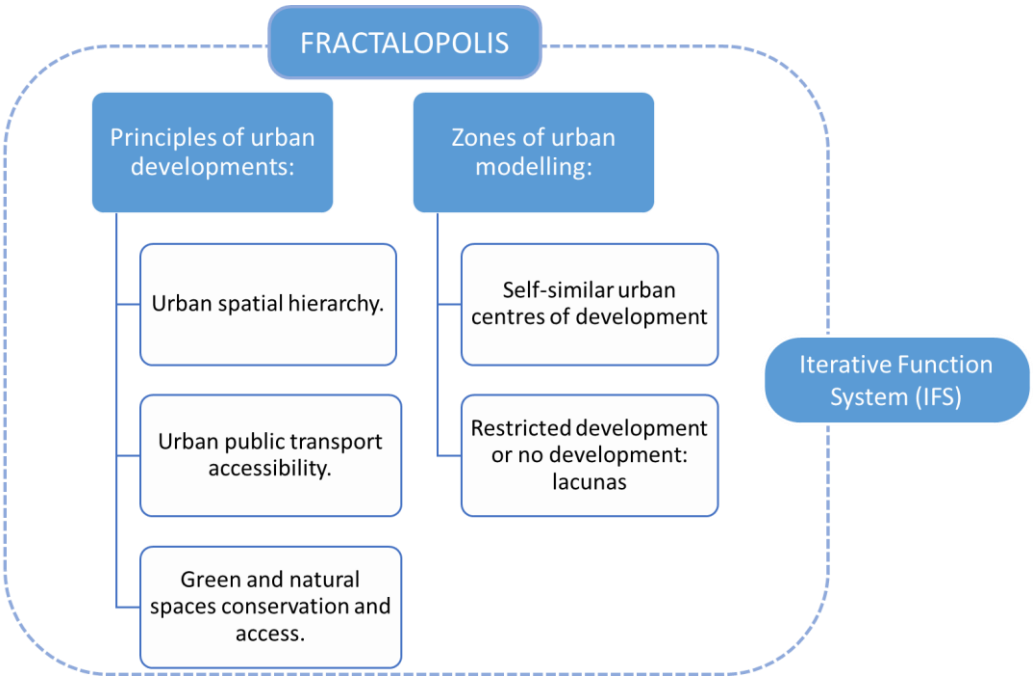

Figure 3.7. Working principles of Fractalopolis.

Urban spatial patterns and urban dynamics can vary between the regional and the urban scale. In fact, according to Frankhauser in Borsdorf & Zembri (2021) morphology of the built-up structure is mainly determined by phenomena occurring in both scales. Hence, a different fractal primitive can be used over every range of scales in Fractalopolis.

The creation of the fractal primitive based on an IFS implies the following process:

i) Designing a generator and defining scale or reduction factors.

ii) Placing an initiator (e.g., square, circle) over the area of analysis (e.g., area to be densified).

iii) Creating a nested iteration logic of the pre-defined generator (i.e., every feature of the generator will host a copy of itself).

The design of the generator and the location of the initiator can be inspired by existing urban patterns and driven by the interest of urban planners.

For the downscaling iteration process in Figure 3.8, it is necessary to define a square as initiator, and the reduction factors r_1 and r_2. Hence, the downscaling iteration process creates a hierarchy of urban centres (in white) and lacunas (in grey) of different sizes within the urban system.

It is important to note that to the extent that the Sierpinski carpet is iterated, the surface of the centres decrease whereas its perimeter length increases. This implies the mass of buildings within a centre is vanished with iterations. Then, the number of iteration steps should be selected carefully in order to keep this mass.

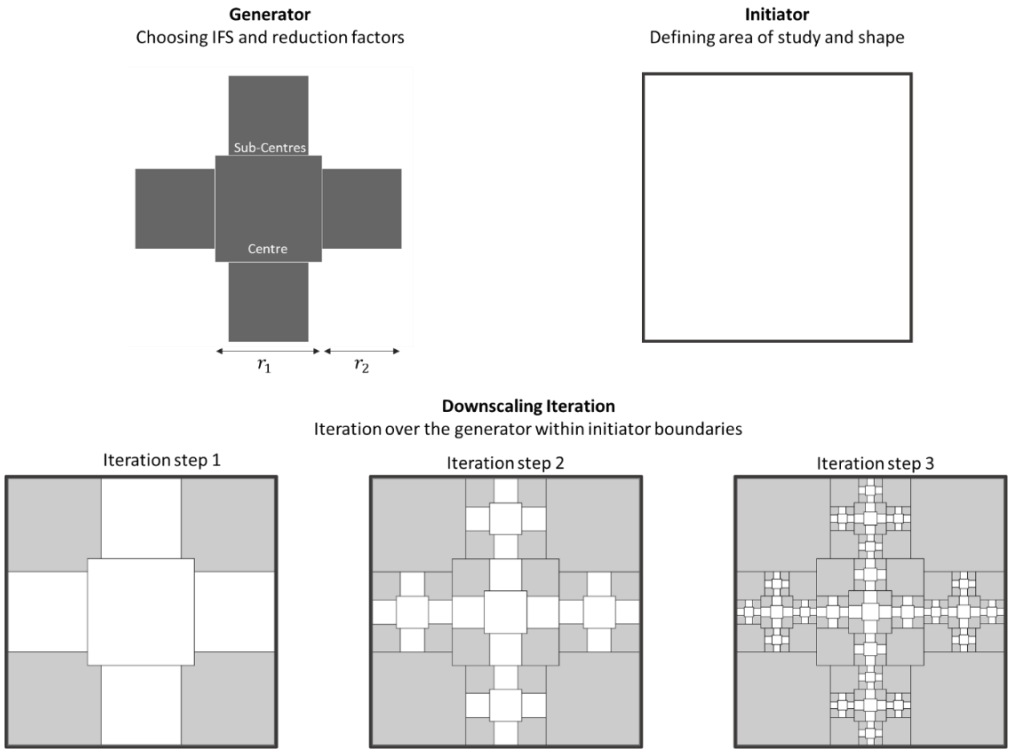

Figure 3.8. Development of an IFS and downscaling iteration of a Sierpinski carpet with two reduction factors. Adapted from Frankhauser et al. (2018).

To be able to fit the fractal form to an actual territory, Fractalopolis allows for displacement of squares at each scale with the limits defined by the previous scale. Thus, the fractal form obtained for is no longer strictly self-similar, but only statistically.

Because of the spatial hierarchy created in the course of the downscaling iteration process, a ranking of urban centres and lacunas is developed. A binomial coding

system is introduced in the program in order to distinguish the rank of urban centres, classed between 1 and 0, and that determines their frequency of visit by residents. This logic is inspired by the Central place theory of Christaller. Therefore, main centres that are more appealing because they offer more facilities and services, are denoted by 1 and sub-centres by 0 at each iteration step.

Following the same downscaling logic of centres, the lacunas (R) are coded at every iteration step. The notation adds a digit 0 or 1 according to its embedding urban centre rank, as shown in Table 3.1.

Table 3.1. Binomial code system of spaces.

Iteration	**Urban centres code**								**Lacuna code**			
Step 1	0				1				R			
Step 2	00		01		10		11		R0		R1	
Step 3	000	001	010	011	100	101	110	111	R00	R01	R10	R11

Linked to the code system, a housing distribution model is involved in Fractalopolis (see more on Frankhauser, 2012; Frankhauser et al., 2018). At each iteration step a given number of housings is assigned to each urban centre by weighting factors, according to its hierarchical rank. By this model, scenarios that consider the increase of the housing number can be simulated and the suitability of its construction evaluated.

Fractalopolis includes a module for the assessment of accessibility to different types of amenities, such as green spaces and/or services. An indicator is used in the program to assess the accessibility to each urban centre. It varies between 0 and 1, being bad and good accessibility, respectively.

Depending on the spatial scale of analysis, the conditions of accessibility vary. The principle of accessibility assumes the distance from urban centres to green spaces is more relevant at the urban scale, as this supports a pedestrian-friendly environment. Meantime, at the region scale, the presence or not of large spaces is more significant (Czerkauer-Yamu & Frankhauser, 2013).

Moreover, accessibility to amenities depends on usage frequency by the inhabitants: daily, weekly, monthly, or occasionally. Therefore, daily amenities are the nearest to urban centres at the urban scale. Being NBS deployment the main purpose of the next sections, the rules of accessibility to green spaces are only considered. All the details of accessibly rules are described by Czerkauer-Yamu & Frankhauser (2015).

Based on the formalisation of the fractal properties of the urban organisation and their recourse for the spatial modelling with Fractalopolis, let's now deal with the characterisation of the scale invariance properties on an existing territory as well as the application of Fractalopolis to deploy NBS over the site.

3.2 A case study in Parisian area: Est-Ensemble

Est-Ensemble is a Public Territorial Establishment (EPT, in French) of the Metropolis of Greater Paris (MGP) located at the east of Paris. This territory is close to the Cité Descartes, where the ET campaign over the BGW was carried out.

Est-Ensemble is one of the largest urban agglomerations in Ile de France region, and it concentrates 422,744 inhabitants (Insee, 2017) within 9 municipalities (communes): Bagnolet, Bobigny, Bondy, Le Pré-St-Gervais, Les Lilas, Montreuil, Noisy-le-sec, Pantin and Romanville.

The competences of the EPT include urban planning and environmental protection. According to the local urban plan of Est-Ensemble, 26,000 new housings should be created in 2030 (Est-Ensemble, 2020). Therefore, one of the main concerns of authorities is the management of potential densification areas, increasing both population and dwelling density in this Parisian-east area, while preserving natural green spaces.

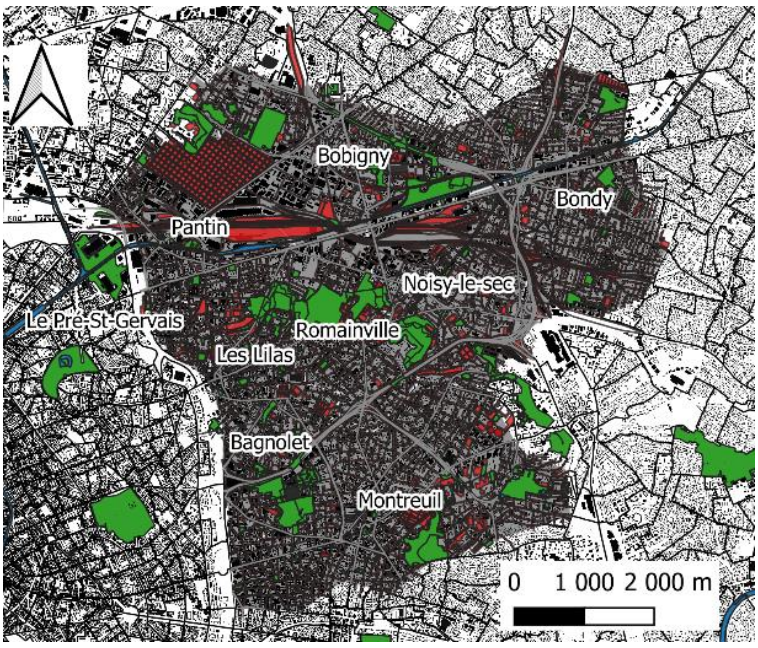

Figure 3.9. Communes of Est-Ensemble.

3.2.1 Green spaces to preserve

Because of the high pressure of building density in Est-Ensemble, and the potential impacts regarding urban resilience, it is essential to preserve the green spaces already present in the territory before simulating any scenario of urban densification or NBS installation. Therefore, green spaces recognised by urban planning and management tools, as well as those registered on the database of existing public green spaces open to the public from Paris Region Institute (L'Institut Paris Region, 2020) are listed. Missing and incomplete information of the database was completed with the Seine-St-Denis department GIS database of green spaces (Département de la Seine-Saint-Denis, 2014).

Some green spaces and water bodies of essential importance to keep free of urban development have been declared so by local authorities, based on the recognition of their ecosystem functions and services. These spaces include the Romainville Parc and the Canal de l'Ourcq, which are inscribed in the land-use, biodiversity life and regional ecosystems equilibrium plans: "*Schema Regional de Coherence Ecologique d'Ile de France*" (SRCE) and "*Schema de Trame verte et bleue*" (TVB).

Figure 3.10. Urban plans of local governance and management of green spaces in Est-Ensemble.

Other green spaces are included in the *local governance* and management plan of the Est-Ensemble territory, and in the future urban planning project *Parc d'hauteurs*, which connects several green spaces at the east of Paris in a loop of 32 km that pass-through Est-Ensemble. The list of urban plans and details of all green spaces that they include are presented in Appendix D, and summarised in Figure 3.10.

3.2.2 *Fractal dimension of built-up and green areas in "Est-Ensemble"*

The heterogeneity of spatial distribution of the built-up structure and the green spaces of the urban agglomeration of Est-Ensemble is analysed through the grid-counting approach in Fractalyse. This method was chosen as this adjusts the position of the grid to the image with the minimum coverage.

For this study, GIS database from the Institut Géographique National (IGN) was used to download the buildings map of Est-Ensemble, while final map of green spaces cited in the previous section was used to calculate the D_f. The size of the raster maps was

8,192x8,192 px (pixel of size 1 m). The results are presented in Figure 3.11 and Figure 3.12:

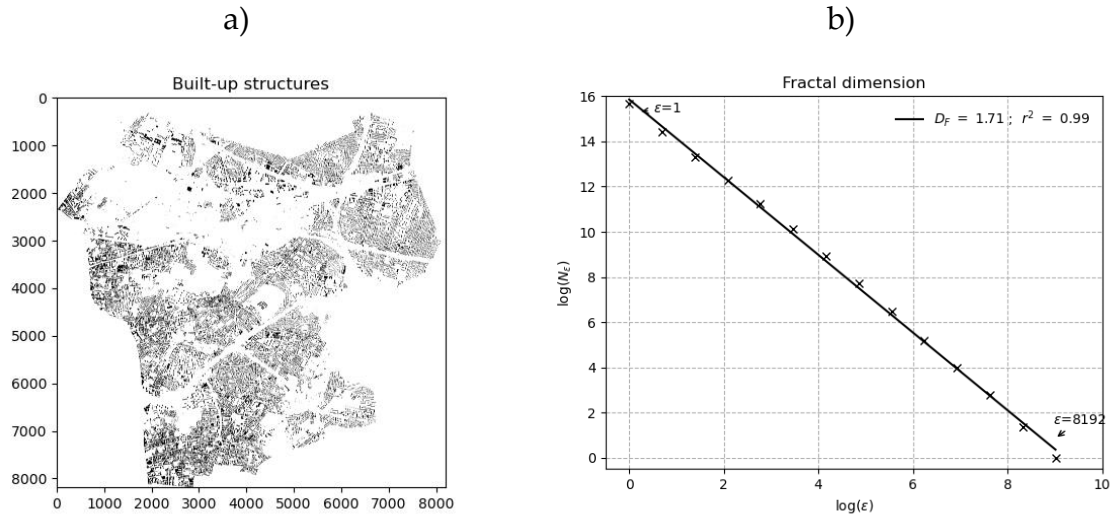

Figure 3.11. a) Built-up structures map and b) fractal dimension.

According to the results, the spatial organisation of the built-up structure is regular over all the agglomeration. Indeed, the D_f is approximately 1.71, which agrees with the results of Frankhauser (1997), who notes the D_f of urban form of several cities in Europe varies around 1.6.

Opposite to built-up areas, the D_f of green spaces indicated fragmentation and heterogeneity. The two breaks of the linear regression confirm a hierarchical distribution of green spaces characterised by three scaling ranges, represented by different D_f. The first and third scaling range have value of D_f close to 2 (1.9 and 1.81, respectively). In fact, the first scaling regime corresponds to a scale of observation smaller or equal to the footprint of the green spaces (1 to 16 m). Thus, the value of D_f describes a uniform distribution of green spaces with size length between 1 and 16 m. Contrary, the second regime of green spaces that characterises the middle scales (from 16 to 512 m) has a D_f of 1.4. This indicates green spaces at these scales are more concentrated as clusters. This would be related to the differences in the number and the size of green spaces per community. Finally, the D_f of the third scaling range of the

larger scales (512 to 8,192m), corresponds to the Euclidean dimension of the embedding space (filled when the resolution of the image decreases).

a) b)

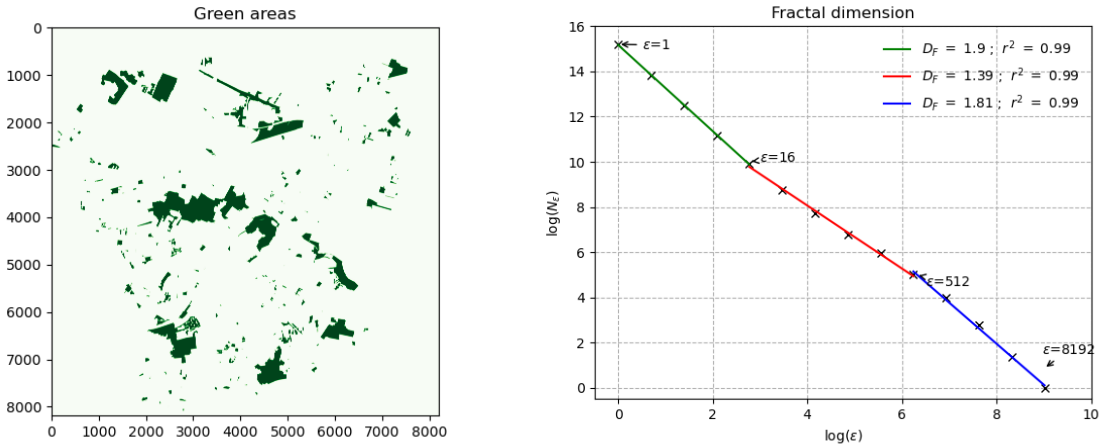

Figure 3.12. a) Green spaces map and b) fractal dimension.

3.2.3 *Alignment of N4C guideline classes: classification of green spaces database by types of NBS*

To avoid confusion between green spaces denominations and NBS terminology, green spaces database of Est-Ensemble was classified according to the NBS typology defined by Nature4Cities (N4C) project (Nature4Cities, 2018). The latter documented 56 types of NBS based on their urban and temporal scales, ways of intervention, thematic and land use, and local environment. The green spaces in Est-Ensemble database with no specific category, such as "autre" or "espace vert en projet" were classed as *Public Urban Green Spaces*.

Table 3.2 summarises five main categories of NBS with ground as physical support, that includes one or several types of green spaces.

Table 3.2. Classification of green spaces according to N4C classes of NBS.

N4C	Green Spaces in Est-Ensemble (FR)
Public urban green space with specific uses: including schools, playgrounds, campgrounds, sport fields, community gardens.	• Plaine de jeux • Parc sportif • Base de loisirs régionale • Base de loisirs
Public Urban Green Spaces: including parks, places, squares, green space, etc.	• Grand parc urbain • Parc de ville • Square et jardin public • Autre • Espace vert en projet
Botanical Garden: heritage garden.	• Parcs et jardins patrimoniaux • Espace naturel caractère pédagogique
Urban Forest	• Espaces bois et naturels
Vegetables Garden	• Jardin partagée • Jardin non identifié • Jardin familial • Autre jardin

From this classification, an overview of the current distribution of NBS by class is examined. The access point to every NBS extracted and classed in Figure 3.13. The main type of NBS in the territory is the *Public urban green space* (in orange). This category together with *Public urban green space with specific uses* (blue) group most of NBS managed by the local authorities of Est-Ensemble.

Regarding the *Vegetable gardens*, most of them are concentrated in the south of the territory, in Montreuil commune where is located the historical urban agriculture project Mûrs à Peches. By contrast, less numerous are the *Botanical gardens* and *Urban Forest*, present in the communes of Bondy and Romainville respectively. In this latter is located the Romainville Parc, the larger NBS of the whole territory.

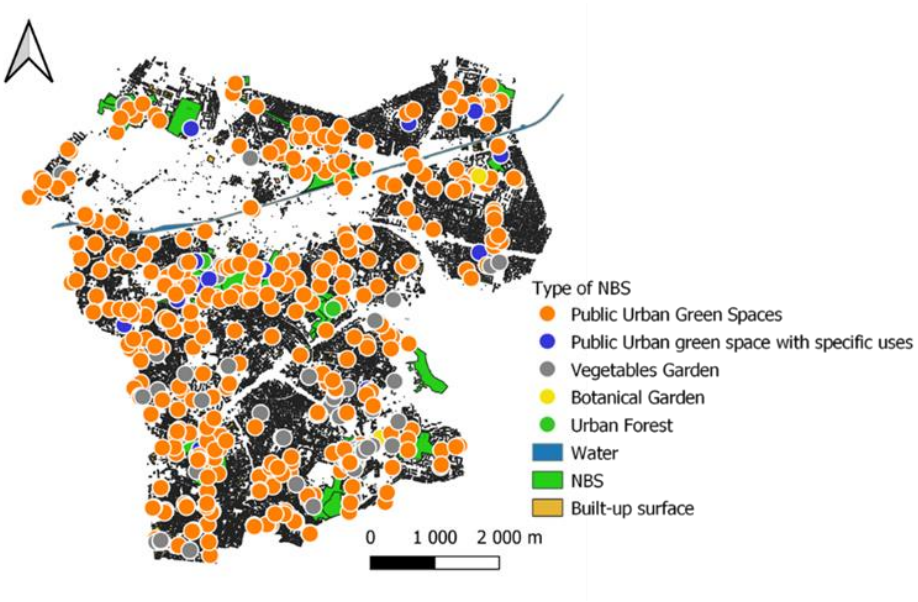

Figure 3.13. Distribution of NBS by typology.

This representation demonstrated in the Le Pré-St-Gervais commune there are few access points to NBS, which could be explained by the fact that this is the smaller commune in Est-Ensemble. However, these results are significantly different to Les Lillas, which is the second smallest commune, but has several *Public Urban green spaces* represented by access points to the Ile de Loisirs de Romainville.

An important feature in the distribution of NBS is their low availability at the north-west of the territory, mainly in the communes of Pantin and Bobigny. There, it is located Pantin's cemetery, the widest cemetery in the Paris region. Despite green spaces on Pantin's cemetery, which occupies 107 ha and 1/7 of the total commune surface (Pantin, 2020), those are not included in any of the original databases of green spaces.

Besides, at northern communes there is a large warehouse of the national railway company (SNCF). Hence, the urban footprint between the cemetery and the SNCF's warehouse, and water channel Canal de l'Ourcq, is not empty. Instead, there are numerous industrial buildings, as well as the national road N3.

If the total area of NBS is deduced, we found 401.97 (ha) of NBS in Est-Ensemble, which represents to 9.97 m² of NBS per individual. This is slightly higher than the minimum

threshold recommended by the World Health Organization (WHO) (i.e., 9 m² per capita). Therefore, from the perspective of population growth, just as the urban planning of Est-Ensemble specifies, this indicator of availability of public NBS per capita would be easily exceeded.

The proximity to NBS from housings is evaluated following WHO recommendations too. Since this specifies NBS should be installed close to people, all housing should have access within 300 metres' linear distance to NBS of at least 0.5 – 1 ha (World Health Organization Regional Office For Europe, 2017). In the case of Est-Ensemble, this evaluation indicated 89.6% of the total number of housings are near to minimum 0.5 ha of any type of NBS. Thus, it is necessary that NBS are deployed over the territory to insure their access at different urban scales.

3.2.4 Design of an IFS to spatially fit the green spaces with a fractal primitive

The elaboration of a scenario of deployment of NBS based on fractal geometry in Fractalopolis requires exploring scenarios of urban development over the built-up structure, i.e., according to the classical applications of the software (Czerkauer-Yamu & Frankhauser, 2015; Frankhauser et al., 2018), in order to extract the lacunas that will serve as support where the new NBS will be located.

The simulation of both the built-up and NBS structure, consider that urban patterns follow a fractal law, that is represented by a fractal primitive. However, the self-organising process varies for each structure. Whereas the urban centres try to cover the built-up structure in the best possible way, the design of the new NBS is inspired by the self-similarity properties of the current distribution of green spaces.

3.2.4.1 Iteration over built-up structure

The arrangement of the IFS over the built-up areas of Est-Ensemble adopts two different approaches according to the scale of iteration: regional or urban scale.

- *At the regional scale*: The polycentric and heterogenic morphology of the Metropolis of Greater Paris (MGP).

Given the territory of the Est-Ensemble is located within Seine-St-Denis, one of Petite Couronne departments of the MGP, the design of the IFS at the regional scale is inspired by the polycentric distribution of the MGP's plan. This is composed of the city of Paris and nearby suburbs of the departments of the Petite Couronne: Hauts de Seine, Seine-St-Denis and Val de Marne. Therefore, the spatial logic of the IFS follows an adaptation of the classic Sierpinski carpet, consisting of a large centre of first rank and six smaller centres of second rank. Two reduction factors are used for the centre of each rank: $r_1 = 0.35$ and $r_2 = 0.25$, leading to find 1.46 as fractal dimension in the generator.

The main centre (of rank 1) is placed in Paris, where a wide range of facilities is provided, and two sub-centres in each of three surrounding departments, as shown in Figure 3.14. One sub-centres of the Seine-St-Denis department is placed over Est-Ensemble.

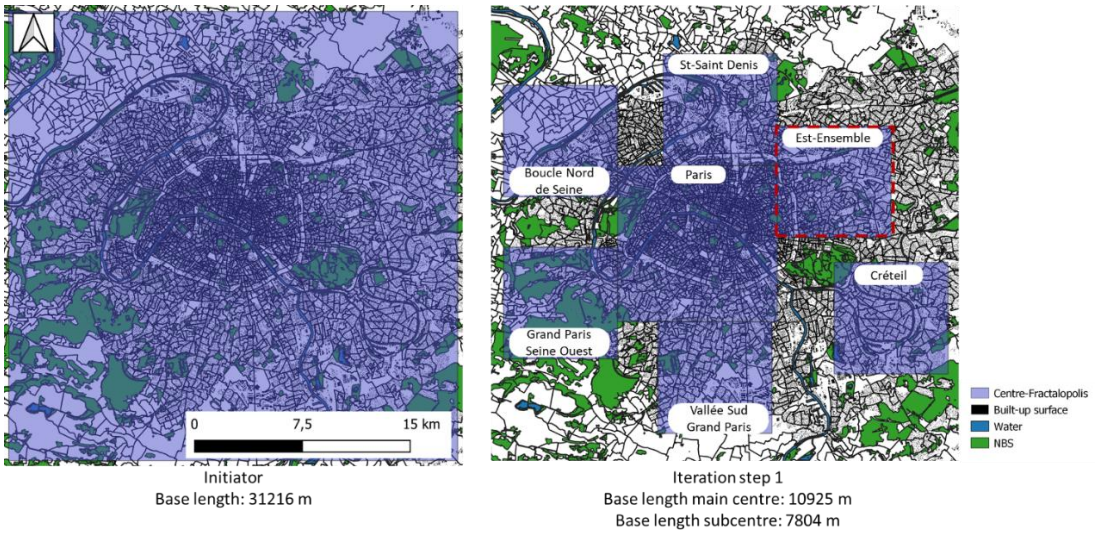

Figure 3.14. Simulation of urban centres at the regional scale.

The sub-centre representing Est-Ensemble is set as the initiator of the urban scale (in Figure 3.15). Therefore, the iterative downscaling logic is developed exclusively over

this territory with the same fractal generator, keeping self-similarity properties of built-up structure across all scales.

- *At the urban scale*: The urban centres are positioned in such a way that the NBS of Est-Ensemble are free from interventions. This means that the set of existing NBS ends up located in the lacunas.

At the iteration step 2, the placement of urban centres takes into consideration the total number of housing units by communities (see details in Appendix E). Hence, the main centre was placed over the communes of Montreuil and Bagnolet, with a high number of houses, whereas sub-centres are over the remaining communes. Because of Montreuil's extension, it is necessary to locate an additional sub-centre. By contrast, communes such as Le-Pré-St Gervais and Les Lillas share the same sub-centre, since they are not very large, and the housing number is lower.

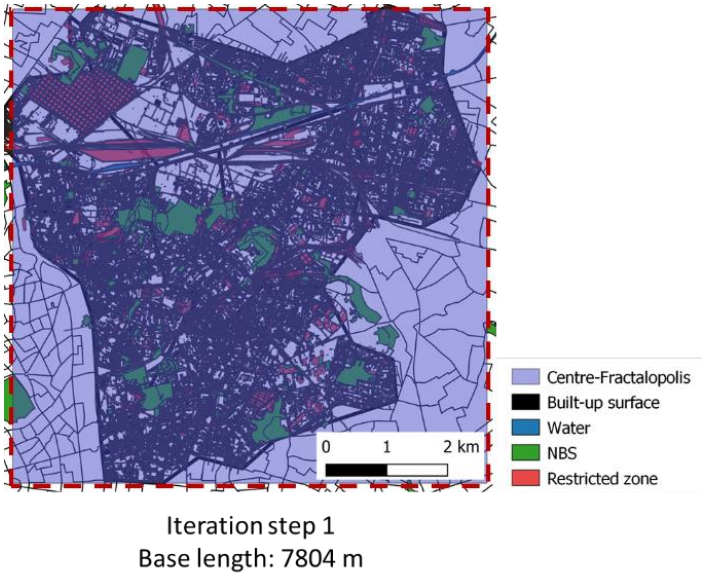

Figure 3.15. Sub-centre at iteration 1 and initiator at the scale of Est-Ensemble.

The iteration step 3, in the right of Figure 3.16, shows a good fit between the urban centres and the existing building structure, which would allow enough place for the NBS. Indeed, it can be observed how the placement of centres (in blue) attempts to leave, all NBS already existing on the territory and listed previously, free of interventions, especially the Romainville Parc and the Canal de l'Ourcq. Thus, the number of iterations is considered sufficient.

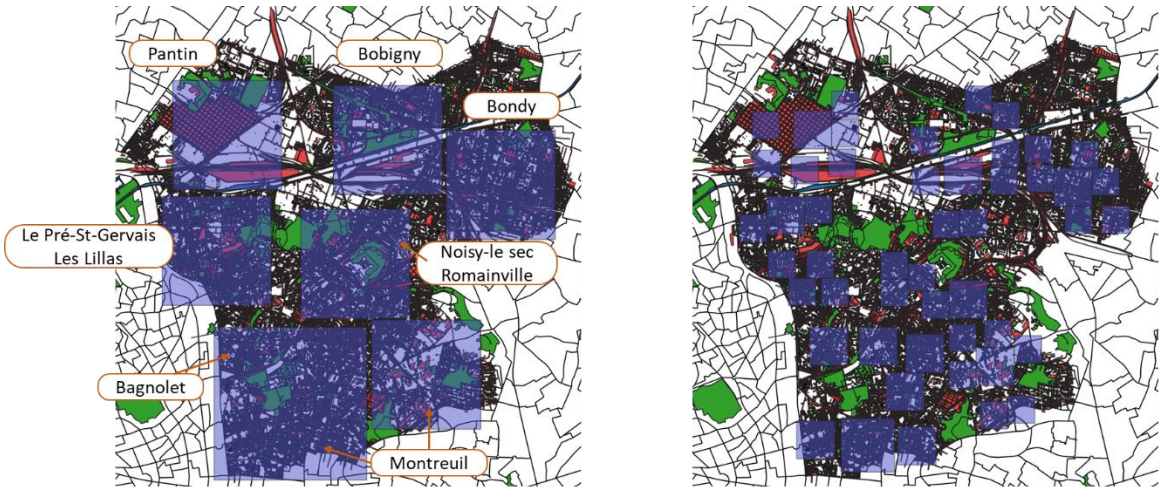

Figure 3.16. Scenario of development of urban centres.

If the housing density of this scenario is analysed, we found the highest values at the western of the territory centres, mainly in the communes of Le-Pré-St-Gervais and Les Lillas, as can be seen in the Figure 3.17. On the contrary, the number of housing units per hectare is lower in the centres located at the eastern and mainly in the north. These results (see all details in Appendix F) confirm jointly with the NBS distribution in Section 3.2.3, the deficit of NBS in communes with high housing density.

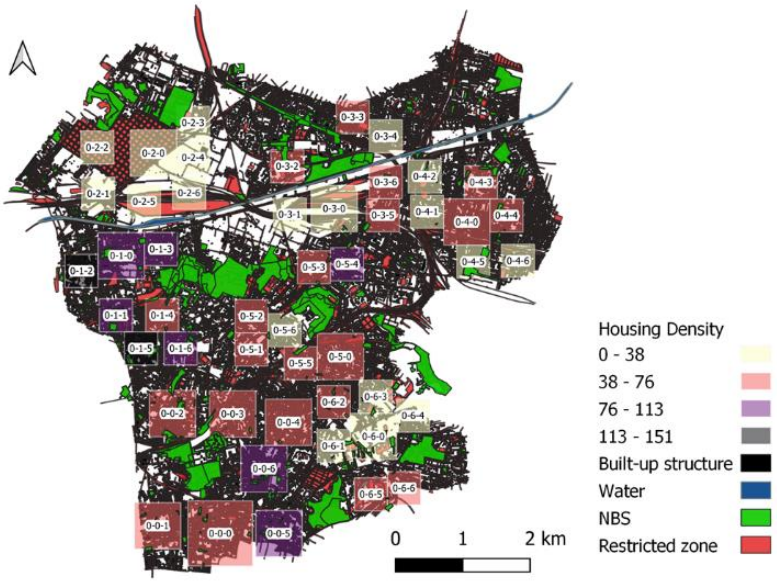

Figure 3.17. Housing density (housing/ha) in urban centres.

3.2.4.2 *Iteration of new NBS*

The unoccupied sites by urban centres, includes built-up structure, NBS, road network, transport network, etc. All the ensembles of these sub-sets of the built-up pattern comprises the lacunas. In these spaces with limited urbanisation strategy, we will develop a scenario of installation of NBS, that is based on the existing distribution of NBS.

Since the distribution of NBS in Est-Ensemble seems to follow a fractal law, we adopt the approach to define another fractal primitive for the NBS that will be deployed in the lacunas of the fractal primitive describing the built area. Lacunas of a fractal form do not constitute a fractal, but let us recall that the lacunas may contain many other urban objects, including streets, places and public infrastructure.

To preserve the self-organisation properties of NBS on the territory, the design of the fractal generator of NBS will rely on the analysis of the fractal dimension of existing NBS. This means the downscaling logic of the IFS matches the self-similar properties of the original distribution of NBS. As the results of the box-counting analysis demonstrated (in the Section 3.2.2), the NBS are not homogeneously allocated over the urban agglomeration and its clustering distribution is described by three scaling ranges.

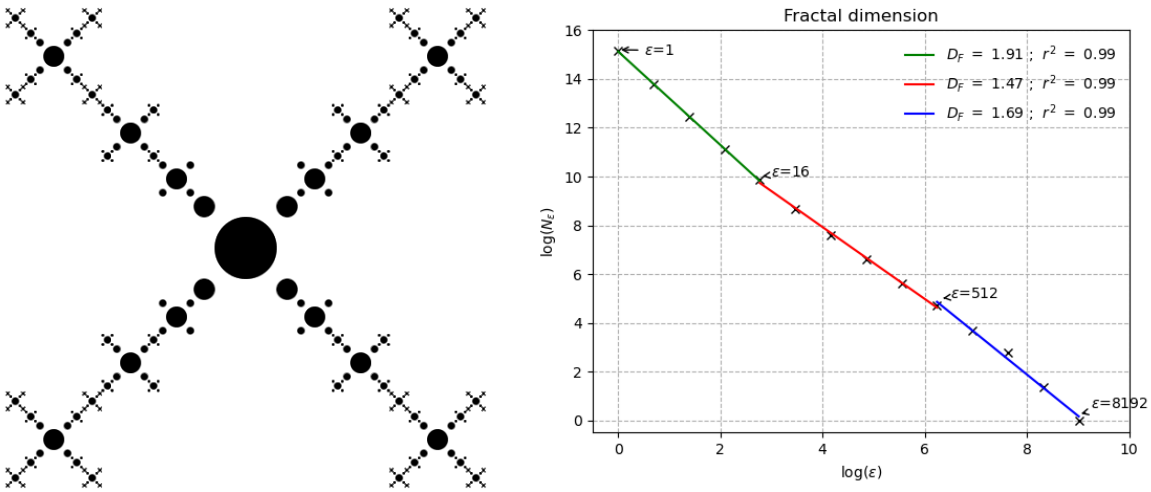

Figure 3.18. IFS at iteration 4 and D_f.

The open-source software GenFrac (https://sourcesup.renater.fr/www/genfrac/), devoted to the creation of fractals was used to design the IFS of new NBS, verify its fractal dimension and scaling behaviour before to use it in the spatial modelling of Fractalopolis.

The generator is inspired by a Sierpinski carpet and the geometry of the initiator was chosen to be a circle (as shown in Figure 3.18). The generator is constructed over a grid of 10x10 with two reductions factors, $r_1 = 0.6$ and $r_2 = 0.2$, and its D_f is 1.30. The choice of the reduction factors is based on the ratio between the side-length of NBS and the horizontal extension of Est-Ensemble territory.

After four iterations of the IFS, the D_f is computed considering 8,192 m as the largest side of the box. This corresponds to the horizontal size of the distribution map of NBS. The results in Figure 3.18, indicated two breakups and three scaling regimes, just like the original NBS distribution. The values of the D_f are compared in Table 3.3.

Table 3.3. Fractal Dimension of NBS

Scale Range	D_f of original NBS distribution	D_f of NBS generator
8,192 – 512 m	1.81	1.69
512 – 16 m	1.39	1.47
16 – 1 m	1.9	1.91

These values demonstrated the D_f of NBS generator have quite similar scale invariance properties to the original distribution of NBS. Consequently, a self-similar scenario of NBS deployment is generated by setting the characteristics of the generator in Fractalopolis, and iteratively downscaling four times. Their location at early steps attempts to avoid centres of urban development, which leads lacunas to be partially covered.

The current distribution of NBS, called "baseline" from now, and the multiscale scenario of NBS's deployment are compared through the assessment of accessibility in the fractal scenario of urban development. For this purpose, the frequency of visits to

NBS, according to the type of NBS and their area is defined by rules explained in Table 3.4. The area used to classify NBS are consistent with the characteristic scales of NBS side-length. This means that 16 and 512 m scales, determined an area of 256 and 262,144 m². In this way, small NBS as urban parks or squares, are busier places than a large forest.

Table 3.4. Frequency of visit to NBS.

Frequency	Type of NBS
Occasional (1)	• Urban Forest
Monthly (2)	• Public Urban Green Spaces, and Public Urban green space with specific uses, with area > 262,144 m² • Heritage and botanical gardens
Weekly (3)	• Public Urban Green Spaces, and Public Urban green space with specific uses, with 256 ≤ area ≤ 262,144 m² • Vegetable gardens
Daily (4)	• Public Urban Green Spaces, and Public Urban green space with specific uses, with area < 256 m²

The indicator of accessibility of each urban centre considers its proximity to NBS. The distances that should be respected according to the frequency of use of NBS, are established conforming to the characteristic scales of NBS distribution. This means proximity to daily NBS is between 1 to 16 m, weekly between 16 to 512 m, monthly between 512 to 8,192 m and occasionally NBS are less than 8,192 m.

For any frequency, in Fractalopolis the nearest distance between the centroid of the urban centre and every NBS (with corresponding frequentation of analysis) is calculated, and the rules of accessibility are applied, as described in Table 3.5. Thus, the final indicator of accessibility by frequency in the urban centre, corresponds to the average of accessibilities to NBS. The distance to NBS is estimated to the access point if the NBS area ≥ 5,000 m² or to the centroid for smaller NBS.

Table 3.5. Rule distances to NBS by frequency.

Frequency	Evaluation
Occasional (1)	$A_0 = \begin{cases} 1, & d_i \leq 8{,}192\ m \\ 1 - \dfrac{d_i - 8192}{10000 - 8192}, & 8192\ m < d_i \leq 10{,}000\ m \\ 0, & d_i > 10{,}000\ m \end{cases}$
Monthly (2)	$A_m = \begin{cases} 1, & d_i \leq 512m \\ 1 - \dfrac{d_i - 512}{8192 - 512}, & 512\ m < d_i \leq 8192\ m \\ 0, & d_i > 8{,}192\ m \end{cases}$
Weekly (3)	$A_w = \begin{cases} 1, & d_i \leq 16\ m \\ 1 - \dfrac{d_i - 16}{512 - 16}, & 16m < d_i \leq 512m \\ 0, & d_i > 512\ m \end{cases}$
Daily (4)	$A_d = \begin{cases} 1, & d_i \leq 1m \\ 1 - 1 - \dfrac{d_i - 1}{16 - 1}, & 1\ m < d_i \leq\ 16m \\ 0, & d_i > 16\ m \end{cases}$

3.2.5 Evaluation of the beneficiates of the multiscale scenario of NBS deployment with Fractalopolis

The visual outcome of the scenario of deployment of NBS following a fractal logic is presented in Figure 3.19. The NBS are located around almost all the territory, with the exception of the southern area. Despite their location in the first iterations aims the lacunas of the scenario of urban development, at a more local scale the local context influences the final NBS emplacement:

i) The largest element is placed in the Parc departemental de la Bergère and the Canal de L'Ourcq, as a strategy of protection of the cooling corridor in the north of the territory. Given this space represents the future construction area of new housing by 2030, in accordance with the urban management plan (Est-

Ensemble, 2020), the installation of NBS would represent a strategy for the construction of urban resilience.

ii) Because of the high housing density and the low number of NBS, the deployment of small NBS is encouraged at the western of Est-Ensemble (i.e., Le Pré-St-Gervais, Bagnolet).

iii) Given Pantin' cemetery is a type of NBS according to N4C classification, but whose ESS have been unvalued by local authorities, this is included as a new NBS.

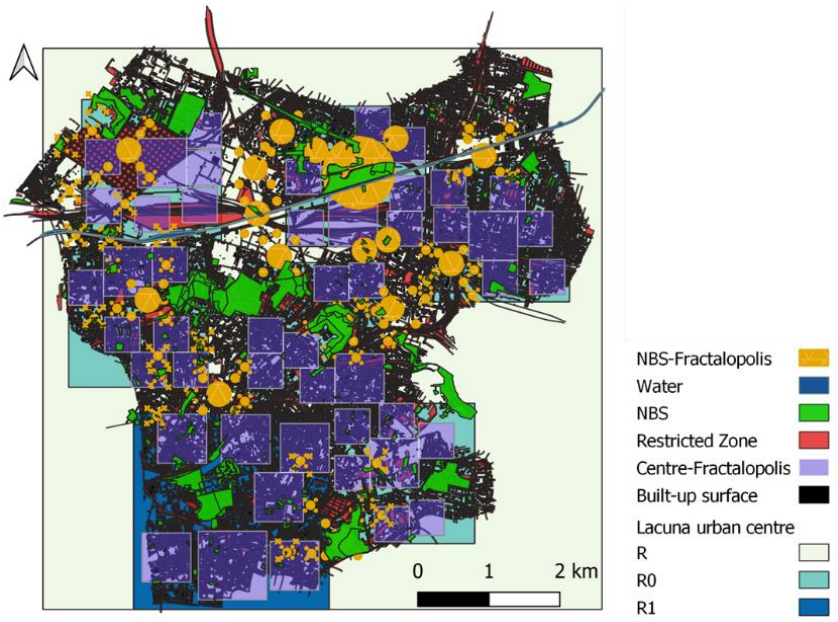

Figure 3.19. Fractal scenario of NBS deployment.

The location of NBS created by the fractal logic in high-density areas in the western communes, implies NBS over lacunas is not fully respected and there is an overlapping with the current distribution of the built-up structure, as can be seen in the Figure 3.19. For these conditions of high-density areas, the installation of a new type of NBS can be considered. According to the classification of N4C, some types of NBS can use the buildings and current urban structure as physical support. Those NBS include green roofs and green walls. As well, structures associated with urban networks on the ground, such as green tram tracks, street trees, green strips, or green parking lots. The arrangement of this kind of NBS would represent an opportunity for the installation

of a new type of NBS in the areas with an extended urban footprint with low space for green.

Moreover, this scenario creates a hierarchy of spaces to the same extent as the fractal object was iterated. Thus, 625 new polygons representing new NBS with a different level were designed at the iteration step 4. The size of the fractal objects (i.e., the diameter of circles) varies between 11 and 892 m, and at a given level the objects could have different sizes (see more details in the Table 3.6). Thus, a hierarchy of NBS is created, just like the fractal structures.

Table 3.6. Level, number and size of objects representing multiscale scenario of NBS.

Level	Number of objects	Size (m)
1	1	892.44
2	4	297.48
3	20	99.16, 297.48
4	100	33.05, 99.16, 297.48
5	500	11.02, 33.05, 99.16, 297.48

The accessibility of the baseline distribution of NBS was compared with that of the multiscale scenario of NBS' deployment. All the NBS created through NBS' fractal logic were classified as a Public Urban Green Space and its frequency is determined by their area, following conditions in Table 3.4. Therefore, the final classification of NBS involves those that are visited on a daily, weekly, or monthly basis. By contrast, the Romainville's Parc is the only urban forest that can be visited occasionally in both scenarios.

The results of the evaluation of accessibility at the urban scale do not highlight a significant amelioration between the multiscale scenario and the baseline. The indicator shows the overall accessibility (average of accessibilities) is 0.517 for the multiscale scenario of NBS's deployment and 0.504 for the baseline (see indicators in

the Appendix G). This means access to any type of NBS is not excellent, but not extremely bad either.

Regarding every temporal scale of NBS visit from urban centres, a significant improvement of accessibility at daily and weekly frequencies was expected, since the number of NBS visited at this rate substantially increased in the multiscale scenario. However, just a slight improvement of accessibility is noticed. The maps in Figure 3.20.a, and Figure 3.20.b, show the indicator of those frequencies hardly changes. In the daily case, just one centre at the west has a value of 0.4 and in the weekly case, few squares on the west increased their access value. This would mean the distance thresholds (i.e., 16 and 512 m for daily and weekly visit, respectively) are not enough to reach the access point of NBS from the centroid of urban centres.

The higher indicator of accessibility corresponds to monthly NBS. It is superior to 0.7 for both scenarios (Appendix G), but it decreases in the multiscale scenario of NBS (Figure 3.20.c). This can be explained by the method of estimation of accessibility: In the baseline scenario, two NBS have monthly frequency of visit. In addition, both NBS have the same category or type: botanical garden, thus, only the accessibility indicator to the nearest botanical garden is estimated. The integration of a new NBS at the north (in the Parc departamental de Bergère) in the multiscale scenario, introduced a different category of NBS: Public Urban Green Space. Hence, the accessibility is estimated to the nearest NBS for each category and then all categories are combined by evaluating their average. Thus, access in urban centres on the western of the territory (close to the new NBS) improved, but in some urban centres of Montreuil was declined, as the distance from centres on south to the Parc de Bergère is long. This implies accessibility to this NBS is very low, leading to reduce the overall average.

Finally, all the urban centres have good accessibility to Romainville Parc, which is considered the only urban forest that is visited occasionally by the inhabitants of Est-Ensemble.

Multiscale scenario of NBS	Baseline scenario of NBS
a) Daily	
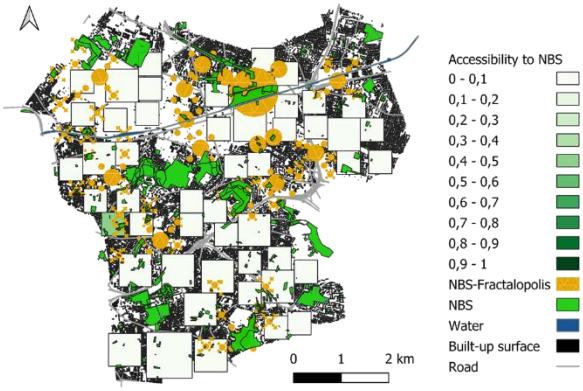	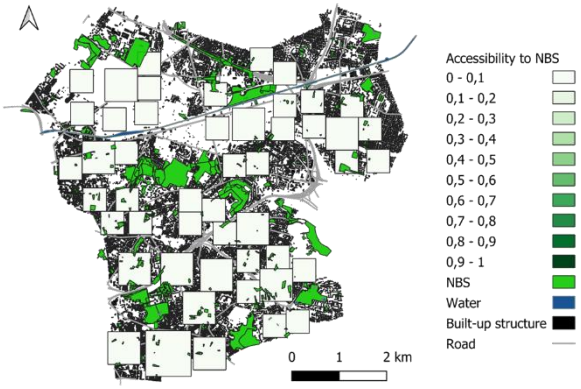
b) Weekly	
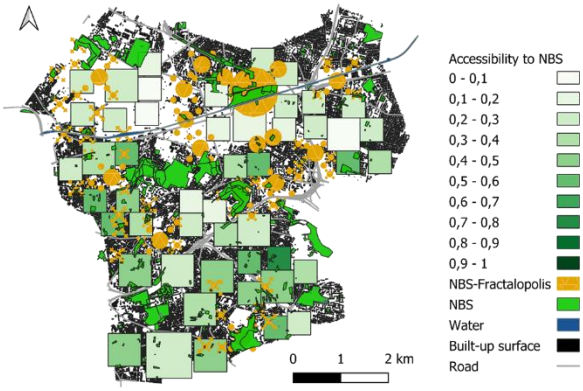	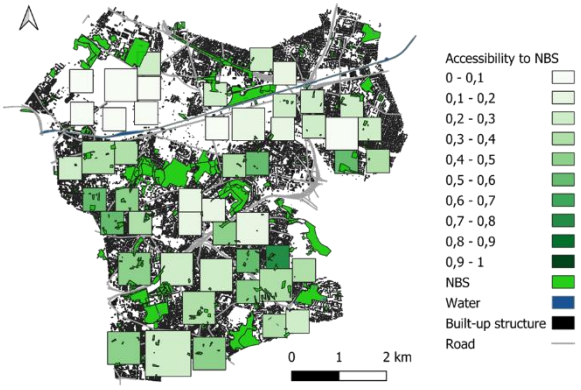
c) Monthly	
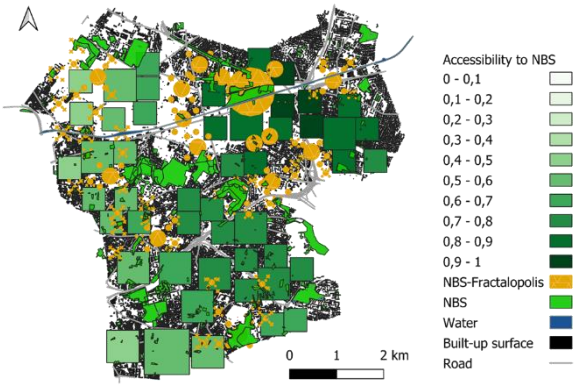	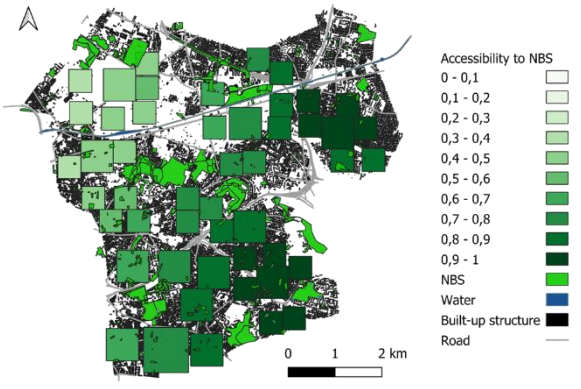

Multiscale scenario of NBS	Baseline scenario of NBS
d) Occasionally	
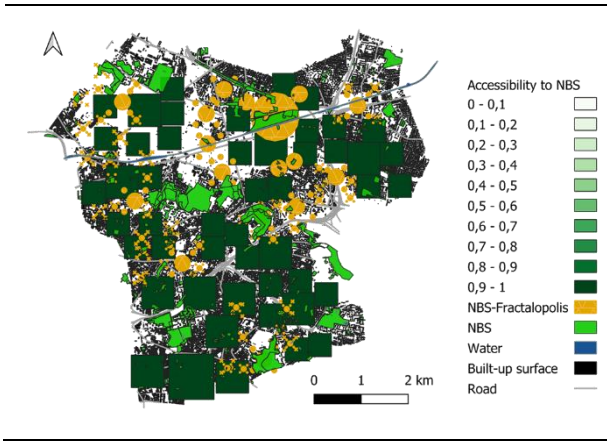	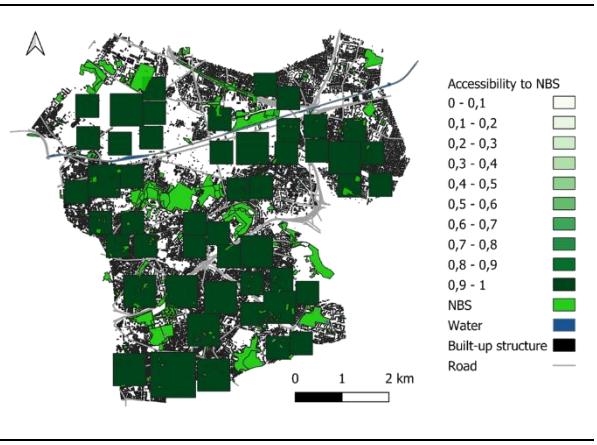

Figure 3.20. Accessibility to NBS, multiscale (left) and baseline (right) scenario with different frequency rate of visit: a) daily, b) weekly, c) monthly, and d) occasionally.

Given that at the urban scale the proximity to one NBS is more significant than access to different categories of NBS (because of scarcity of vegetation), it was considered the evaluation of accessibility from the urban centres to the closest NBS instead of the average to all NBS. Thus, the proximity procedure is kept.

The accessibility to the nearest NBS in the multiscale and the baseline scenario were compared in Figure 3.21. The results of this methodology demonstrated the indicator of accessibility in the multiscale scenario is higher than the baseline, from the weekly frequency.

Most of the urban centres in the multiscale scenario have good accessibility (greater than 0.5) to at least one SNB with a weekly or monthly frequency. This weekly frequency indicator is less than 0.2 in only two centres near the Pantin cemetery (north) and in the commune of Bondy (northeast). While in the monthly frequency, the indicator is almost homogeneous and higher than 0.6, which is much better than the previous evaluation of accessibility. Regarding on a day-to-day basis, accessibility to NBS within 16 m only increase in one centre in western. Indeed, accessibility could hardly change as at small scales the distribution of NBS is almost uniform in the baseline scenario ($D_f = 1.9$).

Multiscale scenario of NBS	Baseline scenario of NBS
a) Daily	
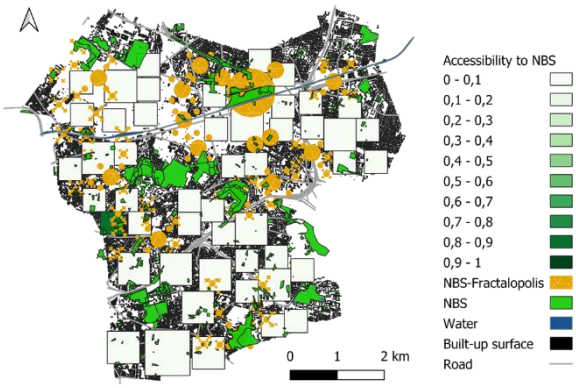	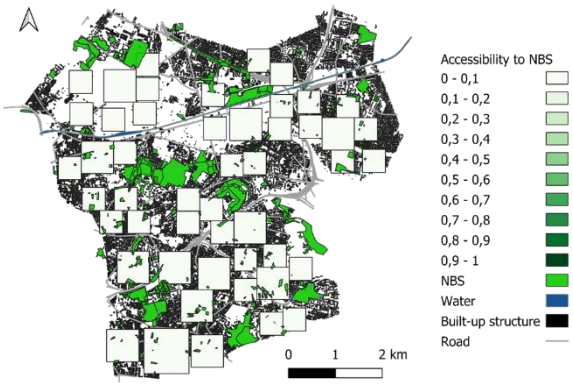
b) Weekly	
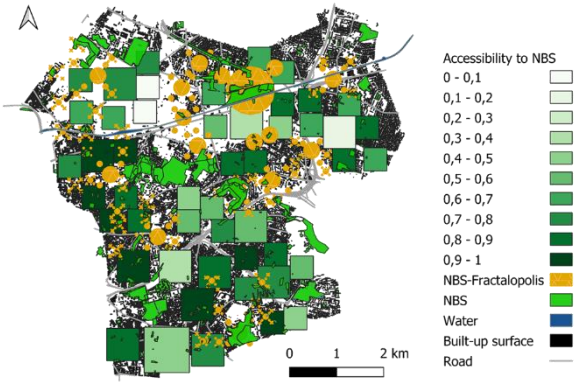	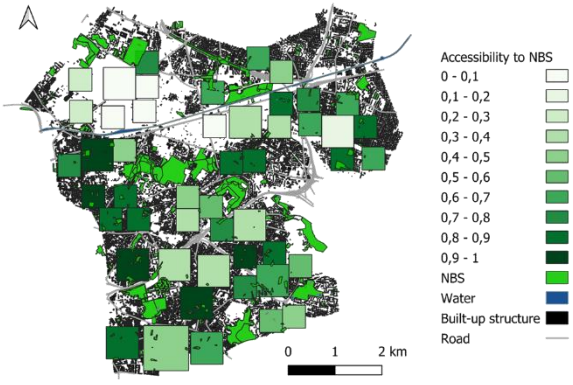
c) Monthly	
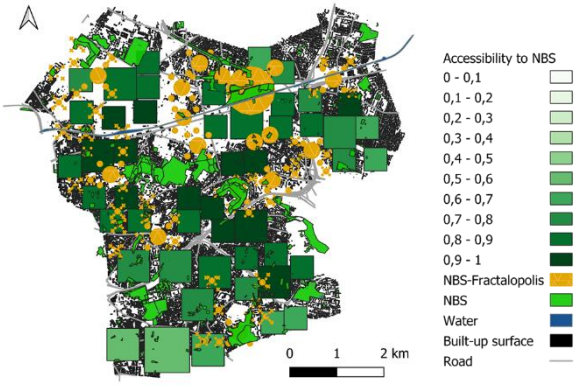	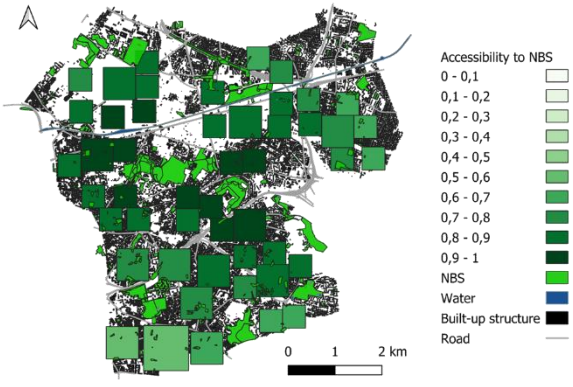

Figure 3.21. Accessibility to the nearest NBS, multiscale (left) and baseline (right) scenario with different frequency rate of visit: a) daily, b) weekly, and c) monthly.

3.3 Conclusions and Perspectives

To maximise the number of beneficiates of NBS across several scales of a territory, we use the fractal geometry to simulate a scenario of NBS's deployment. By means of an iterative downscaling logic in the spatial simulation model of Fractalopolis, an urban development scenario that follows a fractal law was created. The location of planned urban centres was determined according to the conditions of urban development and planning. This allowed to obtain the lacunas of the fractal object as support for the location of new NBS.

In the case study of Est-Ensemble, the lacunas of urban development scenario comprised several urban sets, such as the NBS, the railway structure, the transport axes, etc. The complexity of such sets could be characterised by the fractal dimension, as was the case of the NBS. Because the fractal dimension results highlighted the hierarchical distribution of NBS according to a power law, they were simulated as a fractal object in the spatial modelling of Fractalopolis, just like the built-up structure. Furthermore, self-similarity properties of NBS were used to define properties of the fractal object representing NBS deployed over the territory.

This simulation allowed to create a hierarchy of NBS of different sizes over the lacunas of Est-Ensemble. However, the emplacement of NBS over the lacunas was not fully respected, because overlapping between the fractal with the zones of urbanisation, which lead to proposing the installation of a new type NBS over the existing urban structure, such as the green roof or the green parking. In this way, the original approach of Fractalopolis, where the green spaces, or NBS in this study, are represented by the lacunas or the complement of the fractal structure (i.e., the buildings) was modified.

The suitability of the multiscale scenario of NBS deployment was assessed through the accessibility from the urban centres to NBS, and the results were compared to the baseline. The evaluation of accessibility took into consideration the overall average

access to all types of NBS. The proximity evaluation rules, were determined according to the characteristic horizontal scales of self-similarity distribution of NBS.

The indicator of accessibility for NBS visited occasionally was good throughout the territory. Moreover, a slight improvement of the accessibility to daily and weekly NBS was observed in the multiscale scenario. However, a significant improvement was expected as the number of NBS with these frequencies increased considerably in the multiscale scenario. The distance to reach those spaces from the centroid of urban centres was not long enough to ensure a good access. Finally, the indicator of monthly access to NBS was lower than the baseline, as a new type of NBS was included in the analysis, whose access value was low in the centres located in the south of the territory.

Given the initial way of evaluation of the indicator of accessibility did not exhibit suitability of NBS multiscale scenario, the method of evaluation only considered the accessibility to the nearest NBS. The results demonstrated high values of accessibility in the multiscale scenario for all frequencies of visit, except for NBS visited daily.

Because the installation of NBS requires considerable investment, the evaluation of the economic cost of installation and maintenance of the multiscale scenario regarding their temperature reduction performance, would be very useful. This would allow to determine the minimum number of NBS necessary to ensure the cooling effect, while respecting self-organisation of the space.

As well, under the perspective of temperature reduction because of the ET effect from the NBS, the characterisation of its scaling behaviour through statistical-based methods, such as the multifractal analysis, would enable to determine the main spatial scales of installation of NBS. To attempt this, in the next section, scaling properties of related thermal fluxes to the ET from the BGW, the $C_n{}^2$ and the air temperature are investigated.

Chapter 4 Scaling properties of atmospheric fluxes in the BGW

In Chapter 3 fractals were introduced as self-similar complex patterns across different scales, which follows a power law and are characterised by the fractal dimension D_f. Fractals have not only been useful in the study of scaling laws of urban morphology, but also in the analysis of scaling properties of dynamic and non-linear geophysical fields.

Geophysical fields usually exhibit fluctuations that follow scaling power laws. Hence, they were first approached as a fractal set. However, it was found they did not have a unique scaling exponent. When different thresholds (singularities) were set to estimate the distribution pattern of a field, for each singularity a different fractal dimension appeared. This led to define multifractals and their properties, which serves for the analysis and modelling of fields.

Since the field measurements are generally conducted at a given unique scale, the properties at other scales must necessarily be deduced from the measurement scale. The main goal of this chapter is to analyse the scale invariance behaviour of experimental thermal fluxes measured in the BGW through the multifractal analysis. For this purpose, statistical approaches, such as the spectral analysis and the structure function, are applied to confirm the scaling behaviour of ${C_n}^2$ and temperature. In addition, the properties that characterise such scaling are investigated by means of the Universal Multifractal framework.

4.1 Scaling invariance laws for describing fluxes

Previously in Chapter 2, the statistical approaches for describing atmospheric fluxes were introduced as well as their use for determining power laws that describe scale invariance behaviours. This is the case of the Fourier transform, through which the

power spectral density of any time series could be estimated. Thus, a time series can be decomposed into frequencies (or wavenumber, by involving the Taylor's hypothesis[6]), in order to analyse the scale distribution of the energy flux. The scale invariance of the atmospheric flux can be detected though the spectral exponent β.

In addition, the structure function and the Kolmogorov's hypothesis were explored. Particularly, the second-order structure function of the velocity fluctuations and the formalisation of the 2/3 law by Kolmogorov, as well as its representation in the Fourier space, which led to deduce the universal power law of 5/3 in the inertial range.

To better understand the statistical properties of the fluxes, let's see now a power law that serves for the generalisation of the structure function of an arbitrary statistical moment of order q (i.e., integer and non-integer moments q) at any point x. Thus, Eq. (2.11) can be written as[7]:

$$S_q(r) = \langle |\Delta u(r)|^q \rangle$$
$$S_q(r) = \langle |u(x+r) - u(x)|^q \rangle \tag{4.1}$$

Under the K41 hypothesis of constant energy flux density $\bar{\epsilon}$ and self-similar turbulent flux at small scales, the structure function follows a power law $\zeta(q) = q/3$ as follows:

$$S_q(r) = \bar{\epsilon}^{q/3} r^{q/3}$$
$$S_q(r) \propto r^{\zeta(q)} \tag{4.2}$$

where, $\zeta(q)$ is the scaling moment function, related to the similarity exponent $H = 1/3$ by the Kolmogorov theory. In the absence of corrections due to turbulent intermittency of the flux, a perfect linear relation $\zeta(q) = qH$ is expected. Then, for any order moments q:

[6] The Taylor's hypothesis of frozen turbulence states that temporal and spatial fluctuations of a flux can be related by a constant velocity. If the turbulence intensity u' is small compared to the mean flux speed $\langle u \rangle$, the temporal response at a fixed point in space can be view as the result of a spatial pattern advected by the mean velocity $\langle u \rangle$.

[7] We will use here the compact notation that is rather usual for the multiplicative processes.

$$q = 1 \rightarrow \zeta(1) = H$$
$$q = 2 \rightarrow \zeta(2) = 2H \quad (4.3)$$
$$q = 3 \rightarrow \zeta(3) = 3H$$

Then, the mean of the field corresponds to $q = 1$. For $q = 2$, the second-order moment structure function $\zeta(2)$ is related to the scaling exponent of the spectral analysis β in the following manner:

$$\zeta(2) = \beta - 1$$
$$\beta = 1 + 2H \quad (4.4)$$

Then the skewness coefficient that measures the asymmetry in the distributions could be deduced with the help of third order moment $q = 3$.

The intermittency is responsible of the extreme variability of the turbulent fluxes in the Atmospheric Boundary Layer (ABL). Hence, for models considering intermittency, there may be a variation of $\zeta(2) = 2/3$, hence the spectral exponent β will differ from the expected 5/3.

The intermittency could be characterised by the fully knowledge of $\zeta(q)$ and q. The relationship between S_q and r on logarithmic scale, allows to deduce the scaling exponent $\zeta(q)$ as the slope of the linear regression. Hence, the characterisation of $\zeta(q)$ over different moments order q enables to determinate the scaling behaviour of the flux (e.g., Calif & Schmitt, 2014). Mono-scaling (or monofractal) processes are described by a linear relation $\zeta(q) = qH$. By contrast, the $\zeta(q)$ deviation of the linear trend indicates intermittent multifractal fluctuations (introduced in Section 4.2), where $\zeta(q)$ is no longer linear, but concave.

4.1.1 The intermittency and Refined Similarity Hypothesis

Despite K41 demonstrated its utility under homogeneous and isotropic turbulence conditions, deeper studies have shown the limits of these scaling laws. The intermittency of turbulent fluxes is characteristic of strong fluctuations at all scales.

Hence, the mean value energy dissipation rate is not constant and K41 approximation appears to be insufficient to fully characterise the turbulence.

This variability motivated Kolmogorov (1962) and Obukhov (1962) to purpose a new theory that considers the intermittency of nonlinear dynamical systems. This theory known as K62 considers the structure function of velocity increments is a function of locally averaged energy flux density over a volume of linear dimension r (ϵ_r). In addition, the energy dissipation rate ϵ_r follows a lognormal distribution, with the variance σ_r^2 of $log(\epsilon_r)$ given by:

$$\sigma_r^2 = B + \mu\, log(L/r) \tag{4.5}$$

where, B is a constant associated to the macrostructure of the flux, μ is a universal constant, and L the largest external scale, while $\lambda = L/r$ defines the ratio of scales. The equality in probabilities (denoted here by $' =^p '$) can be written as follows:

$$\langle|\Delta u|\rangle =^p \langle\epsilon_r^{q/3}\rangle\, r^{q/3} \tag{4.6}$$

This law is known as the Refined Similarity Hypothesis (RSH) of Kolmogorov. By considering $\zeta(3) = 1$ from the Eq. (4.3), while the non-linearity of the scaling exponent function is given by the non-linearity of the scaling moment function $K(q)$:

$$\zeta(q) = qH - K\left(\frac{q}{3}\right) = \frac{q}{3} - \frac{\mu}{2}\left(\left(\frac{q}{3}\right)^2 - \frac{q}{3}\right) = \frac{q}{3} - \frac{\mu}{18}(q^2 - 3q) \tag{4.7}$$

Yaglom (1966) proposed the first model of nonlinear dynamical system, the lognormal multiplicative cascade model, capable to better understand the effect of intermittency and to reproduce its lognormal statistics in accordance with K62.

Schertzer & Lovejoy (1987) developed the Universal Multifractal (UM) framework to widely generalise the concept of multiplicative cascades (see more details in Section 4.2.3). The UM framework covers the full spectrum of intermittent processes, with the scaling moment function $K(q)$, that for the conservative fields depends on only two parameters. One of them is the non-linearity/multifractality parameter $\alpha \in [0 : 2]$. The bounding value $\alpha = 0$ corresponds to the case of monofractal β −model, while the multifractality parameter $\alpha = 2$ corresponds to the lognormal model. All intermediate

α values englobe the multiplicative Lévy processes resulting in a very reach variety of intermittency, as highlighted by behavioural distinctions of the corresponding extremes.

4.2 Self-similarity extension: from fractal sets to multifractals

Based on the fractal geometry, Parisi & Frisch (1985) coined the term "multifractal" to explain the nonlinearity of the scaling exponent function.

To give an example, by considering a turbulent velocity field u on a d-dimensional space S, the points $u(r)$ of the velocity field have a singular behaviour of the order $h > 0$ at the point x if:

$$\lim_{r \to 0} \frac{u(x+r) - u(x)}{r^h} \neq 0 \tag{4.8}$$

This leads to say that:

$$\Delta u \approx r^{-h} \tag{4.9}$$

In this way, $S(h)$ is the set of points for which the field has a singularity of order h, called the "Hölder" exponent, or singularity strength. Hence $S(h) \subset S$, and the set $S(h)$ has a fractal dimension D_h. Thus, multiplicative singularities $\gamma = \log(\epsilon_\lambda) / \log(\lambda)$ are associated with fractal sets having different dimensions D_h, which leads to say that $u(r)$ is multifractal (see more details in Lovejoy & Schertzer, 2013).

From the definition of fractal dimension and box-counting, D_h is nonnegative and its link with the multifractal codimension function $c(\gamma)$ bounded by d (Schertzer & Lovejoy, 1987) was found:

$$c(\gamma) = d - D_h \tag{4.10}$$

Hence, the events with low occurrence have a dimension of 0 and those with more frequency fill the space, the $0 \leq c(\gamma) \leq d$.

4.2.1 Statistical properties of multifractal fields

The statistical properties of a multifractal field ϵ_λ at a given resolution λ are defined by two scaling laws (Lovejoy & Schertzer, 2013; Schertzer & Lovejoy, 1987, 1991): the probability distribution of the (energy) flux density ϵ_λ and the statistical moments, involving the codimension function $c(\gamma)$ and the scaling moment function $K(q)$, respectively.

The probability that ϵ_λ exits a given scaling singularity threshold λ^γ, is described by the relation:

$$P(\epsilon_\lambda \geq \lambda^\gamma) \approx \lambda^{-c(\gamma)} \tag{4.11}$$

As before, the resolution $\lambda = L/r$ is defined as the scale ratio between the outer scale L and the scale of observation r, ϵ_λ being the renormalized intensity of the field.

Via the Mellin transform, Schertzer & Lovejoy (1987) demonstrated that the description of the stochastic multifractal field ϵ_λ by the codimension function of Eq. (4.11) is equivalent to the one by scaling moment function $K(q)$:

$$\langle \epsilon_\lambda^q \rangle \approx \lambda^{K(q)} \tag{4.12}$$

where, q is the statistical moments order and $\langle \epsilon_\lambda^q \rangle$ is the mean of the q^{th} moment intensity at the scale ratio λ.

4.2.2 Legendre Transform

The local scale-invariance approach of Parisi & Frisch (1985), , which was further adopted by Halsey et al (1986) to the "geometric attractor" multifractals, has been then fully reoriented within the UM framework to co-dimensions instead of fractal dimensions, to avoid the use of ill-defined negative statistical moments. Then, the statistical moments as well as the probability distribution of singularities are indeed equivalent through the involutive Legendre Transform between $c(\gamma)$ and $K(q)$ (Schertzer & Lovejoy, 1987):

$$K(q) = \max_{\gamma}\big(q\gamma - c(\gamma)\big) = q\gamma - c(\gamma)$$
$$c(\gamma) = \max_{q}(q\gamma - K(q)) = q\gamma - K(q) \qquad (4.13)$$

$c(\gamma)$ and $K(q)$ functions are convex (see Figure 4.1) and differentiable, Eq. (4.13) becomes:

$$K(q) = q\gamma - c(\gamma);\ q = c'(\gamma) = \frac{dc(\gamma)}{d\gamma}$$
$$c(\gamma) = \ q\gamma - K(q); \gamma = K'(q) = \frac{dK(q)}{dq} \qquad (4.14)$$

These relations demonstrate every moment of order q is related to only one singularity γ. Because of the conservation of flux from one scale to another, implies for $q = 1$:

$$K(1) = 0 \ and \ C_1 = K'(1) \rightarrow \ C_1 = \gamma_1 = c(\gamma_1) \qquad (4.15)$$

C_1 is the "co-dimension of the mean" and it represents a characterisation of the variability near the mean.

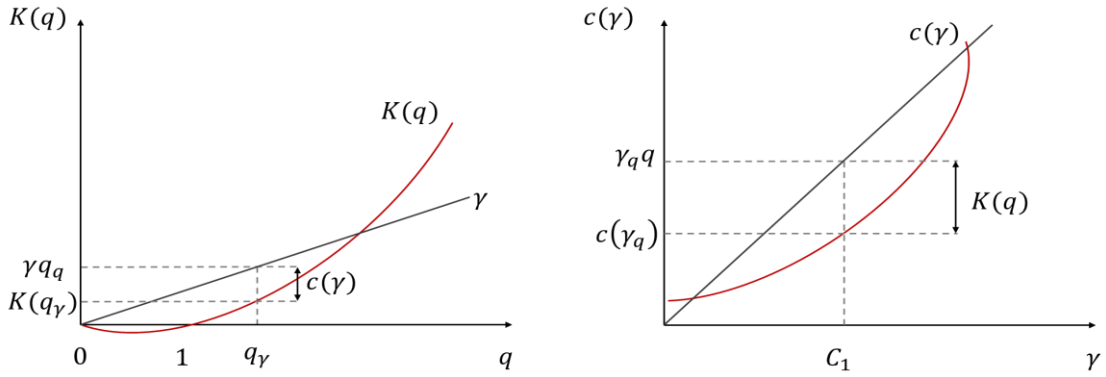

Figure 4.1. Legendre transform between $c(\gamma)$ and $K(q)$ functions. Adapted from Lovejoy & Schertzer (2013).

4.2.3 *Universal Multifractals (UM)*

As previously demonstrated, because of convexity of $c(\gamma)$ and $K(q)$, both functions depend on an infinity of parameters. Nevertheless, through a multiplicative central limit theorem, Schertzer & Lovejoy (1987) proposed the Universal Multifractal model, for which only few parameters are necessary to characterise $c(\gamma)$ and $K(q)$:

$$K(q) + Hq = \begin{cases} \frac{C_1}{\alpha - 1}(q^{\alpha} - q) & \alpha \neq 1 \\ C_1 q ln q & \alpha = 1 \end{cases} \tag{4.16}$$

$$c(\gamma) = \begin{cases} C_1 \left(\frac{\gamma + H}{C_1 \alpha'} + \frac{1}{\alpha} \right)^{\alpha'} & \alpha \neq 1 \\ C_1 \, exp\left(\frac{\gamma + H}{C_1} - 1 \right) & \alpha = 1 \end{cases} \tag{4.17}$$

where $\frac{1}{\alpha} + \frac{1}{\alpha'} = 1$ with α, C_1 and H being the three basic universal multifractal parameters:

- The mean singularity C_1 measures the clustering of the mean intensity (i.e., the fractality/sparseness of the mean field), and at the same time it corresponds to the codimension of the mean field:

  $$c(C_1 - H) = C_1 \tag{4.18}$$

  Note that for $C_1 = 0$ the field is homogeneous, and for greater values of C_1 field becomes sparser and sparser.

- The Lévy index α, which indicates the extent of multifractality. This measures the mean intermittency evolves when considering higher singularities. The values of α varies between 0 and 2, where $\alpha = 0$ is the characteristic of monofractal fields, and $\alpha = 2$ is the characteristic of maximal occurrence of extremes (log-normal fields).

- The Hurst exponent H, that measure the degree of non-conservation of the mean field (for a conservative field $H = 0$):

  $$\langle \epsilon_{\lambda} \rangle = \lambda^{-H} \tag{4.19}$$

To explore the scaling behaviour of the field and to determinate the values of the universal multifractal parameters, the Trace Moment (TM) and Double Trace Moment (DTM) techniques based on the function $K(q)$ are generally used.

4.2.4 *Trace Moments (TM)*

The Trace Moment technique allows to calculate the function $K(q)$ by means of the scale invariance moments of order q of the conservative field ϵ_λ (Schertzer & Lovejoy, 1987):

$$\langle \epsilon_\lambda^q \rangle \approx \lambda^{K(q)} \tag{4.20}$$

where $\langle \epsilon_\lambda^q \rangle$ is the q^{th} moment mean of the intensities at the scale resolution λ and $\approx$ denotes the asymptotic equivalence. The function $K(q)$ is convex and it characterises the scaling invariance of the field (multifractal behaviour), showing the asymptotic behaviour of moment of order q.

To apply the TM method, the field should be normalised so that:

$$\langle \epsilon_\lambda \rangle \equiv 1 \tag{4.21}$$

The normalised temporal data series could be also sub-divided into non-overlapping samples of a given length that will define the outer scale and in turn a certain effective resolution λ. At each resolution λ, the sample is up scaled independently and the moment of order q is calculated ϵ_λ^q. Then, the q^{th} moment average is calculated over all resolutions $\langle \epsilon_\lambda^q \rangle$, as follows:

$$\langle \epsilon_\lambda^q \rangle = \frac{\sum \epsilon_\lambda^q}{\lambda^D} \tag{4.22}$$

The scaling behaviour of the field can be then validated as a function λ, by plotting the logarithm of $\langle \epsilon_\lambda^q \rangle$ versus the logarithm of λ for different q values. The slopes of the linear regressions correspond to the estimations of $K(q)$, and the value of r^2 is used to validate the accuracy of the straight-line fit. Then, the different $K(q)$ values and the associated q allows the estimation of the empirical $K(q)$ function.

Then, the UM parameters C_1 and α can be estimated using the $K(q)$ properties of the empirical curve, by estimating the first two derivates of $K(q)$:

$$C_1 = K'(1)$$
$$\alpha = C_1/K''(1) \tag{4.23}$$

The appearance of the $K(q)$ function specifies the type of scaling it involves: a straight line implies a monofractal structure whereas a convex curve implies a multifractal structure.

4.2.5 Double Trace Moments (DTM)

This technique is a direct method to obtain UM parameters, for a conservative multifractal field ϵ_λ. DTM generalise the TM technique based on the introduction of an additional exponent η. Hence, this method consists of performing a TM analysis on a renormalised η-power of ϵ_λ.

For this purpose, firstly the field must be normalised, by arising the initial conservative field to the power η at the highest resolution and then normalising it by the mean, in the following way:

$$\epsilon_\lambda{}^{(\eta)} = \frac{\epsilon_\lambda{}^{\eta}}{\langle \epsilon_\lambda{}^{\eta} \rangle} \tag{4.24}$$

Then, the average statistical moments $\langle \epsilon_\lambda^{(\eta)q} \rangle$ also scales with the resolution λ:

$$\langle \epsilon_\lambda^{(\eta)q} \rangle \approx \lambda^{K(q,\eta)} \tag{4.25}$$

In this manner, the original field ϵ_λ is transformed into $\epsilon_\lambda{}^{\eta}$ and the function $K(q)$ into $K(q,\eta)$. Then, the q^{th} order moments of the renormalised field remain scale invariant:

$$\langle \epsilon_\lambda^{(\eta)q} \rangle \approx \lambda^{K(q,\eta)} \Rightarrow \left\langle \frac{\epsilon_\lambda{}^{\eta q}}{\langle \epsilon_\lambda{}^{\eta} \rangle^q} \right\rangle \approx \frac{\lambda^{K(q\eta)}}{\lambda^{qK(\eta)}} = \lambda^{K(q\eta)-qK(\eta)}$$
$$K(q,\eta) = K(q\eta) - qK(\eta) \tag{4.26}$$

When $\eta = 1$, $K(q,\eta)$ is reduced to $K(q)$. The expression above can be solved from the universality of the $K(q)$ function:

$$K(q,\eta) = \eta^{\alpha} K(q) \tag{4.27}$$

With this expression, UM parameters can be directly estimated. In a log-log plot, $K(q,\eta)$ is plotted as a function of η, for a fixed value of q. The diagram allows to estimate α as the slope of the linear part of $K(q,\eta)$ around $\eta = 1$, and the intercept with the vertical axis is used to determinate the parameter C_1.

A divergence of empirical functions of $K(q)$, deduced from the slope of $\langle \epsilon_\lambda^q \rangle$ and λ in logarithmic scale for different q values, and theoretical functions from the UM parameters with TM and DTM methods can occur. Then, after a given value of q the theoretical function of $K(q)$ becomes linear, leading to a departure from the UM behaviour. This phenomenon is known as the multifractal phase transitions (Lavallée et al., 1991; Schertzer & Lovejoy, 1989), and it could be caused by the critical moment order of divergence q_D and/or the undersampling q_s. According to Lavallée et al. (1991), in the case of one-dimensional field ($D = 1$) and the use of a unique sample ($N_s = 1$), which implies $D_s = \frac{\ln(N_s)}{\ln(\lambda)} = 0$, the value of q_s is given by the simplified formula:

$$q_s = \left(\frac{D + D_s}{C_1}\right)^{1/\alpha} = \left(\frac{1}{C_1}\right)^{1/\alpha} \tag{4.28}$$

The critical order of divergence of moments q_D represents q value for which the extreme values of the field are dominant. Thus, the average statistical moment of order $q \geq q_D$ tends to infinity.

4.3 Scaling invariance behaviour of the BGW's thermal fluxes

In order to explore the scaling behaviour of micrometeorological measures carried out over the BGW, the scaling behaviour of the power spectra and of the structure functions are investigated.

As detailed in Chapter 2, some data collected from techniques of ET measure were not exploitable and because of the frequency of measure and/or the length of campaigns, the number of datapoints were limited (maximum of 32 data points). However, as the

application of statistical analysis requires sufficient data, a new campaign of measurements was performed with the LAS MKI and the CNR4 for a longer period. Due to irregularity of measurements with the Ch and missing values of CWS665 sensors (which is not favourable to the application of the FFT), the Ch and WB were not analysed.

4.3.1 Data set

Despite the fact that the principal interest of this research concerns the fluxes over the BGW site during summer months, particularly during UHI events, the longest campaign with the LAS MKI scintillometer was conducted during the winter months of December 2019 and January 2020 due to logistic conveniences. Hence, this could be considered as preliminary tests of the variability of thermal fluxes over the BGW site.

The LAS MKI transmitter and receiver units were mounted respectively over the roofs of the Bienvenüe and Carnot buildings, at the core of the Cité Descartes, to monitor C_n^2 variations. The CNR4 was located next to the LAS receiver, 1.5 m above the ground, to monitor radiation components and approximate the conditions of atmospheric stability. Finally, as optical LAS MKI is more sensitive to temperature fluctuations, the air temperature was monitored as well.

Figure 4.2. Plan view of beam in winter months.

The elevations (including the height of buildings) are 119.15 m and 117 m for the transmitter and the receiver, respectively. Just like the summer set-up campaign, the effective beam height was calculated through EVATION software from the elevation of units and the surface topography of the transect profile (see Figure 4.3).

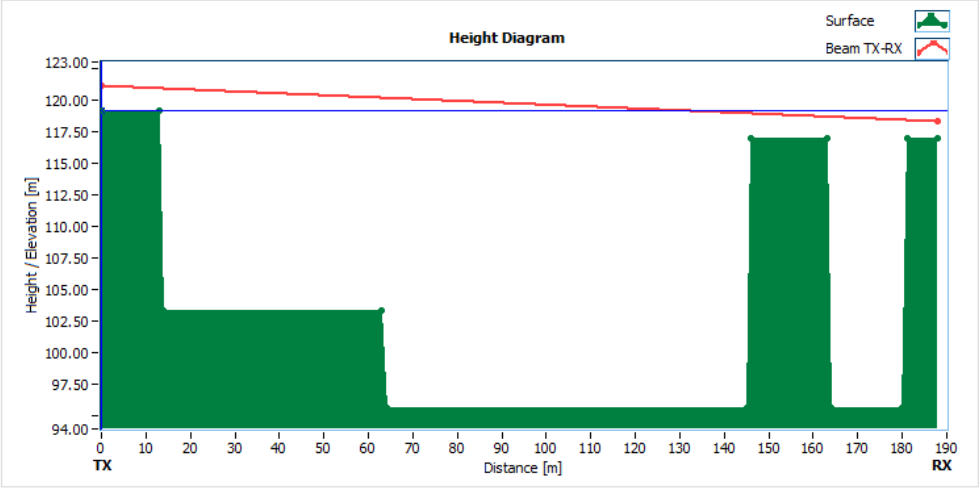

Figure 4.3. Horizontal path length and effective height of LAS during winter months.

The path length between both units was 190 m, hence diaphragms for short-range applications were necessary. The EM alignment pass over the BGW, stone floor and buildings roofs (see Figure 4.2).

Table 4.1. LAS MKI Setting Experiment on winter months.

Feature	**Value**
D [cm]	10
R [m]	190
z_{LAS} [m]	11.679
z_0 [m]	0.5
d [m]	0
z_T [m]	2
z_R [m]	1.4
Duration	2019/12/18 - 2020/01/17

The sampling frequency was 1 Hz with 10 minutes average for the LAS and 5 minutes average for the CNR4. The output LAS signals were controlled via the QC parameter as explained in the Section 2.4.2.5. The measurements represented in the Figure 4.4 shows two periods of time where the values of $Demod$ and UCn_2 exceed -50 mV and 0 V respectively:

- 2020/01/01 03:00 to 2020/01/01 19:00
- 2020/01/16 02:00 to 2020/01/16 10:30

Without these disruptions, the values of UCn_2 range between -1.5 and -2V, while $Demod$ values do not go beyond -350 mV.

Figure 4.4. LAS MKI signals: UCn_2(upper) and $Demod$ (middle) and $C_n{}^2$ calculations (bottom). The QC parameters are marked with the grey dotted line.

To understand potential causes of intensity reduction in LAS MKI measurements, the rainfall data were considered on Figure 4.5. The rainfall intensity was collected every 5 minutes by three optical disdrometers of the Fresnel Platform from HM&Co Laboratory (see more details in Gires et al., 2018), located just next to the LAS MKI receiver unit on the roof of the Carnot building. A significant event of rainfall of 30 mm/h was recorded on December 27th, which caused slight alterations on the *Demod*

signal, but that did not affect the QC parameter. The rest of the rainfall events were lightly or moderated without significant consequence on the scintillometer measure.

Regarding the atmospheric conditions during the campaign, most of the days in December were sunny and cloudy, while in January low rates of solar radiation *Sw* were more frequent. Daily fluctuations of temperature were large during cloudless days (12/29 to 01/01), ranging from 10 to 0 °C. However, there was no specific temperature variation having an impact on the LAS measurements. Hence, meteorological conditions can be discarded from LAS signal disruption.

The values of *Rn* were used to determinate the stability of the atmosphere since there are no measures of thermal gradient between the ground and the upper atmosphere. Thus, just like works of Han et al. (2019) and Kohsiek et al. (2006), measurements taken under conditions of *Rn* greater than 10 W/m² were considered as unstable atmosphere.

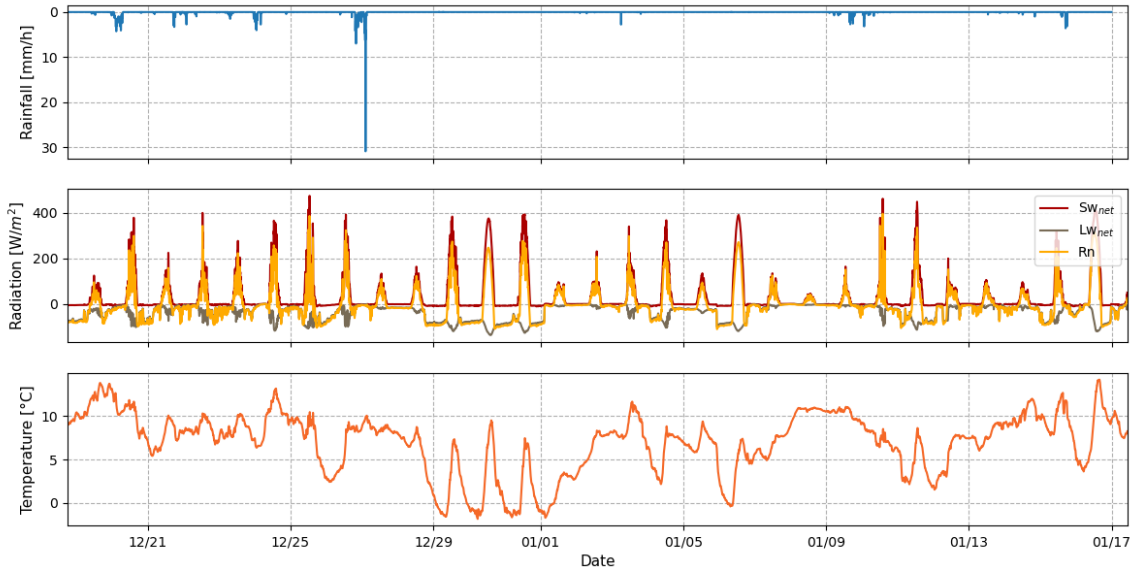

Figure 4.5. Meteorological conditions during winter months.

4.3.2 *Spectral analysis*

To avoid errors in the statistical analysis due to an inaccuracy of SEB fluxes measurements that may be transferred into Qe, as well as the uncertainties involved in the deduction of SEB parameters, the spectral analysis was applied to raw data of ${C_n}^2$ from LAS MKI, using the FFT algorithm.

The three methods to estimate ${C_n}^2$ from the output signals of LAS, discussed in Chapter 2 can be appreciated at the bottom of Figure 4.4. There is a good fit between ${C_n}^2$ from UCn_2 (green) and $PUCn_2$ (yellow) ranging around 10-14 and 10-13. Concerning ${C_n}^2$ from $\sigma^2 \ln(I)$ (red), there are more significant fluctuations producing lower (10-15) or higher (10-12) turbulence intensity compared to the other estimations of ${C_n}^2$. As in Chapter 2, ${C_n}^2$ from Eq. (2.49) and UCn_2 was used in the analysis.

The original data sets of ${C_n}^2$ in Figure 4.4 was divided into two periods (displayed in Figure 4.6) to avoid the signal disruption of January 1st, 2020 and rainfall event on December 27th, 2019. Since the computation of FFT uses sample length being power of 2, both series of ${C_n}^2$ are composed of 1024 data points, equivalent to 7 continuous days of measure.

A good linear scaling behaviour is observed for the first period in Figure 4.6.c. This scaling of ${C_n}^2$ ranges from log (f)=2.5 up to 5.5, corresponding to timescales of 14 h and 41 min, respectively. The spectral slope is 1.649, comparable to the slope 5/3~1.66 in the inertial range of isotropic and homogeneous turbulence from K41. Regarding the second period in Figure 4.6.d, a similar behaviour is observed from log (f)=3 up to 5.5, corresponding to timescales of 8.5 h and 41 min, slighted lower that the 5/3 of Kolmogorov.

The time scale of 8.5 h represented by the dotted vertical line is associated with the period of daylight time or solar forcing during a winter day. The radiation from the sun is fundamental, as it creates buoyancy heterogeneities and unstable atmospheric conditions when MOST theory is fully valid to deduce Qh. Regarding the 41 min, this

is the timescale of transition between unstable and stable atmosphere, this means the sunrise and sunset duration.

The spectral slopes of $C_n{}^2$ for both periods coincide with the assumption of Monin & Yaglom (1971) that power spectral density of turbulent fluctuations for a scalar follows the 5/3 law (see Appendix H). These results also agrees with the investigation of Maronga et al. (2013), where the power spectral density of the structure parameters of temperature $C_T{}^2$ and humidity $C_Q{}^2$ from Large Eddy Simulations in the convective boundary layer (where LAS is typically operated) followed a power law of 5/3 in the inertial range.

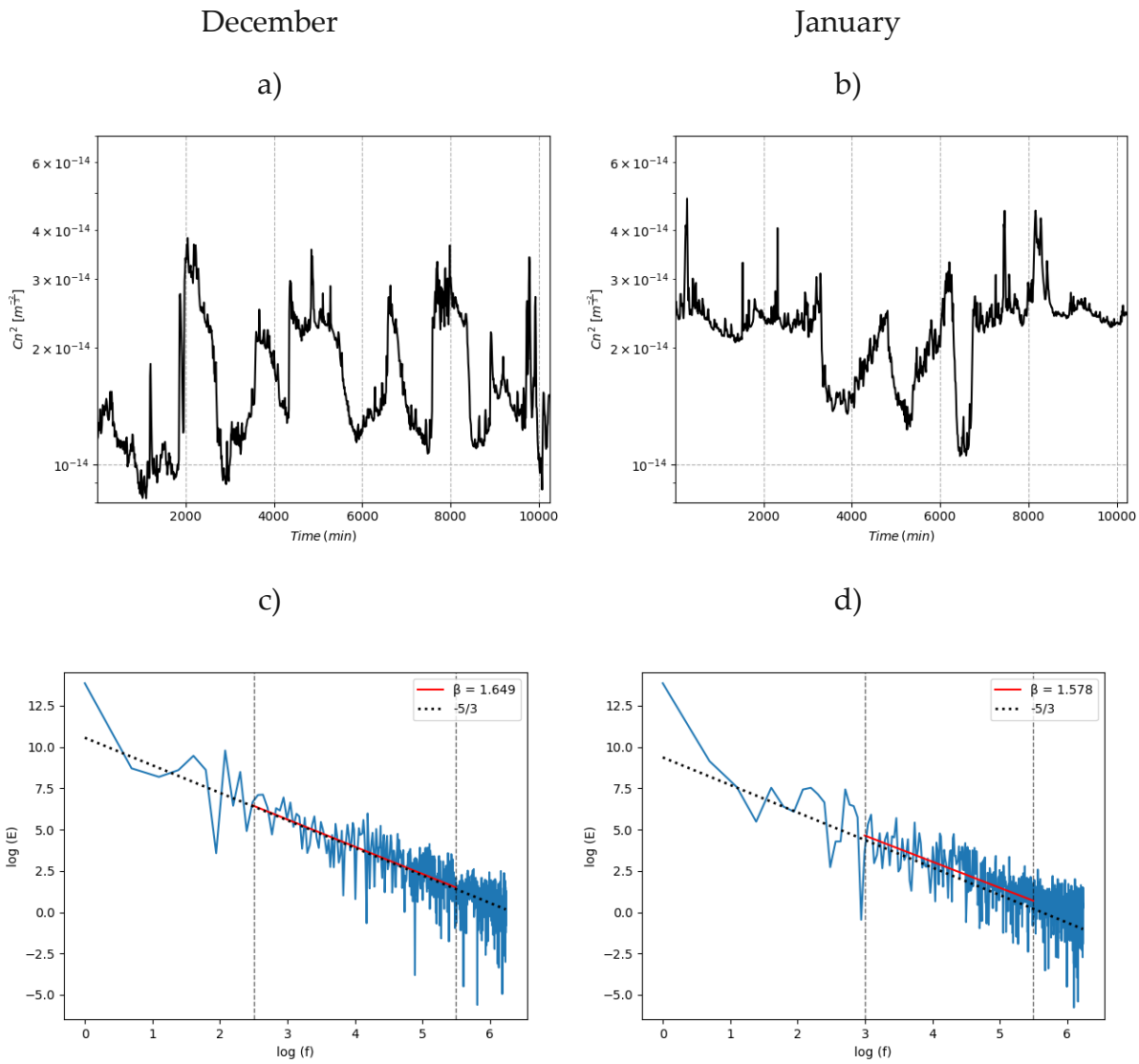

Figure 4.6. Two series of 10 minutes average of $C_n{}^2$ in December and January and their respective power spectra density.

Since the fluctuations of the refractive index are caused by eddies with different temperature and humidity in the PBL, and the LAS's wavelength is mainly sensitive to temperature fluctuations, we have performed a spectral analysis of temperature measurements from the CNR4 (bottom of Figure 4.5). The same periods of analysis that $C_n{}^2$ were considered and the size of the data sets was the double that $C_n{}^2$ as the time period of measurement was 5 min, which corresponds to 2048 data points represented in Figure 4.7.

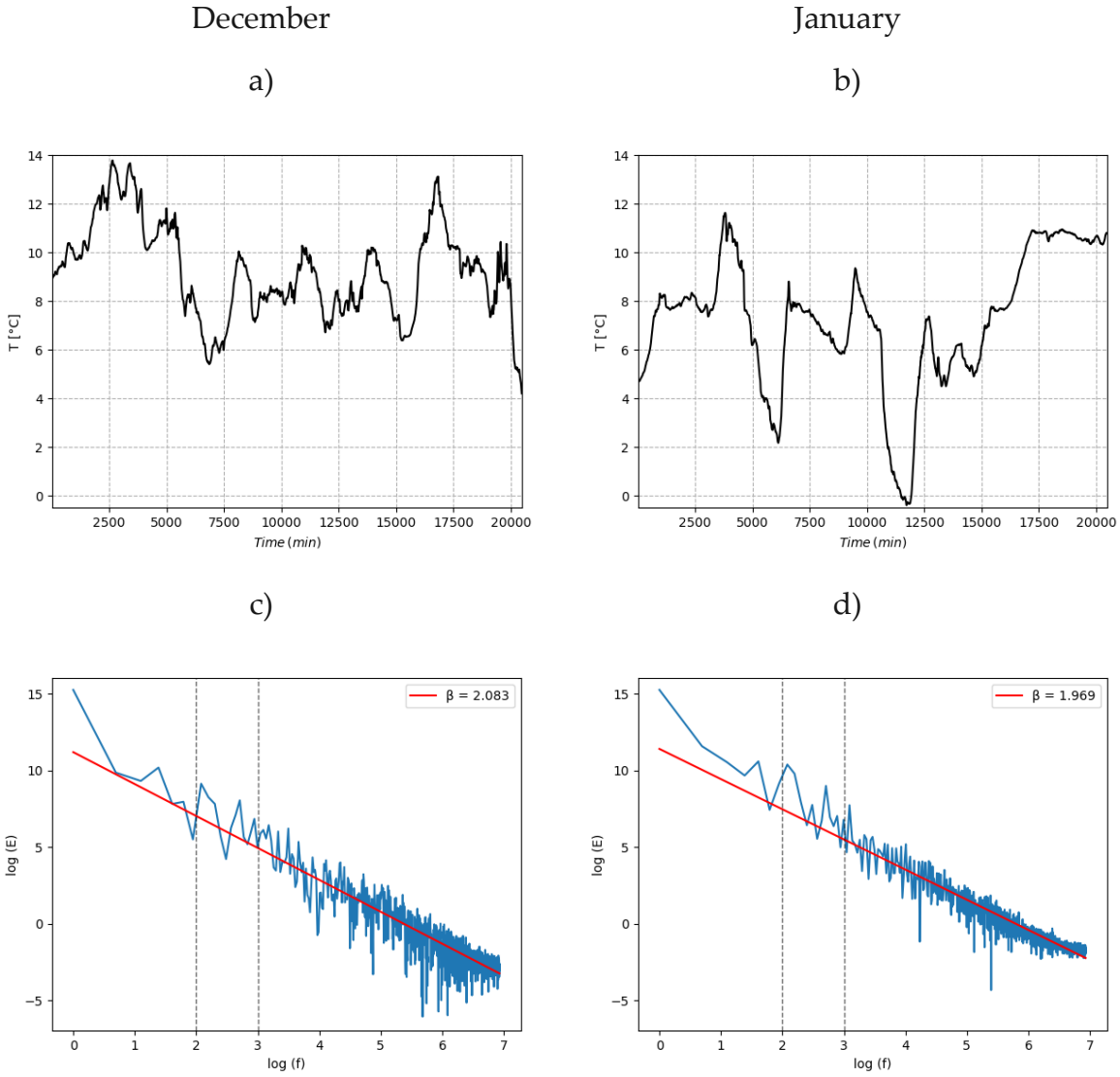

Figure 4.7. Two series of 5 minutes average of the air temperature in December and January and their respective power spectra density.

Timescales related to solar forcing are marked in the energy spectrum of temperature: 24 h of diurnal cycle and 8.5 h of solar radiation. A single scaling range is observed

after the 8.5 h up to 30 min (log (f)= 6.5). The spectral slope was 2.083 in December and 1.969 in January. This behaviour is associated with buoyancy effects and convective process in the atmosphere. In fact, these slopes are near to 11/5 scaling law predicted by Bolgiano-Oboukhov (BO) spectra, for a scaling stable stratified turbulence. Similar values of the spectral exponent were obtained when analysing the scaling behaviour of air temperature (Fitton, 2013; Karatasou & Santamouris, 2018) and water temperature in a lake (Mezemate, 2014). The flattering of spectrum of both series at highest frequencies (after 30 min), could be related to a white noise induced by an imperfect precision of measuring devices.

In conclusion, the scaling invariance of ${C_n}^2$ and temperature were verified through this spectral analysis. The spectral exponents are close to 5/3 for ${C_n}^2$ and 2 for the temperature, which indicates the fluxes are non-stationary ($\beta > 1$, the process is nonstationary). In addition, the spectral analysis proves to be a statistical tool of analysis to identify main frequencies influencing measurements, as well as potential sources of error. To fully describe the statistical properties of the fluctuations (over several order moments) and their multifractal behaviour, the structure function was calculated.

4.3.3 Structure function scaling exponent

The structure function introduced earlier allows to characterise the fluctuations of the flux, through the estimation of the scaling exponent function $\zeta(q)$ over several orders of statistical moments q. As we are dealing with time series, the structure function in Eq. (4.2) is written for time series fluctuations as $S_q(\tau) = \tau^{\zeta(q)}$.

The structure function of ${C_n}^2$ was estimated over 1024 data points, for both periods of analysis, with $600s \leq \tau \leq 6.141 \times 10^5 s$ and the statistical order moments $q = [0.1: 20]$ with increments of 0.1. Figure 4.8 shows the results of the structure function obtained of December and January, for $q = 0.5, 1, 2, 2.5$ and 3. A good scaling behaviour was observed in the range from $600s$ up to $8.5h$ for ${C_n}^2$ measurements for both periods,

being globally in agreement with the scaling analysis performed previously with the power spectra in the inertial range.

December January

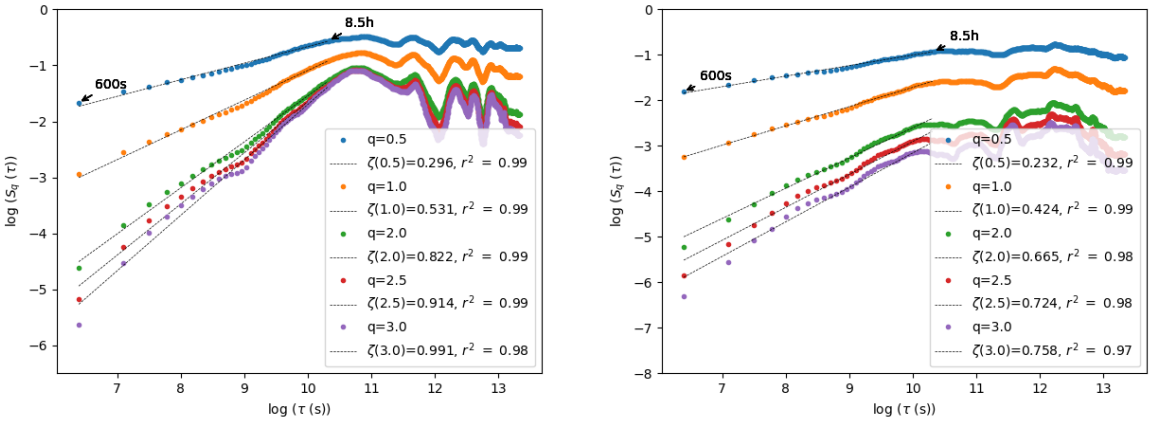

Figure 4.8. Structure function of C_n^2 increments in December and January.

The values of the scaling exponent $\zeta(q)$ were estimated from the slopes of linear regressions in Figure 4.8 and were plotted in Figure 4.9. From the relations presented in Eq. (4.3) and Eq. (4.4), the estimates of H from the structure function exponent $\zeta(q)$ and from the spectral slope exponent β were compared. The results presented in the Table 4.2 demonstrate that the values of $H_{\zeta(1)}$ from $\zeta(q)$ were higher than those obtained from the spectral exponent H_β. The discrepancy between both methods is kept for the second-order moment in both periods. The average of H was predicted from the relation of the scaling exponent $\zeta(q)$ evaluated for all the moments q through Eq. (4.3). For the period of December $H = 0.248 \pm 0.1$ and for January $H = 0.139 \pm 0.1$.

Table 4.2. $\zeta(q)$ estimates of C_n^2 following K41.

$\boldsymbol{\zeta(q) = qH}$	**December**	**January**
$H_{\zeta(1)} = \zeta(1)$	0.51	0.424
$H_\beta = (\beta - 1)/2$	0.324	0.289
$\zeta(2)$	0.822	0.665
$\zeta(2)_\beta = \beta - 1$	0.649	0.578
H	0.248±0.1	0.139±0.1

The non-linearity and concavity of $\zeta(q)$ in Figure 4.9 is undisputable for both periods, and it is given by the non-linearity of $K(q)$. This indicates the multifractal nature of the structure parameter ${C_n}^2$. These results agree with the research of Pérez et al., (2014), which showed fractal dimension of surface patterns of a wavefront, measured through the box counting dimension, is not unique and it changed as convective turbulence is developed. Hence, fluctuations of ${C_n}^2$ from the BGW are not monofractal but multifractal. The linearity over the higher moments corresponds hence to the multifractal phase transitions, as discussed in section 4.2.5.

December January

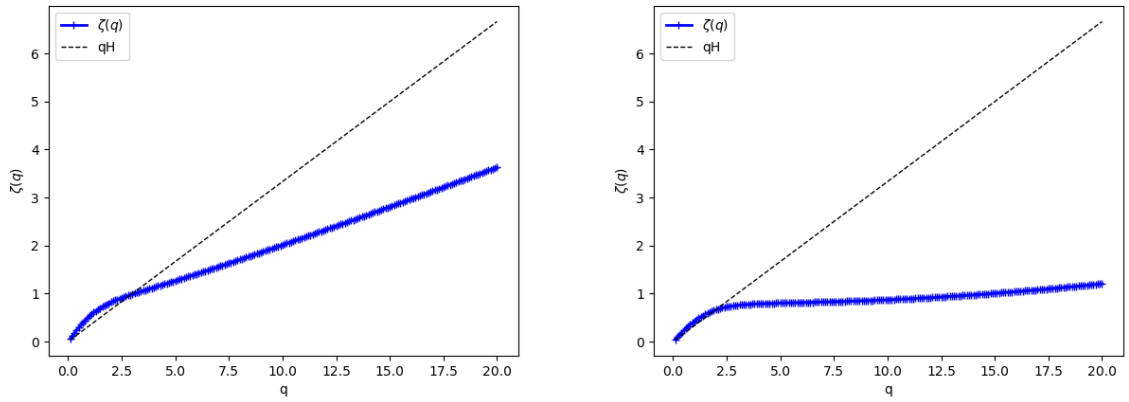

Figure 4.9. Scaling exponent $\zeta(q)$ of ${C_n}^2$ increments in December and January. The dotted line corresponds to the structure function with $H = 1/3$ for linear model of turbulence K41.

As ${C_n}^2$, the structure function of temperature series was evaluated, with 2048 data points, for the statistical order moments $q = [0.1: 20]$ with increments of 0.1 and for each 300s interval, $300s \leq \tau \leq 6.141 \times 10^5 s$. Figure 4.10 plots the straight lines of the linear regression, which indicates the scaling is well respected over the range of time from $300s$ up to $8.5h$. This behaviour is expected to be associated with the buoyancy effects and convective processes in the atmosphere.

December January

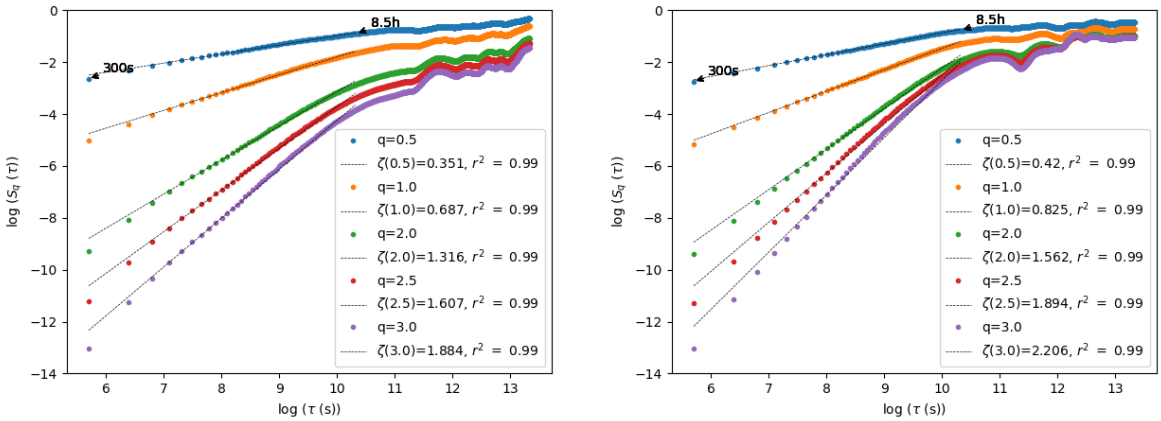

Figure 4.10. Structure function of temperature increments in December and January.

The empirical scaling exponent of the temperature for both periods of measurements, estimated from the slopes in Figure 4.10, is shown in Figure 4.11. In comparison with the monofractal process from the classical BO theory of buoyancy-driven turbulence, it is demonstrated the deviation of $\zeta(q)$ and the intermittent character of the temperature. For December period, the estimates of H from the spectral exponent β ($H_\beta = (\beta - 1)/2$) and the first-order structure function $\zeta(1)$ ($H_{\zeta(1)} = \zeta(1)$) are 0.541 and 0.674 respectively. However, for the period of January there is a larger discrepancy of the order of 0.3 between H_β and $H_{\zeta(1)}$.

December January

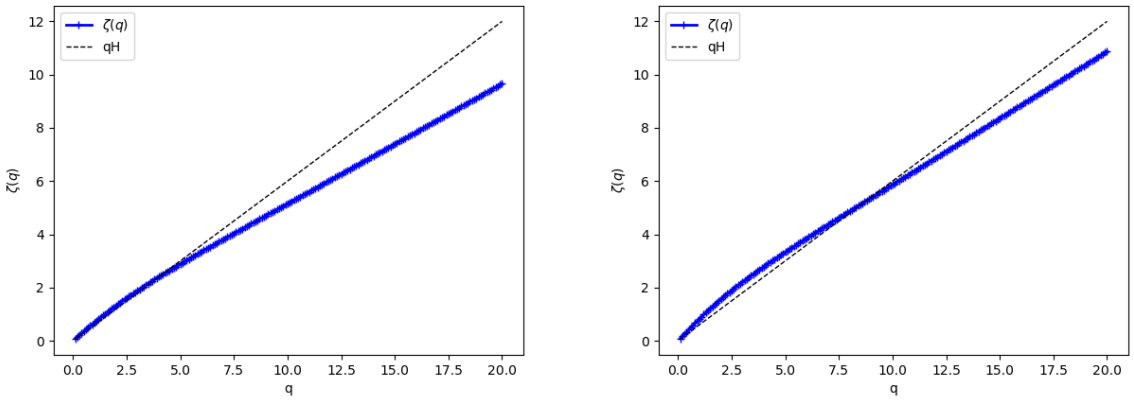

Figure 4.11. Scaling exponent $\zeta(q)$ of temperature increments in December and January. The dotted line corresponds to the structure function with $H = 3/5$ for BO theory.

From the results of the spectral analysis, one may note that the experimental data from the BGW are scaling and strongly non-conservative. In addition, the premised K41 hypothesis that the structure function follows a power law given by $\zeta(q) = qH$ and represents a (mono)-fractal behaviour, is not respected neither by ${C_n}^2$ no by air temperature. This means a unique self-similarity law does not describe the fluctuations of ${C_n}^2$ and/or temperature because of the strong intermittency, which is characterised by many (multi)fractal (co-)dimensions. Therefore, to fully characterise this non-linearity and scaling properties, the intermittency correction given by $K(q)$ should be taken into account, which will be estimated using the TM and DTM techniques in the UM framework.

4.4 Characterisation of the scale invariance properties

The TM and the DTM techniques are now applied to the experimental data from the BGW. The spectral slopes of ${C_n}^2$ and temperature, in both periods of analysis, indicate that fluctuations are non-conservative since $\beta \gg 1$. Therefore, the approach of Lavallée et al. (1993) from the absolute values of data increments was used to transform the non-conservative fields into conservative proxies (which implies to approach $H = 0$). This method was successfully applied by Stanic, (2020), to characterise UM parameters of spatial and temporal variability of the water balance components of the BGW: soil water content and drained discharge, while the data of rainfall was analysed directly as is.

The statistical moments $\langle \epsilon_\lambda^q \rangle$ of ${C_n}^2$ fluctuations, were evaluated for different values of $q = [0.05, 3]$, for a series length of 1024 data points. Then, we processed to display the scaling of statistical moments at the top of Figure 4.12. The fluctuations of ${C_n}^2$ shows a good scaling given by the sufficiently high values of r^2, mainly for the period of December. However, for both periods, the lowest value of r^2 is observed for $q = 0.1$.

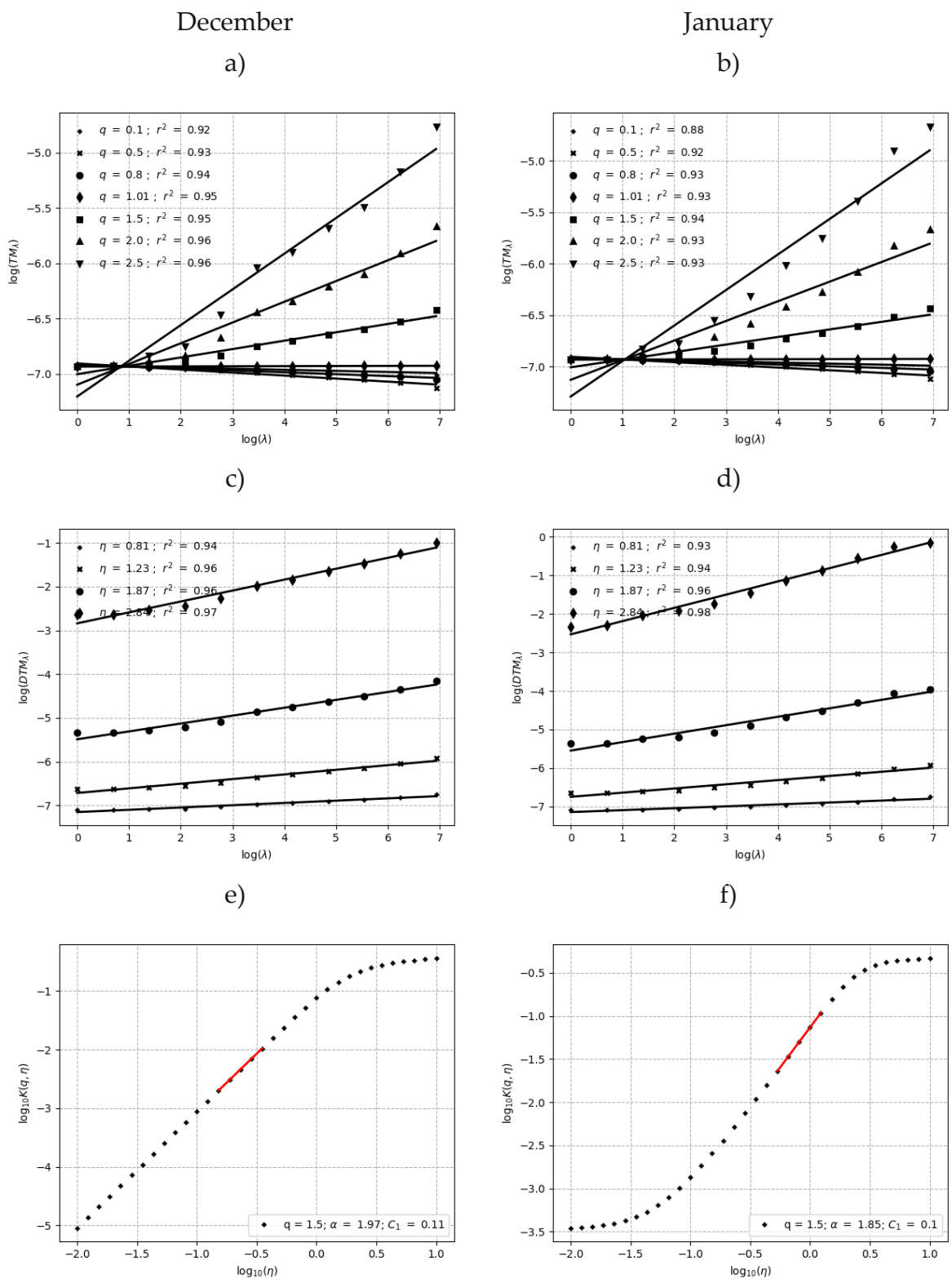

Figure 4.12. Characterisation of UM parameters on experimental $C_n{}^2$ data; a) and b) TM technique for different q values; c) and d) DTM technique with $\eta \in [0.01:10]$ and $q = 1.5$; e) and f) Statistical moment function $K(q,\eta)$ for different values of η, the red line represents the linear regression from which UM parameters are determined.

The Figure 4.12 b) and c) displays the statistical moments $\langle \epsilon_\lambda^{(\eta)q} \rangle$ as function of the resolution λ on a log-log plot, with different values of η for $q = 1.5$. The accuracy of the linear regressions for any η is higher than 0.9 (even better than for TM), which demonstrates the scaling is well respected over the full range of scales.

The slope of the linear regression $K(q, \eta)$ is obtained for every value of η and displayed on Figure 4.12 d) and e), from which α and C_1 parameters were deduced over the range of the η marked with the red line. In December, the multifractality of the order of $\alpha = 1.97$ is observed in the range $0.15 < \eta < 0.35$ (although the same estimate could be obtained at least up to $\eta = 1$), while in January the range varies to $0.53 < \eta < 1.23$ with lower $\alpha = 1.85$.

Table 4.3 presents the UM parameters (α and C_1) estimated through the TM and DTM techniques. The values of α and C_1 are similar between both periods and techniques, which suggests that the fluctuations have comparable features giving the reliable estimates. The estimates of α in both periods, demonstrate strong multifractality of ${C_n}^2$ fluctuations, as α is nearly reaches its maximum 2 (with both techniques). With regards to C_1, the estimates are not very large, which indicates mean intensity is not very sparse. Such order of C_1 values could also indicate that the obtained conservative proxies were not sufficiently close to the expected conservative fluxes.

Table 4.3. UM parameters estimates of ${C_n}^2$.

Technique	**TM**		**DTM**	
Period	α	C_1	α	C_1
December/2019	1.839	0.106	1.97	0.11
January/2020	1.879	0.10	1.85	0.10

The slopes of linear regression in Figure 4.12 a) and b) for each q, give the values of the empirical function $K(q)$. As well, based on the UM parameter estimates, a semi-theoretical function $K(q)$ can be computed. The results in Figure 4.13 shows there is a good agreement between empirical and theoretical functions for approximatively q

lower than 2.5 in December, and q lower than 3 in January. This divergence was assessed though Eq. (4.28) from the UM parameters deduced with DTM method. Thus, q_s in December and January are 3.06 and 3.43 respectively, which is close to the values in Figure 4.13.

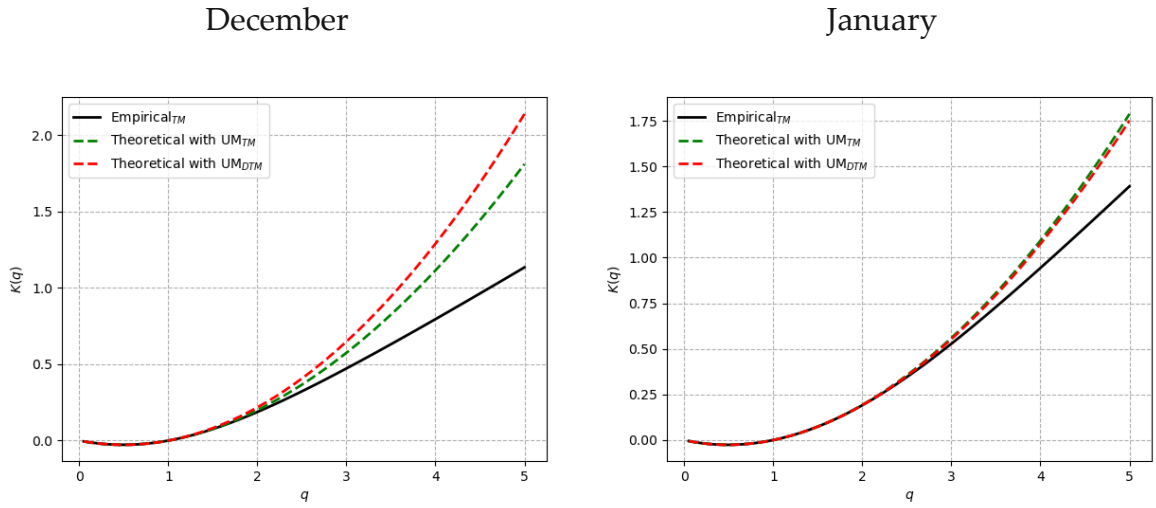

Figure 4.13. Comparison between curves of $K(q)$ of ${C_n}^2$, from the empirical value of the TM regression in Figure 4.12 a) and b), and from UM parameters and the Eq.(4.16).

The intermittency of temperature fluctuations has been estimated following the same procedure as previously established for ${C_n}^2$. The TM and DTM estimates over the whole range of scales, for December and January periods, are presented in Figure 4.14 and the UM parameters summarized in Table 4.4.

For both techniques, the accuracy of the linear regression for lower moment and particular for $q = 0.1$ is not so good compared with higher values of q. However, the scale invariance of temperature fluctuations is well observed over the full range of scales of DTM. The curves of $K(q,\eta)$ as function of η in the log-log plot, with $q = 1.5$ is presented in Figure 4.14. e) and f). The slope of the order of $\alpha = 1.6$ was evaluated in the range of η between 0.81 and 1.87 for December, and between 0.65 and 1.52 for January.

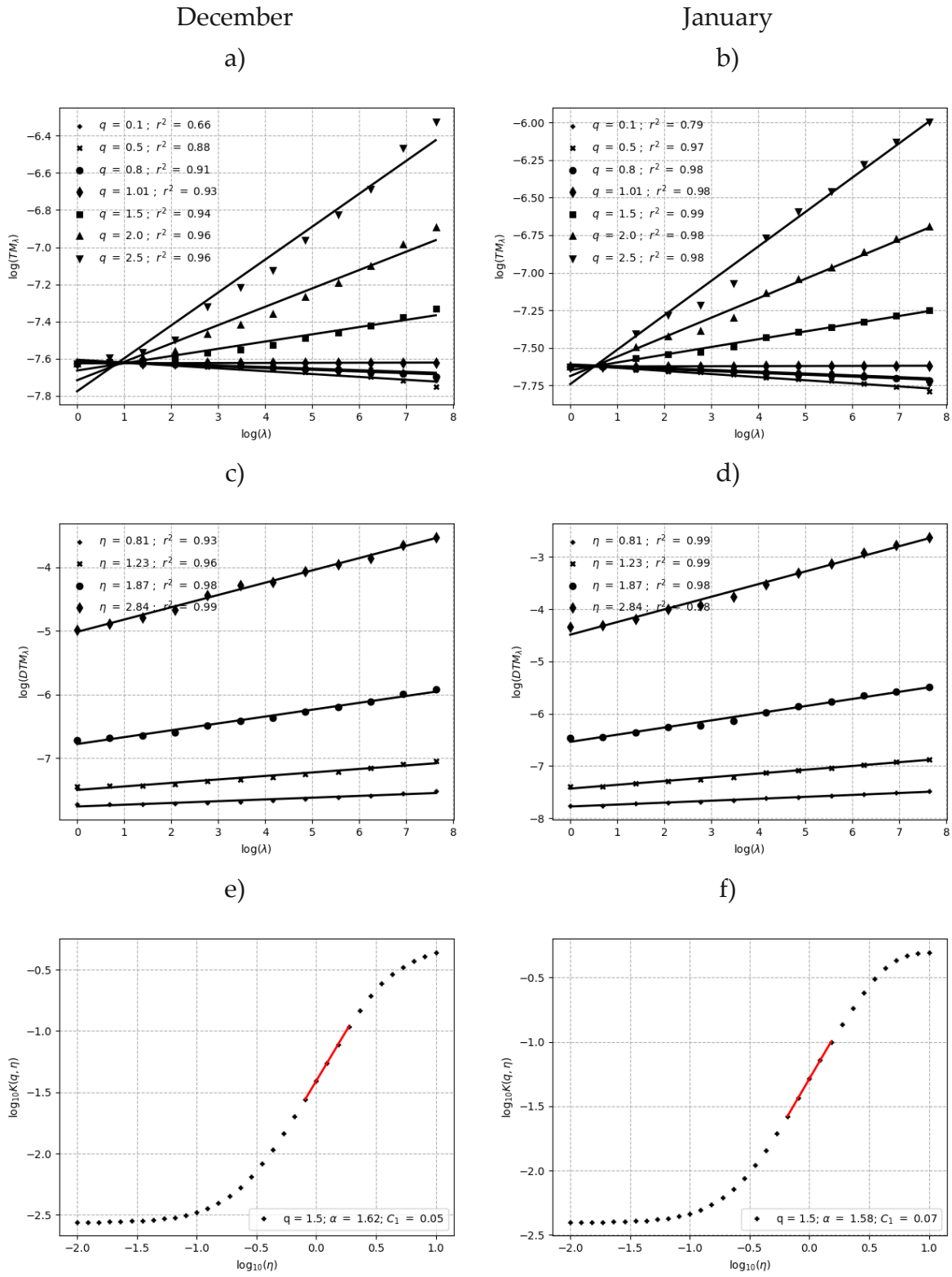

Figure 4.14. Characterisation of UM parameters on experimental temperature data; a) and b) TM technique for different q values; c) and d) DTM technique with $\eta \in [0.01,10]$ and $q = 1.5$; e) and f) Statistical moment function $K(q,\eta)$ for different values of η, the red line represents the linear regression from which UM parameters are determined.

Table 4.4. UM parameters estimates of temperature.

Technique	**TM**		**DTM**	
Period	α	C_1	α	C_1
December/2019	1.702	0.055	1.625	0.056
January/2020	1.680	0.073	1.587	0.075

The values of α and C_1, slightly differ from those obtained with turbulent velocity measurements in the atmospheric boundary layer in Paris, $\alpha = 1.45$ and $C_1 = 0.29$ (Schmitt et al., 1993). However, the estimates of C_1 are similar to the values found by Mezemate (2014) from water temperature data measured at different depths in the Creteil lake (Paris region). C_1 varies between 0.085 and 0.016, for the nearest depth to the surface of the lake (0.5m) and the deepest (4.5 m), respectively. In addition, the multifractal analysis conducted by Bodri & Cermak (2005) for two temperature series measured in boreholes in Kamchatka Peninsula (Russia), led similar values of C_1 (0.097 and 0.098) with somewhat lower values of α (1.32 and 1.24) compared to the BGW.

December January

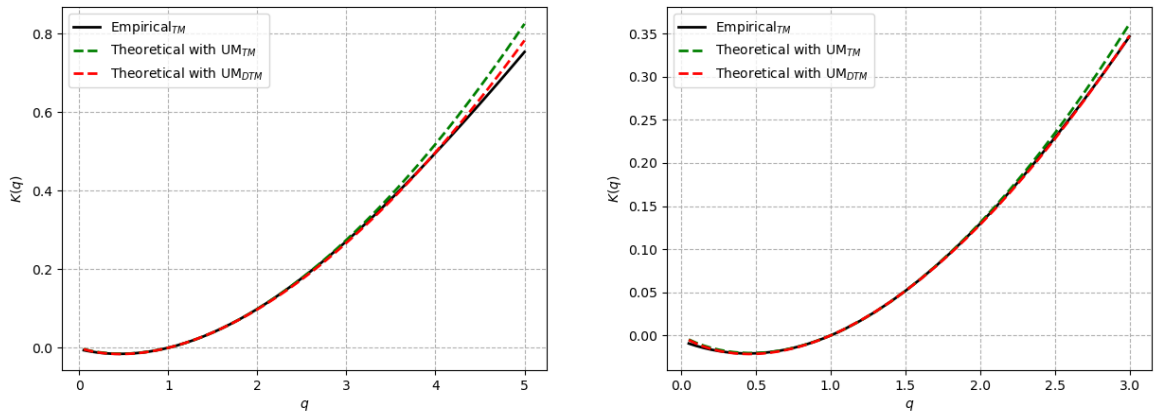

Figure 4.15. Comparison between curves of $K(q)$ of temperature, from the empirical value of the TM regression in Figure 4.12 a) and b), and from UM parameters and the Eq.(4.16).

The curves of $K(q)$ on Figure 4.15 are convex in both periods. This confirms that the temperature time fields over the BGW are multifractal. In addition, $K(q)$ functions resulting from the TM and DTM have a very good agreement with the semi-analytical

curves of $K(q)$. A slight deviation apparently occurs over $q = 4$ in December and $q = 3$ in January. According to estimation of q_s in December and January, the multifractal phase transitions are expected to occur after reaching q values of 5.86 and 5.10, respectively.

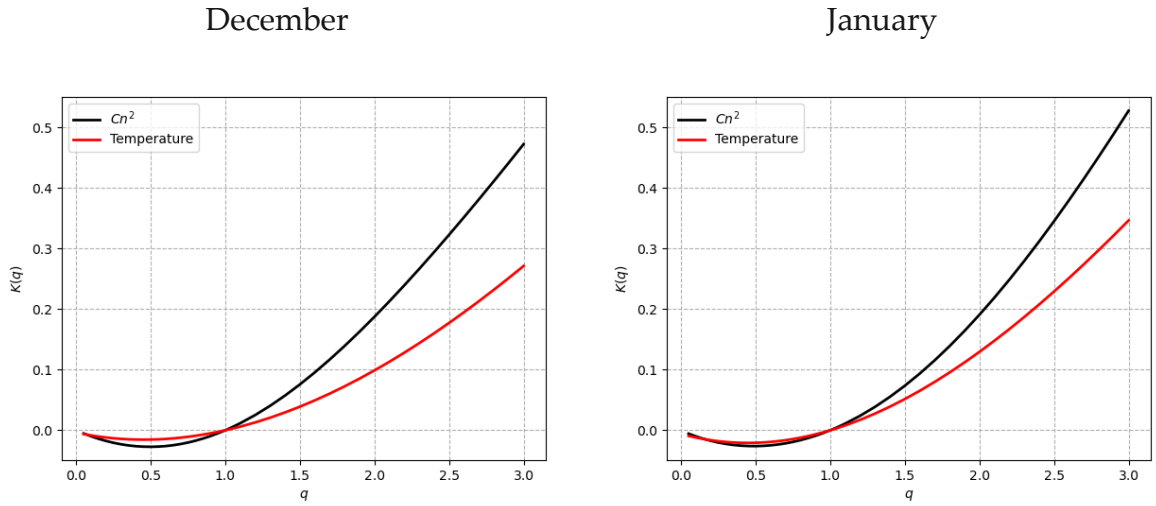

Figure 4.16. Empirical $K(q)$ functions of $C_n{}^2$ and temperature data measured in the BGW in December and January.

It appears reasonable to expect that a space-time variability of $C_n{}^2$ is close to that of the temperature as LAS MKI is mainly sensitive to temperature fluctuations in the horizontal path-length between transmitter and receiver. The empirical functions $K(q)$ of $C_n{}^2$ and temperature in December and January, displayed in Figure 4.16, partially validate this assumption, as $K(q)$ of $C_n{}^2$ during both periods is more convex than the one of temperature. It is useful to mention that this is mainly due to a decries of mean singularity values for the temperature. This may suggest $C_n{}^2$ winter measurements are the results of additional turbulent processes that have a stronger impact on the heat convection than conventionally expected. Therefore, it may be useful some additional experimentation, that includes wind speed, to better capture the physical mechanisms relating the variability of $C_n{}^2$ measured by the scintillometer LAS MKI and the temperature fluctuations at the BGW.

Although our timeseries were investigated using the universal multifractals, in section 4.2 we already mentioned the existence of several alternative multifractal formalisms.

Here we would like to briefly discuss the results of intercomparison of the UM formalism, using the singular densities (γ, $c(\gamma)$), with that proposed by Halsey et al (1986), using singular measures (a_D, $f(a_D)$).

Let us just remind here that in parallel to the development of multifractal cascades in turbulence, they were also developed for applications in chaos. Dealing with strange attractors, one deals with potentially infinite number of points, generated by a non-linear system having very small number of degrees of freedom. These points are then understood as realizations of a multifractal probability measure in the limit of the number of points tending to infinity. This probability measure is a geometric multifractal: although it represents the probability of finding the system at a point in the phase space, it is not random. Furthermore, rather than considering the density of the multifractal measure, remaining the non-random analog of the turbulent ϵ_λ, the authors considered the measure itself, integrated over a box size λ^{-1}. The order of singularity a_D remains then *D*-dependent, *D* being the dimension of the phase space. For the box counting algorithm, each box can thus be indexed according to a_D and the number of boxes at each resolution corresponding to this a_D then defines the dimension $f(a_D)$. The ensemble of $f(a_D)$ is also known as the 'singularity spectrum' or 'multifractal spectrum'.

Through the codimension function $c(\gamma)$, the singularity spectrum $f(a_D)$ can be deduced. Figure 4.17.a shows the corresponding estimates of $c(\gamma)$ in the framework of the codimension multifractal formalism, using the UM parameters and Eq. (4.17) with $D = 1$ for timeseries. Then, for each singularity $a_D = D - \gamma$ the dimension $f(a_D)$ is linked to the codimensions as $f(a_D) = D - c(\gamma)$.

The values of fractal dimension $f(a_D)$ were plotted as a function of the order of singularity a_D (Hölder exponents) for ${C_n}^2$ and temperature measured during December and January on Figure 4.17.b. On this plot of the singularity spectrum, multifractality is corroborated since for all temporal series and for both periods, a_D ranges from 0.6 up to 1.1 with $D = 1$.

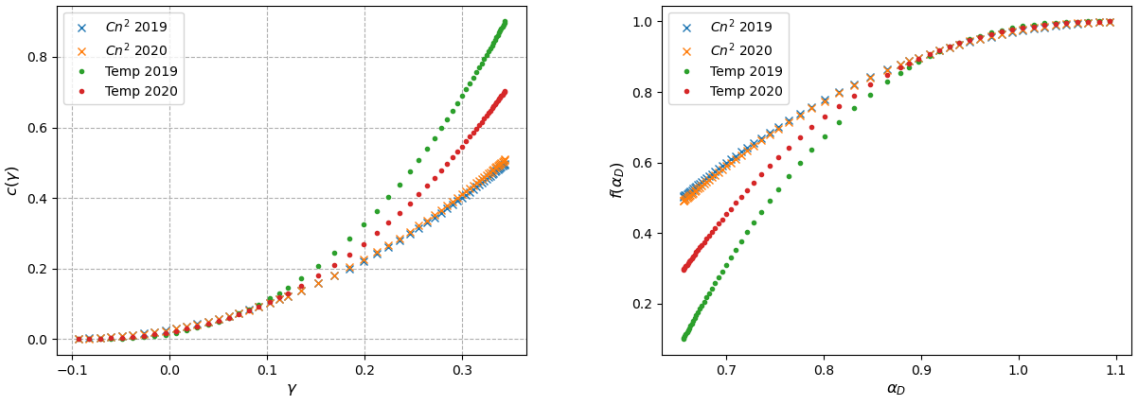

Figure 4.17. a) The codimension $c(\gamma)$ function of ${C_n}^2$ and temperature. b) Singularity spectrum, $f(a_D)$ as a function of singularities a_D.

Since the probability of exceedance is considered within the UM framework (see Eq. (4.11)), the resulting multifractal spectra are asymmetric. Indeed, the resulting spectra are left-skewed as only the fluctuations corresponding to the positive statistical moments ($q > 0$) are evaluated. Being evaluated as the difference between max and min values of singularities a_D, one observes a quite similar multifractal behaviour among the investigates data, in agreement with the UM estimates. One may note that when $f(a_D)$ converges to the dimension of the observing space, without exceeding it, the singularities of ${C_n}^2$ and temperature for both periods converge to the maximum value $a_D = 1.1$. For stochastic multifractals with probability spaces $D \to \infty$, the D-dependence represent a fundamental limitation. Similarly, the geometric framework brings unnecessary complications when looking at subspaces with dimension smaller than D. Overall, this may explain the choice of the UM framework for the multifractal analysis of the geophysical space-time fields.

4.5 Conclusions and Perspectives

In this chapter statistical tools and multifractals were used to address the scaling behaviour of measurements of scintillometry and temperature over the BGW. The

spectral analysis, as well as the scaling exponent of the parameter of refraction index of air ${C_n}^2$, demonstrated its scale invariance behaviour. The spectral analysis put on evidence a good scaling behaviour in the timescale range of 14-8h to 41 min with the slopes close to that of K41, 1.64 in December and 1.57 in January. Regarding the temperature, a linear behaviour for the whole range of scales was observed and the spectral exponent is close to that of BO (2.09 and 1.97). Although remaining close to the theoretically predicted laws, the small observed differences indicated that intermittency of these measurements should not be neglected.

More precisely, the structure function that characterises the statistical properties of the fluctuations confirmed the good scaling over timescales in between 300s and 8.5h. In addition, the strong nonlinearity of the scaling exponent function $\zeta(q)$ shows that ${C_n}^2$ and temperature fluctuations are affected by intermittency, and they are strongly multifractal ($\alpha \gg 1$).

Indeed, the UM parameters were estimated to characterise the corrections of intermittency $K(q)$. The obtained values of Lévy index α and the mean codimension C_1 demonstrates that fluctuations of ${C_n}^2 (\alpha = 1.97 - 1.85$ and $C_1 = 0.11 - 0.10$ based on DTM) and temperature ($\alpha = 1.625 - 1.587$ and $C_1 = 0.056 - 0.075$ based on DTM) measured over the BGW in both periods of analysis, are strongly multifractal. The estimates of the UM parameters of the ${C_n}^2$ and temperature remain close to those to those obtained previously for velocity and temperature measurements in the turbulent atmospheric boundary layer.

Such high values of the multifractality parameter implies that the corresponding all obtained scaling moment functions $K(q)$ are nonlinear and convex. In addition, the empirical functions $K(q)$ of ${C_n}^2$ and temperature increments do not coincide, mainly due to a significant difference in mean singularities, indicating that although ${C_n}^2$ is mainly affected by temperature fluctuations, additional geophysical fields would impact heat convection in the surrounded atmosphere of the BGW, such as wind speed. Therefore, the temporal variability of thermal fluxes in the BGW requires a further analysis with more geophysical data, such as wind speed. This would allow to

better characterise the scaling invariance as well as the statistical properties presented in this work, that in turn will help to better master the physical processes involved and their complex interactions.

Finally, through the codimension function $c(\gamma)$ and the UM parameters, the singularity spectrum of ${C_n}^2$ and temperature was characterised, to deduce the multifractality of their fluctuations, being approached this time by the difference in singularities $\alpha_{D,max} - \alpha_{D,min}$. The results confirmed the multifractal behaviour deduced by the UM framework, which is the most appropriated approach for the analysis of geophysical fields scaling properties.

Conclusions & Perspectives

This chapter summarizes the main conclusions and results of this research, and it also review the limitations noted and the perspectives of further research.

A text-mining analysis was carried out on three EU project reports on an in-depth review of services provided by NBS in urban areas to consolidate consensus on the impacts and benefits of them, readily for implementation policies. The methodology of complex systems coupled with a data visual representation allowed to convert the text of these reports (corpus) into a meaningful neural network structure. Thus, the concepts, patterns, approaches, and stakeholders involved in the NBS deployment in urban areas have been objectively identified.

In this way, it has been revealed that temperature reduction (or urban cooling) through shading and ET effects, is documented as one of the most significant ecosystem services (ESS) provided by the NBS to address the challenges created by climate change and urbanisation. In parallel, this analysis demonstrated the need to quantify the ESS through a performance indicator that will be pertinent at multiple spatial scales.

To quantify the benefit of urban cooling and the ET process on an extensive green roof (BGW), three different methods were implemented: the SEB, the evapotranspiration chamber, and the water balance. A LAS MKI with short distances diaphragms was used for the first time on a green roof, to measure the variation of ${C_n}^2$ every 10 minutes. Through MOST and additional meteorological parameters, Qh was estimated. Additionally, with a net radiometer and thermo-couples installed in the ground, additional components of SEB, Rn and Qg, were monitored to infer Qe. Due to energy closure, the accuracy of SEB components measurements had a significant impact on the final Qe estimate. Therefore, the use of meteorological and terrain variables (e.g., such as U and k), which were not specific for the BGW case study, impacted the Qe result.

The evapotranspiration chamber was considered as the reference method because it provided direct measurements of Qe, from the variation of absolute humidity for 30 seconds over 1 m² of BGW. Qe rates on the BGW varied with the net radiative energy flux and soil moisture. Low Qe values were found under conditions of direct sunlight and limited soil moisture, barely reached 13 W/m².

The estimation of ET through the WB under dry conditions was affected by the variability of soil water content measurements in the BGW and the spatial heterogeneity of soil properties where the sensors were installed, which did not provide reliable measurements of ET. Indeed, the exploitation of spot measurements of soil moisture with CWS665 sensors was conditioned to dry periods longer than 7h and k_a values higher than 1 (which corresponds to k_a of air in pores of the substrate).

The results of the three measurement methods demonstrated the complexity of quantifying the ET process, which was influenced by factors such as soil moisture, net radiative energy or temperature on the BGW. Moreover, ET estimates depended on the temporal and spatial scale of measurement, which made their comparison difficult.

The development of a new measurement campaign with a scintillometer specifically devoted for short distances, together with in situ meteorological conditions on the BGW (e.g., U, WD, P) should prove useful to characterise the causes of the overestimation of the Qe flux. Moreover, it could allow to estimate the footprint or source area of the fluxes detected by the scintillometer, as well as the impact of the undulating shape of the BGW. Furthermore, it could be also convenient to determine the influence of soil water content on the thermal properties of the BGW substrate, such as the thermal conductivity (k). Through laboratory tests, the relationship between the thermal conductivity and the soil moisture measured with the CWS665 sensors could be determined. To improve the understanding of the thermal performance of green roofs, additional monitoring campaigns should be carried out on different types of vegetation and substrate, as these can influence the ET flux.

To consider the challenges of deploying NBS at different spatial scales, an iterative downscaling spatial modelling was performed over an area located east of Paris. Fractal geometry has been used as a practical approach to analyse and model urban structures. The fractal dimension as an indicator of scale invariance has demonstrated that there is a homogeneous distribution of buildings at all scales, while NBSs are fragmented and more concentrated in certain areas of the territory. Such distribution of urban structures means that the accessibility of NBSs is not equal over the territory of Est-Ensemble. Thus, in a perspective of demographic growth by 2030, as projected by urban planning of Est-Ensemble, accessibility to NBS could deteriorate.

The deployment scenario of NBS through Fractalopolis (an open-source software based on properties of fractal geometry and conditions of territory development), represented NBS through a fractal primitive (since fractal dimension of NBS described their self-similar distribution over three scaling ranges), creating clusters of different sizes that were not strictly located over the lacunas of the fractals, but also on the existing building structures. This implies that (i) the original Fractalopolis approach has been altered since NBSs (or green spaces) are not just the lacunas of fractals, but lacunas would contain NBSs that also have fractal characteristics; and (ii) territories with limited spaces for nature and strong urbanisation pressure, may now use Fractalopolis to plan integration of new NBSs on the current urban structure, including such as green roofs on buildings.

Regarding the evaluation of the accessibility to the different types of NBS according to their frequentation by the inhabitants, the proximity distance was defined according to the three characteristic scales, i.e., changing for each of them the fractal dimension of self-similar distribution of the NBS, although termed as the ‘multiscale scenario’. The results of the classical evaluation method, which considers the average accessibilities to the different types of NBS, indicated that the distances from the centroid of urban centres were not long enough to ensure good access to the different NBSs. Nevertheless, the indicator of accessibility has increased over each of the characteristic scales when accessibility to the nearest NBS was considered. Most urban

centres had good access to the NBS at all visitation frequencies, with an exception for a daily basis.

Exploring an economic valuation of NBS installation and maintenance regarding a particular ecosystem service would make the multiscale NBS deployment scenario more suitable for city planners. Therefore, the characterisation of the scale behaviour of NBS benefit is necessary to determine the major spatial scales of NBS deployment, over which their performance is either most effective or need to be improved.

The observed spatial inhomogeneity of green space distribution further suggests the inhomogeneity (either spatial or temporal) of heat transfer processes between NBSs. It was therefore a question of evaluating the impact of the strong fluctuations of the heat flux, the most studied over time due to the limited availability of spatial data, then of extending the results to space by the hypothesis by Taylor.

A first attempt concerning the temporal variability of the temperature reduction due to the ET was carried out by using the Universal Multifractal (UM) framework. Although the Qe values appeared to be overestimated from SEB, the ${C_n}^2$ measurements were valid since they were performed under the 'saturation free' zone. Therefore, ${C_n}^2$ could be an acceptable indicator of convective turbulence over the horizontal path. Therefore, the scaling behaviour of thermal fluxes related to ET, ${C_n}^2$ and air temperature, measured on the BGW during winter months with the LAS MKI and CNR4 was confirmed though the power spectra and the structure function analysis.

The spectral slopes of ${C_n}^2$ were about ~1.6, while that of temperature were ~2. This suggests that ${C_n}^2$ followed a scaling behaviour close to that predicted by Kolmogorov for well-developed turbulence in the inertial scale (5/3), while the spectral exponent of temperature, is characteristic of the scale-stable stratified turbulence law predicted by Bolgiano-Oboukhov (11/6). The structure function was used to demonstrate the scale invariance of different order statistical moments, including non-integer moments that account for the multiplicative processes. The results indicate that the fluctuations of

the empirical BGW data are affected by intermittency and therefore cannot be determined by a single fractal dimension (as in the monofractal case) over the scaling range. Such intermittency results in multifractality.

Accordingly, the UM framework was used to characterise intermittency. The UM parameters from TM and DTM techniques confirmed that those fluctuations are strongly multifractal given $\alpha \approx 2$, and their mean singularity is not too sparse with $C_1 \approx 0.1$. In addition, the results demonstrated that variations of ${C_n}^2$ have a stronger multifractal behaviour than temperature. Therefore, a future analysis including more geophysical data would be very valuable to better understand the ensemble of physical processes inducing such intermittency of ${C_n}^2$ in green roofs.

Although the scaling analysis of heat fluxes on the BGW was carried out on time series, this analysis can be extended to the spatial variability by evoking the Taylor hypothesis. However, to perform a more rigorous analysis of the spatial variability of the ET flux of NBS, a new measurement campaign at different spatial scales is necessary. It should be planned so that the multifractal intersection theorem could be used to infer the effective impact of the fractal dimensions characterising NBS settlement on the spatial variability and scale invariance of resulting heat fluxes. Then, a new spatial modelling of the NBS deployment could be developed, based on the multifractal nature of the heat fluxes induced by NBS (see Chapter 4), while considering scale invariance of the spatial organisation of the territory, like the one developed in Chapter 3.

Thus, this research not only demonstrated the need to quantify the benefit of thermal reduction by NBS, but also characterised the ET process in a green roof. Moreover, the complexity of both, the heterogeneity of the space where NBS are deployed and the intermittency of heat fluxes, have been confirmed either by fractal geometry or by multifractal statistics. As so, this research provides new information on the main challenges regarding the quantification of the ET process, how NBS are and should be deployed in urban areas, regarding the scaling properties and the multifractality of thermal processes influencing ET.

References

Andreas, E. L. (1988). *Estimating Cn2 over snow and sea ice from meteorological data.* https://doi.org/10.1364/JOSAA.5.000481

Ayata, T., Tabares-Velasco, P. C., & Srebric, J. (2011). An investigation of sensible heat fluxes at a green roof in a laboratory setup. *Building and Environment*, *46*(9), 1851–1861. https://doi.org/10.1016/j.buildenv.2011.03.006

Bao, T., Li, X., Zhang, J., Zhang, Y., & Tian, S. (2016). Assessing the Distribution of Urban Green Spaces and its Anisotropic Cooling Distance on Urban Heat Island Pattern in Baotou, China. *ISPRS International Journal of Geo-Information*, *5*(2), 12. https://doi.org/10.3390/ijgi5020012

Bevilacqua, P., Mazzeo, D., Bruno, R., & Arcuri, N. (2016). Experimental investigation of the thermal performances of an extensive green roof in the Mediterranean area. *Energy and Buildings*, *122*, 63–79. https://doi.org/10.1016/j.enbuild.2016.03.062

Bodri, L., & Cermak, V. (2005). Multifractal analysis of temperature time series: Data from boreholes in kamchatka. *Fractals*, *13*(04), 299–310. https://doi.org/10.1142/S0218348X05002957

Borsdorf, A., & Zembri, P. (2004). *European cities insights on outskirts: Structures*.

Bouda, M., Caplan, J. S., & Saiers, J. E. (2016). Box-Counting Dimension Revisited: Presenting an Efficient Method of Minimizing Quantization Error and an

Assessment of the Self-Similarity of Structural Root Systems. *Frontiers in Plant Science*, *7*. https://doi.org/10.3389/fpls.2016.00149

Bozovic, R., Maksimovic, C., Mijic, A., Smith, K. M., Suter, I., & van Reeuwijk, M. (2017). *A Systems Approach to Sustainable, Resilient and Cost-Efficient Urban Development* [Technical Report]. Imperial College London. https://www.climate-kic.org/wp-content/uploads/2017/10/BGD-Guide.compressed.pdf

Brander, L. M., & Koetse, M. J. (2011). The value of urban open space: Meta-analyses of contingent valuation and hedonic pricing results. *Journal of Environmental Management*, *92*(10), 2763–2773. https://doi.org/10.1016/j.jenvman.2011.06.019

Brown, P. (2014). Basics of Evaporation and Evapotranspiration. *College of Agriculture and Life Sciences (The University of Arizona)*.

Bush, J., & Doyon, A. (2019). Building urban resilience with nature-based solutions: How can urban planning contribute? *Cities*, *95*, 102483. https://doi.org/10.1016/j.cities.2019.102483

Calif, R., & Schmitt, F. G. (2014). Multiscaling and joint multiscaling description of the atmospheric wind speed and the aggregate power output from a wind farm. *Nonlinear Processes in Geophysics*, *21*(2), 379–392. https://doi.org/10.5194/npg-21-379-2014

Cascone, S., Catania, F., Gagliano, A., & Sciuto, G. (2018). A comprehensive study on green roof performance for retrofitting existing buildings. *Building and Environment*, *136*, 227–239. https://doi.org/10.1016/j.buildenv.2018.03.052

Cascone, S., Coma, J., Gagliano, A., & Pérez, G. (2018). The evapotranspiration process in green roofs: A review. *Building and Environment*. https://doi.org/10.1016/j.buildenv.2018.10.024

Chavalarias, D., & Delanoe, A. (2017). *Gargantex* (Blue Jasmine Version) [Computer software]. https://gargantext.org/

Chen, Y. (2011). Fractal systems of central places based on intermittency of space-filling. *Chaos, Solitons & Fractals*, *44*(8), 619–632. https://doi.org/10.1016/j.chaos.2011.05.016

Cirkel, D. G., Voortman, B. R., Van Veen, T., & Bartholomeus, R. P. (2018). Evaporation from (Blue-)Green Roofs: Assessing the Benefits of a Storage and Capillary Irrigation System Based on Measurements and Modeling. *Water*, *10*(9), 1253. https://doi.org/10.3390/w10091253

Cohard, J.-M., Rosant, J.-M., Rodriguez, F., Andrieu, H., Mestayer, P. G., & Guillevic, P. (2018). Energy and water budgets of asphalt concrete pavement under simulated rain events. *Urban Climate*, *24*, 675–691. https://doi.org/10.1016/j.uclim.2017.08.009

Cohen-Shacham, E., Andrade, A., Dalton, J., Dudley, N., Jones, M., Kumar, C., Maginnis, S., Maynard, S., Nelson, C. R., Renaud, F. G., Welling, R., & Walters, G. (2019). Core principles for successfully implementing and upscaling Nature-based Solutions. *Environmental Science & Policy*, *98*, 20–29. https://doi.org/10.1016/j.envsci.2019.04.014

Corrsin, S. (1951). On the Spectrum of Isotropic Temperature Fluctuations in an Isotropic Turbulence. *Journal of Applied Physics*, *22*(4), 469–473. https://doi.org/10.1063/1.1699986

Coutts, A. M., Daly, E., Beringer, J., & Tapper, N. J. (2013). Assessing practical measures to reduce urban heat: Green and cool roofs. *Building and Environment*, *70*, 266–276. https://doi.org/10.1016/j.buildenv.2013.08.021

Crawford, B., Grimmond, C. S. B., Ward, H. C., Morrison, W., & Kotthaus, S. (2017). Spatial and temporal patterns of surface–atmosphere energy exchange in a dense urban environment using scintillometry. *Quarterly Journal of the Royal Meteorological Society*, *143*(703), 817–833. https://doi.org/10.1002/qj.2967

Czembrowski, P., & Kronenberg, J. (2016). Hedonic pricing and different urban green space types and sizes: Insights into the discussion on valuing ecosystem services. *Landscape and Urban Planning*, *146*, 11–19. https://doi.org/10.1016/j.landurbplan.2015.10.005

Czerkauer-Yamu, C., & Frankhauser, P. (2013). Development of Sustainable Metropolitan Areas Using A Multi-Scale Decision Support System. Fractalopolis Model – Accessibility, Evaluation and Morphological Rules. *Development of Sustainable Metropolitan Areas Using A Multi-Scale Decision Support System. Fractalopolis Model – Accessibility, Evaluation and Morphological Rules*.

Czerkauer-Yamu, C., & Frankhauser, P. (2015). Spatial accessibility to amenities, natural areas and urban green spaces: Using a multiscale, multifractal

simulation model for managing urban sprawl. *Environment and Planning B Planning and Design*, *42*. https://doi.org/10.1068/b130171p

De Munck, C. S., Lemonsu, A., Bouzouidja, R., Masson, V., & Claverie, R. (2013). The GREENROOF module (v7.3) for modelling green roof hydrological and energetic performances within TEB. *Geosci. Model Dev.*, *6*(6), 1941–1960. https://doi.org/10.5194/gmd-6-1941-2013

Demuzere, M., Orru, K., Heidrich, O., Olazabal, E., Geneletti, D., Orru, H., Bhave, A. G., Mittal, N., Feliu, E., & Faehnle, M. (2014). Mitigating and adapting to climate change: Multi-functional and multi-scale assessment of green urban infrastructure. *Journal of Environmental Management*, *146*, 107–115. https://doi.org/10.1016/j.jenvman.2014.07.025

Département de la Seine-Saint-Denis. (2014). *Espaces verts publics*. Département de La Seine-Saint-Denis - Système d'information Géographique Départemental (SIGD). http://data.seine-saint-denis.fr/Espaces-verts-publics.html

DiGiovanni, K., Montalto, F., Gaffin, S., & Rosenzweig, C. (2013). Applicability of Classical Predictive Equations for the Estimation of Evapotranspiration from Urban Green Spaces: Green Roof Results. *Journal of Hydrologic Engineering*, *18*(1), 99–107. https://doi.org/10.1061/(ASCE)HE.1943-5584.0000572

Domínguez-Niño, J. M., Oliver-Manera, J., Arbat, G., Girona, J., & Casadesús, J. (2020). Analysis of the Variability in Soil Moisture Measurements by Capacitance Sensors in a Drip-Irrigated Orchard. *Sensors*, *20*(18), 5100. https://doi.org/10.3390/s20185100

Dooley, J. F., & Creech-Eakman, M. J. (2018). Initial steps toward a new method of atmospheric characterization over long baseline arrays. *Optical and Infrared Interferometry and Imaging VI*, *10701*, 107010I. https://doi.org/10.1117/12.2313853

Est-Ensemble. (2020). *Plan local d'urbanisme intercommunal*. https://www.est-ensemble.fr/plui

European Commission. (2016). *Policy topics: Nature-based Solutions.* https://ec.europa.eu/research/environment/index.cfm?pg=nbs

European Commission Directorate General, Research and Innovation. (2015). *Towards an EU research and innovation policy agenda for nature-based solutions & re-naturing cities: Final report of the Horizon 2020 expert group on "Nature-based solutions and re-naturing cities".* Publications Office.

European Commission & Directorate-General for Research and Innovation. (2015). *Towards an EU research and innovation policy agenda for nature-based solutions & re-naturing cities: Final report of the Horizon 2020 expert group on "Nature-based solutions and re-naturing cities".* Publications Office. http://bookshop.europa.eu/uri?target=EUB:NOTICE:KI0215161:EN:HTML

Faivre, N., Fritz, M., Freitas, T., de Boissezon, B., & Vandewoestijne, S. (2017). Nature-Based Solutions in the EU: Innovating with nature to address social, economic and environmental challenges. *Environmental Research*, *159*, 509–518. https://doi.org/10.1016/j.envres.2017.08.032

Feng, C., Meng, Q., & Zhang, Y. (2010). Theoretical and experimental analysis of the energy balance of extensive green roofs. *Energy and Buildings*, *42*(6), 959–965. https://doi.org/10.1016/j.enbuild.2009.12.014

Fitton, G. (2013). *Analyse multifractale et simulation des fluctuations de l'énergie éolienne* [These de doctorat, Paris Est]. http://www.theses.fr/2013PEST1110

Francis, L. F. M., & Jensen, M. B. (2017). Benefits of green roofs: A systematic review of the evidence for three ecosystem services. *Urban Forestry & Urban Greening*, *28*, 167–176. https://doi.org/10.1016/j.ufug.2017.10.015

Frankhauser, P. (1997). Fractal Geometry of Urban Patterns and their Morphogenesis. *Discrete Dynamics in Nature and Society*, *2*. https://doi.org/10.1155/S1026022698000107

Frankhauser, P. (1998). The fractal approach. A new tool for the spatial analysis of urban agglomerations. *Population*, *10*(1), 205–240.

Frankhauser, P. (2012). *The Fractalopolis model—A sustainable approach for a central place system*. https://hal.archives-ouvertes.fr/hal-00758864

Frankhauser, P., Tannier, C., Vuidel, G., & Houot, H. (2018). An integrated multifractal modelling to urban and regional planning. *Computers, Environment and Urban Systems*, *67*, 132–146. https://doi.org/10.1016/j.compenvurbsys.2017.09.011

Frantzeskaki, N. (2019). Seven lessons for planning nature-based solutions in cities. *Environmental Science & Policy*, *93*, 101–111. https://doi.org/10.1016/j.envsci.2018.12.033

Fung, C. K. W., & Jim, C. Y. (2017). Assessing the Cooling Effects of Different Vegetation Settings in a Hong Kong Golf Course. *Procedia Environmental Sciences*, *37*, 626–636. https://doi.org/10.1016/j.proenv.2017.03.049

Garcia, C. A., Johnson, M. J., Andraski, B. J., Halford, K. J., & Mayers, C. J. (2003). *Portable Chamber Measurements of Evapotranspiration at the Amargosa Desert Research Site near Beatty, Nye County, Nevada,* (No. 2008–5135; p. 10). U.S. Geological Survey. https://pubs.usgs.gov/sir/2008/5135/

Gires, A., Tchiguirinskaia, I., & Schertzer, D. (2018). Two months of disdrometer data in the Paris area. *Earth System Science Data*, *10*(2), 941. https://doi.org/10.5194/essd-10-941-2018

Gires, A., Tchiguirinskaia, I., Schertzer, D., Ochoa-Rodriguez, S., Willems, P., Ichiba, A., Wang, L.-P., Pina, R., Van Assel, J., Bruni, G., Murla Tuyls, D., & ten Veldhuis, M.-C. (2017). Fractal analysis of urban catchments and their representation in semi-distributed models: Imperviousness and sewer system. *Hydrology and Earth System Sciences*, *21*(5), 2361–2375. https://doi.org/10.5194/hess-21-2361-2017

Guyot, A., Cohard, J.-M., Anquetin, S., Galle, S., & Lloyd, C. R. (2009). Combined analysis of energy and water balances to estimate latent heat flux of a sudanian small catchment. *Journal of Hydrology*, *375*(1–2), 227–240. https://doi.org/10.1016/j.jhydrol.2008.12.027

Han, P.-F., Wang, X.-S., & Wang, J.-Z. (2019). Using Large-Aperture Scintillometer to Estimate Lake-Water Evaporation and Heat Fluxes in the Badain Jaran Desert, China. *Water*, *11*(12), 2575. https://doi.org/10.3390/w11122575

Hein, L., van Koppen, K., de Groot, R. S., & van Ierland, E. C. (2006). Spatial scales, stakeholders and the valuation of ecosystem services. *Ecological Economics*, *57*(2), 209–228. https://doi.org/10.1016/j.ecolecon.2005.04.005

Heusinger, J., & Weber, S. (2017). Surface energy balance of an extensive green roof as quantified by full year eddy-covariance measurements. *Science of The Total Environment*, *577*, 220–230. https://doi.org/10.1016/j.scitotenv.2016.10.168

Hill, R. J, Ochs, G. R., Wilson, J. J. (1992). Measuring surface-layer fluxes of heat and momentum using optical scintillation. Boundary-Layer Meteorol 58, 391–408 (1992). https://doi.org/10.1007/BF00120239

Insee. (2017). *Recensement 2017: Résultats sur un territoire, bases de données et fichiers détail*. Institut National de La Statistique et Des Études Économiques. https://www.insee.fr/fr/information/4467366

IPCC. (2021). *Climate Change 2021: The Physical Science Basis. Contribution of Working Group I to the Sixth Assessment Report of the Intergovernmental Panel on Climate Change.* Cambridge University Press. https://www.ipcc.ch/report/ar6/wg1/downloads/report/IPCC_AR6_WGI_Full_Report.pdf

Irvine, M. R., Lagouarde, J.-P., Dayau, S., Brut, A., Solignac, P.-A., Selves, J.-L., Cohard, J.-M., Najjar, G., Quentin, C., Rodriguez, F., & Mestayer, P. (2011,

April 18). *Variations in Cn2 measured by LAS scintillometery over the city of Nantes during the FluxSAP 2010 measurement campaign*. 3rd Scintillometer Workshop. https://hal.inrae.fr/hal-02806505

Ives, C. D., Lentini, P. E., Threlfall, C. G., Ikin, K., Shanahan, D. F., Garrard, G. E., Bekessy, S. A., Fuller, R. A., Mumaw, L., Rayner, L., Rowe, R., Valentine, L. E., & Kendal, D. (2016). Cities are hotspots for threatened species. *Global Ecology and Biogeography*, *25*(1), 117–126. https://doi.org/10.1111/geb.12404

Jevric, M., & Romanovich, M. (2016). Fractal Dimensions of Urban Border as a Criterion for Space Management. *Procedia Engineering*, *165*, 1478–1482. https://doi.org/10.1016/j.proeng.2016.11.882

Juidías, E. R. (2017). Evolution and Dynamics of Fractal Growth of the Urban Green Spaces in Seville (Spain). In *Landscape Architecture—The Sense of Places, Models and Applications*. IntechOpen. https://doi.org/10.5772/intechopen.72924

Kabisch, N., Frantzeskaki, N., Pauleit, S., Naumann, S., Davis, M., Artmann, M., Haase, D., Knapp, S., Korn, H., Stadler, J., Zaunberger, K., & Bonn, A. (2016). Nature-based solutions to climate change mitigation and adaptation in urban areas: Perspectives on indicators, knowledge gaps, barriers, and opportunities for action. *Ecology and Society*, *21*(2). https://doi.org/10.5751/ES-08373-210239

Kabisch, N., Korn, H., Stadler, J., & Bonn, A. (Eds.). (2017). *Nature-Based Solutions to Climate Change Adaptation in Urban Areas*. Springer International Publishing. https://doi.org/10.1007/978-3-319-56091-5

Karatasou, S., & Santamouris, M. (2018). Multifractal Analysis of High-Frequency Temperature Time Series in the Urban Environment. *Climate*, *6*(2), 50. https://doi.org/10.3390/cli6020050

Kesteren, A. J. H. van. (2012). *Measuring water-vapour and carbon-dioxide fluxes at field scales with scintillometry* (p. 212) [Phd, Wageningen University]. https://library.wur.nl/WebQuery/wurpubs/431579

Kipp & Zonen B.V. (2003). Instruction Manual. Kipp & Zonen B.V. https://www.kippzonen.com/Product/390/LAS-MkI-150-Upgrade#.YrsHp3ZBzIU

Kipp & Zonen B.V. (2015). *EVATION* (V2R5) [Computer software]. Kipp & Zonen B.V. https://www.kippzonen.com/Product/193/LAS-MkII-Scintillometer?item=undefined

Kohsiek, W., Meijninger, W. M. L., Debruin, H. A. R., & Beyrich, F. (2006). Saturation of the Large Aperture Scintillometer. *Boundary-Layer Meteorology*, *121*(1), 111–126. https://doi.org/10.1007/s10546-005-9031-7

Kolmogorov, A. N. (1962). A refinement of previous hypotheses concerning the local structure of turbulence in a viscous incompressible fluid at high Reynolds number. *Journal of Fluid Mechanics*, *13*(1), 82–85.

Lavallée, D., Lovejoy, S., Schertzer, D., & Ladoy, P. (1993). Nonlinear variability and landscape topography: Analysis and simulation. *Fractals in Geography*, 158–192.

Lavallée, D., Schertzer, D., & Lovejoy, S. (1991). *On the Determination of the Codimension Function*. https://doi.org/10.1007/978-94-009-2147-4_7

Li, X., Wang, X., Zhang, J., & Wu, L. (2015). Allometric scaling, size distribution and pattern formation of natural cities. *Palgrave Communications*, *1*(1), 1–11. https://doi.org/10.1057/palcomms.2015.17

Liang, J., Hu, Y., & Sun, H. (2013). The Design Evaluation of the Green Space Layout of Urban Squares Based on Fractal Theory. *Nexus Network Journal*, *15*(1), 33–49. https://doi.org/10.1007/s00004-012-0135-3

L'Institut Paris Region. (2020). *Espaces verts et boisés surfaciques, ouverts ou en projets d'ouverture au public d'Île-de-France*. Plataforme Open Data De L'Institut Paris Region. https://data.iledefrance.fr/explore/dataset/espaces-verts-et-boises-surfaciques-ouverts-ou-en-projets-douverture-au-public/

Lopez, G. A. P., Souza, L. C. L. de, Lopez, G. A. P., & Souza, L. C. L. de. (2018). Urban green spaces and the influence on vehicular traffic noise control. *Ambiente Construído*, *18*(4), 161–175. https://doi.org/10.1590/s1678-86212018000400299

Lovejoy, S., & Schertzer, D. (2013). *The Weather and Climate: Emergent Laws and Multifractal Cascades*. Cambridge University Press. https://doi.org/10.1017/CBO9781139093811

Luttik, J. (2000). The value of trees, water and open space as reflected by house prices in the Netherlands. *Landscape and Urban Planning*, *48*(3), 161–167. https://doi.org/10.1016/S0169-2046(00)00039-6

Mandelbrot, B. (1967). How Long Is the Coast of Britain? Statistical Self-Similarity and Fractional Dimension. *Science*, *156*(3775), 636–638. https://doi.org/10.1126/science.156.3775.636

Mandelbrot, B. (1982). *The Fractal Geometry of Nature*. W.H. Freeman and Company.

Marasco, D. E., Culligan, P. J., & McGillis, W. R. (2015). Evaluation of common evapotranspiration models based on measurements from two extensive green roofs in New York City. *Ecological Engineering*, *84*, 451–462. https://doi.org/10.1016/j.ecoleng.2015.09.001

Marino, S., Hogue, I. B., Ray, C. J., & Kirschner, D. E. (2008). A methodology for performing global uncertainty and sensitivity analysis in systems biology. *Journal of Theoretical Biology*, *254*(1), 178–196. https://doi.org/10.1016/j.jtbi.2008.04.011

Maronga, B., Moene, A. F., van Dinther, D., Raasch, S., Bosveld, F. C., & Gioli, B. (2013). Derivation of Structure Parameters of Temperature and Humidity in the Convective Boundary Layer from Large-Eddy Simulations and Implications for the Interpretation of Scintillometer Observations. *Boundary-Layer Meteorology*, *148*(1), 1–30. https://doi.org/10.1007/s10546-013-9801-6

Masoudi, M., & Tan, P. Y. (2019). Multi-year comparison of the effects of spatial pattern of urban green spaces on urban land surface temperature. *Landscape and Urban Planning*, *184*, 44–58. https://doi.org/10.1016/j.landurbplan.2018.10.023

Masson, V., Gomes, L., Pigeon, G., Liousse, C., Pont, V., Lagouarde, J.-P., Voogt, J., Salmond, J., Oke, T. R., Hidalgo, J., Legain, D., Garrouste, O., Lac, C., Connan, O., Briottet, X., Lachérade, S., & Tulet, P. (2008). The Canopy and Aerosol Particles Interactions in TOulouse Urban Layer (CAPITOUL) experiment. *Meteorology and Atmospheric Physics*, *102*(3–4), 135–157. https://doi.org/10.1007/s00703-008-0289-4

McLeod, M. K., Daniel, H., Faulkner, R., & Murison, R. (2004). Evaluation of an enclosed portable chamber to measure crop and pasture actual evapotranspiration at small scale. *Agricultural Water Management*, *67*(1), 15–34. https://doi.org/10.1016/j.agwat.2003.12.006

Meijninger, W. M. L., Green, A. E., Hartogensis, O. K., Kohsiek, W., Hoedjes, J. C. B., Zuurbier, R. M., & De Bruin, H. A. R. (2002). Determination of Area-Averaged Water Vapour Fluxes with Large Aperture and Radio Wave Scintillometers over a Heterogeneous Surface – Flevoland Field Experiment. *Boundary-Layer Meteorology*, *105*(1), 63–83. https://doi.org/10.1023/A:1019683616097

Meili, N., Manoli, G., Burlando, P., Carmeliet, J., Chow, W. T. L., Coutts, A. M., Roth, M., Velasco, E., Vivoni, E. R., & Fatichi, S. (2021). Tree effects on urban microclimate: Diurnal, seasonal, and climatic temperature differences explained by separating radiation, evapotranspiration, and roughness effects. *Urban Forestry & Urban Greening*, *58*, 126970. https://doi.org/10.1016/j.ufug.2020.126970

Mezemate, Y. (2014). *Analyse et modélisation multifractales des interactions ondes-turbulence-biologie dans un lac urbain* [These de doctorat, Paris Est]. http://www.theses.fr/2014PEST1166

Millennium Ecosystem Assessment. (2003). *Ecosystems and human well-being: A framework for assessment*. Island Press.

Moene, A. F. (2003). Effects of water vapour on the structure parameter of the refractive index for near-infrared radiation. *Boundary-Layer Meteorology*, *107*(3), 635–653. https://doi.org/10.1023/A:1022807617073

Moene, A. F., Meijninger, W. M. L., Hartogensis, O. K., Kohsiek, W., & de Bruin, H. (2004). *A review of the relationships describing the signal of a Large Aperture Scintillometer*.

Monin, A. S., & Yaglom, A. M. (1971). *Statistical Fluid Mechanics: Mechanics of Turbulence* (J. L. Lumley, Ed.; Vol. 1). MIT Press.

Moorhead, J., Marek, G., Colaizzi, P., Gowda, P., Evett, S., Brauer, D., Marek, T., & Porter, D. (2017). Evaluation of Sensible Heat Flux and Evapotranspiration Estimates Using a Surface Layer Scintillometer and a Large Weighing Lysimeter. *Sensors*, *17*(10), 2350. https://doi.org/10.3390/s17102350

Nature4Cities. (2018). *NBS multi-scalar and multi-thematic typology and associated database* (D1.1; p. 455). Nature4Cities. https://docs.wixstatic.com/ugd/55d29d_8813db2df690497e80740537b6a8a844.pdf

Neuvonen, M., Sievänen, T., Tönnes, S., & Koskela, T. (2007). Access to green areas and the frequency of visits – A case study in Helsinki. *Urban Forestry & Urban Greening*, *6*(4), 235–247. https://doi.org/10.1016/j.ufug.2007.05.003

Norton, B. A., Coutts, A. M., Livesley, S. J., Harris, R. J., Hunter, A. M., & Williams, N. S. G. (2015). Planning for cooler cities: A framework to prioritise green infrastructure to mitigate high temperatures in urban landscapes. *Landscape and Urban Planning*, *134*, 127–138. https://doi.org/10.1016/j.landurbplan.2014.10.018

Obukhov, A. M. (1941). On the distribution of energy in the spectrum of turbulent flow. *Bull. Acad. Sci. USSR, Geog. Geophys.*, *5*, 453–466.

Obukhov, A. M. (1949). *Structure of temperature field in turbulent flow*. Air Force Systems Command Wright-Patterson Afb Oh Foreign Technology Division.

Obukhov, A. M. (1962). Some specific features of atmospheric turbulence. *Journal of Fluid Mechanics*, *13*(1), 77–81. https://doi.org/10.1017/S0022112062000506

Oke, T. R. (1982). The energetic basis of the urban heat island. *Quarterly Journal of the Royal Meteorological Society*, *108*(455), 1–24. https://doi.org/10.1002/qj.49710845502

Oke, T. R. (1987). *Boundary Layer Climates* (2nd ed). Routledge.

O'Malley, C., Piroozfar, P., Farr, E. R. P., & Pomponi, F. (2015). Urban Heat Island (UHI) mitigating strategies: A case-based comparative analysis. *Sustainable Cities and Society*, *19*, 222–235. https://doi.org/10.1016/j.scs.2015.05.009

Panofsky, H. A., & Dutton, J. A. (1984). *Atmospheric turbulence: Models and methods for engineering applications*. Wiley.

Pantin. (2020, April 4). *Cimetière parisien*. Pratique Ville Pantin : Site Internet. https://pratique.pantin.fr/cimetieres/cimetiere-parisien

Pappalardo, V., La Rosa, D., Campisano, A., & La Greca, P. (2017). The potential of green infrastructure application in urban runoff control for land use planning: A preliminary evaluation from a southern Italy case study. *Ecosystem Services*, *26*, 345–354. https://doi.org/10.1016/j.ecoser.2017.04.015

Parisi, G., & Frisch, U. (1985). A multifractal model of intermittency. *Turbulence and Predictability in Geophisical Fluid Dynamics and Climate Dynamics*, 84–88.

Pérez, D. G., Barillé, R., Morille, Y., Zielińska, S., & Ortyl, E. (2014). Multifractal characteristics of optical turbulence measured through a single beam holographic process. *Optics Express*, *22*(16), 19538–19545. https://doi.org/10.1364/OE.22.019538

Poë, S., Stovin, V., & Berretta, C. (2015). Parameters influencing the regeneration of a green roof's retention capacity via evapotranspiration. *Journal of Hydrology*, *523*, 356–367. https://doi.org/10.1016/j.jhydrol.2015.02.002

Qiu, G., Li, H., Zhang, Q., Chen, W., Liang, X., & Li, X. (2013). Effects of Evapotranspiration on Mitigation of Urban Temperature by Vegetation and Urban Agriculture. *Journal of Integrative Agriculture*, *12*(8), 1307–1315. https://doi.org/10.1016/S2095-3119(13)60543-2

Ramier, D., Chollet, J., Berthier, E., Sabre, M., Tétard, Y., Flori, J.-P., & Bouyer, J. (2015). *Mesure de l'évapotranspiration à petite échelle spatiale: Applications aux toitures végétalisées* [Poster].

Rana, G., & Katerji, N. (2000). Measurement and estimation of actual evapotranspiration in the field under Mediterranean climate: A review. *European Journal of Agronomy*, *13*(2), 125–153. https://doi.org/10.1016/S1161-0301(00)00070-8

Richardson, L. F. (1965). *Weather prediction by numerical process.* Dover Publications.

Rogov, M., & Rozenblat, C. (2018). Urban Resilience Discourse Analysis: Towards a Multi-Level Approach to Cities. *Sustainability*, *10*(12), 4431. https://doi.org/10.3390/su10124431

Rozos, E., Makropoulos, C., & Maksimović, Č. (2013). Rethinking urban areas: An example of an integrated blue-green approach. *Water Supply*, *13*(6), 1534–1542. https://doi.org/10.2166/ws.2013.140

Savage, M. J. (2009). Estimation of evaporation using a dual-beam surface layer scintillometer and component energy balance measurements. *Agricultural and Forest Meteorology*, *149*(3), 501–517. https://doi.org/10.1016/j.agrformet.2008.09.012

Schertzer, D., & Lovejoy, S. (1987). *Physical modeling and analysis of rain and clouds by anisotropic scaling multiplicative processes*. https://doi.org/10.1029/JD092ID08P09693

Schertzer, D., & Lovejoy, S. (1989). Nonlinear Variability in Geophysics: Multifractal Simulations and Analysis. In L. Pietronero (Ed.), *Fractals' Physical Origin and Properties* (pp. 49–79). Springer US. https://doi.org/10.1007/978-1-4899-3499-4_3

Schertzer, D., & Lovejoy, S. (Eds.). (1991). *Non-Linear Variability in Geophysics: Scaling and Fractals*. Springer Netherlands. https://doi.org/10.1007/978-94-009-2147-4

Schmitt, F., Schertzer, D., Lovejoy, S., & Brunet, Y. (1993). Estimation of universal for atmospheric turbulent multifractal indices velocity fields. *Fractals*, *01*(03), 568–575. https://doi.org/10.1142/S0218348X93000599

Secretariat of the Convention on Biological Diversity. (2009). *Connecting Biodiversity and Climate Change Mitigation and Adaptation: Report of the Second Ad Hoc Technical Expert Group on Biodiversity and Climate Change.* (CBD Technical Series No. 41; p. 126 pages). https://www.cbd.int/doc/publications/cbd-ts-41-en.pdf

Sharma, A., Conry, P., Fernando, H. J. S., Hamlet, A. F., Hellmann, J. J., & Chen, F. (2016). Green and cool roofs to mitigate urban heat island effects in the Chicago metropolitan area: Evaluation with a regional climate model. *Environmental Research Letters*, *11*(6), 064004. https://doi.org/10.1088/1748-9326/11/6/064004

Shashua-Bar, L., Pearlmutter, D., & Erell, E. (2009). The cooling efficiency of urban landscape strategies in a hot dry climate. *Landscape and Urban Planning*, *92*(3–4), 179–186. https://doi.org/10.1016/j.landurbplan.2009.04.005

Stanic, F. (2020). *Suivi et modélisation à haute résolution des flux hydriques d'une toiture végétalisée* [These de doctorat, Paris Est]. http://www.theses.fr/2020PESC1012

Stovin, V., Vesuviano, G., & Kasmin, H. (2012). The hydrological performance of a green roof test bed under UK climatic conditions. *Journal of Hydrology*, *414–415*, 148–161. https://doi.org/10.1016/j.jhydrol.2011.10.022

Stull, R. B. (1988). *An Introduction to Boundary Layer Meteorology*. Springer Netherlands. https://doi.org/10.1007/978-94-009-3027-8

Tabares, P. C., & Srebric, J. (2012). A heat transfer model for assessment of plant based roofing systems in summer conditions. *Building and Environment*, *49*, 310–323. https://doi.org/10.1016/j.buildenv.2011.07.019

Tannier, C. (2009). Formes de villes optimales, formes de villes durables. Réflexions à partir de l'étude de la ville fractale. *Espaces et societes*, *n° 138*(3), 153–171.

Tannier, C., & Pumain, D. (2005). Fractals in urban geography: A theoretical outline and an empirical example. *Cybergeo : European Journal of Geography*. https://doi.org/10.4000/cybergeo.3275

Tatarski, V. I., Silverman, R. A., & Chako, N. (1961). Wave Propagation in a Turbulent Medium. *Physics Today*, *14*(12), 46–51. https://doi.org/10.1063/1.3057286

Thorp, R. (2014). *Observations of heat, water vapor and carbon dioxide exchanges over a living roof using eddy covariance*. San Francisco State University.

Threlfall, C. G., Mata, L., Mackie, J. A., Hahs, A. K., Stork, N. E., Williams, N. S. G., & Livesley, S. J. (2017). Increasing biodiversity in urban green spaces through

simple vegetation interventions. *Journal of Applied Ecology*, *54*(6), 1874–1883. https://doi.org/10.1111/1365-2664.12876

Topp, G. C., Davis, J. L., & Annan, A. P. (1980). Electromagnetic determination of soil water content: Measurements in coaxial transmission lines. *Water Resources Research*, *16*(3), 574–582. https://doi.org/10.1029/WR016i003p00574

Toxopeus, H., & Polzin, F. (2017). *Characterizing nature-based solutions from a business model and financing perspective* (Deliverable 1.3 Part V; p. 30). NATURVATION: NATure-based URban innoVATION.

United Nations, Department of Economic and Social Affairs, Population Division. (2019). *World Urbanization Prospects: The 2018 Revision* (p. 126). https://population.un.org/wup/Publications/Files/WUP2018-Report.pdf

Valayamkunnath, P., Sridhar, V., Zhao, W., & Allen, R. G. (2018). Intercomparison of surface energy fluxes, soil moisture, and evapotranspiration from eddy covariance, large-aperture scintillometer, and modeling across three ecosystems in a semiarid climate. *Agricultural and Forest Meteorology*, *248*, 22–47. https://doi.org/10.1016/j.agrformet.2017.08.025

Van Kesteren, B., & Hartogensis, O. K. (2011). Analysis of the Systematic Errors Found in the Kipp & Zonen Large-Aperture Scintillometer. *Boundary-Layer Meteorology*, *138*(3), 493–509. https://doi.org/10.1007/s10546-010-9564-2

Vera, S., Pinto, C., Tabares-Velasco, P. C., & Bustamante, W. (2018). A critical review of heat and mass transfer in vegetative roof models used in building energy

and urban enviroment simulation tools. *Applied Energy*, *232*, 752–764. https://doi.org/10.1016/j.apenergy.2018.09.079

Vera, S., Pinto, C., Tabares-Velasco, P. C., Bustamante, W., Victorero, F., Gironás, J., & Bonilla, C. A. (2017). Influence of vegetation, substrate, and thermal insulation of an extensive vegetated roof on the thermal performance of retail stores in semiarid and marine climates. *Energy and Buildings*, *146*, 312–321. https://doi.org/10.1016/j.enbuild.2017.04.037

Versini, P.-A., Gires, A., Tchiguirinskaia, I., & Schertzer, D. (2020). Fractal analysis of green roof spatial implementation in European cities. *Urban Forestry & Urban Greening*, *49*, 126629. https://doi.org/10.1016/j.ufug.2020.126629

Versini, P.-A., Kotelnikova, N., Poulhes, A., Tchiguirinskaia, I., Schertzer, D., & Leurent, F. (2018). A distributed modelling approach to assess the use of Blue and Green Infrastructures to fulfil stormwater management requirements. *Landscape and Urban Planning*, *173*, 60–63. https://doi.org/10.1016/j.landurbplan.2018.02.001

Versini, P.-A., Stanic, F., Gires, A., Schertzer, D., & Tchiguirinskaia, I. (2020). Measurements of the water balance components of a large green roof in the greater Paris area. *Earth System Science Data*, *12*(2), 1025–1035. https://doi.org/10.5194/essd-12-1025-2020

Vicari, R., Tchiguirinskaia, I., Tisserand, B., & Schertzer, D. (2019). Climate resilience in Paris: A network representation of online strategic documents released by

public authorities. *Progress in Disaster Science*, *3*, 100040. https://doi.org/10.1016/j.pdisas.2019.100040

Voyde, E., Fassman, E., Simcock, R., & Wells, J. (2010). Quantifying Evapotranspiration Rates for New Zealand Green Roofs. *Journal of Hydrologic Engineering*, *15*(6), 395–403. https://doi.org/10.1061/(ASCE)HE.1943-5584.0000141

Wadzuk, B. M., Schneider, D., Feller, M., & Traver, R. G. (2013). Evapotranspiration from a Green-Roof Storm-Water Control Measure. *Journal of Irrigation and Drainage Engineering*, *139*(12), 995–1003. https://doi.org/10.1061/(ASCE)IR.1943-4774.0000643

Ward, H. C., Evans, J. G., & Grimmond, C. S. B. (2015). Infrared and millimetre-wave scintillometry in the suburban environment – Part 2: Large-area sensible and latent heat fluxes. *Atmospheric Measurement Techniques*, *8*(3), 1407–1424. https://doi.org/10.5194/amt-8-1407-2015

World Health Organization. (2016). *Urban green spaces and health* (WHO/EURO:2016-3352-43111-60341). World Health Organization. https://apps.who.int/iris/handle/10665/345751

World Health Organization Regional Office For Europe. (2017). *Urban green spaces: A brief for action.* (p. 24). https://www.euro.who.int/en/health-topics/environment-and-health/urban-health/publications/2017/urban-green-spaces-a-brief-for-action-2017

Yang, J., Mohan Kumar, D. llamathy, Pyrgou, A., Chong, A., Santamouris, M., Kolokotsa, D., & Lee, S. E. (2018). Green and cool roofs' urban heat island mitigation potential in tropical climate. *Solar Energy*, *173*, 597–609. https://doi.org/10.1016/j.solener.2018.08.006

Yee, M. S., Pauwels, V. R. N., Daly, E., Beringer, J., Rüdiger, C., McCabe, M. F., & Walker, J. P. (2015). A comparison of optical and microwave scintillometers with eddy covariance derived surface heat fluxes. *Agricultural and Forest Meteorology*, *213*, 226–239. https://doi.org/10.1016/j.agrformet.2015.07.004

Zhang, Y., Murray, A. T., & Turner, B. L. (2017). Optimizing green space locations to reduce daytime and nighttime urban heat island effects in Phoenix, Arizona. *Landscape and Urban Planning*, *165*, 162–171. https://doi.org/10.1016/j.landurbplan.2017.04.009

Zwierzchowska, I., Fagiewicz, K., Poniży, L., Lupa, P., & Mizgajski, A. (2019). Introducing nature-based solutions into urban policy – facts and gaps. Case study of Poznań. *Land Use Policy*, *85*, 161–175. https://doi.org/10.1016/j.landusepol.2019.03.025

Appendix

Appendix A. Text-mining of NBS

Table A.1. General NBS projects information.

Project	Start Date	End Date	Budget	Framework	Coordinator
EKLIPSE	1 February 2016	31 July 2020	€ 2 997 272,49	H2020-EU	United Kingdom Research and Innovation
NATURVATION	1 November 2016	31 October 2020	€ 7 797 877,50	H2020-EU	University of Durham
ESMERALDA	1 February 2015	31 July 2018	€ 3 133 306	H2020-EU	Gottfried Wilhelm Leibniz Universität Hannover
MAES—Urban Ecosystems				Action 5 of the EU Biodiversity Strategy to 2020	Joint Research Centre Dutch National Institute for Public Health and the Environment (RIVM) European member states

Table A.2. Main attributes of Eklipse network.

Nodes Degree		**Edge Weight**	
Label	*Degree*	*Label*	*Weight*
NBS	36	Physical activity-Green spaces	0.182
Impacts	29	Building-Tropical nights	0.143
Indicators	22	Tropical nights-Indicators	0.143
Water	22	Tropical nights-Temperature reduction	0.143
Climate	19	Tropical nights-Microscale	0.143

Table A.3. List of main nodes EKLIPSE by cluster, (a) NBS Planning, Governance and Management, (b) NBS to Tackle Urban Challenges, (c) NBS Indicators and Scale, (d) Ecosystem Services Provided by the NBS, (e) Action, Temporal Scale and Health Benefits, (f) Social Benefit and Economic Opportunities if NBS and (g) Social Opportunities.

(**a**)		(**b**)	
NBS Planning, Governance and Management		**NBS to Tackle Urban Challenges**	
Node	*Degree*	*Node*	*Degree*
nbs	36	water	22
impacts	29	management	19
climate	19	evapotranspiration	12
assessment	19	pollutants	11
urban contexts	13	spatial scale	11

(**c**)		(**d**)	
NBS Indicators and Scale		**Ecosystem Services Provided by the NBS**	
Node	*Degree*	*Node*	*Degree*
indicators	22	services	16
building	16	ecosystem services	13
street	14	blue infrastructure	12
microscale	14	biodiversity	10

scale	13	people	10

(e)

Action, Temporal Scale and Health Benefits

Node	*Degree*
actions	13
health indicators	9
challenge	8
temporal scale	8
nbs actions	7

(f)

Social Benefit and Economic Opportunities of NBS

Node	*Degree*
benefits	12
costs	5
real estate values	4
social benefits	4
coastal resilience	3

(g)

Social Opportunities

Node	*Degree*
environmental justice	5
social groups	5
trade-offs	4
potential success factors	4
synergies	3

Table A.4. Main attributes of MAES-Urban ecosystems network.

Node Degree		**Edge Weight**	
Label	*Degree*	*Label*	*Weight*
Urban	35	Environment-City council	0.097
Ecosystems	34	Biodiversity-City council	0.097
Green	33	City level-Urban	0.093
Services	30	Vegetation-Vegetation series	0.088
Urban ecosystems	28	Potential natural vegetation-Vegetation series	0.088

Table A.5. List of main nodes MAES—Urban Ecosystem by cluster, (a) Urban Policies and NBS, (b) Ecosystems Services Provided by NBS, (c) Urban Land Use, (d) Urban Planning, (e) Ecosystem Services Assessment and (f) Tools to Assess ESS.

(**a**)	
Urban Policies and NBS	
Node	*Degree*
ecosystems	34
urban ecosystems	28
green infrastructure	25
cities	21
pilot	19

(**b**)	
Ecosystem Services Provided by NBS	
Node	*Degree*
services	30
water	24
community gardening	15
maintenance	13
trees	12

(**c**)	
Urban Land Use	
Node	*Degree*
green	33
land	25
agriculture land	14
land use	12
green spaces	11

(**d**)	
Urban Planning	
Node	*Degree*
urban	35
land use plans	9
management	8
policy context	5
implementation	4

(**e**)	
Ecosystem Services Assessment	
Node	*Degree*
ecosystem services	19
indicators	11
quality	10
ecosystem condition	8
water framework directive	6

(**f**)	
Tools to Assess ESS	
Node	*Degree*
data	10
assessment	9
maps	7
land cover	7
urban scale	7

Table A.6. Main attributes of NATURVATION network.

Node Degree		**Edge Weight**	
Label	*Degree*	*Label*	*Weight*
NBS	22	UHI effect- Services	0.143
Services	20	UHI effect- Ecosystem services	0.143
Nature	18	UHI effect- Mitigation	0.143
Valuation	18	UHI effect- Recreation	0.143
Space	12	UHI effect- Green roofs	0.143

Table A.7. List of main nodes of NATURVATION by cluster. (a) Economic Valuation, (b) Types of NBS, (c) Ecosystem Services Provided by NBS, (d) NBS Terms and (e) Types of Values.

(**a**)		(**b**)	
Economic Valuation		**Types of NbS**	
Node	*Degree*	*Node*	*Degree*
nature	18	services	20
valuation	18	space	12
monetization	12	vegetables	12
differences	11	canals	7
particular study	9	urban heat island effect	7
(c)		**(d)**	
Ecosystem Services Provided by NBS		**NBS Terms**	
Node	*Degree*	*Node*	*Degree*
nbs	22	landscape domains	11
nbs goals	8	project	9
health	7	supports	9
regulating	6	ecosystem approach	9
air quality	6	ecosystem-based adaptation	9

(**e**)

Types of Values	
Node	*Degree*
economic values	9
benefits	7
option values	7
assessment	5
goods	5

Appendix B. Volumetric water content and soil temperature in the BGW during 2020's summer dry periods.

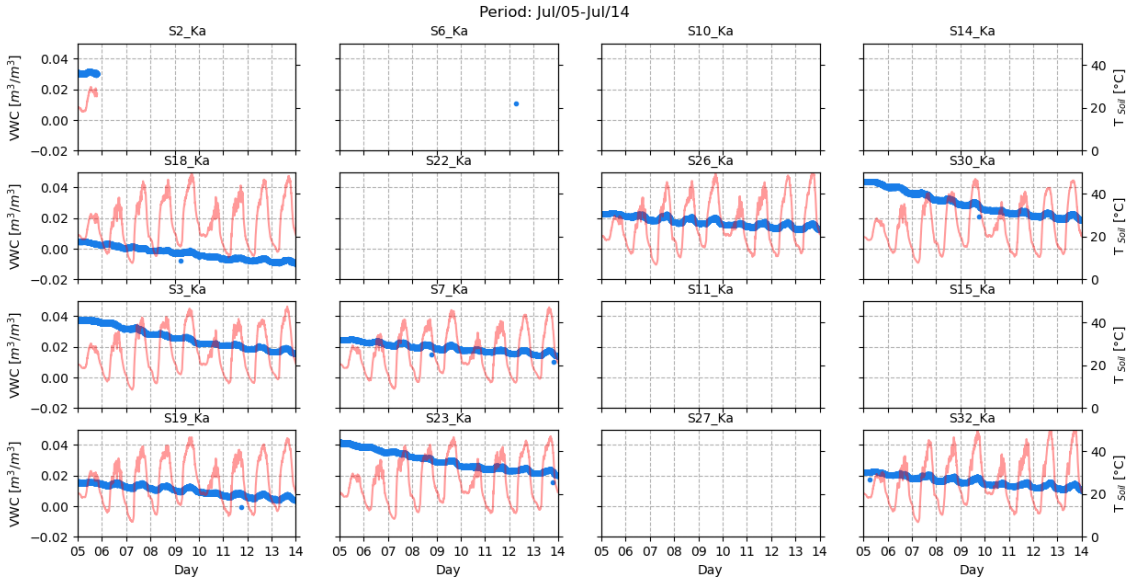

Figure B.1. Volumetric water content (blue) and soil temperature of 16 sensors located in the BGW during 5th and 14th of July 2020.

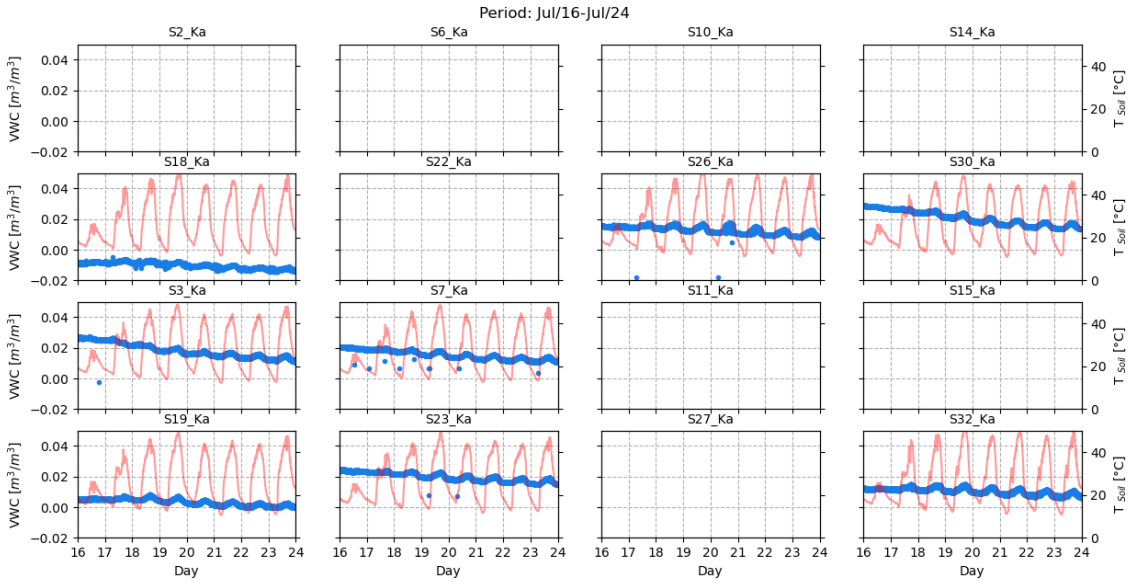

Figure B.2. Volumetric water content (blue) and soil temperature of 16 sensors located in the BGW during 16th and 24th of July 2020.

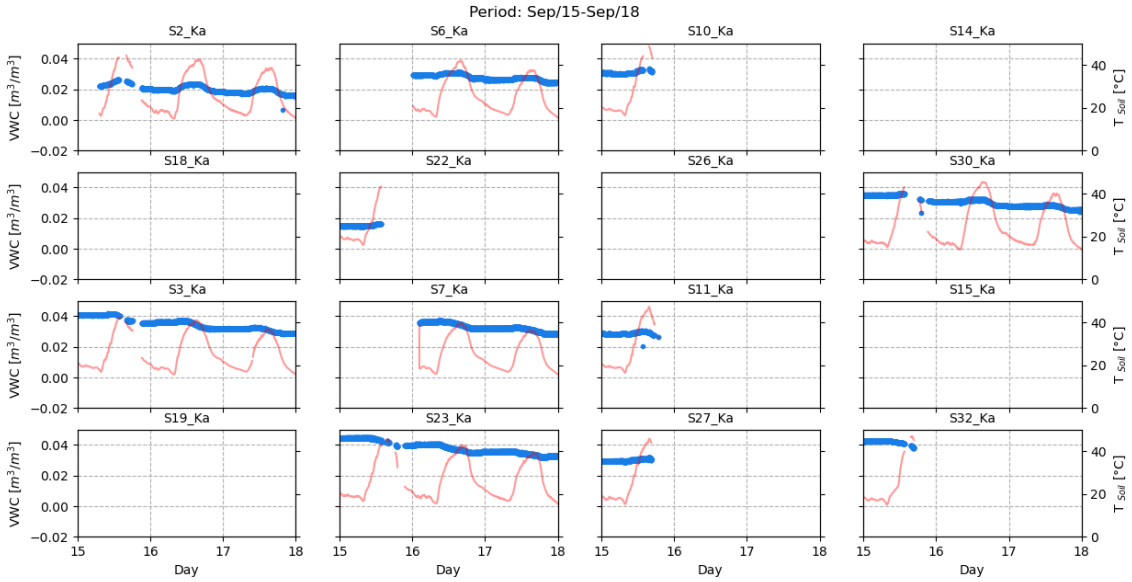

Figure B.3. Volumetric water content (blue) and soil temperature of 16 sensors located in the BGW during 15th and 18th of September 2020.

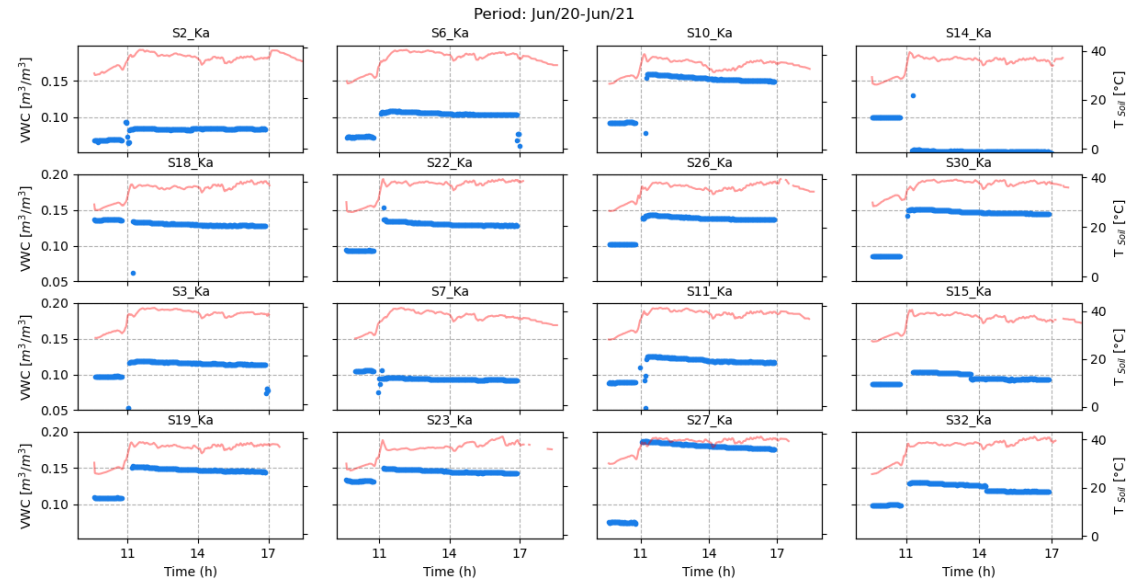

Figure B.4. Volumetric water content (blue) and soil temperature of 16 sensors located in the BGW during 20th of June 2018.

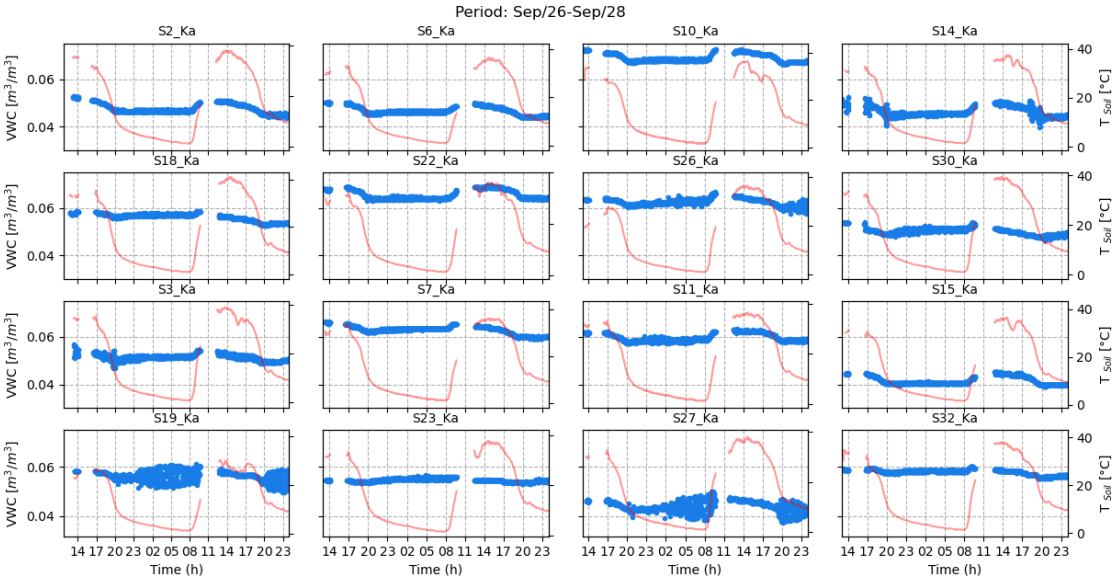

Figure B.5. Volumetric water content (blue) and soil temperature of 16 sensors located in the BGW during 26th and 27th of September 2018.

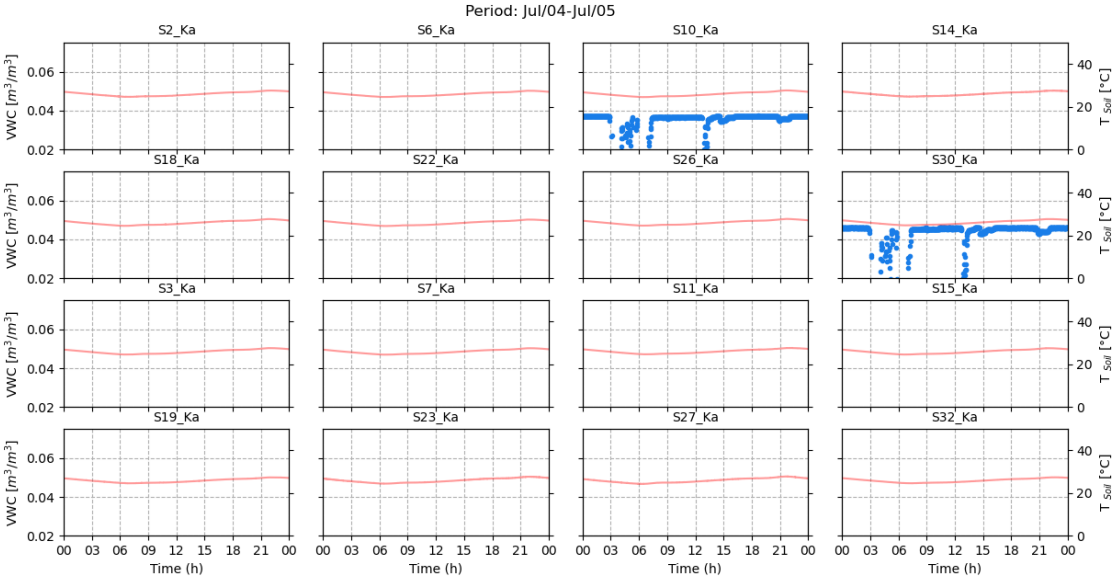

Figure B.6. Volumetric water content (blue) and soil temperature of 16 sensors located in the BGW during 4th of July 2019.

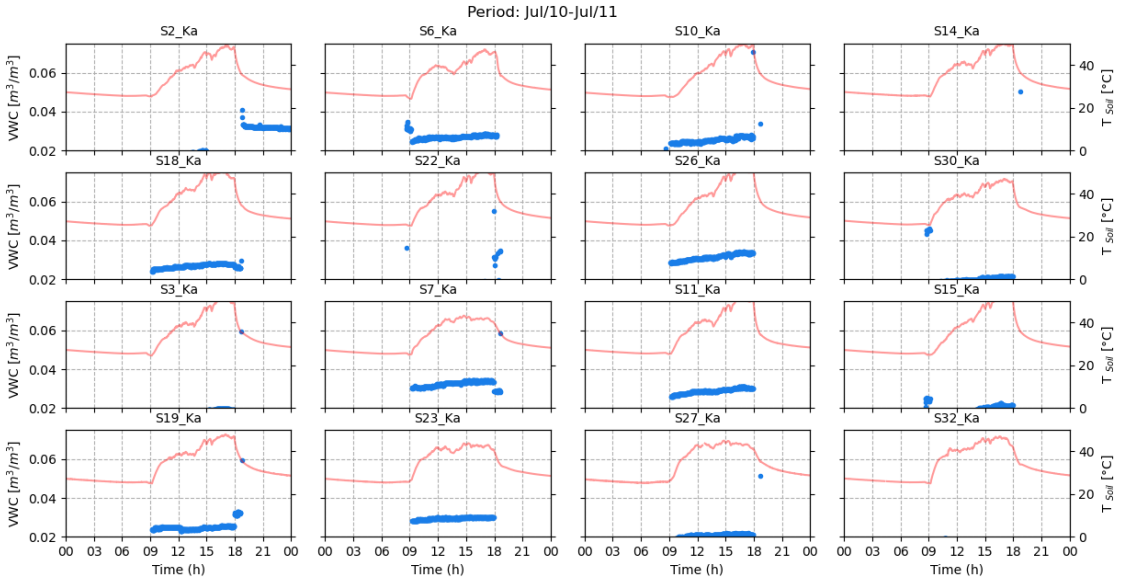

Figure B.7. Volumetric water content (blue) and soil temperature of 16 sensors located in the BGW during 10th of July 2019.

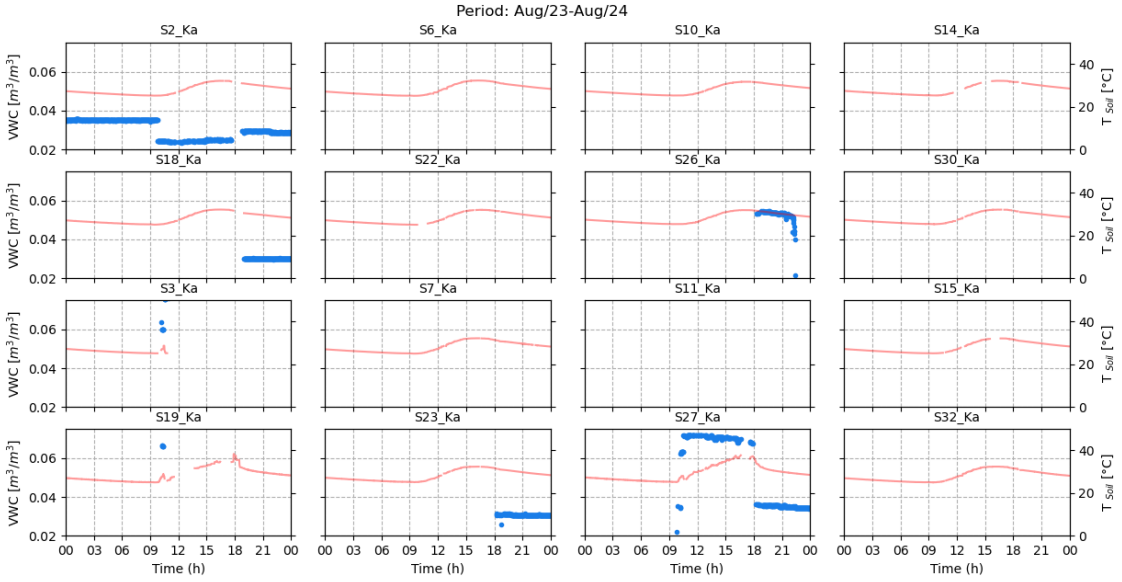

Figure B.8. Volumetric water content (blue) and soil temperature of 16 sensors located in the BGW during 23rd of August 2019.

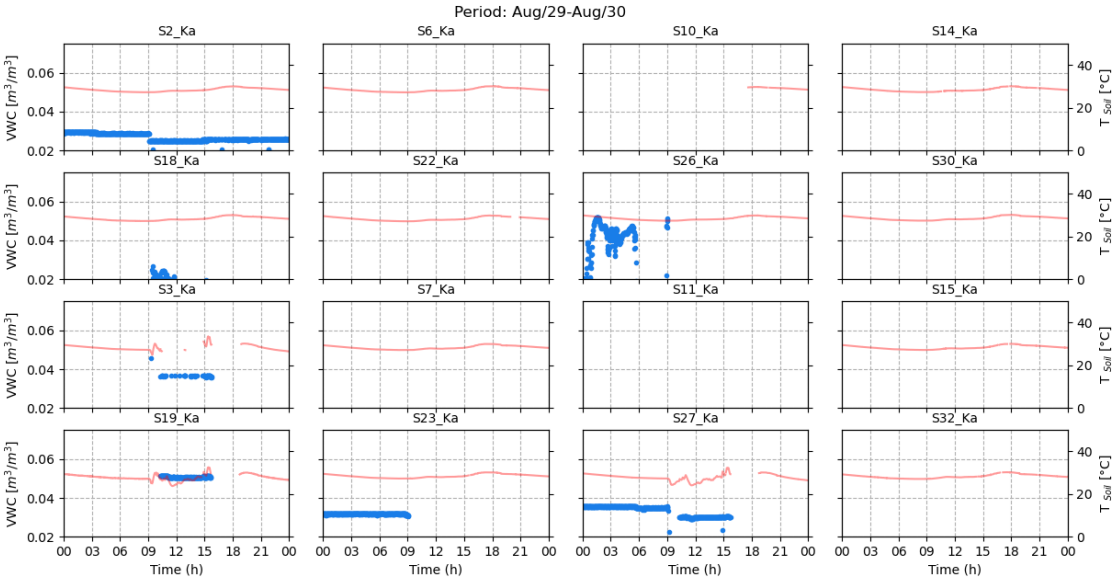

Figure B.9. Volumetric water content (blue) and soil temperature of 16 sensors located in the BGW during 30th of August 2019.

Appendix C. Hausdorff dimension

This mathematical proposition made by Felix Hausdorff and Abram Besicovitch allowed to define dimensions with non-integer values. They proposed the set A can be covered by a finite set of n disks of different diameter $l_i < l$, $i = 1,2, \dots, n$. Then, the D-dimensional Hausdorff measure $M_D(A)$ can be defined as:

$$M_D(A) = \lim_{l \to 0} \inf_{l_i < l} \sum_{i=1}^{N} l_i^D$$

where the critical dimension of the Hausdorff measure D_H of A, is defined as follows:

$$M_D(A) = 0, if\ D > D_H$$

$$M_D(A) = \infty, if\ D < D_H$$

Because several disk sizes are required, limited practical applications of Hausdorff dimension have been found.

Appendix D. Green spaces of Est-Ensemble

The aim and the spaces involved in each planning strategy are described below:

- SRCE: At Ile de France Region the main purpose of the SRCE is the land-use management and natural resources protection. Three green spaces within Est-Ensemble are of special interest to create or expand following the SRCS:
    - *Ile de loisirs de Romainville*: It is a project of leisure areas built over 4,5 ha and 20 ha of forest area of public restriction, which aims the protection of biodiversity. This is located between Romainville, Pantin, Les Lilas and Noisy-le-Sec, and it involves the only natural forest at eastern of Paris. Some parcs as "Romanville" and "Henri-Berbusse" make part of this project too.
    - *Murs à Pêches*
    - *Parc Jean-Moulin-Les Guilands*
- TVB: It is a tool of management, aiming the connection of green and blue spaces in the territory, to keep ecosystems continuity and functionality. These spaces allow the free transit of species, increase urban resilience and promote social interaction. Apart from SCRE spaces, the TVB includes the Canal d'Ourcq, in the northern area of Est-Ensemble, corresponding to the main ecologic network of the territory.
- Local governance: Since 2017 local authorities of Est-ensemble are responsible for the management and maintenance of three public green spaces:
    - Bois de Bondy
    - Parc des Beaumonts
    - Parc des Guillaumes
- Parc d'hauteurs: This is project created with the goal of revaluate and transform the territory in an urban natural parc of 320 ha of 17 linked open green spaces, including spaces of other communities (i.e., Paris, Rosny-sous-Bois and Fontenay-sous-Bois) to create a continuous loop-walk of 32 km at the east of Paris:

- Cimetière du Père-Lachaise (Paris 20)
- Parc de Belleville (Paris 20)
- Parc de Buttes Chaumont (Paris 19)
- Parc de la Butte du Chapeau Rouge (Paris 19)
- Parc Henri Barbusse (Pré-Saint-Gervais)
- Corniche des Forts - en cours d'aménagement (Les Lilas, Romainville)
- Parc Lucie Aubrac (Les Lilas)
- Parc de Romainville
- Parc Huvier (Noisy-le-Sec)
- Parc des Guillaumes (Noisy-le-Sec)
- Parc de Nanteuil (Rosny-sous-Bois)
- Parc de Charcalet (Rosny-sous-Bois)
- Parc Montreau (Montreuil)
- Parc des Carrières (Fontenay-sous-Bois)
- Parc des Beaumonts (Montreuil)
- Parc Jean Moulin Les Guilands (Montreuil-Bagnolet)
- Parc du Château de l'Etang (Bagnolet)

Appendix E. Total dwelling by commune of Est-Ensemble.

Commune	1968	1975	1982	1990	1999	2007	2012	2017
Bagnolet	13232	14340	13884	13994	14497	15176	15047	15968
Bobigny	11851	14346	15469	15799	16258	17012	17778	20184
Bondy	16097	16737	17038	17859	18958	20004	20162	20912
Le Pré-St-Gervais	6341	6332	6738	7705	8278	8631	8656	8920
Les Lilas	6925	8856	9418	9728	10215	11112	11394	11690
Montreuil	35667	39496	41266	43115	43226	44871	46417	50709
Noisy-le-sec	11487	14020	14563	14635	15750	16120	16757	17756
Pantin	18946	19290	21701	22791	24318	24458	24974	26554
Romainville	8276	8995	9665	9699	10322	10582	10716	11822

Appendix F. Housing density in fractal scenario of urban centres.

Id Centre	Code centre	Base length (m)	Built-area (m^2)	Housings units	Housing density (Housing/ha)
0-0-0	11	964	567018	6371	69
0-0-1	10	689	313430	3364	71
0-0-2	10	689	225942	3040	64
0-0-3	10	689	166886	2338	49
0-0-4	10	689	255162	2659	56
0-0-5	10	689	224786	3852	81
0-0-6	10	689	266716	3936	83
0-1-0	01	689	247618	4879	103
0-1-1	00	492	97885	2169	90
0-1-2	01	492	163915	3166	131
0-1-3	02	492	152286	2721	112
0-1-4	03	492	127154	1621	67
0-1-5	04	492	170330	3656	151
0-1-6	05	492	113038	2205	91
0-2-0	01	689	6012	39	1
0-2-1	00	492	20717	299	12
0-2-2	00	492	2101	13	1
0-2-3	00	492	27939	527	22
0-2-4	00	492	17282	57	2
0-2-5	00	492	674	4	0
0-2-6	05	492	3084	16	1
0-3-0	01	689	26330	331	7
0-3-1	00	492	4906	10	0
0-3-2	00	492	55696	1384	57
0-3-3	00	492	95973	1076	44

Id Centre	Code centre	Base length (m)	Built-area (m^2)	Housings units	Housing density (Housing/ha)
0-3-4	00	492	86321	529	22
0-3-5	00	492	73388	1192	49
0-3-6	00	492	59190	926	38
0-4-0	01	689	191530	2373	50
0-4-1	00	492	66438	695	29
0-4-2	01	492	74628	837	35
0-4-3	02	492	71727	1108	46
0-4-4	03	492	98185	1317	54
0-4-5	04	492	77806	463	19
0-4-6	05	492	59556	907	37
0-5-0	01	689	227185	2653	56
0-5-1	00	492	102311	1234	51
0-5-2	00	492	166141	1741	72
0-5-3	00	492	110498	1485	61
0-5-4	00	492	116092	2129	88
0-5-5	00	492	112917	1615	67
0-5-6	00	492	108750	824	34
0-6-0	01	689	56790	561	12
0-6-1	00	492	74101	692	29
0-6-2	00	492	107778	1122	46
0-6-3	00	492	53764	849	35
0-6-4	00	492	51598	825	34
0-6-5	00	492	59690	1384	57
0-6-6	00	492	48538	1061	44

Appendix G. Accessibility from urban centres to NBS

Id Centre	Code centre	Baseline Scenario						NBS Fractal Scenario				
		Level	Occas	Monthly	Weekly	Daily	Total	Occas	Monthly	Weekly	Daily	Total
0-0-0	11	1	1	0,71	0,28	0,00	0,50	1	0,51	0,28	0,00	0,45
0-0-1	10	3	1	0,60	0,45	0,00	0,51	1	0,44	0,45	0,00	0,47
0-0-2	10	3	1	0,66	0,41	0,00	0,52	1	0,57	0,41	0,00	0,50
0-0-3	10	3	1	0,77	0,21	0,00	0,50	1	0,66	0,21	0,00	0,47
0-0-4	10	3	1	0,88	0,21	0,00	0,52	1	0,72	0,41	0,00	0,53
0-0-5	10	3	1	0,80	0,43	0,00	0,56	1	0,57	0,47	0,00	0,51
0-0-6	10	3	1	0,83	0,34	0,00	0,54	1	0,64	0,34	0,00	0,50
0-1-0	01	2	1	0,45	0,31	0,00	0,44	1	0,53	0,31	0,00	0,46
0-1-1	00	3	1	0,50	0,56	0,00	0,51	1	0,52	0,56	0,00	0,52
0-1-2	01	3	1	0,40	0,25	0,00	0,41	1	0,46	0,25	0,00	0,43
0-1-3	02	3	1	0,50	0,35	0,00	0,46	1	0,59	0,53	0,00	0,53
0-1-4	03	3	1	0,58	0,43	0,00	0,50	1	0,59	0,43	0,00	0,51
0-1-5	04	3	1	0,57	0,54	0,00	0,53	1	0,55	0,57	0,42	0,64
0-1-6	05	3	1	0,64	0,37	0,00	0,50	1	0,62	0,38	0,00	0,50
0-2-0	01	2	1	0,43	0,00	0,00	0,36	1	0,57	0,24	0,00	0,45
0-2-1	00	3	1	0,34	0,09	0,00	0,36	1	0,47	0,21	0,00	0,42
0-2-2	00	3	1	0,32	0,08	0,00	0,35	1	0,46	0,24	0,00	0,42
0-2-3	00	3	1	0,50	0,24	0,00	0,43	1	0,63	0,24	0,00	0,47
0-2-4	00	3	1	0,50	0,00	0,00	0,38	1	0,64	0,00	0,00	0,41
0-2-5	00	3	1	0,41	0,00	0,00	0,35	1	0,55	0,23	0,00	0,44
0-2-6	05	3	1	0,49	0,00	0,00	0,37	1	0,63	0,03	0,00	0,42
0-3-0	01	2	1	0,77	0,12	0,00	0,47	1	0,87	0,12	0,00	0,50
0-3-1	00	3	1	0,68	0,00	0,00	0,42	1	0,80	0,19	0,00	0,50
0-3-2	00	3	1	0,69	0,21	0,00	0,47	1	0,82	0,21	0,00	0,51
0-3-3	00	3	1	0,79	0,22	0,00	0,50	1	0,88	0,22	0,00	0,53

Id Centre	Code centre	Baseline Scenario						NBS Fractal Scenario				
		Level	Occas	Monthly	Weekly	Daily	Total	Occas	Monthly	Weekly	Daily	Total
0-3-4	00	3	1	0,87	0,14	0,00	0,50	1	0,92	0,22	0,00	0,53
0-3-5	00	3	1	0,85	0,13	0,00	0,50	1	0,89	0,15	0,00	0,51
0-3-6	00	3	1	0,87	0,28	0,00	0,54	1	0,92	0,28	0,00	0,55
0-4-0	01	2	1	0,96	0,07	0,00	0,51	1	0,88	0,08	0,00	0,49
0-4-1	00	3	1	0,93	0,23	0,00	0,54	1	0,90	0,23	0,00	0,53
0-4-2	01	3	1	0,95	0,24	0,00	0,55	1	0,93	0,29	0,00	0,55
0-4-3	02	3	1	1,00	0,22	0,00	0,55	1	0,90	0,23	0,00	0,53
0-4-4	03	3	1	0,97	0,28	0,00	0,56	1	0,85	0,28	0,00	0,53
0-4-5	04	3	1	0,88	0,57	0,00	0,61	1	0,81	0,57	0,00	0,60
0-4-6	05	3	1	0,88	0,31	0,00	0,55	1	0,77	0,31	0,00	0,52
0-5-0	01	2	1	0,88	0,14	0,00	0,51	1	0,79	0,23	0,00	0,50
0-5-1	00	3	1	0,76	0,13	0,00	0,47	1	0,71	0,21	0,00	0,48
0-5-2	00	3	1	0,72	0,15	0,00	0,47	1	0,72	0,15	0,00	0,47
0-5-3	00	3	1	0,70	0,31	0,00	0,50	1	0,78	0,31	0,00	0,52
0-5-4	00	3	1	0,74	0,56	0,00	0,58	1	0,81	0,56	0,00	0,59
0-5-5	00	3	1	0,85	0,45	0,00	0,57	1	0,76	0,45	0,00	0,55
0-5-6	00	3	1	0,78	0,17	0,00	0,49	1	0,75	0,18	0,00	0,48
0-6-0	01	2	1	1,00	0,37	0,00	0,59	1	0,77	0,45	0,00	0,55
0-6-1	00	3	1	0,97	0,45	0,00	0,61	1	0,75	0,45	0,00	0,55
0-6-2	00	3	1	0,95	0,56	0,00	0,63	1	0,77	0,56	0,00	0,58
0-6-3	00	3	1	0,98	0,76	0,00	0,68	1	0,79	0,76	0,00	0,64
0-6-4	00	3	1	0,99	0,35	0,00	0,58	1	0,77	0,35	0,00	0,53
0-6-5	00	3	1	0,96	0,33	0,00	0,57	1	0,69	0,51	0,00	0,55
0-6-6	00	3	1	0,97	0,23	0,00	0,55	1	0,70	0,23	0,00	0,48
Total			1	0,74	0,28	0,00	0,50	1	0,71	0,32	0,01	0,51

Appendix H. Power spectral of the refractive index in the variance, inertial-convective and dissipation range

When analysis the spatial behaviour of the turbulence, it must be considered the fluctuations of atmospheric fluxes occurs in the three dimensions of the space. The power spectral in the three dimensions has been widely studied and discussed, because its relevance to determinate statistics of measures from the scintillometer.

The 5/3 power law in the inertial range was extended to the three dimensions. Then, Kolmogorov (1941) derived the spectrum model that follows a 11/3 power law in the inertial-convective range as:

$$\phi_{3n} = 0.033{C_n}^2 k^{-11/3}$$

where, k is the three-dimensional wave number. This form is known as Kolmogorov's spectrum, but is not more respected in the dissipation range, where $k^{-11/3}$ overestimates ϕ_n. In this scale, the spectrum is better described by Hill's theory, adding the function $f_A(kl_0)$ that describes the deviation from the inertial range into the dissipation range:

$$\phi_{3n} = 0.033{C_n}^2 k^{-\frac{11}{3}} f_A(kl_0)$$

The Hill's theory directly relates the power spectra to the thermodynamic state of the air. Since several studies have found this deviation or transition has a bump shape, this is called the Hills bump.

It is important to note that Laser scintillometers primarily operate in the inertial range, as well as the dissipation range. Moreover, the intensity fluctuations of the EM detected by the scintillometer are related to eddies at the scale of the aperture diameter (0.10 m).

The three-dimensional power spectral ϕ_{3n} in the inertial-convective range of one-dimension become:

$$\phi_n = 0.0249{C_n}^2 k^{-5/3}$$

Publications

Papers:

- Castellanos, L.A.; Versini, P.-A.; Bonin, O.; Tchiguirinskaia, I. A Text-Mining Approach to Compare Impacts and Benefits of Nature-Based Solutions in Europe. Sustainability 2020, 12, 7799. https://doi.org/10.3390/su12187799

Communications:

- Characterization of the Evapotranspiration flux on a Blue Green Solution. EGU 2019 (April 2019).
- Large Aperture Scintillometer measurements above a large green roof to assess the evapotranspiration flux. EGU 2020 (Mars 2020).
- A text-mining approach to assess impacts and benefits of Nature-Based Solutions. EGU 2020 (Mars 2020).
- Multifractal approach to urban green spaces distribution in Est-Paris agglomeration (France) and potential benefits. AGU 2020 (December 2020).
- Analysis of spatial dimensions and explicit multifractal modelling for the deployment of green areas in an urban agglomeration. EGU 2021 (April 2021).
- Scaling invariance behaviour of thermal fluxes from an extensive green roof. EGU 2022 (May 2022).